Experimental and Numerical Investigation of the Hydrodynamics of Microfiltration Processes Using a Multi-Scale Approach

Von der Fakultät für Maschinenwesen der Rheinisch-Westfälischen Technischen Hochschule Aachen zur Erlangung des akademischen Grades eines Doktors der Ingenieurwissenschaften genehmigte Dissertation

vorgelegt von

Steffen Bütehorn

Berichter: Universitätsprofessor Dr.-Ing. Thomas Melin

Professor Anthony Gordon Fane, Ph.D.

Tag der mündlichen Prüfung: 26. Oktober 2010

Berichte aus der Verfahrenstechnik

Steffen Bütehorn

Experimental and Numerical Investigation of the Hydrodynamics of Microfiltration Processes Using a Multi-Scale Approach

Shaker Verlag
Aachen 2011

Bibliographic information published by the Deutsche Nationalbibliothek
The Deutsche Nationalbibliothek lists this publication in the Deutsche Nationalbibliografie; detailed bibliographic data are available in the Internet at http://dnb.d-nb.de.

Zugl.: D 82 (Diss. RWTH Aachen University, 2010)

Printed in Germany.

ISBN 978-3-8440-0061-0
ISSN 0945-1021

Shaker Verlag GmbH • P.O. BOX 101818 • D-52018 Aachen
Phone: 0049/2407/9596-0 • Telefax: 0049/2407/9596-9
Internet: www.shaker.de • e-mail: info@shaker.de

Acknowledgements

The thesis at hand is an outcome of my research activities at the Chair of Chemical Process Engineering (AVT.CVT) at RWTH Aachen University from October 2005 to October 2010. During my time as a Ph.D. student, a number of institutions and colleagues were contributing to my work and I would like to take this opportunity to gratefully acknowledge all their good efforts. In particular, I would like to thank

- Prof. Thomas Melin for giving me the great chance to join his group after my studies, for the supervision of my Ph.D. and for his inspiration and kindness.
- Prof. Anthony Gordon Fane for being my external examiner and the great honour to discuss my ideas with him.
- Prof. Reinhold Kneer for being the chairman of my Ph.D. defence.
- Prof. Matthias Wessling for sharing his enthusiasm and scientific spirit.
- the European Commission, the German Research Foundation (DFG) and the German Academic Exchange Service (DAAD) for their financial support.
- Prof. TorOve Leiknes, Boris Lesjean and Rita Hochstrat on behalf of all institutions involved in the MBR-Network Cluster for the fruitful discussions.
- Klaus Voßenkaul and Dirk Volmering from Koch Membrane Systems GmbH for providing membrane samples and the very good collaboration.
- Roland Büchele and Peter Greenwood from Eka Akzo Nobel for providing silica suspensions.
- Prof. Vicki Chen, Prof. Greg Leslie, Pierre Le-Clech, Matthew Brannock, Shane Cox and Yuan Wang from the UNESCO Centre for Membrane Science and Technology at the University of New South Wales (UNSW) in Sydney, Australia, for giving me the great chance to work in their lab and all their support.
- Markus Küppers and Lavinia Utiu from Macromolecular Chemistry (ITMC) at RWTH Aachen University for sharing their NMR skills and being excellent project partners.
- Bastian Mahr and Martin Behling from the Institute for Multiphase Processes (IMP) at the Leibniz University of Hannover (LUH) for conducting the CT measurements and all their good efforts.
- my mentors Prof. Thomas Wintgens, Chen Ning Koh and Sven Lyko for their advice during the earlier days of my Ph.D. studies and their continuous support.
- Gero Gerhards and Hans Breisig for reviewing this manuscript and the helpful inputs.

- the whole AVT family for their contributions and the warm atmosphere during the past years. I really enjoyed the time we have spent together – both at work and for leisure!

- all student assistants and student researchers who made this possible, namely Hicham Ait El Haj, Mubashir Ali, Thomas Blach, Hans Breisig, Frederike Carstensen, Adele Clausen, Ervina Ervina, Gero Gerhards, Xue Han, Thomas Harlacher, Sebastian Hartmann, Daas Jabbour, Venugopal Kandi, Hans Kilian, Malte Köchling, Clemens Lattermann, Yang Liu, Nicolas Nauels, Caio Prado, Khairul Azman Rahmat, Wolfgang Schulz, Irene Somoza Parada, Jan Stodollick, Alexander Tollkötter, Xu Wang and Christina Winterscheid. I thank you all for your tremendous efforts!

- my friends from both Aachen and my home-town Wedemark who kept on supporting me also in busier times.

- Alexander Scharf and Malte Petersen as well as Annette and Nils Beeckmann for their support and the great time during our studies in Hannover.

- Nils Vatheuer who helped me getting settled in Aachen.

- my family Monika and Hans-Heinrich Bütehorn as well as Claudia and Sieghard Schneider for their continuous support during my studies.

Aachen, April 2011

Steffen Bütehorn

"*Concepts that have proven useful in ordering things easily achieve such authority over us that we forget their earthly origins and accept them as unalterable givens*"

Albert Einstein (*1879, †1955, German-Swiss-Austrian-American physicist)

Dedicated to my family.

Abstract

Submerged membrane bioreactor (MBR) processes for treating municipal or industrial wastewater are one of the most promising applications of microfiltration membranes. Previous studies were spread over various fields of research including water science, microbiology, chemical engineering, material science and process control. All of the above research societies contributed comprehensively to a further improvement of the technology. Nevertheless, it is known that higher operational expenses compared to conventional water treatment strategies weaken the competitiveness of MBRs. More precisely, recent energy efficiency analyses identified the coarse bubble aeration of the membrane unit to consume the biggest proportion of the overall energy input.

Therefore, hydrodynamic conditions in submerged microfiltration processes were investigated experimentally and numerically on three different scales in the framework of this study. The overall objective was to evaluate the impact of operating parameters, feed characteristics and module design features on the efficiency of air bubbling to control cake layer formation. On a micro-scale, local phenomena such as permeate flow, particle deposition and cake removal were non-invasively visualised with nuclear magnetic resonance (NMR) imaging. Complementary filtration experiments were conducted by applying a number of test facilities equipped with single hollow-fibres (meso-scale) or single hollow-fibre bundles (macro-scale) in different modes of operation. The bubble-induced fibre movement as a key parameter affecting the overall process performance was tracked with a direct observation (DO) technique (meso-scale). A macroscopic computational fluid dynamics (CFD) approach based on X-ray computer tomography (CT) scans and calibrated with numerical pressure loss correlations was established.

The investigations have shown the impact of lumen-side pressure losses on the distribution of local permeate flux. Cake formation appeared to be heterogeneous, with thicker cakes close to the point of permeate extraction. The cake growth was in good agreement with the fouling rate dTMP/dt as a function of permeate flux, solids concentration and aeration conditions. Cake layer removal was enhanced with an increase in net aeration rate, bubble-induced fibre movement and background circulation flow. Interestingly, a higher aeration frequency for the same net aeration rate and an optimal gross aeration rate were observed, which outlines potentials for reducing aeration requirements. Fibre motion was more intensive for higher aeration rates, but insensitive to packing density variations. The CFD results were indicating a clear impact of fibre arrangement, superficial inlet velocity and solids concentration on the local cross-flow velocity and turbulence intensity. A well-defined slug flow was observed before the Taylor bubble penetrates into the porous medium. Moving forward, different module configurations will be evaluated with CFD, thus providing insights into the complex multi-phase flow pattern which are not accessible with experimental observation techniques.

Zusammenfassung

Getauchte Membranbioreaktoren (MBRs) in der kommunalen und industriellen Abwasserbehandlung stellen eine der vielversprechendsten Anwendungen von Mikrofiltrationsmembranen dar. Zahlreiche Forschungsaktivitäten auf dem Gebiet der Wasserchemie, Mikrobiologie, Verfahrenstechnik, Materialwissenschaften sowie der Prozesssteuerung haben zur Weiterentwicklung dieser Technologie beigetragen. Dennoch beeinträchtigen höhere Betriebskosten eines MBRs im Vergleich zu konventionellen Behandlungsstrategien dessen Wettbewerbsfähigkeit. Studien zum Energieverbrauch haben zudem gezeigt, dass der größte Anteil der Gesamtenergie für die grobblasige Belüftung der Membranstufe aufgebracht werden muss.

Die Hydrodynamik in getauchten Mikrofiltrationsprozessen wurde im Rahmen der vorliegenden Arbeit auf unterschiedlichen Skalen sowohl experimentell als auch numerisch untersucht. Ziel dieser Studien ist es, den Einfluss von Betriebs-, Stoff- und Moduldesignparametern auf die Effizienz der Luftblasenspülung zur Kontrolle der Deckschichtbildung zu bewerten. Auf mikroskopischer Ebene wurden lokale Phänomene wie Permeatströmung, Partikelablagerung und Deckschichtabtrag nicht-invasiv mithilfe der Magnetresonanztomographie (NMR) untersucht. Ergänzende Filtrationstests wurden mit einer Reihe von Einzelfaser- (Mesoskala) bzw. Einzelbündelanlagen (Makroskala) und unterschiedlichen Betriebsweisen durchgeführt. Die blaseninduzierte Faserbewegung wurde mithilfe einer digitalen Bildauswertung (DO) quantifiziert (Mesoskala). Zudem wurde ein Ansatz zur numerischen Strömungssimulation (CFD) auf makroskopischer Ebene basierend auf Röntgentomographie (CT)-Scans und Druckverlustkorrelationen entwickelt.

Die Untersuchungen haben gezeigt, dass der permeatseitige Druckverlust einen Einfluss auf den lokalen Permeatfluss hat. Die Deckschicht ist dicker in der Nähe des Permeatabzugs und deren Anwachsen stimmt mit der Fouling-Rate dTMP/dt als Funktion des Permeatflusses, der Feststoffkonzentration und der Belüftungsparameter gut überein. Der Abbau der Deckschicht wird durch eine höhere Nettobelüftungsrate, eine blaseninduzierte Faserbewegung sowie eine Zirkulationsströmung begünstigt. Zudem konnte eine Verbesserung der Filtrationsleistung durch eine höhere Belüftungsfrequenz mit konstanter Nettobelüftungsrate sowie eine optimale Bruttobelüftungsrate beobachtet werden. Die Faserbewegung wird durch eine höhere Belüftungsrate begünstigt, weist jedoch keine klare Abhängigkeit von der Packungsdichte auf. Erste Simulationsergebnisse haben gezeigt, dass die Faseranordnung, die Zulaufgeschwindigkeit und der Feststoffgehalt einen Einfluss auf die lokale Überströmung und die Turbulenz haben. Eine definierte Kolbenblasenströmung wurde vor dem Eintritt der Blase in das poröse Medium beobachtet. In zukünftigen Untersuchungen sollen unterschiedliche Modulkonfigurationen verglichen werden. Dies ermöglicht Einblicke in das komplexe mehrphasige Strömungsfeld, welche messtechnisch nur schwer zugänglich sind.

Table of contents

Symbols

Symbol	Unit	Meaning
a	[µm]	Edge length
A	[m^2]	Area
A, B, C, D	see equation (3.6)	Model parameters (see equation (3.6))
B	[T]	Magnitude of the static magnetic field
c	[vol. %], [g/L]	Concentration
C	[-]	Model parameter (see equation (5.3))
C, D	[-]	Model parameters (see equation (4.25))
Co	[-]	Courant number
d	[m]	Diameter
f	[1/s]	Frequency
FA	[mm]	Fibre amplitude
FOV	[mm x mm x mm]	Field of view
G	[T/m]	Magnitude of the applied gradient
H	[m]	Height
HRT	[h]	Hydraulic retention time
J	[L/(m^2 h)] = [LMH]	Permeate flux
k	depends on n (*)	Fluid consistency index
k	[m^2/s^2]	Turbulence kinetic energy
k, n	see Hermia [1982]	Model parameters (see equation (3.9))
K	[L/(m^2 h bar)]	Permeability (T = 20 °C)
L	[m]	Length
m	[kg]	Mass
m	[T s/m] OR [T s^2/m]	Moment of the gradient
MLSS	[g/L]	Mixed liquor suspended solids concentration
n (*)	[-]	Flow behaviour index (*)

N	[-]	Number
p	[bar]	Pressure
pH	[-]	pH value
Pe	[-]	Péclet number
PWP	[L/(m^2 h bar)]	Pure water permeability (T = 20 °C)
r	[m]	Spatial position
R	[(m^2 h bar)/L]	Resistance (T = 20 °C)
Re	[-]	Reynolds number
SAD	[m^3/(m^2 h)]	Specific aeration demand
SRT	[d]	Sludge retention time
t	[s]	Time
T	[°C]	Temperature
T	[s]	Relaxation time
TE	[ms]	Echo time
TMP = Δp	[bar]	Transmembrane pressure difference
dTMP/dt	[bar/min], [mbar/s]	Fouling rate
TR	[ms]	Repetition time
v	[m/s]	Velocity
V	[L], [m^3]	Volume
x, y, z	[m], [m], [m]	Coordinates
X	[%]	Rejection

α	[rad]	Angle of radio frequency pulse
β	[°]	Friction angle
δ	[µm]	Cake layer thickness
δ	[s]	Pulse duration

Δ	[s]	Pulse time separation
ε	[m^2/s^3]	Dissipation rate of turbulence kinetic energy k
ϕ	[rad]	Phase of spins precessing in magnetic field
γ	[-]	Shear angle
γ	[Hz/T]	Gyromagnetic ratio
η	[Pa s]	(Dynamic) Viscosity
φ	[-]	Porosity
ρ	[kg/L], [kg/m^3]	Density
τ	[N/m^2]	Shear stress
ω	[mm/(s m)]	Angular velocity
ω	[1/s]	Specific dissipation rate of turbulence kinetic energy k
ω	[rad/s]	Larmor frequency
ξ	[-]	Friction factor
ζ	[mV]	Zeta-potential

Subscripts

Subscript	**Meaning**
20	@ T = 20 °C
a	Apparent
ad	Adsorption
air	Air
avg	Average
bub	bubble
bundle	Bundle
cl	Cake layer

CFD	Computational fluid dynamics
crit	Critical
cum	Cumulative
cyc	Cycle
db	Dispersed bubble
dextran	Dextran
drop	drop/droplet
exp	Experimental
fib, fibre	fibre
film	Liquid film
fin	Final
frame	Frame
F	Feed
Forch	Forchheimer
gross	Gross (i.e. averaged over the cycle duration)
local	local
m	Membrane (unit)
max	Maximum
meas., measured	Measured value
min	Minimum
n	Indexed variable
n-N	Non-Newtonian
net	Net (i.e. averaged over the entire test run)
Newton	Newtonian
o	outer
OFF	Aeration off
oil	Oil
ON	Aeration on

part	Particle
pb	Pore blocking
phase	Phase-encoding
pix	Pixel
P	Permeate
h	hydraulic
i	Internal
i	Component i
i	Indexed variable
inlet	Inlet
iron	Iron (III) oxide
irr	Irreversible
read	Frequency-encoding
ref	Reference
rev	Reversible
seq	Sequence
sil	Silica
slice	Slice-selection
slug	Gas or liquid slug
ss, steady-state	Steady-state conditions
tot	Total
turb	turbulent
T	@ temperature T
vel	Velocity-encoding
wall	Wall
μ	Index of model parameter

Abbreviations

Abbreviation	**Meaning**
AFM	Atomic force microscopy
ASM1	Activated sludge model no. 1
CAD	Computer-aided design
CF	Cross-flow
CT	X-ray computer tomography
CFD	Computational fluid dynamics
DLS	Dynamic light scattering
DO	Direct observation
DOTM	Direct observation through the membrane
EPS	Extracellular polymeric substances
EKA	Electro kinetic analyser
F2, F3, F5	Classification of hollow-fibre membranes
FI	Flow meter
FS	Flat-sheet membrane
GKW	Gruppenklärwerk
HF	Hollow-fibre membrane
HPLC	High performance liquid chromatography
LES	Large eddy simulation
LDV	Laser Doppler velocimetry
MBR	Membrane bioreactor
MF	Microfiltration
MT	Multi-tubular membrane
MW	Molecular weight
MWCO	Molecular weight cut-off
NF	Nanofiltration

NMR	Nuclear magnetic resonance
(N)MRI	(Nuclear) Magnetic resonance imaging
NOM	Natural organic matter
PDF	Probability density function
PES	Polyether sulphone
PFG	Pulsed field gradient
PGSE	Pulsed gradient spin echo
PI	Pressure transducer
PIV	Particle image velocimetry
PWP	Pure water permeability
RANS	Reynolds-averaged Navier-Stokes equations
RF	Radio frequency
RNG	Renormalisation group
RO	Reverse osmosis
SAD	Specific aeration demand
SEM	Scanning electron microscopy
SST	Shear stress transport
STL	Stereolithography file format
TOF	Time of flight
TI	Thermocouple
TMP	Transmembrane pressure
UF	Ultrafiltration
VOF	Volume of fluid
WWTP	Wastewater treatment plant
XPS	X-ray photoelectron spectroscopy

(1) Motivation

Synthetic microporous membranes were patented in 1922 [Zsigmondy and Bachmann, 1922] and commercialised in 1929 for drinking water analytics. Further applications in the field of cell harvesting, clarification and sterilisation contributed to a growing market of microfiltration in the automobile, metal processing, battery, pharmaceutical, biomedical, food and beverage as well as water treatment industry [Belfort *et al.*, 1994]. Nowadays, one of the most important applications of microfiltration processes are so-called membrane bioreactors (MBRs). These membrane units are commonly used in municipal and industrial wastewater treatment for rejecting suspended microorganisms from biologically cleaned water. Most of the medium- to large-scale MBRs in municipal sewage treatment are operated in submerged mode [Judd, 2006]. For this mode of operation, air bubbling is applied to control cake layer formation by generating surface shear [Cui *et al.*, 2003]. MBRs are known to be advantageous compared to the conventional activated sludge process regarding the overall foot print, effluent quality and process control. However, higher operating expenses are still a bottleneck, which weakens the competitiveness of MBR technology (adapted from [Melin and Rautenbach, 2007]). Therefore, efforts are made in research and development to evaluate potentials for a further process optimisation from both phenomenological and economical points of view.

The Pöyry GKW GmbH conducted a comprehensive study on the energy consumption of full-scale wastewater treatment plants (WWTPs) based on MBR technology. They have chosen one of the world's largest MBR plants located at the WWTP Nordkanal in Kaarst (NRW, Germany) as a case study. This plant is operated by the Erftverband with a capacity of 80,000 population equivalents and a total membrane area of 84,480 m^2 [Lyko *et al.*, 2007+2008]. Main outcomes of this study are presented in **Figure (1.1)**, with kind reprint permission of the Erftverband.

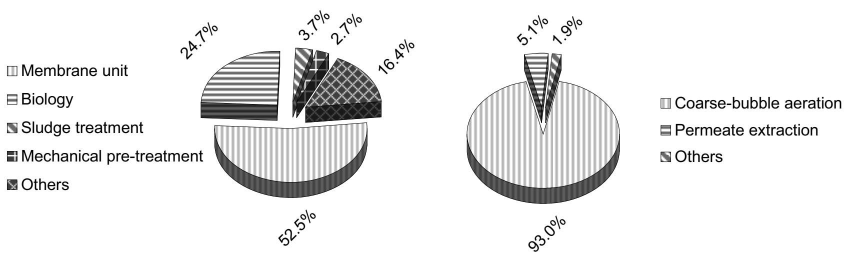

Figure (1.1) Relative contributions to the overall energy consumption (left) and the energy consumption of the membrane unit (right) of the WWTP Nordkanal (Germany) in the year 2007 [Pöyry, 2009].

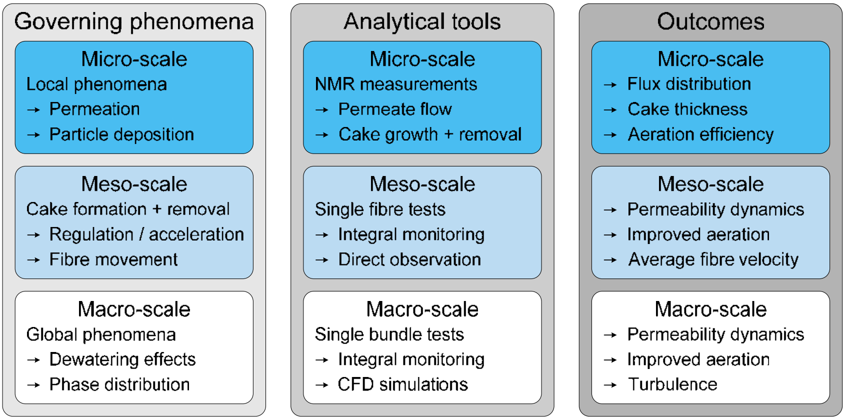

Figure (1.2) Motivation of this study: Governing phenomena (left), applied analytical tools (centre) and outcomes (right) on a micro- (top), meso- (centre) and macro-scale of microfiltration processes (bottom).

The overall energy consumption was distributed among the membrane compartment, the biology, sludge treatment and mechanical pre-treatment stages. It was found that the membrane unit consumes the biggest proportion of the overall energy input with 52.5 %. The energy consumption of the membrane unit originates firstly from the coarse bubble aeration (93 %) and secondly from the permeate extraction (5.1 %). Hence, the highest potential for energy saving is linked to an optimised use of air bubbling applied for a mechanical membrane cleaning.

In the scope of a further understanding of phenomena governing the microfiltration performance, a number of analytical tools were applied on three different scales in the framework of this study, see **Figure (1.2)**. In addition to comprehensive experimental and numerical investigations, also the development of the underlying methodology was part of these activities. Depending on the desired degree of detailedness, these observations were conducted on a micro-, meso- or macro-scale as summarised below.

- On a **micro-scale**, local phenomena such as the permeation of water and particles smaller than the pore size and the deposition of particles larger than the pore size are occurring. The resulting distribution of permeate flux and cake growth along the membrane were non-invasively measured with nuclear magnetic resonance (NMR) imaging. In addition to parameters such as setpoint permeate flux and solids concentration, the efficiency of cake layer removal due to air bubbling was quantified for different aeration strategies. The experiments were undertaken for a filtration of a model suspension using a single hollow-fibre and the results are summarised in section (5.1).

- Cakes with multiple layers are formed as particle deposition progresses, which causes a self-regulating or self-accelerating permeability decline. An optimisation of aeration parameters was the focus of this part of the study. The bubble-induced tangential flow interacts with the fibres, thus leading to additional shear forces as a consequence of fibre motion and fibre-fibre interactions. This fibre movement is known to enhance cake layer removal [Wicaksana *et al.*, 2006] and was tracked as a function of vertical position, aeration rate and packing density with a direct observation technique. These **meso-scale** phenomena were investigated in a number of filtration experiments with single fibres or bundles with few fibres and an integral monitoring of the filtration performance as presented in section (5.2).

- **Macro-scale** effects such as dewatering of the suspension and gas-liquid phase distribution gain more relevance in a bundle of 228 hollow-fibres. The integral TMP rise at constant permeate flux was monitored for a filtration of the same model suspension used for the single fibre studies. In addition to an operation in quasi-submerged mode, a superposed cross-flow was applied to account for a background circulation velocity as observed in full-scale units [Drews *et al.*, 2008; Prieske *et al.*, 2008]. A comparison of different aeration strategies was performed on the basis of critical flux and critical aeration rate tests, see section (5.3). Complementary computational fluid dynamics (CFD) simulations were conducted to evaluate the impact of fibre arrangement on the flow through hollow-fibre bundles. The CFD approach established in this study and presented in section (5.4) is applicable to both single- and multi-phase flows for module design optimisation purposes.

In the following section, fundamentals of micro- and ultrafiltration processes, modes of operation, submerged membrane modules and submerged MBR processes are introduced. Subsequently, a literature review focussing on the rheology of suspensions, hydrodynamic conditions, observation techniques and CFD simulations in MBR research is given. The materials and methods are subdivided into membrane and membrane module characteristics, properties of the model suspension and experimental setups used. Furthermore, methodologies applied for NMR imaging, direct observation of fibre movement and CFD simulations are introduced. The results are presented in section (5) following the structure shown in **Figure (1.2)**. Section (6) provides a summary of major outcomes, general conclusions and recommendations and outlines potentials or limitations for future studies.

(2) Fundamentals

This chapter provides details about micro- and ultrafiltration processes, modes of operation in general and submerged membrane modules in membrane bioreactors treating municipal wastewater in particular. The corresponding terms and definitions are slightly differing in reference books [Mulder, 1996; Pinnekamp and Friedrich, 2003; Judd, 2006; Melin and Rautenbach, 2007]. Therefore, the main aim of the following sections is to briefly outline fundamentals related to the study at hand rather than giving a comprehensive overview.

(2.1) Micro- (MF) and ultrafiltration (UF) processes

The driving force of membrane processes such as microfiltration (MF), ultrafiltration (UF), nanofiltration (NF) and reverse osmosis (RO) is a pressure difference across the membrane, the so-called **transmembrane pressure (TMP)**

$$\Delta p = TMP = p_F - p_P \,. \tag{2.1}$$

In equation (2.1), p_F corresponds to the pressure at the inlet of the membrane unit (the so-called feed side) and p_P to the pressure at the outlet for the filtrate or permeate stream (the so-called permeate side). The outlet for the concentrate or retentate stream is referred to as retentate side. While typical TMPs for MF processes are in the range of 0.3 to 3 bar, UF processes are operated at TMPs of 0.5 to 10 bar.

In MF and UF processes, porous membrane materials are used with a pore size in the range of 0.08 to 10 µm and of 0.007 to 0.12 µm, respectively. In these processes, diffusive and convective mass transport through the membrane pores occurs simultaneously. In addition to the pore size distribution, the **molecular weight cut-off** (MWCO) of a membrane is a well-known parameter to characterise the separation performance. The MWCO is defined as the molecular weight of a feed component which is rejected to a degree of 90 % by the membrane,

$$X_i = \frac{c_{F,i} - c_{P,i}}{c_{F,i}} = 1 - \frac{c_{P,i}}{c_{F,i}} = 90\,\% \quad \Rightarrow \quad MW_i = MWCO\,. \tag{2.2}$$

In equation (2.2), X_i corresponds to the rejection, $c_{F,i}$ to the feed concentration, $c_{P,i}$ to the permeate concentration and MW_i to the molecular weight of component i. MF membranes are frequently used for a separation of solids from suspensions, whereas UF membranes are more often applied to remove dissolved macromolecules. For this reason, the filtration tests conducted in this study are referred to as MF rather than UF, although a nominal pore diameter of 50 nm suggests that the membrane belongs to the UF group.

(2.2) Modes of operation

Membrane filtration processes are operated with a constant permeate flux or a constant TMP, in outside-in or inside-out mode or as a dead-end, cross-flow or submerged filtration. The filtration performance in general is characterised by the **permeability**

$$K = \frac{J}{TMP} \tag{2.3}$$

as the ratio of **permeate flux**

$$J = \frac{\dot{V}_P}{A_m} \tag{2.4}$$

and TMP. The permeate flux is equal to the permeate flow rate $\dot{V}_P$ divided by the membrane area A_m. The reciprocal of the permeability (adapted from Song [1998])

$$R_{tot} = \frac{1}{K} = \frac{TMP}{J} \tag{2.5}$$

is known as the total resistance of the filtration process R_{tot}. This **total filtration resistance** is equal to the sum of membrane resistance R_m, resistance due to adsorption of dissolved or dispersed matter R_{ad}, resistance due to pore blocking R_{pb} and resistance due to reversible ($R_{cl,rev}$) and irreversible cake layer formation ($R_{cl,irr}$),

$$R_{tot} = R_m + R_{ad} + R_{pb} + R_{cl,rev} + R_{cl,irr}\,. \tag{2.6}$$

It is important to note that other definitions of filtration resistance exist (see Darcy's law as described in e.g. Romero and Davis [1990]). However, the definitions introduced above have been used throughout the experimental section of this thesis. One of the major bottlenecks in MF and UF processes is **membrane fouling**, which is a general term for micro-scale phenomena negatively affecting the filtration performance. All impacts can be subdivided into groups of fouling factors such as (i) the nature of the feed to the membrane, (ii) membrane properties and (iii) the hydrodynamic environment experienced by the membrane [Zhang *et al.*, 2006]. In the framework of this study, all phenomena leading to an increase in R_{tot} are regarded as membrane fouling, except for an increase in the reversible cake layer resistance $R_{cl,rev}$. Typical fouling mechanisms include irreversible cake layer formation, pore blocking, inner pore adsorption and biofouling as presented in **Figure (2.1)** and further discussed by Melin and Rautenbach [2007]. As being one form of irreversible cake formation, the term "cake compaction" is used in the following sections to represent cake compression, particle migration and the infiltration of smaller particles into the existing cake structure. All these phenomena lead to a reduced porosity of the cake.

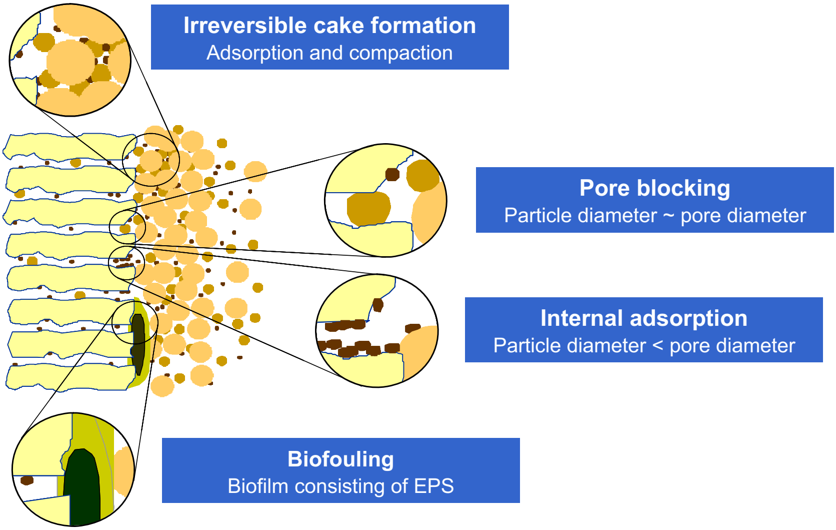

Figure (2.1) Membrane fouling due to irreversible cake layer formation, pore blocking, internal adsorption and biofouling (adapted from Melin and Rautenbach [2007]).

(2.2.1) Constant flux vs. constant TMP

Two different process control strategies are established for the operation of MF and UF units. These are schematically shown in **Figure (2.2)**. The operation at **constant permeate flux** is advantageous from an operator's point of view, since the membrane unit is filtrating with the desired throughput at all times. The increase in filtration resistance is compensated by an increase in TMP. After reaching a maximum TMP due to a limited mechanical stability of the membrane, a permeate backwashing cycle (i.e. a temporary reversal of flow direction with TMP < 0) is initiated. This leads to a partial removal of the cake layer before the next filtration cycle starts. The permeability decline is in this case self-accelerating, since an increase in TMP is coupled with an increase in overall driving force, although the cake thickness may significantly vary along the membrane. This leads to an increase in local permeate flux in regions of thinner cakes, which is followed by an enhanced local particle deposition [Chang *et al.*, 2002a; Bacchin, 2004; Zhang *et al.*, 2006].

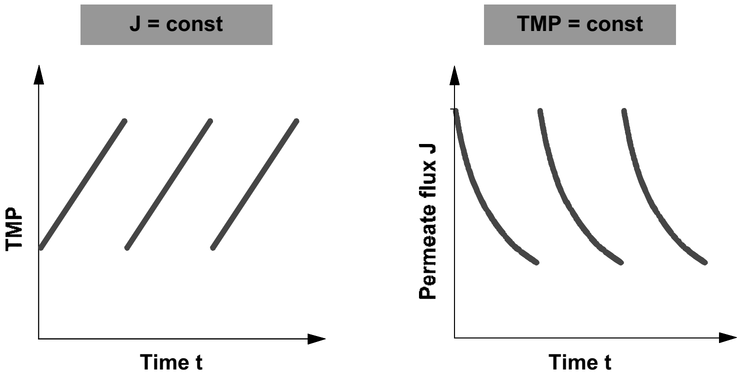

Figure (2.2) TMP rise for an operation at constant permeate flux (left) and permeate flux decline for an operation at constant TMP (right) with filtration time (adapted from Melin and Rautenbach [2007]).

In contrast, an operation at **constant TMP** is a rather simple approach since a constant hydrostatic head in the feed channel is sufficient to assure stable filtration conditions. The cake formation is in this case causing a decline in permeate flux until backwashing cycles are initiated. An operation at constant TMP (i.e. at constant driving force) is characterised by a self-regulation of permeability decline. This means that the local cake build-up influences the local permeate flux directly without affecting the overall driving force of the process. However, it is important to note that variations in average permeate flux are coupled with variations in average particle transport to the membrane. Hence, plotting the total filtration resistance

$$R_{tot} = f(m_P) \tag{2.7}$$

as a function of extracted permeate mass m_P is recommended for comparative studies with differences in permeate flux decline.

(2.2.2) Dead-end filtration mode

In 2-end or dead-end filtration mode, the retentate side of the module is opened for backwashing or feed channel flushing purposes only. The entire amount of feed is either permeating through the pore structure or rejected and accumulating on the membrane surface. Mechanical cleaning cycles are performed as soon as a minimum permeability due to cake layer formation is reached. Only gravitational or diffusive effects are contributing to the removal of deposited matter, since no tangential shear forces are imposed by the perpendicular flow pattern. For this reason, dead-end filtration is restricted to feed streams of relatively low solids concentration.

(2.2.3) Cross-flow filtration mode

The retentate side of the membrane unit is open during cross-flow filtration, so that a continuous tangential flow in the feed channel occurs. Hence, this so-called 3-end mode is characterised by a removal of deposited matter due to surface shear. Cross-flow filtration can be applied over a wide range of solids concentration by adjusting the throughput of the feed pump correspondingly. It is worth mentioning that the pressure loss in the feed channel leads to differences in local driving force along the membrane, which may affect the permeate composition and the product purity.

(2.2.4) Submerged filtration mode

A suction pump is applied in submerged filtration to reduce the pressure in the permeate channel, see bottom part of **Figure (2.3)**. Thus, this operating mode is restricted to relatively low driving forces, which limits its applicability to low-flux processes. In addition to the above-mentioned backwashing cycles, air bubbling is applied to control cake layer formation by generating surface shear. Submerged membrane units are low-cost modules without housing and are directly immersed into the suspension to be purified. Typical applications are the so-called membrane bioreactors (MBRs) as introduced in section (2.4). Please note that submerged filtration processes are often referred to as cross-flow filtration with bubble-induced instead of pump-induced tangential flow. In the latter case, submerged filtration is not regarded as a filtration mode on its own, but as a special form of cross-flow filtration.

(2.2.5) Outside-in vs. inside-out

The feed stream of a membrane filtration process can be charged to either the shell (outside-in filtration) or the lumen of the membrane unit (inside-out filtration). A shell-side feed flow is in many cases less confined compared to the lumen-side flow, which is advantageous due to a lower risk of channel blocking. On the other hand, a feed flow in the membrane lumen allows a proper adjustment of hydrodynamic conditions for both single- and multi-phase flow patterns because of defined feed channel dimensions.

(2.3) Submerged membrane modules

The investigations conducted in the framework of this study are related to submerged membrane bioreactor (sMBR) processes. For this reason, only submerged membrane modules are introduced below.

(2.3.1) Submerged flat-sheet modules

Two membrane sheets connected to the flat sides of a structured permeate spacer form a single plate of a flat-sheet module as schematically shown in the centre-left of **Figure (2.3)**.

The distance between the plates corresponds to the dimension of the feed channel, which significantly affects characteristics of the multi-phase flow and the affinity to channel blocking. The packing density of flat-sheet membrane units is typically lower than that of hollow-fibre units. Moreover, limitations in mechanical stability of the sealed membrane plates inhibit permeate backwashing, so that relaxation periods (i.e. a sequence of continuous aeration without filtration) are applied to remove the cake layer. However, flat-sheet systems are less prone to clogging in the presence of fibrous material and allow an operation with accurately managed tangential flow conditions due to a relatively confined feed channel.

(2.3.2) Submerged hollow-fibre modules

Capillary or hollow-fibre modules as shown in the centre-right of **Figure (2.3)**) are consisting of a large number of membrane filaments. These hollow-fibres are arranged to form compartments such as bundles or rows, which in turn form an entire membrane module. Depending on the supplier of the membrane unit, these vertically or horizontally oriented fibres are connected to the frame at both ends or at the bottom end only. Fibres fixed at the bottom end only are free to move laterally at the top end. Fibres fixed at both ends are usually longer than the distance between the upper and the lower fixing element, so that a certain degree of fibre movement takes place as well. The hollow-fibre itself consists of several layers. A supporting tissue provides tensile strength and flexibility, a porous support layer provides break strength and an active separation layer serves as a barrier for components to be rejected. The packing density can be further increased by increasing the number of fibres per bundle, which significantly affects hydrodynamic conditions. Furthermore, the large number of fibres moving in response to the unconfined and transient multi-phase flow makes an accurately managed flow of bubble-entrained biomass difficult. Compared to flat-sheet configurations, hollow-fibre modules show a higher packing density and are backwashable, but are more prone to clogging in the presence of fibrous material.

(2.4) Submerged membrane bioreactors (sMBRs) in wastewater treatment

In municipal or industrial wastewater treatment, microorganisms are responsible for the biodegradation of water pollutants. These biochemical reactions take place in the biological stage of a wastewater treatment plant. The biology is subdivided into unaerated (denitrification – reduction of nitrate to nitrogen gas) and aerated (nitrification – oxidation of ammonia to nitrate) compartments. Prior to the biological stage, an appropriate mechanical pre-treatment is performed. Further downstream, sedimentation of microorganisms and additional post-treatment steps are applied before discharging the cleaned water.

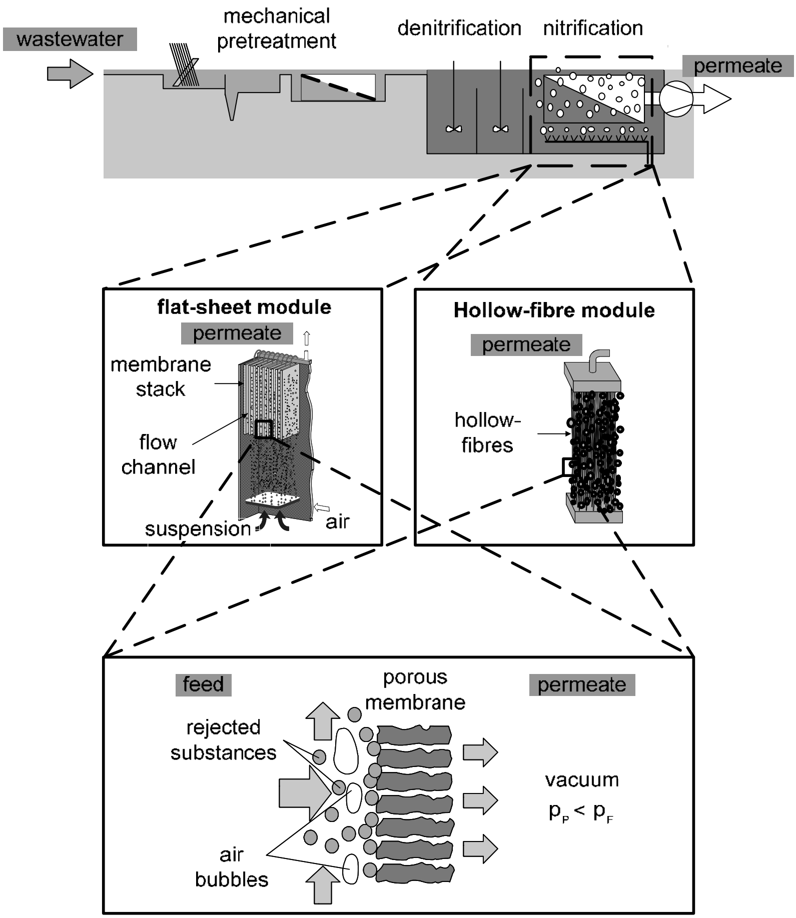

Figure (2.3) Schematics of the integration of membrane units into biological wastewater treatment (top), flat-sheet and hollow-fibre membrane modules (centre) and the submerged microfiltration process (bottom) (adapted from Melin and Rautenbach [2007]).

Membrane technology has been increasingly applied for separating biomass from cleaned water as a replacement for the conventional sedimentation and all additional post-treatment steps. Mainly submerged membrane units are used in medium- to large-scale municipal wastewater treatment plants [Judd, 2006]. First, efforts were made to double-use the fine bubble aeration in the nitrification compartment for both oxygen supply and cake layer removal as presented at the top of **Figure (2.3)**. However, it was found that fine bubbles are advantageous for oxygen transfer, whereas coarse bubbles are favourable to generate surface shear [Cui *et al.*, 2003]. Thus, a coarse bubble aeration of the membrane unit supplied to separate membrane tanks is state-of-the-art. More details on membrane-based wastewater treatment strategies can be found elsewhere [Pinnekamp and Friedrich, 2003; Judd, 2006].

Membrane bioreactors show several **advantages** compared to conventional wastewater treatment plants. These include (i) a lower footprint due the replacement of sedimentation tanks and other post-treatment steps, (ii) a higher effluent quality due to an operation at higher biomass concentration and a complete rejection of bacteria as well as (iii) a simpler process control due to decoupled hydraulic (HRT) and sludge retention times (SRT). Nevertheless, it is important to note that operational expenses of MBRs are still beyond that of the conventional activated sludge process. The coarse-bubble aeration to mechanically clean the membrane module was found to be a major cost factor [PÖYRY, 2009]. Therefore, the overall objective of this study is to further understand the role of hydrodynamics to enhance the filtration performance. An optimised membrane module design and optimised aeration conditions were envisaged to further improve the competitiveness of MBRs.

(3) Literature review

In the following sections, a literature review focussing on (i) the rheology of suspensions, (ii) hydrodynamics in membrane filtration processes, (iii) observation techniques and (iv) computational fluid dynamics (CFD) is given. This review is not aimed at covering all topics related to microfiltration processes in general, but to provide a basis for the investigations conducted in the framework of this study. Therefore, an overview of previous research activities is complemented with the underlying phenomenological background.

(3.1) Rheology of suspensions

All experimental investigations in this study are related to hydrodynamic conditions in the membrane compartment of MBRs treating municipal wastewater. A suitable model suspension had to be identified for these lab- and pilot-scale tests. The use of a model suspension ensures stable and reproducible conditions and allows a proper representation of rheological characteristics of MBR sludge. Activated sludge is a mixture of water, pollutants and microorganisms [Rosenberger, 2003] and shows **shear-thinning characteristics** [Lotito *et al.*, 1997; Moeller and Torres, 1997; Proff and Lohmann, 1997] and in some cases a **limiting shear stress** [Battistoni, 1997; Günder, 1999; Mikkelsen, 2001; Slatter, 1997]. Both effects are taken into account in the Hershel-Bulkley approach [Rosenberger *et al.*, 2002]

$$\tau = \tau_0 + k\left(\frac{dv}{dy}\right)^n . \tag{3.1}$$

In equation (3.1), τ and τ_0 correspond to the shear stress and the limiting shear stress, k to the fluid consistency index, v to the flow velocity, y to the coordinate perpendicular to v and n to the flow behaviour index. The limiting shear stress is originating from ionic bonds or van-der-Waals forces [Moshage, 2004] and causes the fluid to behave like elastic solid matter. This means that no viscous flow occurs for a shear exposure with $\tau < \tau_0$. The response to a shear exposure with $\tau > \tau_0$ is characterised by either Newtonian ($n = 1$) or non-Newtonian ($n \neq 1$) flow behaviour. With $\tau_0 = 0$, the Hershel-Bulkley approach is equal to the Ostwald-de Waele approach

$$\tau = k\left(\frac{dv}{dy}\right)^n . \tag{3.2}$$

The fluid consistency index k is resulting from van-der-Waals forces and the Brownian movement [Sigloch, 1991]. In case of a Newtonian fluid, k corresponds to the dynamic viscosity $\eta_{Newton} = k = const$ and is independent of the shear rate $\dot{\gamma}$. Therefore, the shear stress is proportional to the velocity gradient $\tau \propto dv/dy = \dot{\gamma}$. In contrast, the apparent (non-Newtonian) viscosity [Rosenberger *et al.*, 2002]

$$\eta_a = \eta_{n-N} = \frac{\tau}{\frac{dv}{dy}} = k\left(\frac{dv}{dy}\right)^{n-1} \quad , \tau_0 = 0 \tag{3.3}$$

is decreasing or increasing for a shear-thinning or shear-thickening fluid, respectively. In **Figure (3.1)**, the shear stress is plotted versus the shear rate for a Newtonian ($\tau_0 = 0$, $n = 1$), shear-thinning ($\tau_0 = 0$, $n < 1$), shear-thickening ($\tau_0 = 0$, $n > 1$) and Bingham fluid ($\tau_0 > 0$, $n = 1$).

The rather complex rheology of **activated sludge** is originating from the degree of cross-linking in the network of microorganisms [Rosenberger, 2003]. The network is more or less oriented depending on the shear exposure, leading to a reduction of viscosity with an increase in shear rate. Conflicting results were published concerning the limiting shear stress. Some research groups did not observe any minimum shear stress for viscous flow. Others determined a limiting shear stress occurring above mixed liquor suspended solids (MLSS) concentrations of 3 to 5 g/L [Günder, 1999] or above 80 g/L [Lotito *et al.*, 1997]. It was assumed that these discrepancies are due to significant measurement errors at low shear rates, which are depending on the accuracy of the measurement device and the test protocol used [Rosenberger, 2003].

Other parameters such as the concentration of fibrous microorganisms [Rosenberger, 2003] and extracellular polymeric substances (EPS) [Günder, 1999; Nagaoka *et al.*, 1996] are affecting the rheological properties. Nevertheless, the MLSS concentration was found to be the most relevant parameter [Rosenberger, 2003]. An increase in solids concentration leads to an increase of electrostatic attraction or repulsion [Moshage, 2004]. This causes a higher degree of cross-linking and a higher capacity for water to bind in the network of microorganisms, which results in a higher apparent viscosity of the medium. An increase in shear rate causes a partial breakup of this network and a reduction of apparent viscosity [Dentel, 1997; Proff and Lohmann, 1997]. Thixotropic effects are characterised by reversible changes in rheological properties over time. These effects are caused by a mechanical break-up of hydrogen or ionic bonds [Moshage, 2004] and are often in the range of the measurement inaccuracy [Rosenberger, 2003].

Rosenberger [2003] investigated rheological properties of sludge samples taken from 9 different MBRs and modelled the results with the above-mentioned approaches. The best correlation of apparent viscosity, shear stress and MLSS concentration was observable for a parameter fitting with the Hershel-Bulkley approach. However, the Ostwald-de Waele approach leading to the correlation [Rosenberger *et al.*, 2002]

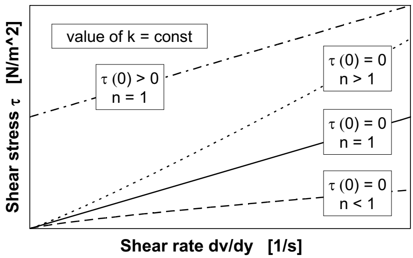

Figure (3.1) Shear stress as a function of shear rate for a Newtonian ($\tau_0 = 0$, n = 1), shear-thinning ($\tau_0 = 0$, n < 1), shear-thickening ($\tau_0 = 0$, n > 1) and Bingham fluid ($\tau_0 > 0$, n = 1).

$$\eta_a = \exp\left(2\ \text{MLSS}^{0.41}\right)\left(\frac{dv}{dy}\right)^{\left(-0.23\ \text{MLSS}^{0.37}\right)} \tag{3.4}$$

was favoured since the parameter range was more reasonable. In equation (3.4), η_a corresponds to the apparent viscosity of activated sludge, which is a function of MLSS concentration and shear rate $\dot{\gamma} = dv/dy$. An increase in MLSS concentration leads to an increase in fluid consistency index k and a decrease in flow behaviour index n. This means that activated sludge samples at higher solids content show higher apparent viscosities and more pronounced shear-thinning characteristics.

The filtration performance of a wastewater treatment plant is significantly affected by seasonal **temperature variations**. A decrease in ambient temperature in winter is leading to a higher viscosity of the activated sludge, which negatively affects filtration conditions. The impact of pressure fluctuations on the viscosity is less pronounced [Truckenbrodt, 1988]. Therefore, the permeability is temperature-corrected according to

$$K_{20} = K_T\ \frac{\eta_T}{\eta_{20}}, \tag{3.5}$$

with the permeability at T = 20 °C, K_{20}, the permeability at temperature T, K_T, the dynamic viscosity at temperature T, η_T, and the dynamic viscosity at T = 20 °C, η_{20}. Günder [1999] assumed that the temperature dependence of activated sludge can be sufficiently represented by the well-known characteristics of water as the main component of the mixture. Therefore, the temperature dependence is taken into account by the expression [Reid *et al.*, 1987]

$$\frac{\eta_T}{1\ \text{mPas}} = \exp\left(A + \frac{B}{\left(T + 273.15\ \text{K}\right)} + C\left(T + 273.15\ \text{K}\right) + D\left(T + 273.15\ \text{K}\right)^2\right), \tag{3.6}$$

with A = -24.71, B = 4209 K, C = 0.04527 1/K and D = -0.00003376 $1/K^2$.

The apparent viscosity of activated sludge is influencing the wastewater treatment process in terms of (i) oxygen mass transfer relevant for the respiration of microorganisms, (ii) pressure losses in pipes, (iii) transport phenomena near the membrane and (iv) sludge conditioning [Rosenberger *et al.*, 2002]. In this study, a proper representation of hydrodynamic conditions is the main objective of the rheological characterisation of the model suspensions used.

(3.2) Hydrodynamics in membrane filtration processes

(3.2.1) Hydrodynamic conditions

In microfiltration processes, dispersed particles are rejected by the membrane due to a size exclusion mechanism [Melin and Rautenbach, 2007]. Particles smaller than the pore size of the membrane are penetrating through the pore structure. Internal pore blocking occurs due to electrochemical or mechanical interactions with the pore wall, which is known to be largely irreversible by surface shear [Cui *et al.*, 2003; van der Marel *et al.*, 2009]. Therefore, inner pore adsorption is a major fouling mechanism for particles smaller than the nominal pore diameter of the membrane. In addition, irreversible pore blocking caused by particles of similar size compared to the effective pore diameter is leading to a higher filtration resistance [Melin and Rautenbach, 2007]. The deposition and entrainment of particles larger than the pores of the membrane are significantly affected by hydrodynamic conditions and are the focus of this study.

These hydraulics are characterised by the shear stress in the vicinity of the membrane originating from (i) the cross-flow in the feed channel (cross-flow filtration), (ii) the bubble-induced flow and the bubble-induced fibre movement (submerged filtration) or (iii) the rotation of internals in the membrane tank (adapted from Melin and Rautenbach [2007]). While both cross-flow and submerged filtration tests are presented in sections (5.1) to (5.3), the rotation of internals as a strategy to control cake layer formation is not part of this study.

Cross-flow filtration

In cross-flow microfiltration, feed pumps are applied to allow for a continuous tangential flow along the membrane with steep velocity gradients in the boundary layer, see section (2.2.3). The resulting shear forces at the membrane surface are easily predictable if the pump characteristics, the channel dimensions and the exact position of the membrane and other internals are known. However, (i) non-Newtonian characteristics of the feed, (ii) a constriction of the channel due to e.g. cake layer formation, (iii) a motion of the membrane due to an interaction with the flow pattern or (iv) changes in feed flow rate and composition due to permeate extraction make a prediction of surface shear more difficult. Nevertheless, hydrodynamic conditions in cross-flow mode are well-defined compared to more complex multi-phase flow patterns in submerged mode [Cui *et al.*, 2003; Le-Clech *et al.*, 2006; Drews, 2010]. Please refer to Belfort *et al.* [1994] for more details on cross-flow microfiltration of suspensions or macromolecular solutions.

Submerged filtration

In submerged membrane bioreactors, air bubbling is applied to provide oxygen for the biomass, to overcome sludge settling and to remove the cake layer [Le-Clech *et al.*, 2006]. Efforts have been made in scientific research to investigate the impact of bubble size and shape on the efficiency of cake layer removal. It was found that the bubble size can be influenced by the injection method, the sparger type and the aeration rate. The rise velocity increases as the size of the bubble increases and the bubble changes shape from spherical to ellipsoidal and finally to spherical cap [Clift *et al.*, 1978], see **Figure (3.2)**. This bubble shape dictates the strength and extent of the wake region behind the bubble, which shows a high degree of mixing and affects the efficiency of cake layer removal. Characteristics of bubbles relevant for submerged filtration processes are summarised below [Cui *et al.*, 2003].

- **Spherical bubbles** (d_{bub} < 1 mm) are stable in shape, similar to solid particles. The boundary layer does not separate from the bubble surface, so that no wake region occurs. The rise velocity of a spherical bubble is reduced as the apparent viscosity of the continuous liquid phase increases or if the bubble is part of a bubble swarm.

- For **ellipsoidal bubbles** (1.5 mm < d_{bub} < 15 mm), the boundary layer separates at a certain point at the bubble rim, so that a wake region with helical vortices along the non-straight-lined bubble path is formed. Also in this case, the rise velocity is reduced as the apparent viscosity of the continuous liquid phase increases or if the bubble is part of a bubble swarm.

- For **spherical cap bubbles** (d_{bub} > 15 mm), the boundary layer separates at the entire circular circumference of the bubble, so that a wake region consisting of vortex rings is formed. This wake region is characterised by a strong secondary flow, which enhances the degree of mixing in the liquid phase.

The ratio of bubble size to channel dimension dictates the characteristics of the multi-phase flow pattern. A dispersed bubble flow occurs if the bubbles are much smaller than the channel (size ratio < 60 %). The vicinity of the channel wall significantly affects the shape and the flow behaviour of the bubble for larger size ratios. This leads to a **slug flow** with bullet-shaped bubbles as shown on the right-hand side of **Figure (3.2)**.

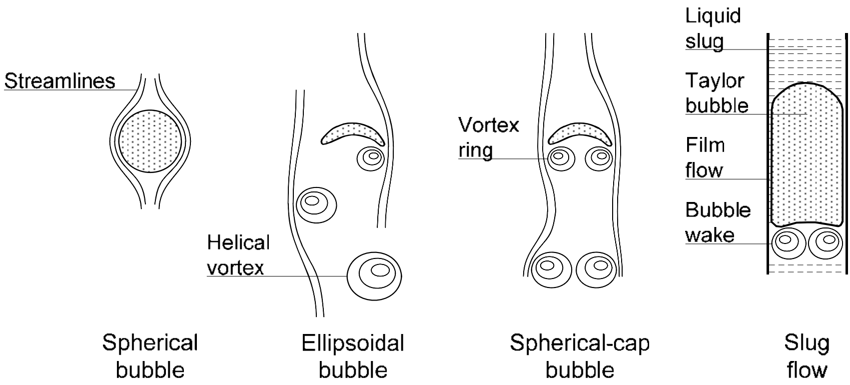

Figure (3.2) Schematic of multi-phase flow patterns with spherical, ellipsoidal, spherical-cap and Taylor bubbles (adapted from Cui *et al.* [2003]).

The slug size is approaching the size of the channel as the aeration rate increases, so that the motion of the slug is mainly controlled by the channel dimension. The overall slug velocity v_{slug} is lower than that of a dispersed bubble of similar size, v_{db}, and is in the range of $v_{slug} \approx 0.5\ v_{db}$. Characteristic flow regions around a gas slug are (i) the liquid flow in front of the bubble (length $\approx 0.5\ d_{tube}$), (ii) the falling liquid film between the bubble and the channel wall ($v_{film} \leq 1$ m/s) and (iii) the wake region behind the bubble (length $\approx 2\ d_{tube}$) [Hout *et al.*, 2002]. Slug flow conditions are advantageous compared to a dispersed bubble flow due to a larger wake region, stronger secondary flows, a higher degree of local mixing and an easy separation of bubbles from the liquid [Cui *et al.*, 2003].

(3.2.2) Impact of operating parameters and feed characteristics

The impact of operating parameters and feed characteristics on the performance of cross-flow and submerged microfiltration processes has been investigated experimentally by a number of research groups. In the studies summarised below, filtration experiments were conducted using model suspensions and lab-scale setups equipped with a single membrane.

Cross-flow filtration

A typical cross-flow microfiltration is characterised by an operation at constant TMP and consists of two filtration stages. Particle deposition is initiated during the first stage, so that a rapid decline in transient permeate flux occurs. Steady-state filtration conditions are reached as soon as particle deposition and entrainment by the cross-flow are in equilibrium. The most relevant factors influencing the microfiltration performance are operating parameters and characteristics of the model suspension as summarised below.

- Investigations with cross-flow configurations have shown that the **transient permeate flux** decreases faster as the TMP or the particle concentration increases [Hong *et al.*, 1997; Wang and Song, 1999; Zhang and Song, 2000]. These trends are due to an increased particle transport to the membrane and rapidly growing cake layers. It was also found that a cake consisting of smaller particles shows a higher specific resistance, which leads to a more rapid decline of transient permeate flux. Moreover, the transient permeate flux is not influenced by variations in cross-flow velocity. This indicates that the early stage of a cross-flow filtration can be approximated by simple dead-end filtration theories [Davis, 1992; Belfort *et al.*, 1994]. The contribution of the membrane resistance to the total filtration resistance was found to be negligible under steady-state conditions [Song, 1998; Wang and Song, 1999; Zhang and Song, 2000; Tarabara *et al.*, 2004].

- The **time to reach steady-state conditions** can vary from minutes to several hours [Hong *et al.*, 1997]. It was found that the steady-state filtration stage is reached faster with a decrease in TMP [Zhang and Song, 2000], a decrease in particle size [Hong *et al.*, 1997; Wang and Song, 1999; Zhang and Song, 2000; Tarabara *et al.*, 2004], an increase in particle concentration and an increase in shear rate [Wang and Song, 1999; Zhang and Song, 2000].

- After reaching **steady-state conditions**, the permeate flux was found to increase with an increase in cross-flow velocity and is not affected by variations in TMP [Hong *et al.*, 1997; Wang and Song, 1999; Zhang and Song, 2000]. These trends are consistent with the limiting flux theory introduced in section (3.2.3). Moreover, the steady-state permeate flux decreases with an increase in particle concentration [Wang and Song, 1999; Zhang and Song, 2000] and a decrease in particle size [Hong *et al.*, 1997; Tarabara *et al.*, 2004]. The particle deposition rate increases with an increase in particle concentration, which leads to thicker steady-state cake layers. Cake layers out of smaller particles form packings of higher specific resistance.

- In addition, **the aggregation of particles** in suspension was investigated [Wiesner *et al.*, 1989; Hlavacek and Remy, 1995; Waite *et al.*, 1999; Pignon *et al.*, 2000; Hwang and Liu, 2002]. These studies have shown that the particle surface charge and the affinity to particle aggregation are depending on the electrolyte concentration [Hwang and Liu, 2002], the coagulant concentration [Wiesner *et al.*, 1989; Hlavacek and Remy, 1995] or the pH of the model suspension. An increase in aggregate size reduces the amount of pore blocking, decreases the specific cake resistance and enhances the hydraulic particle back-transport [Wiesner *et al.*, 1989; Hlavacek and Remy, 1995].

- For the filtration of suspensions containing polydisperse particles, more complex cake morphologies are formed. These are due to an **infiltration of smaller particles** into the cake, so that voids in the existing cake structure are filled [Melin and Rautenbach, 2007]. This leads to a decrease in cake porosity and an increase in specific cake resistance. Furthermore, the formation of two layers of different cake porosity due to a **selective particle deposition** was reported [Hwang and Liu, 2002]. The first layer formed in the vicinity of the membrane surface is compact and shows a high filtration resistance. The second layer close to the cake surface is of higher porosity and lower filtration resistance. This phenomenon is more pronounced for an operation at constant TMP and a decrease in local permeate flux, i.e. when the deposition-enhancing drag forces caused by permeation weaken with time. Please refer to section (3.2.3) for more details on mass transport phenomena.

- Tarabara *et al.* [2004] attributed the formation of multiple layers of different porosity to a **collapse of the initial cake layer** formed until a critical mass is reached [Harmant and Aimar, 1996; Hwang *et al.*, 1998]. The thickness and the structure of the cake are depending both on the particle size and the solution ionic strength, with an abrupt transition from dense to porous layers. It is assumed that the contribution of the collapsed part of the cake to the total filtration resistance is dominating.

- In contrast to this abrupt collapse of the cake layer, the **deformation of non-rigid particles** such as microbes is a creeping form of cake compression [Hwang *et al.*, 2001]. Therefore, significantly different phenomena governing the cake formation process are occurring when filtrating deformable particles [Nakanishi *et al.*, 1987]. However, the filtration of biological suspensions is not a focus of the thesis at hand. For the same reason, numerous studies about the filtration of complex fluids consisting of both soluble and dispersed compounds are not part of this review. Please refer to Le-Clech *et al.* [2006] or to Drews [2010] for more details.

Air bubbling is applied to create an axial flow pattern in submerged filtration processes. This multi-phase flow is more difficult to be accurately managed compared to an operation in cross-flow mode [Le-Clech *et al.*, 2006]. However, cross-flow filtration setups are frequently used in scientific research, whereof the findings are transferred to submerged filtration processes.

Submerged filtration

Mostly **slug flow conditions** are occurring in close proximity to the membrane when air bubbling is applied to enhance the filtration performance. Although external slugs are more loosely defined by flow path boundaries such as membrane fibres, the mechanisms are comparable to the ones observed in pipes [Cui *et al.*, 2003]. For microfiltration processes, this slug flow leads to a periodic disruption of the cake layer [Sur and Cui, 2001], to a cake structure of lower specific resistance because of expanded and more porous cakes [Laborie *et* *al.*, 1997; Cabassud *et al.*, 2001] and to less irreversible fouling [Chang and Fane, 2000a]. The enhancement in filtration performance by using a two-phase flow is particularly high if concentration polarisation or cake layer formation is more severe.

Ghosh and Cui [1999] have shown that the mass transfer coefficient is highest in the falling film zone, slightly lower in the bubble wake and more than one order of magnitude lower in the liquid slug region. The film velocity is insensitive to variations in the two-phase mixture velocity [Chang and Fane, 2000b]. Increasing the slug length above a critical value has little impact on the wake length [Campos and Guede de Carvalho, 1988]. Pressure pulses due to air bubbling were observed, which are a consequence of a higher pressure in the bubble front and a lower pressure in the wake region. An increase in bubble frequency for the same aeration rate enhances the overall shear generated by air bubbling. Therefore, optimal aeration conditions are expected to occur for medium-size bubbles as a compromise of shear generated per bubble (favouring large bubbles) and the number of shear events per unit time (favouring small bubbles) [Buwa and Ranade, 2002; Cui *et al.*, 2003; Sofia *et al.*, 2004; Wicaksana *et al.*, 2006; Yeo *et al.*, 2006].

Nakoryacov *et al.* [1989] and Taha and Cui [2002] have shown that the circular wall jet behind the bubble originates from the liquid film falling with a high velocity. The penetration of this wall jet into the liquid slug is responsible for the high degree of mixing in the wake region. While the transition from upward to downward flow at the bubble nose is rather smooth, the transition from downward to upward flow at the bubble tail is abrupt. It was also found that a passing slug induces transient shear stresses, particularly in case of long bubbles for which the bubble tail becomes wavy, see section (3.4.2) for more details.

A well-known aeration parameter for the operation of a submerged membrane unit is the **specific aeration demand**

$$SAD_m = \frac{\dot{V}_{air,net}}{A_m} = \frac{\dot{V}_{air,gross}\ \Delta t_{on}\ N_{cyc}}{\Delta t_{seq}\ A_m}, \tag{3.7}$$

with the net aeration rate $\dot{V}_{air,net}$, the membrane area A_m, the gross aeration rate $\dot{V}_{air,gross}$, the duration of an aeration cycle Δt_{on}, the number of aeration cycles per sequence N_{cyc} and the duration of an aeration sequence Δt_{seq}. The parameters required for estimating the net aeration rate or the specific aeration demand are presented in **Figure (3.3)**. Please note that the term "cycle" does not refer to the periodicity of permeate extraction, but solely to the sequence of air injection and aeration pause with continuous filtration.

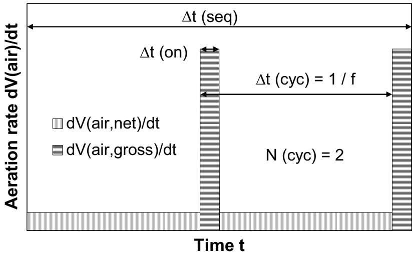

Figure (3.3) Parameters affecting the net aeration rate and the specific aeration demand of the membrane unit.

In addition to the overall specific aeration demand, also the **aeration frequency**

$$f_{cyc} = \frac{N_{cyc}}{\Delta t_{seq}} \quad \Rightarrow \quad SAD_m = \frac{\dot{V}_{air,gross}\, \Delta t_{on}\, f_{cyc}}{A_m} \tag{3.8}$$

affects the efficiency of air bubbling to enhance the filtration performance. Guibert *et al.* [2002] have found that a localised and intermittent air-cycling aeration leads to a significant reduction of aeration requirements. According to this strategy, only one half of the membrane tank is aerated at a time, so that the density gradient between aerated and unaerated compartments induces a superposed horizontal liquid flow.

In submerged hollow-fibre units, **fibre motion** due to the interaction of the multi-phase flow pattern and the fibre enhances the filtration performance in addition to the bubble-induced cross-flow [Wicaksana *et al.*, 2006; Yeo *et al.*, 2007; Buetehorn *et al.*, 2009]. This benefit is presumably caused by additional shear forces due to a lateral fibre movement and fibre-fibre interactions. According to studies conducted by Bérubé and co-workers [Bérubé and Lei, 2006; Bérubé *et al.*, 2006; Chan *et al.*, 2007], mainly fibre collisions are affecting the removal of the cake layer. A higher **packing density** of the module was found to reduce cake layer formation due to an acceleration of flow [Ueda *et al.*, 1997]. However, detrimental effects such as permeate competition [Yeo *et al.*, 2006] and dewatering are more pronounced as the packing density increases.

Also the **orientation and the diameter of the fibre** affect the filtration performance. For a single-phase flow, a horizontal fibre orientation is advantageous due to a frequent boundary layer renewal, eddy formation and an improved flow distribution [Futselaar *et al.*, 1993]. Air bubbling is more efficient for vertically oriented fibres due to a more intensive bubble-membrane interaction [Chang *et al.*, 2002b]. A decrease in fibre diameter is leading to a higher flexibility of the fibre, causing a greater enhancement of the filtration performance due to air bubbling [Wicaksana *et al.*, 2006]. However, a decrease in fibre diameter is followed by a higher risk of membrane breakage and a greater pressure drop in the membrane lumen [Chang and Fane, 2001].

(3.2.3) Mass transport phenomena

In the previous section, the influence of operating parameters and feed characteristics on the performance of microfiltration processes is reported. Numerous approaches have been identified to describe the underlying mass transport phenomena. In the following paragraphs, a selection of these approaches dealing with (i) blocking filtration laws, (ii) back-transport mechanisms, (iii) selective particle deposition, (iv) fouling stages, (v) transition from concentration polarisation to particle deposition, (vi) critical pressure and limiting flux as well as (vii) critical flux and critical aeration rate are highlighted.

Blocking filtration laws

A number of blocking filtration laws were established to predict the permeate flux decline for a cross-flow microfiltration at constant TMP. Hermia [1982] compared the approaches introduced below and applied the models to non-Newtonian fluids following the Ostwald-de Waele approach.

- The **complete blocking filtration law** assumes that particles deposit only on the membrane surface and not on top of each other, so that only one particle layer is formed. Moreover, particles depositing on a membrane pore are assumed to seal the pore completely. This leads to an interrelationship between permeate flux J and filtration time t of $J \propto \exp(-t)$.

- Similarly, the **intermediate blocking filtration law** assumes that every particle depositing on a membrane pore seals the pore completely. Particles are allowed to settle on top of each other, so that multi-layer deposits are formed on the membrane surface. This is achieved by estimating the reduction of the active surface area due to cake layer formation and estimating the probability of particle deposition. The intermediate blocking filtration law is characterised by $J \propto 1/t$.

- The **standard blocking filtration law** is based on the assumption that particles are capable of depositing on the inner pore wall. This reduces the effective pore diameter and increases the filtration resistance. The time-dependent permeate flux for a standard blocking filtration can be described as $J \propto 1/t^2$.

- The **cake filtration law** neglects internal particle deposition and assumes that the total filtration resistance corresponds to the sum of membrane and cake resistance. The permeate flux evolution is described by $J \propto 1/\sqrt{t}$. As a follow up, additional resistances due to e.g. fouling layers removable by rinsing, backwashing or chemical cleaning were taken into account [Metzger *et al.*, 2006]. However, neither backwashing nor chemical cleaning is investigated in this study.

Hermia [1982] concluded that a common filtration equation of the form

$$\frac{d^2t}{dV^2} = k\left(\frac{dt}{dV}\right)^n \tag{3.9}$$

describes the permeate flux decline for all filtration laws introduced above. In equation (3.9), k and n are model parameters, t corresponds to the filtration time and V to the permeate volume. A stochastic modelling approach suggested by Wessling [2001] provides evidence that a simple comparison of filtration results with equation (3.9) may cause misleading conclusions. The diffusion-limited aggregation simulation technique predicted that the evolution of permeate flux fits best to the intermediate blocking filtration law. However, pore blocking was observed during the very end of the simulation run only. Moreover, higher cake porosities next to the pore entrance compared to the cake deposited on the membrane material were predicted by the simulation. This discrepancy weakens the validity of an evaluation of filtration regimes solely based on monitoring the average permeate flux decline.

Back-transport of deposited particles

The transport of deposited particles back into the bulk phase can be described by taking Brownian diffusion, inertial lift, shear-induced diffusion and a concentrated flowing layer into account. The principles of these transport phenomena are summarised below (adapted from [Sethi and Wiesner, 1997]).

- The **Brownian diffusivity** is inversely proportional to the particle size and is more pronounced for macromolecular feed components of sub-micron dimension. Other influencing parameters are the temperature and the apparent viscosity of the particle-free fluid. Well-known modelling approaches such as the gel-polarisation model [Brian, 1965; Michaels, 1968; Blatt *et al.*, 1970; Porter, 1972; Sulaiman *et al.*, 2001] are solely based on Brownian diffusion described by the Stokes-Einstein equation. Therefore, these models underestimate the steady-state permeate flux for a filtration of colloids and small particles due to their low diffusivity.

- Another mechanism is based on the assumption that the particle transport to the membrane is partly compensated by **inertial lift** induced by the presence of a wall (also referred to as inertial particle migration) [Green and Belfort, 1980; Altena and Belfort, 1984, Weigand *et al.*, 1985; Drew *et al.*, 1991]. Inertial lift is observed for a passage of particle-loaded flows in close proximity to the channel wall, leading to a particle-free layer adjacent to the wall. This phenomenon is also known as tubular pinch effect [Meier, 2008] and is caused by differences in fluid velocity and pressure along the circumference of a particle [Green and Belfort, 1980]. For fast laminar flows with Re >> 1, the maximum lift velocity is proportional to the third power of particle size and the second power of shear rate. This indicates the significance of inertial lift for larger particles and for filtration processes with higher shear rates. Furthermore, the fluid density and the apparent viscosity of the dispersant are affecting the maximum lift velocity.

- Particle-particle interactions in a shear field are leading to a lateral displacement of the particles and are taken into account by the **shear-induced diffusion** approach (also referred to as integral theory) [Davis and Leighton, 1987; Meier, 2008]. Empirical equations were established to correlate the diffusion coefficient of the suspension with parameters such as shear rate, particle radius and local particle volume fraction. These correlations are restricted to a certain type of particle, e.g. to rigid and spherical particles [Leighton and Acrivos, 1987a+b].

- The concept of a **concentrated flowing layer** assumes that particles accumulate in a boundary layer flowing parallel to the membrane [Leonard and Vassilieff, 1984; Davis and Birdsell, 1987; Meier, 2008]. Deposition is taking place as soon as the particle concentration increases and exceeds a threshold. The cake layer formed on the membrane surface constricts the feed channel, which causes an increase in cross-flow velocity and an increase in surface shear. The critical time until the cake layer starts to form and the corresponding position on the membrane surface is predicted by the model. In addition, the cake growth and the resulting flux decline rate are estimated.

A theoretical study conducted by Sethi and Wiesner [1997] as a follow-up of Romero and Davis [1988+1990] is based on a combination of all transport phenomena mentioned above. Their objective was to predict the transient permeate flux evolution for a rejection of macromolecules, colloids and fine and large particles. From these theoretical approaches, an **unfavourable particle size** in the range of 0.01 to 0.1 µm was identified. This particle size is characterised by a minimum in back-transport efficiency and corresponds to a maximum in cake thickness and a minimum in permeability. The existence of an unfavourable particle size was previously observed by Rautenbach and Schock [1988] and was experimentally confirmed by Chellam and Wiesner [1997]. For particles larger than this unfavourable size, an increase in inertial lift and shear-induced diffusion is occurring, whereas smaller particles show higher diffusion coefficients. Both trends are followed by an enhancement in particle back-transport. It was found that this characteristic particle diameter varies during the experiment in response to changes in particle deposition rate and hydrodynamic conditions, which leads to the formation of inhomogeneous cakes.

Selective particle deposition

The selective deposition of particles was studied as a function of interparticle forces, shape and size of the particles and operating conditions [Fischer and Raasch, 1984; Lu and Ju, 1989; Stamatakis and Tien, 1993; Lu and Hwang, 1993+1995]. The overall modelling approach is based on the estimation of a critical friction angle β_{crit} as a depositing particle approaches the cake layer. Particles with an angle of friction smaller than the critical value deposit permanently. Particles with friction angles exceeding the critical value are assumed to be removed by the cross-flow immediately. The critical friction angle is linked to the critical cut diameter and the probability of particle deposition. Particles smaller than the **critical cut diameter** deposit permanently and larger particles are entrained by the cross-flow. The **probability of particle deposition** is defined as the ratio of cake surface area for a stable deposition (characterised by $\beta < \beta_{crit}$) to the total cake surface area and is influenced by the particle size. Therefore, a selective deposition of particles of different size is occurring.

The **solid compressive pressure** originating from the liquid permeating through the porous cake is leading to a continuous cake compression [Lu and Hwang, 1995; Hwang and Liu, 2002]. The forces acting on the outermost particle layer are transmitted to the surrounding particles at particle-particle contact points. Therefore, the compressive pressure increases from the cake surface towards the membrane. A continuous cake compression during filtration and a further **migration of already deposited particles** in the cake were observed by Lu and Hwang [1995]. The authors have found that an increase in cross-flow velocity and a decrease in TMP are leading to a decrease in cut diameter, a shift to smaller particles in the cake and a higher specific cake resistance. These studies were indicating that the specific filtration resistance is highest in the vicinity of the membrane due to a higher local concentration of smaller particles.

Stages of membrane fouling

Song [1998] investigated dynamics of local cake layer formation along the membrane in cross-flow filtration at constant TMP by a model based on three different fouling stages. The local permeate flux evolution and the time to reach steady-state conditions were described as a function of applied pressure, shear rate and particle size. During the first fouling stage, the permeate flux rapidly drops due to initial pore blocking. This is followed by a long-term gradual permeate flux decline (stage 2) and finally steady-state conditions (stage 3). Stage 1 and 2 are occurring under various operating conditions. Stage 3 is only observable if the TMP and the particle concentration are sufficiently high and the duration of the experiment is long enough. This is consistent with the finding that the time-scale for pore blocking is much shorter than the time-scale for cake layer formation (see also [Hermina, 1982; Hlavacek and Bouchet, 1993]). Therefore, the pores are primarily blocked prior to the development of the entire first layer of the cake. It was also found that the concentration polarisation layer develops simultaneously with the process of pore blocking during the first fouling stage. Experimental [Wakeman, 1994] and theoretical studies [Song, 1998] suggest that steady-state conditions are reached at the inlet of the test cell first and subsequently progress towards the outlet. Hence, a **particle deposition front** occurs, which is moving downstream and accelerates with time. It is worth mentioning that these findings are conflicting with observations reported by Bacchin *et al.* [2002], see below.

Zhang *et al.* [2006] have found that also for a submerged activated sludge filtration at constant permeate flux, three stages of membrane fouling are observable. The first two stages are similar to the ones described above for a filtration at TMP = const. An abrupt permeability decline due to pore blocking and adsorption of dissolved or dispersed matter (stage 1) is followed by a longer period of gradual permeability decline (stage 2). The third stage is characterised by a **TMP-jump** (stage 3) originating from the self-accelerating nature of a filtration at imposed permeate flux [Cho and Fane, 2002]. The duration of the first two filtration stages before a rapid TMP jump occurs was envisaged as an appropriate parameter for evaluating the long-term filtration performance [Le-Clech *et al.*, 2003].

Transition from concentration polarisation to particle deposition

Bacchin *et al.* [2002] introduced a model covering both concentration polarisation and cake layer formation for a cross-flow filtration of macromolecules and colloids at steady-state. The particle concentration, particle size, ionic strength and zeta-potential of the model suspension are expressed as a function of **osmotic pressure**. This model is taking into account entropic effects and colloidal interactions such as van-der-Waals and electrostatic forces [Petsev *et al.*, 1993; Jönsson and Jönsson, 1996]. It was previously found that mainly repulsive forces between the particle and the membrane surface and drag forces caused by the permeate flux are affecting the initial cake build-up [Bacchin *et al.*, 1995; Harmant and Aimar, 1996]. However, this model is restricted to steady-state filtration conditions.

An increase in particle concentration above a critical volume fraction destabilises the suspension, so that coagulation is taking place. Bacchin *et al.* [2002] attributed the resulting drop in osmotic pressure to a **phase transition** from concentration polarisation (i.e. a higher concentration of particles in the boundary layer) to cake layer formation (i.e. a stable particle deposition on the membrane surface). This phase transition is characterised by a maximum in osmotic pressure at a critical particle volume fraction and a critical Péclet number [Bacchin *et al.*, 2002]. The Pe number describes the ratio of convective to diffusive transport in the boundary layer. An increase in TMP leads to a transition from concentration polarisation to cake layer formation, which is smoother for smaller particles. This is due to a more pronounced concentration polarisation for smaller particles occurring simultaneously along the membrane, whereas cake layer formation is not evenly distributed. Therefore, an abrupt transition is occurring for larger particles as the TMP further increases, which is caused by a less pronounced concentration polarisation.

The steady-state model suggested by Bacchin *et al.* [2002] predicts an initial deposition of large particles close to the outlet of the test cell. This is attributed to unfavourable hydrodynamic conditions, so that the **critical Pe number** is exceeded at the outlet first. Subsequently, the cake formation progresses towards the inlet as the TMP further increases. This theory was experimentally confirmed by Gourgues *et al.* [1992], but is contradictory to previous findings introduced above [Wakeman, 1994; Song, 1998]. This inconsistency is presumably due to differences in the significance of feed-side pressure losses under the corresponding operating conditions [Bacchin *et al.*, 2002].

Concepts of critical pressure and limiting flux

A number of authors postulated that a **critical feed pressure** exists [Song and Elimelech, 1995; Song, 1998; Wang and Song, 1999; Zhang and Song, 2000], which is a function of thermodynamic properties of the suspension and independent of operating parameters such as setpoint TMP [Song, 1998]. For a filtration under sub-critical conditions, the deposition of particles is completely compensated by diffusive or hydraulic back-transport phenomena. Under supercritical conditions, particle deposition temporarily overbalances the back-transport until reaching steady-state. The steady-state filtration stage is characterised by an equilibrium of particle deposition and removal and a constant cake layer thickness.

Another parameter to describe the filtration performance at imposed TMP is the **limiting flux** [Song, 1998; Wang and Song, 1999; Zhang and Song, 2000; Bacchin *et al.*, 2002]. The limiting flux is the maximum steady-state permeate flux and is mostly based on the assumption that the particle transport to the membrane is balanced by back-transport phenomena [Song, 1998]. Therefore, Song and co-workers concluded that the limiting flux is equal to the equilibrium permeate flux. A further increase can be achieved by an increase in cross-flow velocity or a decrease in solids concentration only, whereas higher TMPs are fully compensated by a corresponding increase in filtration resistance.

Concepts of critical flux and critical aeration rate

A well-known method to predict the long-term filtration performance of MBRs is to conduct short-term tests with a step-wise increase in either setpoint permeate flux (**flux-step test**) or in setpoint TMP (**TMP-step test**). Field *et al.* [1995] postulated that a constant permeability is observable under sub-critical conditions. Moreover, it was claimed that the filtration resistance under these conditions equals the pure-water resistance of the membrane [Bacchin *et al.*, 2006]. According to this so-called **strict definition of critical flux**, a sub-critical filtration is characterised by a complete removal of rejected matter by Brownian diffusion or the cross-flow. Under supercritical conditions, a decrease in permeability with time is observable. This means that the transport of foulants to the membrane caused by permeation is at least temporarily exceeding the back-transport.

For a filtration of activated sludge, a slight increase in TMP was observed even for an extremely low setpoint permeate flux of 2 L/(m^2 h) [Le-Clech *et al.*, 2003]. This may be a consequence of the adsorption of dissolved substances or small particles prior to the initial deposition of larger particles. Therefore, a **weaker form of critical flux** (also referred to as sustainable flux [Bacchin *et al.*, 2006]) was suggested. This parameter characterises the transition from acceptable (i.e. sustainable) to higher fouling rates dTMP/dt. While the strict form of critical flux is useful for particle separation processes, the weak form is more appropriate for complex mixtures consisting of both dissolved and dispersed compounds [Bacchin *et al.*, 2006].

Le-Clech *et al.* [2003] performed critical flux tests according to the flux-step method and used an arbitrary fouling rate threshold of the function dTMP/dt = f (J) to determine critical conditions. The authors recommended small flux step heights and moderate step durations of 15 to 30 min. A literature review conducted by Bacchin *et al.* [2006] has shown that the critical flux increases with an increase in pH, a decrease in ionic strength, a decrease in particle concentration and an increase in particle size. Moreover, appropriate hydrodynamics in the feed channel and an enhanced hydraulic back-transport of deposited matter are leading to an increase in critical flux. Cho and Fane [2002] suggested a theory based on **local permeate fluxes** exceeding the overall critical flux. This leads to a localised particle deposition and a self-accelerating character for a filtration at imposed flux.

More recently, Van der Marel *et al*. [2009] suggested an improved flux-step method for a simultaneous determination of critical flux and **critical flux for irreversibility**. The latter parameter is equal to the lowest setpoint permeate flux for which irreversible cake layer formation is occurring. This method consists of relaxation periods at low permeate flux and continuous aeration in-between two flux steps to reduce the influence of fouling history on the TMP evolution. The critical flux for irreversibility is reached as soon as the TMP during a relaxation period is differing significantly from the TMP measured during the previous relaxation step. The critical flux can be also determined by monitoring the particle concentration in the outlet and formulating a **particle mass balance** [Kwon *et al.*, 2000]. However, it was found that this method in most cases underestimates the critical flux according to the flux-step test [Bacchin *et al.*, 2006]. Hence, more insights into the filtration process are required to determine the onset of particle deposition. For this purpose, direct observation through the membrane (DOTM) was used, which is applicable to membranes which are transparent in wet state [Li *et al.*, 1998+2000].

Similar to the critical flux concept, a so-called **critical aeration rate** can be determined by a step-wise decrease in aeration rate for a constant permeate flux. Ueda *et al.* [1997] have shown the existence of optimal aeration conditions for an efficient and cost-effective cake removal. A further increase in aeration rate does not lead to a significantly improved filtration performance, whereas cake layer formation is more pronounced as the aeration rate decreases [Ueda *et al.*, 1997; Chang and Fane, 2002; Liu *et al.*, 2003].

Concluding remarks on mass transport phenomena

In conclusion, a number of mechanisms are governing transport phenomena in microfiltration processes. According to Bacchin *et al.* [2002], these can be subdivided into (i) driving phenomena such as permeation, (ii) regulating phenomena such as repulsive colloidal interactions and diffusive or hydraulic back-transport mechanisms as well as (iii) irreversible phenomena such as attractive interactions (adapted). Most of these phenomena are occurring simultaneously in nearly all membrane filtration processes. Nevertheless, some of them are more relevant than others for specific applications. Brownian diffusion is the dominating regulation mechanism when filtrating small particles at low shear rates. Inertial lift and shear-induced diffusion are more pronounced for the filtration of larger particles at high shear rates [Sethi and Wiesner, 1997]. Therefore, an essential step of every modelling study is to carefully distinguish negligible effects to reduce the complexity of the model as far as possible.

(3.3) Observation techniques

During the last decades, efforts have been made to further understand phenomena governing microfiltration processes by applying observation techniques. A variety of monitoring tools and methodologies were established and reviewed in previous publications [Chen *et al.*, 2004a+b]. These investigations can be subdivided into an observation of microscopic effects, meso-scale phenomena and macroscopic effects. The following review is restricted to investigations related to NMR imaging (micro-scale) and direct observation of fibre movement (meso-scale). Please refer to sections (4.4.1) and (4.4.2) for more details on the fundamentals of the applied observation techniques.

(3.3.1) Nuclear magnetic resonance (NMR) imaging

Nuclear magnetic resonance (NMR) imaging is known as a powerful tool for a non-invasive observation of synthetic membrane processes [Blümich, 2000; Chen *et al.*, 2004a+b]. Typical applications are summarised in **Table (3.1)** and include the visualisation of flow patterns, concentration polarisation and cake layer formation. Please refer to section (4.4.1) for more details on the fundamentals of NMR imaging.

Reference	Focus of the study	Application
Hammer *et al.* [1990], Heath *et al.* [1990]	Shell-side nutrient supply for biological cells	Bioreactors equipped with hollow-fibres
Chung *et al.* [1993]	Dean vortices to control concentration polarisation	Membrane filtration processes
Laukemper-Ostendorf *et al.* [1998], Poh *et al.* [2003a]; Creber *et al.* [2010]	Mass transfer enhancement	Application of spacers
Poh *et al.* [2003a+b]		Application of baffles
Agranovski *et al.* [2003]		Gas-lquid flow in porous media
Ståhlberg *et al.* [1986]	Lumen-side flow velocity	Blood flow within capillaries
Pangrle *et al.* [1989], Donoghue *et al.* [1992]		Maldistribution of flow within hollow-fibre reactors
Pangrle *et al.* [1992]		Alterations in flow rate due to permeate extraction
Zhang *et al.* [1995], Laukemper-Ostendorf *et al.* [1998], Hardy *et al.* [2002]		Flow patterns within hollow-fibre hemodialyzers
Laukemper-Ostendorf *et al.* [1998]		Alterations in flow rate due to permeate extraction
Hardy *et al.* [2002]		Alterations in filtration rate due to lumen-side pressure losses
Yao *et al.* [1995a,b+1997], Pope *et al.* [1996]	Concentration polarisation	Membrane filtration of oil-water emulsions
Horsfield *et al.* [1989]	Cake layer formation	Membrane filtration of clay suspensions
Dirckx *et al.* [2000]		Deposition of iron (III) oxide particles within cartridge filters
Wandelt *et al.* [1993], Schmitz *et al.* [1993]		Membrane filtration of bentonite suspensions
Airey *et al.* [1998]		Membrane filtration of colloidal silica suspensions

Table (3.1) Overview of previous NMR studies in similar fields of research.

Most of the previous NMR studies were focussing on the optimisation of membrane module design and operating conditions. Belfort and co-workers [Hammer *et al.*, 1990; Heath *et al.*, 1990] investigated the shell-side nutrient supply in bioreactors equipped with hollow-fibres. A later NMR study performed by the same group was dedicated to the observation of Dean vortices as a strategy to control concentration polarisation in membrane filtration [Chung *et al.*, 1993]. Moreover, potentials for enhancing mass transfer by spacers [Laukemper-Ostendorf *et al.*, 1998; Poh *et al.*, 2003a; Creber *et al.*, 2010], baffles [Poh *et al.*, 2003a+b] or gas-liquid flow in porous media [Agranovski *et al.*, 2003] were evaluated by NMR.

Flow patterns in the lumen of tubular membrane configurations were investigated by a number of research groups [Ståhlberg *et al.*, 1986]. Pangrle *et al.* were looking at the flow distribution in hollow-fibre reactors [1989; Donoghue *et al.*, 1992] and tube-and-shell modules [1992]. The maldistribution of flow throughout the hollow-fibre reactor was studied as a function of inlet Reynolds (Re) number. Complementary NMR investigations were focussing on the estimation of axial flow velocity in the membrane lumen by measuring the feed flow rate and assuming a parabolic velocity profile [Pangrle *et al.*, 1992]. It was observed that the lumen-side velocity decreases with increasing distance from the inlet. This expected trend is caused by a reduction in feed flow rate at positions closer to the outlet due to ongoing **permeate extraction along the membrane**.

Similar studies have been performed to visualise the lumen- and shell-side flow in hollow-fibre hemodialyzers [Zhang *et al.*, 1995; Laukemper-Ostendorf *et al.*, 1998; Hardy *et al.*, 2002]. Laukemper-Ostendorf *et al.* [1998] have shown that the lumen-side feed flow rate can be sufficiently approximated by measuring the maximum flow velocity and assuming parabolic velocity profiles. Based on this approach, Hardy *et al.* [2002] investigated **variations in local filtration rate** for different TMPs. The authors attributed the linearly decreasing local filtration rate with increasing distance from the inlet to **lumen-side pressure losses**. The average ultrafiltration coefficient of the membrane was calculated as the cumulative filtration rate divided by the overall TMP.

NMR imaging was also applied to visualise **concentration polarisation** and **cake layer formation** in membrane filtration processes. As a first attempt, Horsfield *et al.* [1989] investigated the cake layer build-up for a filtration of **clay suspensions**. Dirckx *et al.* [2000] studied the deposition of **iron (III) oxide particles** in cartridge filters. The paramagnetic properties of these particles allowed high-contrast imaging, but led to an overestimation of cake height. Nevertheless, a heterogeneous cake layer and areas preferential for particle deposition were observed. Interestingly, areas with thicker cakes were found to be more prone to particle deposition than other regions. This was attributed to an enhanced trapping of small particles in those areas.

Wandelt *et al.* [1993] investigated the deposition of **bentonite particles** on the surface of hollow-fibre membranes during cross-flow filtration. It was found that an increase in cross-flow velocity leads to particle entrainment, thinner cake layers and a decrease in cake porosity [Schmitz *et al.*, 1993]. As a follow up of these efforts, Fane and co-workers used NMR imaging techniques to visualise the filtration of **oil-water emulsions** [Yao *et al.*, 1995a,b+1997; Pope *et al.*, 1996]. For these studies, horizontal cross-flow setups operated at constant TMP and equipped with up to 15 hollow-fibres [Yao et al., 1995a] or a single tubular membrane [Pope *et al.*, 1996; Yao *et al.*, 1995b+1997] were used. The investigations have shown that the oil polarisation layer was thinner where surface shear due to the cross-flow was higher [Yao *et al.*, 1995a]. The oil layer was completely remixed when the filtration was turned off [Yao *et al.*, 1995a,b+1997]. In addition to the oil layer growth, also oil concentration changes in the layer were observed [Pope *et al.*, 1996]. Stagnant liquid due to wall friction and flow channelling in the feed shell were visible under steady-state filtrations conditions [Yao *et al.*, 1995a]. Although high feed velocities in the bulk phase were measured, a shear-induced **flow of the oil layer** was not detectable [Yao *et al.*, 1995a,b+1997].

Complementary studies using suspensions containing **colloidal silica** and tubular membranes were conducted by the same group [Airey *et al.*, 1998]. The authors have chosen the maximum thickness of the asymmetric cake as an indicator for the influence of operating parameters. The permeate flux decline was found to be in good agreement with the increase in maximum cake thickness over time. An increase in cross-flow velocity led to a thinner cake layer, whereas the maximum cake thickness increased with an increase in TMP. Moreover, the cake was thicker in greater distance from the inlet and reaches a plateau. The deposited particles were completely remixed as the filtration was turned off. In contrast to the stationary oil polarisation layer [Yao *et al.*, 1995a,b+1997], a significant **movement of the cake layer** formed out of silica particles was observable [Airey *et al.*, 1998]. This is consistent with the finding that both stagnant and fluidised deposition layers exist simultaneously in cross-flow filtration of suspensions as observed by direct observation (DO) [Marselina *et al.*, 2009].

(3.3.2) Direct observation (DO) of fibre movement

The bubble-induced movement of hollow-fibres is affecting the filtration performance of submerged membrane units as presented in section (3.2.2). Fane and co-workers established a methodology to characterise the movement of single fibres fixed at both ends by using a direct observation technique [Fane *et al.*, 2005; Wicaksana *et al.*, 2005+2006]. The fibre motion was captured by a conventional video camera during the filtration of glycerol-water solutions. The amplitude and frequency were determined by a digital frame-by-frame image processing. Subsequently, yeast filtration experiments were conducted at constant permeate flux with continuous aeration. Fibre movement characteristics were then correlated with the fouling rate dTMP/dt and the critical flux according to its weak form.

The authors observed that fibre motion was enhanced by an increase in aeration rate, an increase in fibre looseness, a decrease in fibre diameter, an increase in fibre length and a decrease in dynamic viscosity of the model solution. Moreover, the fibre displacement was found to be insensitive to variations in setpoint permeate flux and nozzle size [Wicaksana *et al.*, 2005+2006]. Interestingly, a decrease in apparent viscosity was causing an increase in **fibre movement frequency** for relatively tight fibres, whereas the **amplitude of fibre motion** was not affected. In agreement with this, an increase in fibre movement intensity was followed by a reduction in fouling rate and an increase in critical flux. These trends are indicating that a more intensive tangential flow and a higher degree of fibre flexibility are leading to an enhanced movement of the fibre and a more efficient cake layer removal.

In addition, a **limiting aeration rate** for an enhanced fibre movement was observed. A further increase above this critical value does not lead to a significant increase in amplitude or frequency of fibre motion [Wicaksana *et al.*, 2006]. It was also shown that a **mechanical displacement** of the fibre without aeration, but with approximately the same amplitude and frequency is less efficient than air bubbling [Wicaksana *et al.*, 2005+2006].

Yeo *et al.* [2007] conducted particle image velocimetry (PIV) measurements to track bubble-induced fibre movement with a single fibre moving in response to a multi-phase flow pattern. However, these investigations are not part of this review since only DO measurements as presented in section (5.2.3) were conducted in the framework of this study.

(3.4) CFD in MBR research

Monitoring hydrodynamics in MBR units is difficult due to (i) highly transient multi-phase flows, (ii) complex module configurations partly interacting with the flow and (iii) the opacity of the biological suspension. Therefore, computational fluid dynamics (CFD) simulations were frequently used to investigate flow conditions in membrane processes [Ghidossi *et al.*, 2006b] or bubble column reactors [Joshi, 2001]. Previous CFD studies were focussing on phenomena occurring on different scales. In addition to large-scale flow patterns in real wastewater treatment plants, small-scale phenomena such as cake formation and surface shear were investigated. The small-scale approaches can be further subdivided into multi-tubular, flat-sheet and hollow-fibre configurations, with a decrease in confinement of the flow channel as ordered. An overview of previous CFD studies is presented in **Table (3.2)**. Numerous CFD approaches focussing on cake layer formation [Carroll, 2001] and the application of feed spacers [Fimbres-Weihs and Wiley, 2007] are not part of this review, since the corresponding phenomena are not investigated with CFD in this study. Please refer to section (4.5.1) for a brief introduction to the CFD background.

Reference	Module configuration	Focus of the study	Multi-phase model	Turbulence model (liquid phase)
Kang *et al.* [2008]	Full-scale MBRs	Comparison of pilot- and full-scale MBR units	Eulerian	Mixture realisable k-ε
Saalbach and Hunze [2008]		Optimisation of membrane tank design features	Algebraic slip mixture	RNG k-ε
Brannock *et al.* [2009+2010a+b]		(1) Inside vs. outside submerged MT systems. (2) FS vs. HF MBR units.	Euler-Euler	Mixture k-ε
Taha and Cui [2002]	Tubular membranes	2D simulation of a single Taylor bubble flow	VOF	RNG k-ε
Ndinisa *et al.* [2005]		Impact of permeate extraction on the 2D bulk-phase flow field	Euler two-fluid vs. VOF	None (laminar flow)
Ratkovich *et al.* [2009]		2D simulation of a single Taylor bubble of variable size	VOF	RNG k-ε
Ndinisa *et al.* [2006]	Submerged flat-sheets	Shear stress distribution on the membrane surface	Euler two-fluid	Standard k-ε
Jajuee *et al.* [2006]		Water flow in downcomer of airlift membrane contactor	None (water flow only)	Large eddy simulation (LES)
Drews *et al.* [2008+2010], Prieske *et al.* [2008]		(1) Bubble rise, liquid flow and wall shear stress. (2) Prediction of circulation velocity.	(1) VOF. (2) Euler-Euler.	(1) Not mentioned. (2) Shear stress tr. (SST).
Dasilva *et al.* [2004]	Submerged hollow-fibres	Impact of fibre arrangement	None (water flow only)	Standard k-ε vs. SST k-ω
Martinelli *et al.* [2010]		(1) Fine bubble flow. (2) Spherical-cap bubble flow.	(1) Euler-Euler. (2) VOF.	(1) Standard k-ε. (2) Not mentioned.
Ghidossi *et al.* [2006a]		Pressure loss prediction for water flow through inside-out HF units	None (water flow only)	None (laminar flow)

Table (3.2) Overview of previous CFD studies in MBR research.

(3.4.1) **Full-scale MBRs**

Kang *et al.* [2008] investigated differences in flow behaviour between **pilot- and full-scale MBR units** by representing hollow-fibre modules as porous zones. It was observed that the mixed liquor velocity in the full-scale unit is lower compared to the pilot plant. While the average cross-flow velocity in the pilot plant was about 0.3 to 0.4 m/s, the cross-flow velocity in the full-scale plant was in the range of 0.1 to 0.3 m/s. Moreover, it was found that an increase in tank size for the full-scale plant is followed by a more pronounced internal circulation flow.

A similar CFD approach was established by Saalbach and Hunze [2008] to provide recommendations related to the **design and operation of the membrane unit**. While hollow-fibre (HF) modules were represented by a homogeneous porous medium each, every single plate of a flat-sheet (FS) system was modelled separately. A calibration of the CFD model was achieved by defining a single set of friction factor values for all three spatial coordinates. Circulation flows were investigated for a HF MBR operated in air-cycling mode. Upflow regions were observed in aerated and downflow regions in unaerated modules. Interestingly, a downflow occurred in the innermost aerated module due to the proximity to the unaerated compartment of the tank.

Brannock *et al.* compared the **residence time distribution** of outside and inside submerged multi-tubular (MT) MBRs [2009] as well as HF and FS MBRs [2010a+b]. Aeration was found to dominate mixing in MBR units. The internal circulation was more pronounced for the outside compared to the inside configuration. The degree of mixing was very high in all 4 systems, with the outside configuration being slightly closer to plug flow conditions than the inside configuration [Brannock *et al.*, 2009]. Similarly, the HF configuration was slightly closer to complete mixing compared to the FS configuration [Brannock *et al.*, 2010a]. For the latter study, the activated sludge model number 1 (ASM1) [Henze *et al.*, 1987] was implemented into the CFD simulation to predict the impact of design features on nutrient removal.

(3.4.2) **Tubular membranes**

Tubular membranes are usually operated in inside-out mode combined with a **lumen-side slug flow** to promote cake layer removal. A vertical Taylor bubble flow in cylindrical tubes is characterised by axis-symmetric bubbles with a round nose and a flat tail [Taha and Cui, 2002]. Significantly different flow patterns were observed for horizontal or inclined tubular membranes [Taha and Cui, 2006a] or two-phase flows in circular and square micro-channels [Taha and Cui, 2006b]. A model introduced by Cui and co-workers to estimate mass transfer coefficients is based on a computational grid with a reference frame attached to the rising bubble. A first simulation step allows a proper development of the multi-phase flow and provides an estimation of wall shear stress. This outcome was linked to the filtration performance by applying polarisation and osmotic pressure models in a second simulation stage [Taha and Cui, 2002]. The authors have shown that the liquid is pushed sideways by the rising bubble and forms a liquid film. This film accelerates along the bubble length until a terminal liquid velocity is reached. A wavy bubble tail and wall shear stress fluctuations were observed for long bubbles, which leads to an increase in steady-state permeate flux. The annular film jet penetrates into the upflowing liquid slug behind the bubble and causes the formation of vortices in the wake region. It was found that the first change in flow direction close to the bubble nose is smooth, whereas the transition at the bubble tail is rather sudden. Increasing the frequency of air bubbling was followed by an increase in permeate flux.

Ndinisa *et al.* [2005] used a similar approach for investigating the **impact of permeate extraction** and a reduced feed flow rate on the bulk-phase flow field. They have shown that permeate extraction is leading to small oscillations in wall shear stress amplitude and a slight reduction in the magnitude of shear stress. The authors concluded that these alterations in wall shear stress are negligible for operating conditions typical in membrane filtration processes. In contrast to the outcomes presented by Cui and Taha [2002], Ndinisa *et al.* [2005] observed a smooth change in flow direction for both bubble nose and bubble tail.

Gas slugs of variable size were studied by Ratkovich *et al.* [2009]. The shape of the bubble tail was found to fluctuate and the overall bubble shape to be affected by variations in liquid viscosity and surface tension. It was shown that the CFD model overestimates experimental results of shear stress measurements for high gas flow rates, which was attributed to an insufficient turbulence modelling.

(3.4.3) Submerged flat-sheets

Ndinisa *et al.* [2006] investigated the **impact of baffles** mounted in-between flat-sheet membranes on the distribution of air and wall shear stress in the system. Using baffles results in a higher degree of confinement of the flow channel, which promotes slug flow conditions. A defined bubble size was set, which was varied in a series of numerical simulations. It was observed that the bubbles tend to migrate from the centre of the column towards the edges, where a meandering bubble plume was formed on each side. This meandering character is presumably due to vortices in the liquid stream [Delnoij *et al.*, 1997]. The intensity of meandering was found to increase as the aeration rate or the bubble size increases. The presence of bubbles further enhances the shear induced by a single-phase flow of water until reaching a critical aeration rate. Moreover, an increase in aeration rate, bubble size or number of baffles led to an increase in average shear stress.

Jajuee *et al.* [2006] investigated the gas holdup and liquid velocity in **airlift membrane contactors**. In this configuration, horizontal flat-sheet membranes are separating aerated and unaerated compartments of the reactor. A permeation of liquid is driven by a density difference between the unaerated (downcomer) and the aerated zone (riser). The CFD simulations have shown that the liquid flow enters the downcomer as a horizontal surface jet. This surface jet induces a downward liquid jet along the wall and a horizontal flow reflected from the wall towards the membrane. An increase in membrane distance led to a reduction in intensity of the surface jet. An increase in bubble size was followed by a higher rise velocity and shorter residence time of the bubbles in the riser and causes a decrease in horizontal velocity in the downcomer.

The **circulation velocity** in a FS MBR was predicted as a function of aeration rate and geometry parameters by Kraume and co-workers [Drews *et al.*, 2008; Prieske *et al.*, 2008]. Their investigations were based on a similar approach suggested by Chisti *et al.* [1988] for airlift loop reactors without internals. It was found that an increase in bubble size leads to an increase in lifting forces, so that the circulation velocity increases. An increase in distance between the membrane plates is followed by a higher superficial liquid velocity in the riser [Prieske *et al.*, 2008]. The pressure loss between down- and upflow region was significantly affecting the circulation velocity [Drews *et al.*, 2008].

Complementary CFD studies conducted by the same group were focussing on a **single bubble** rising in-between two membrane plates [Drews *et al.*, 2008]. Smaller bubbles were found to rise with the same velocity compared to unconfined conditions. An increase in bubble diameter enhances the effect of the presence of walls on the bubble shape, which leads to a smaller projected area and higher rise velocities. For a bubble rising in a stagnant liquid, the shear stress maximum is located at the largest circular circumference of the bubble. An increase in superposed circulation velocity in the riser is followed by a higher shear stress maximum and its location progresses towards the bubble wake. The predicted two-phase shear stress was much higher than that observed for a single-phase flow of the same liquid velocity, which is consistent with previous findings [Ducom *et al.*, 2002]. Drews *et al.* [2010] have found that the wall shear stress can either decrease or increase as the bubble size increases, depending on the distance between the membrane sheets. Furthermore, it was observed that an increase in cross-flow velocity leads to a decrease in critical flux. This unexpected observation is presumably due to a decrease in critical cut diameter as the tangential liquid velocity increases. Therefore, a **selective particle deposition** is taking place, which leads to a reduced average particle size and a higher specific filtration resistance of the cake layer.

(3.4.4) Submerged hollow-fibres

Dasilva *et al.* [2004] investigated the **impact of fibre arrangement** on the overall flow pattern for both square and triangular fibre arrays. The authors observed low flow areas for a relatively short inter-fibre distance in a square-type configuration. Therefore, the maximum packing density for a square fibre array is lower than that for a triangular fibre arrangement. Moreover, square arrays lead to symmetrical flow patterns, whereas the flow through a triangular fibre array of short fibre distance is of sinusoidal character. It was found that the friction factor decreases significantly as the boundary layer separates form the fibre surface. A reduction in outer diameter of the membrane was followed by more significant back-currents and higher friction factors.

Martinelli *et al.* [2010] applied two different CFD approaches for a detailed modelling of **fine and spherical cap bubble flows**. Interestingly, very low wall shear stress values were observed for all aeration conditions simulated. Furthermore, no significant benefit of using spherical cap instead of fine bubbles was found, which is in contrast to a number of previous studies [Cui *et al.*, 2003]. The authors attributed this unexpected trend to a horizontal flow induced by a rising bubble, which is leading to an enhanced particle transport to the membrane.

Ghidossi *et al.* [2006a] derived a **pressure loss correlation** for a flow through inside-out hollow-fibre ultrafiltration units as a function of membrane characteristics and operating conditions. It was shown that the pressure drop increases as the inlet velocity increases, while the inlet pressure increases and the internal diameter or the permeability of the membrane decreases. The pressure was found to drop linearly along the membrane length. The resulting correlation serves as an adaptation of the well-known Hagen-Poiseuille equation.

In conclusion, extensive research was conducted in the field of CFD applied to MBRs. However, only very few detailed modelling approaches for investigating the flow through submerged hollow-fibre membrane filtration units exist. Therefore, the CFD simulations presented in sections (4.5) and (5.4) aim at a proper representation of irregular fibre arrangement in single hollow-fibre bundles.

(4) Materials and methods

This section provides details about the membranes, membrane modules, model suspensions and setups used for the experimental investigations conducted in the framework of this study. In addition, methodologies applied for nuclear magnetic resonance (NMR) imaging, direct observation (DO) of fibre movement and computational fluid dynamics (CFD) simulations are presented.

(4.1) Membrane and membrane module characteristics

For all filtration tests, hollow-fibre membranes of the PURON® configuration were supplied by Koch Membrane Systems (KMS) GmbH. The single fibres were cut to the desired length (i.e. 0.75 to 1 m). They show an outer diameter of $d_{o,HF}$ = 2.6 mm and a hydraulic internal diameter of $d_{i,HF}$ = 1.7 mm (see section (4.4.1)). According to the supplier, the nominal pore diameter of the membrane (polyether sulphone (PES) membrane supported by a porous polyester tissue) is 0.05 µm [Koch, 2008]. Experimental investigations to characterise the membrane pore structure and membrane material properties were conducted. Results of pure water permeability (PWP), molecular weight cut-off (MWCO), scanning electron microscopy (SEM) and zeta-potential measurements are presented below. Furthermore, atomic force microscopy (AFM), contact angle and X-ray photoelectron spectroscopy (XPS) tests were performed [Buetehorn *et al.*, 2008]. Fouled membranes were sampled during a piloting period of activated sludge filtration and were characterised according to the same protocol [Buetehorn *et al.*, 2007a+b; Schulz, 2007]. However, membrane material characteristics and their alterations due to biological fouling are not part of this report.

(4.1.1) Membrane characterisation

Three membranes manufactured under different chemical post-treatment conditions were compared, see Buetehorn *et al.* [2008] for more details concerning the production process. These variations in production conditions resulted in different pure water permeabilities and MWCO values as presented in **Figure (4.1)**. For the pure water tests, four membrane samples of the same production batch were used for a filtration in submerged outside-in mode with various setpoint permeate fluxes. The rejection of a dextran solution (MW = 1,520,000 g/mol) was determined by high performance liquid chromatography (HPLC) to estimate the average MWCO with a simple experimental method adapted form Mulherkar and Van Reis [2004]. While membrane F3 shows the highest permeability of about 1400 L/(m^2 h bar), the permeability of membrane F5 is the lowest compared to all other samples. In agreement with this, the MWCO of membrane F3 is very high (not detectable with dextran as a model solution), which is indicating an open pore structure. The pore structure of membrane F5 is much denser, as expressed by low MWCO values. The maximum rejection of membrane F3 was 60 % for a molecular weight of 10^7 g/mol, which corresponds to a dextran molecule size of about 55 nm [Granath and Kvist, 1967; Aimar *et al.*, 1990].

SEM images were captured for a qualitative comparison of the cross-sectional pore structure as presented in **Figure (4.2)**. The images show a thin and dense active separation layer of membrane sample F2 compared to a thicker and more porous layer of sample F3. This observation is consistent with the filtration and rejection performances presented above. In agreement with these lab-scale membrane characterisation studies, membrane sample F3 has continuously shown the highest permeability during pilot-scale activated sludge filtration for 15 months [Buetehorn *et al.*, 2007a+b; Schulz, 2007]. Therefore, membrane F3 was chosen for all upcoming filtration tests.

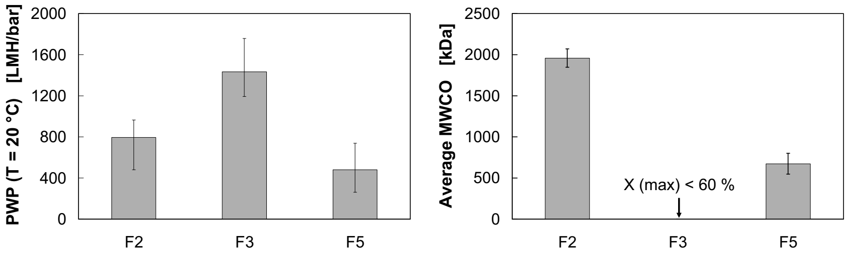

Figure (4.1) Average pure water permeability (PWP) (left) and average molecular weight cut-off (MWCO) (right) of virgin hollow-fibre membranes [Buetehorn *et al.*, 2008].

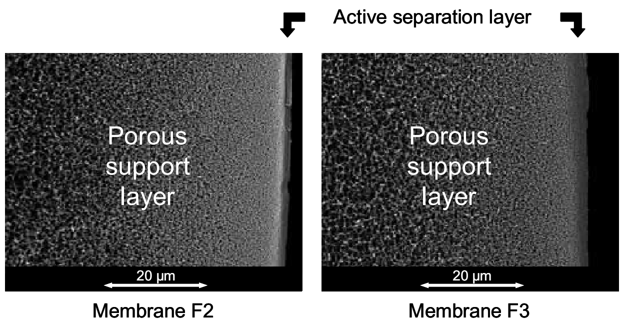

Figure (4.2) Scanning electron microscopy (SEM) images of virgin membrane samples F2 (left) and F3 (right) (acceleration voltage = 3 kV; magnification factor = 2000) [Buetehorn *et al.*, 2008].

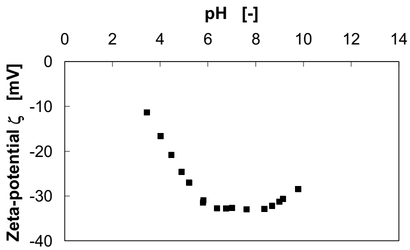

Figure (4.3) Zeta-potential of virgin membrane F3 as a function of pH.

The zeta-potential of virgin membrane F3 was estimated as an indicator of the surface charge and the affinity to solute or particle adsorption, see **Figure (4.3)**. These measurements were conducted with KCl electrolyte solutions and processed using the Fairbrother-Mastin method. For these tests, the membrane fibres were cut in axial direction, unrolled, separated from the support tissue and subsequently glued onto the specimen holder. The streaming potential measurements confirmed that the zeta-potential of virgin membrane F3 is negative with $\zeta < -10$ mV for a pH between 3 and 10. These results are indicating that the membrane is negatively charged for all pH values investigated [Braeken *et al.*, 2006].

(4.1.2) PURON® hollow-fibre bundles

For all macro-scale filtration experiments and CFD simulations, PURON® hollow-fibre bundles supplied by KMS as shown in **Figure (4.4)** were used. The PURON® module consists of hollow-fibres fixed at the bottom end only, which are arranged in bundles of 228 fibres and are submerged vertically into the activated sludge. These bundles are connected to rows, while several rows form a membrane module. Although the membranes are not completely housed or fixed over the length of the module, fibre positioning devices are mounted to the frame to avoid fibre breakage due to excessive fibre motion. A separate gas sparging device is located in the centre of each bundle. Flow channels in the bottom part of the bundle allow the bubble-induced flow of surrounding biomass to enter the bundle for dewatering. In the framework of this study, prototype bundles with a membrane length of 0.85 m and a corresponding membrane area of approximately 1.58 m^2 were provided by KMS. In these bundles, the inter-fibre distance equals 1 mm, the flow channel dimension 5 mm and the outer diameter of the header 73 mm. The gas sparging device is 177 mm long, shows a conical shape with a maximum outer diameter of 21 mm and a gas inlet slit of 5 mm height, which is located 11.5 mm above the fibre potting.

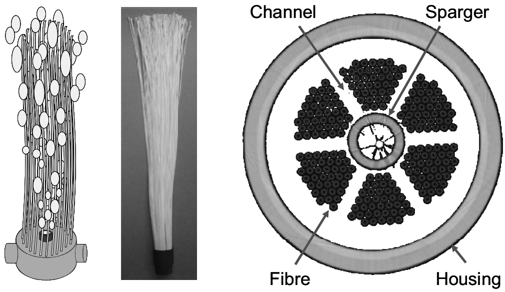

Figure (4.4) PURON® hollow-fibre bundle: Schematic (left), picture (centre) and cross-sectional area close to the fibre potting (right).

(4.2) Characteristics of the model suspension

Since the characteristics of activated sludge are significantly affected by a number of operating parameters [Rosenberger, 2003], a model suspension was used to ensure stable and reproducible conditions. Efforts have been made to find a model substance which suffices the following demands.

- The NMR signal of the particles must significantly vary from the signal of water protons without showing pronounced ferromagnetic properties to allow for a sufficient cake-to-bulk contrast.

- The susceptibility to particle aggregation or sedimentation and adsorption on the membrane surface or in the pore structure should be low. This assures the formation of reversible cake layers with particles of defined size.

- The particles should be spherical in shape, narrow in size distribution and of a significantly larger size than the nominal pore diameter of the membrane. Deviations from these ideal conditions make a comparison to established filtration models more difficult. On the other hand, suspensions containing non-spherical polydisperse particles with a higher affinity to pore blocking are closer to the properties of real MBR sludge.

- The model suspension should be cheap and easy to handle since large amounts are required for the filtration test.

- Rheological properties of the model suspension similar to the ones of activated sludge would allow directly transferring the outcomes to MBR applications.

A high cake-to-bulk contrast is assured by using silica (SiO_2) particles, which do not contribute to the ^{1}H NMR signal and do not show any magnetic properties. For the filtration tests, alkaline, aqueous dispersions of amorphous colloids with spherical shape were used. The stock dispersion BINDZIL® 9950 was provided by Eka Akzo Nobel with a solids concentration of 31.8 vol. %, a specific surface area of 80 m^2/g, a pH of 9.0 and a density of 1.4 kg/L. Furthermore, the stock dispersion contains 0.1 wt. % of Na_2O and small amounts of sodium chlorite which serves as a biocide [Eka Akzo Nobel, 2005]. The desired solids concentrations were adjusted by adding deionised water to the stock dispersion, causing the pH to increase to about 10 due to a reaction of Na_2O and water. Even for this rather high dilution of the stock dispersion, the substance shows a milky appearance. The characteristics of these silica dispersions, which are later on referred to as silica suspensions, were characterised in close collaboration with the MBR-Train consortium (MEST-CT-2005-021050). Therefore, experimental results of particle size, zeta-potential and rheology as presented in **Figure (4.5)** and **Figure (4.6)** were previously published elsewhere [Camacho Ramos, 2009].

The measurements of particle size and zeta-potential shown in **Figure (4.5)** were conducted at room temperature using a dynamic light scattering technique (DLS) combined with laser Doppler velocimetry (LDV). It was found that variations in silica concentration are affecting the average particle size and the zeta-potential of the suspension. This is presumably caused by the addition of different amounts of deionised water followed by variations in pH and surface charge. The particle size averaged over all three solids concentrations is 85.7 nm (as compared to a nominal pore diameter of 50 nm) with an average polydispersity index of 0.23. A pre-treatment of the suspension using a 1.5 µm filter or an ultrasonic bath to remove or disrupt particle aggregates led to a relative deviation in particle size of 0.8 or 4.4 %, respectively. These results are indicating that particle size variations due to different solids concentrations or particle aggregation are negligible.

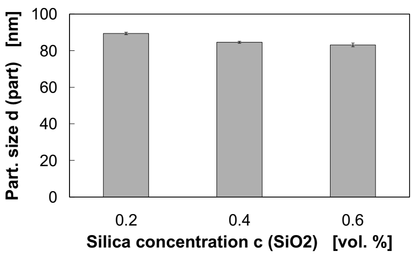

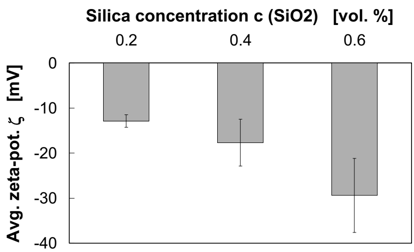

Figure (4.5) Characterisation of the model suspension: Average particle size (left) and average zeta-potential (right) as a function of solids concentration (adapted from Camacho Ramos [2009]).

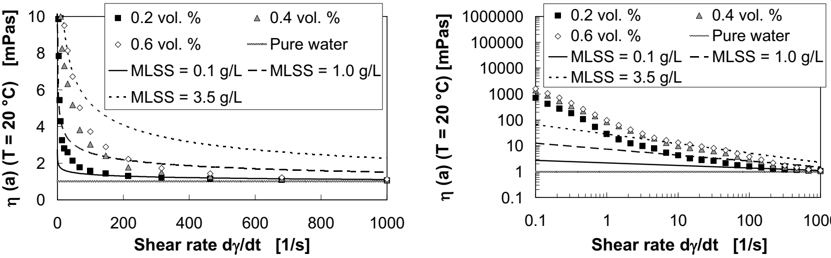

Figure (4.6) Characterisation of the model suspension: Apparent viscosity as a function of shear rate with linear (left) or logarithmic axes (right) for different solids concentrations (adapted from Camacho Ramos [2009]).

The zeta-potential measurements scatter significantly as shown by error bars on the right-hand side of **Figure (4.5)**. In addition, changes in zeta-potential are observable for different silica concentrations. Nevertheless, the measured zeta-potential of the suspensions was negative with $\zeta < -10$ mV for all cases, compared to a zeta-potential of the membrane of $\zeta < -25$ mV for pH = 10. Hence, it is expected that repulsive rather than attractive particle-particle and particle-membrane interactions are occurring.

The rheology of activated sludge of different MLSS concentrations is described by the Rosenberger model, see equation (3.4) in section (3.1). This model accounts for the shear thinning characteristics of the biological suspension, leading to lower apparent viscosities as the shear exposed to the biomass increases. The rheology of the model suspension was investigated by using a rotational rheometer equipped with a cone-plate system and operated at room temperature. These investigations have shown that the apparent viscosity rapidly decreases in the range of very low shear rates, with a decline levelling off for higher shear rates as shown in **Figure (4.6)**. An increase in solids concentration causes the apparent viscosity to increase. According to the Rosenberger model, the rheology of the model suspension corresponds to MLSS concentrations between 0.1 and 3.5 g/L for 10 1/s < $\dot{\gamma}$ < 1000 1/s. In contrast, full-scale MBRs are frequently operated at MLSS concentrations between 10 and 15 g/L [Pinnekamp and Friedrich, 2003], which significantly limits the direct transferability of silica filtration results.

(4.3) Experimental setups and test protocols

A number of lab- and pilot-scale experimental setups were applied in the framework of this study to investigate the silica filtration performance with different degrees of simplification. For the most complex measurements of permeate flow and cake growth, the NMR setup was designed and is introduced in detail in the following section. The methodology established for the operation of this test rig was adapted to other single fibre rigs introduced in sections (4.3.2), (4.3.3) and (4.3.4) as far as possible. Therefore, only the most significant differences to the NMR studies are outlined to provide a better overview. The single bundle setup is introduced in section (4.3.5), which allows a direct comparison of different modes of operation. Please note that the corresponding test protocols and the subsequent data processing are presented along with the descriptions of the test rigs.

All setups introduced below are equipped with either **tight or loose hollow-fibres**. A loose fibre is fixed at the bottom end only, so that the fibre moves in interaction with the shell-side flow pattern. A tight fibre is fixed at both ends to avoid fibre motion, although the permeate is extracted from one end only. Fibres fixed at one end only, but located in narrow feed cannels are referred to as quasi-tight fibres, since an intensive fibre motion is inhibited by the close proximity to the channel wall.

(4.3.1) NMR test rig

The test rig schematically shown in **Figure (4.7)** was built for both permeate-flow and cake-formation visualisation studies by using nuclear magnetic resonance (NMR) imaging. Constraints such as limitations in space, the absence of materials and electronic devices close to the magnet and the need for a mobile and easy-to-connect device had to be met during the design stage. Please refer to section (4.4.1) for more details on the NMR background and the methodology established for process visualisation.

The NMR test rig consists of a flexible tube of 8 mm internal diameter and 2 m in length, which serves as the shell of the test cell filled with stagnant feed (water or silica suspension). A continuous feed supply is ensured by gravity flow from a buffer tank into the test cell. The cell is equipped with a single, quasi-tight hollow-fibre, which is sealed at the bottom and is connected to the permeate extraction line at the top end using heat shrink tubing. This upside-down arrangement of the fibre allows an effective removal of degassing products, which are subsequently entrapped in a bypass loop of the permeate line. A pressure transducer (STS ATM -1 … +1.5 bar r) and a thermocouple (DIN IEC 584 type K) in the permeate line are connected to a data logging system (DASYLab 10.0.0) to measure the filtration parameters online. The setup was operated with constant setpoint permeate flux in submerged outside-in mode. A balance (ACCULAB ALC-3100.2) allows online permeate flux monitoring and a remote control of the rotation speed of the peristaltic pump (ISMATEC MCP Standard, ISM 734B pump head, MASTERFLEX 06409-13 Tygon tubing). This gravimetric flow measurement prevents permeate recirculation, which is commonly applied to avoid concentration changes and variations in hydrostatic height in the feed channel. Therefore, it was assumed that differences in feed composition and feed pressure are negligible.

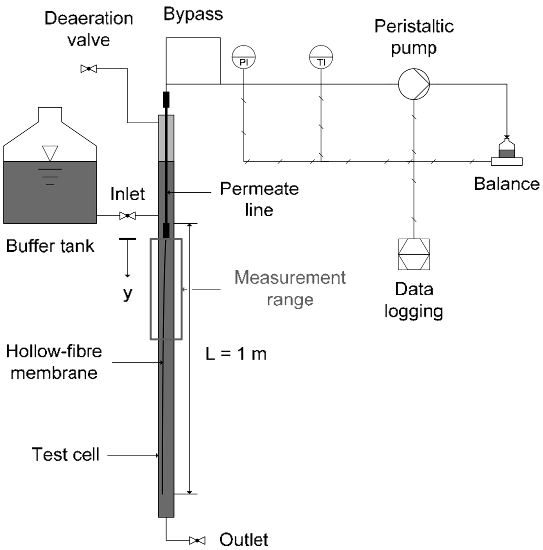

Figure (4.7) Schematic of the NMR test rig.

For comparative experiments, the vertical position of the entire setup can be manually adjusted between y = 0 cm and a maximum distance of y = 40 cm from the point of permeate extraction, see **Figure (4.7)**. This adjustment in height is accurate for the position y = 0 cm next to the point of permeate extraction, but is limited to an accuracy of approximately ± 1.5 cm for all other positions. This positioning inaccuracy was followed by a measurement error of 3 % for the permeate velocity estimation and a measurement error not detectable for the cake formation study.

The permeate flow visualisation was conducted with 1 g/L of copper sulphate ($CuSO_4$) dissolved in deionised water. The addition of this substance reduces the longitudinal relaxation time (T_1) of the water protons and shortens the duration of an NMR measurement, see section (4.4.1). However, adding $CuSO_4$ to the silica suspension causes particle settling, so that combined studies of cake formation and permeate flow were not performed at this stage of investigations.

For the silica filtration tests, the permeate flux was varied between 10 and 30 L/(m^2 h) and the silica concentration in 2 L of suspension between 0.2 and 0.6 vol. %. Prior to the filtration, the membranes were washed with deionised water for approximately 1 h to (i) wet the membrane pores, (ii) remove glycerol from the pore structure and (ii) extract air from the membrane lumen. The pure water permeability (PWP) was measured as an integrity check. The reference (feed) pressure was measured before the filtration was initiated using the transducer in the permeate line. From the measured data, the TMP evolution was calculated and corrected for T = 20 °C using equations (3.5) and (3.6). A final TMP of 800 mbar was chosen as an abort criterion for the filtration test. Settling of particles from the bulk phase was not observed in filtration experiments lasting for up to 8.5 h. After each test run, the setup was rinsed with tap water to remove remnants of the silica suspension. A virgin membrane and fresh silica suspension were used for every single test to achieve a better comparability of results. Permeate backwashing was not involved in the filtration sequence. Please refer to Somoza Parada [2010] for more details concerning the experimental procedure.

The impact of air bubbling on the removal of the cake layer was investigated. For the very first aeration studies, the outlet valve was connected to a central pressurised air line. A continuous or intermittent aeration during the NMR measurement is not feasible since intensive fluid motion negatively affects the cake-to-bulk contrast. Therefore, three aeration cycles with continuous filtration were performed in-between the NMR measurements. The aeration sequence was initiated after a filtration period of 35 min without aeration. Subsequent to this, the NMR measurements were interrupted and a single aeration cycle with an air pressure of 0.3 or 0.5 bar (air flow rates were not measurable) and a duration of 30 to 60 s was conducted. A dead time of 30 s before and after an aeration cycle was provided to control the aeration device manually. Each aeration cycle was followed by a single NMR measurement before the next aeration cycle started. Moving forward, a new sparging device is planned to be built to allow for an operation under more defined conditions (bubble size, air flow rate, duration of aeration and aeration frequency).

(4.3.2) Cross-flow test rig

A simple cross-flow filtration setup as presented in **Figure (4.8)** was equipped with a single, quasi-tight hollow-fibre and operated in outside-in mode at constant TMP. The horizontally oriented bench-scale rig consists of a tubular test cell with an internal diameter of 8.3 mm and a length of 1.21 m. The orientation of the test facility is assumed not to affect the filtration without aeration. This is due to the fact that the difference in hydrostatic height influences the flow in both feed and permeate channel to the same extent. For this reason, the local TMP is expected to be the same for both vertical and horizontal fibre arrangements. The permeate is collected from the feed end of the fibre, while the other end is sealed (membrane length = 0.9 m). The average cross-flow velocity can be adjusted by the flow rate of a gear pump in the feed line (ISMATEC Reglo-Z, Z-140 pump head). Furthermore, a pressure retention valve at the retentate side (BÜRKERT Type 2833) is controlled on the basis of a feed pressure measurement (WIKA S-10), thus allowing an operation at constant feed pressure. The permeate flux decline is gravimetrically measured and corrected according to a feed temperature measurement (RÖSSEL PT100). The retentate is recirculated into the feed tank.

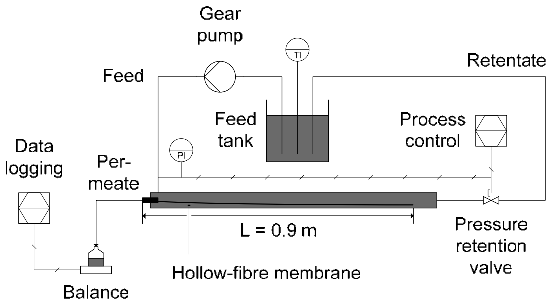

Figure (4.8) Schematic of the cross-flow test rig.

The membrane pre-treatment, the PWP measurement and the silica filtration experiment were conducted following the same protocol as presented for the NMR studies as far as possible. The cross-flow velocity was set between 0.04 and 0.12 m/s, which is in the range of the liquid velocity in submerged MBR processes (slightly lower). The relative feed pressure was varied between 100, 200 and 300 mbar, with TMP = 300 mbar as a common upper threshold in submerged microfiltration.

The discussion of results obtained with the cross-flow test cell focussed on the total filtration resistance R_{tot} as a function of permeate mass m_P as presented in **Figure (4.9)**. This is known to be advantageous for a constant TMP operation as previously discussed in section (2.2.1). Moreover, the time to reach steady-state was expressed as the cumulative permeate mass collected during the transient filtration stage. This characteristic permeate mass and the steady-state filtration resistance were estimated for evaluating the impact of operating parameters and feed characteristics on the overall process performance.

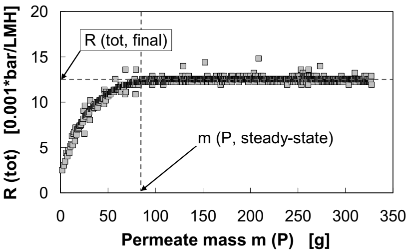

Figure (4.9) Total filtration resistance as a function of cumulative permeate mass: Determination of permeate mass collected during the transient filtration stage and final filtration resistance (v_{CF} = 0.075 m/s, TMP = 200 mbar, c (SiO_2) = 0.4 vol. %).

The rise in filtration resistance with increasing cumulative permeate mass indicates two different filtration stages, which was previously found by numerous researchers (see section (3.2.2)). The transient filtration stage is characterised by a continuous decrease in slope dR_{tot}/dm_P and was lasting for less than 22 min under all operating conditions investigated. Therefore, all following experiments were restricted to 30 min of filtration, which allows monitoring both transient and steady-state filtration conditions. More details on the experimental setup and the corresponding test protocols can be found elsewhere [Kilian, 2009; Buetehorn *et al.*, 2010].

(4.3.3) Single fibre test rig

The single fibre test rig schematically shown in **Figure (4.10)** was equipped with a quasi-tight hollow-fibre and was operated in submerged outside-in mode at constant permeate flux. The development of process parameters was monitored online using the data acquisition, pumping and permeate flux control system of the NMR test rig (see above). In contrast to the NMR setup, the permeate was extracted from the lower end of the fibre located in a vertical tube of 26.7 mm internal diameter and with 1.63 m water level. Air bubbling sequences were included by using a commercial process control software (PROCON-WIN 3.5.0.1), which allows sparging at defined aeration frequencies and durations. The gross aeration rate was adjusted manually by a precision pressure reducer (FESTO MS6-LRP-1/4-D2-A8) and monitored online by a flow meter (FESTO SFAB-10U-WQ6-2SV-M12). A second pressure reducer connected to a central pressurised air line allowed reproducible aeration conditions by buffering pressure fluctuations.

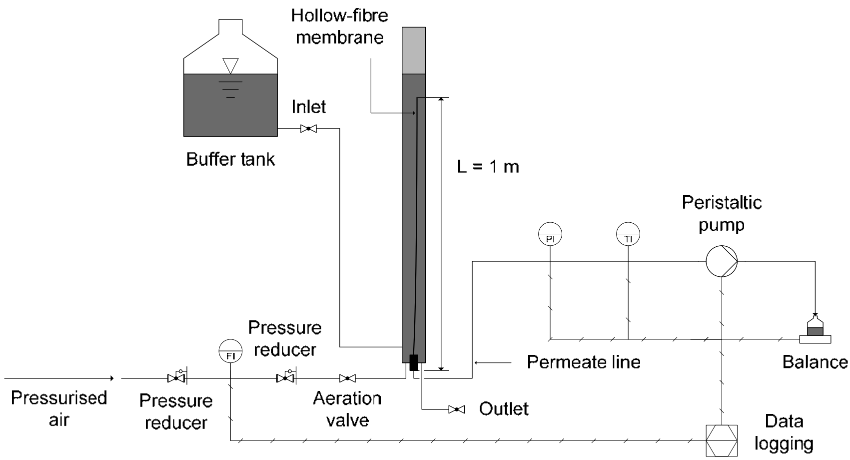

Figure (4.10) Schematic of the single fibre test rig.

The filtration tests were performed using the same pre-treatment strategies and filtration protocols as for the NMR measurements. Therefore, the parameter analysis was mainly focussing on aeration conditions such as duration of aeration (20 to 120 s), frequency of aeration (0.1 or 0.2 cycles/min) or aeration intensity (gross aeration rate = 2.1 to 3.4 L/min). These aeration parameters were introduced in section (3.2.2) and were not studied during the NMR test series. The efficiency of backwashing sequences on the removal of the cake layer was not investigated so far.

Typical evolutions of gross and net aeration rate are plotted on the left-hand side of **Figure (4.11)** for an aeration sequence of 540 s OFF – 60 s ON. A relative air pressure of 0.3 bar corresponds to a maximum gross aeration rate of about 3 L/min. It is important to note that significantly lower values were measured at the very beginning of the aeration sequence. Therefore, an average gross aeration rate for each aeration cycle was determined, indicating a good reproducibility with only 1.4 % relative standard deviation. This gross aeration rate corresponds to a net aeration rate of 0.27 L/min for this sequence. The corresponding TMP and permeate flux evolutions are presented on the right-hand side of **Figure (4.11)**. For this continuous filtration, periods without aeration are characterised by a rapid increase in TMP, whereas air sparging was in almost all cases capable of completely recovering the initial TMP. Nevertheless, a creeping increase of maximum TMP suggests that irreversible fouling occurs. The impact of operating parameters and feed characteristics on the overall filtration performance was evaluated by estimating the fouling rate averaged over 90 min of filtration

$$\left.\frac{\mathrm{dTMP}}{\mathrm{dt}}\right|_{\mathrm{avg}} = \frac{1}{n}\sum_{i=1}^{n}\left.\frac{\mathrm{dTMP}}{\mathrm{dt}}\right|_{i}, \tag{4.1}$$

with the **fouling rate** of the filtration cycle i (adapted from Le-Clech *et al.* [2003])

$$\left.\frac{\mathrm{dTMP}}{\mathrm{dt}}\right|_{i} = \frac{\mathrm{TMP}_i^{\max} - \mathrm{TMP}_i^{\min}}{t_i^{\max} - t_i^{\min}}, \tag{4.2}$$

the number of filtration cycles n and the maximum and minimum TMPs and points in time, TMP_i and t_i. In general, the fouling rate is well-known from critical flux tests as described in section (3.2.3) and indicates the significance of fouling under the corresponding process conditions. Fouling rates close to zero are attributed to the adsorption of dissolved or dispersed matter on the membrane. Higher fouling rates are corresponding to a combination of adsorption, deposition or even compaction phenomena. For filtration experiments with a complete TMP recovery ($\mathrm{TMP}_i^{\min} = \mathrm{const}$) and a constant aeration cycle duration ($t_i^{\max} - t_i^{\min} = \mathrm{const}$), the fouling rate according to equation (4.2) solely represents changes of maximum TMP. Please refer to Han [2010] for more details concerning the test protocol and the subsequent data processing.

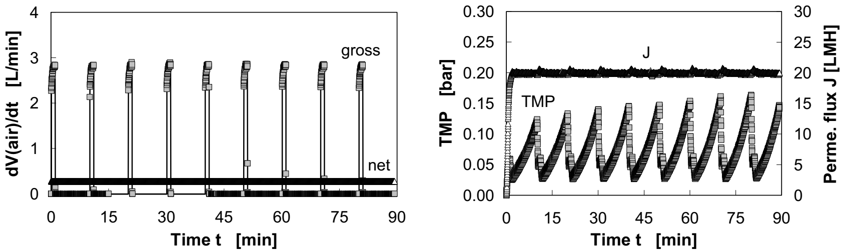

Figure (4.11) Single fibre test rig: Evolutions of gross and net aeration rate (left) and of TMP and permeate flux (right) (J = 20 L/(m^2 h), c (SiO_2) = 0.4 vol. %, p_{air} = 0.3 bar, 540 s OFF – 60 s ON).

(4.3.4) Fibre movement test rig

The setup presented in **Figure (4.12)** is equipped with loose hollow-fibre membranes and is operated in submerged outside-in mode at constant permeate flux. The test facility is located at the UNESCO Centre for Membrane Science and Technology at the University of New South Wales (UNSW) in Sydney, Australia. The rig and the test protocol were adapted from previous studies conducted by Wicaksana *et al.* [2006]. Single fibres and small fibre bundles were loosely hold in position by a support frame, which is capable of housing 4 bundles in parallel. A Plexiglas feed tank (8 cm width, 30 cm length, 120 cm height) allows an observation of bubble-induced fibre movement in different vertical positions.

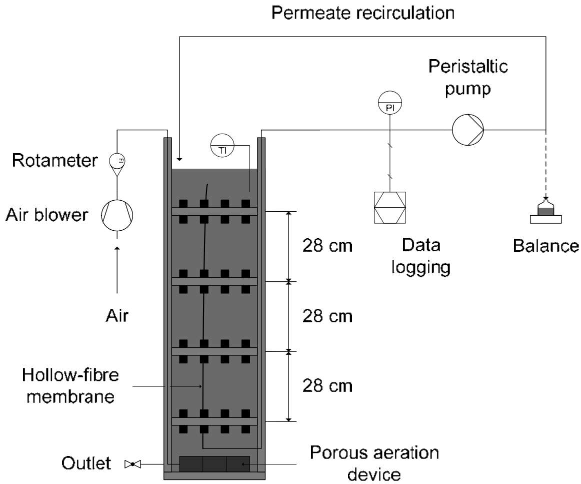

Figure (4.12) Schematic of the fibre movement test rig [Buetehorn *et al.*, 2009].

The permeate was extracted from the bottom end of the fibre. The upper end was either free to move laterally in the support frame (loose fibre) or was fixed to the frame to avoid intensive fibre motion (tight fibre). A constant permeate flux was maintained by a peristaltic pump (MASTERFLEX 7550-30, Easy-Load II 77201-60 pump head, 06409-14 Tygon tubing). The TMP rise was monitored online by a pressure transducer in the permeate line (LABOM CB 1020). The permeate flux was gravimetrically cross-checked by weighing the amount of permeate manually, whereas the permeate was recirculated into the feed tank otherwise. A temperature correction of TMP was achieved by measuring the feed temperature manually. A porous medium was located below the hollow-fibres and connected to a blower (TECHNO TAKATSUKI Hiblow Air Pump HP-80) combined with a rotameter (FISCHER + PORTER 10A6132NB 2B) to allow for a continuous aeration with 1 to 12 L/min aeration rate. The filtration experiments were lasting for up to 3 h. The permeate flow rate was set to either 2 or 3 mL/min due to limitations in adjusting the rotation speed of the pump, which corresponds to pure water fluxes of 16.3 or 24.5 L/(m^2 h), respectively. For the membrane pre-treatment and all filtration experiments, the protocols presented in section (4.3.1) were slightly adapted as far as necessary. In addition to experiments with a constant aeration rate, aeration-step tests were performed with step heights of 1 or 2 L/(m^2 h) and step lengths of 15 or 30 min, see top-left of **Figure (4.13)**.

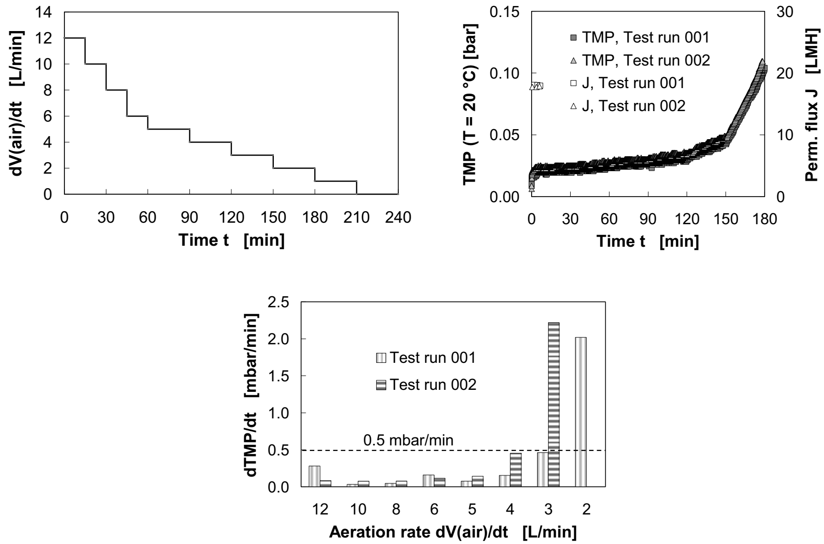

Figure (4.13) Critical aeration rate tests with a single hollow-fibre: Test protocol (top-left), TMP evolution (top-right) and TMP rise for each aeration step (bottom) (N_{HF} = 1 (loose), c (SiO_2) = 0.4 vol. %).

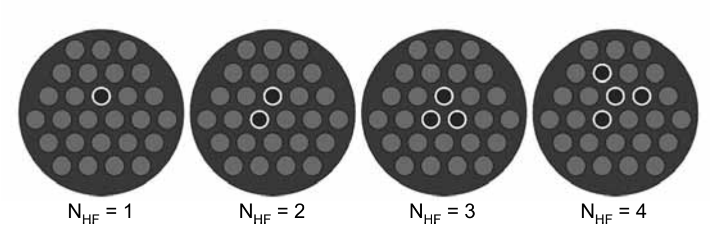

Figure (4.14) Fibre movement studies: Schematics of fibre arrangement of the prototype hollow-fibre bundles.

Relaxation periods in-between two aeration steps were not included since a continuous aeration was applied, i.e. no particle deposition is expected above the critical aeration rate. The corresponding TMP evolution for a filtration at approximately 18 L/(m^2 h) is shown on the right-hand side of **Figure (4.13)**. Relatively low fouling rates solely due to adsorption on the membrane surface were occurring during the first aeration steps. A steeper TMP rise due to particle deposition was observed below aeration rates of 3 L/min as shown at the bottom of **Figure (4.13)**. This critical aeration rate was found to be reproducible within a range of ± 1 L/min for an arbitrary fouling rate threshold [Le-Clech *et al.*, 2003] of 0.5 mbar/min. Please refer to Buetehorn *et al.* [2009] and Kilian [2009] for more details concerning the experimental conditions.

The fibre movement test rig was equipped with membrane bundles consisting of a different number of hollow-fibres N_{HF}, see **Figure (4.14)**. These prototypes are based on a single segment of a PURON® hollow-fibre bundle as introduced in section (4.1.2), in which up to 4 holes are filled with fibres of 0.75 to 0.9 m in length. Therefore, fibre movement and fibre-fibre interactions in response to the multi-phase flow can be observed according to the methodology presented in section (4.4.2). The same bundles and operating conditions were applied for the silica filtration tests to evaluate the impact of fibre motion on the overall filtration performance. Moreover, detailed knowledge about the characteristics of fibre motion at different vertical positions allows evaluating assumptions made for the CFD approach presented in section (4.5.3).

(4.3.5) Single bundle test rig

The single bundle test rig shown in **Figure (4.15)** is equipped with a bundle consisting of 228 loose hollow-fibres of 0.85 m in length. The bundle is housed in a tube which is 1.11 m long and 0.084 m in diameter. This diameter corresponds to the packing density of a full-scale module in real MBR configurations. The setup can be operated in quasi-submerged mode, in submerged mode with a superposed cross-flow or in cross-flow mode. For an operation under **quasi-submerged conditions**, the flow rate in the feed channel is reduced to the minimum value required to keep the hydrostatic feed pressure constant. This leads to a theoretical increase in solids concentration from 0.4 to 2.1 vol. % during 30 min of filtration at $J = 20$ L/(m^2 h). However, this maximum concentration increase is not reached since pump- and bubble-induced cross-flow cause a discontinuous discharge of particles at the overflow weir at the retentate side. The feed flow rate was increased above this threshold to model a superposed background flow caused by recirculation as observed in air-lift reactors [Drews *et al.*, 2008; Prieske *et al.*, 2008]. A separate test series in cross-flow mode is characterised by a tangential flow solely induced by the feed pump (GRUNDFOS CRN1-9 A-P-G-V-HUBV) without aeration. For all three modes of operation, a constant permeate flux was maintained by the permeate pump (LABU BROX Baureihe 2).

Flow rates are measured in the feed (GEMÜ 815 400 or GEMÜ 815 3300), the permeate (ENDRESS + HAUSER Promag 33A T04 – AD1AB11A21A) and the aeration line (Georg Fischer 198 801 885). A single pressure transducer (STS ATM -1 … +1 bar r) installed in the permeate line allows an online monitoring of TMP, which is corrected based on a feed temperature measurement (STS TS 100). A series of pressure reducers (WIKA EN 837-1 + FESTO 345 395 N5) and valves in the aeration line and a commercial process control software (WAGNER & MÜLLER GmbH & Co. KG) allow operating at different specific aeration demands (SAD_m), gross aeration rates and aeration frequencies.

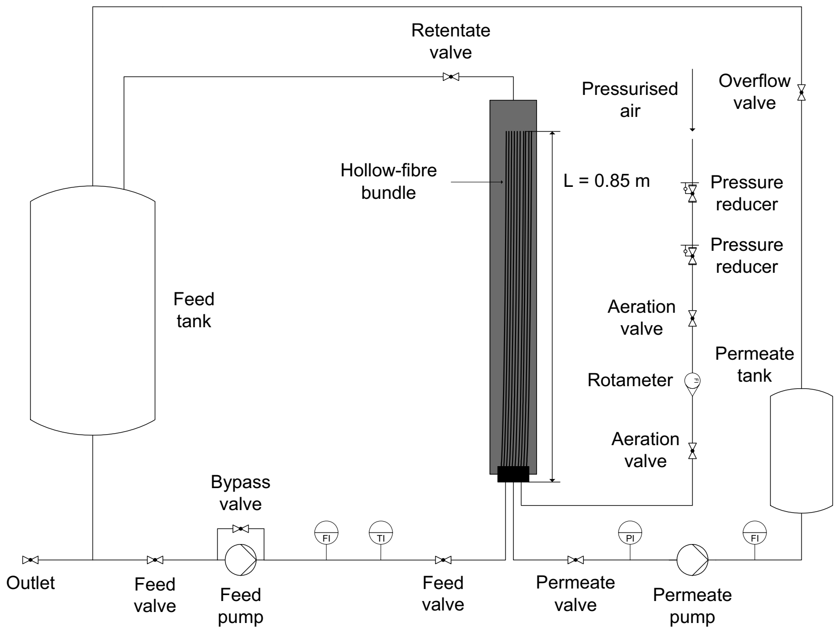

Figure (4.15) Schematic of the single bundle test rig.

The permeate is collected in a separate tank and could be used for backwashing purposes. However, backwashing is not involved in the filtration sequence. Thus, the permeate is recirculated via an overflow into the feed tank, which leads to constant hydrostatic pressures in both tanks. The retentate stream is also recirculated into the feed tank. The latter stream is small for the quasi-submerged mode and increases as the imposed cross-flow in the feed channel increases. The single bundle test series was lasting for about 6 months. The same fibre bundle was used for the whole series, whereas the silica suspension (150 L) was exchanged every 1 to 2 weeks. Pure water tests have shown that irreversible fouling was occurring during the very beginning of the study only, with an initial PWP reduction of 19 % compared to the virgin membrane. Afterwards, almost constant PWPs were measured with a total reduction of 22 % during 6 months of operation. Therefore, only the first test series was affected by the initial membrane fouling, which is not discussed in this report. A complete recovery of the initial PWP by an intensive chemical cleaning using sodium hypochlorite (NaOCl, pH = 11) suggests that adsorbed organic matter was the dominating foulant [Judd, 2006].

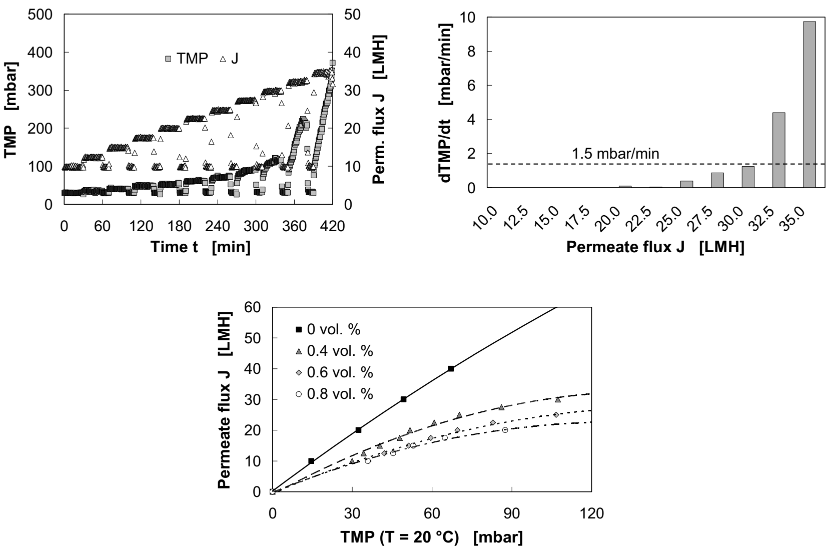

Figure (4.16) Critical flux tests with a single hollow-fibre bundle: TMP and permeate flux evolution (top-left), TMP rise for each flux step (top-right) and deviations from clean water conditions for all solids concentrations investigated (bottom) (SAD_m = 0.18 $m^3/(m^2$ h), $dV_{air,gross}/dt$ = 3 m^3/h, v_{CF} = 0.6 cm/s, c (SiO_2) = 0.4 vol. %).

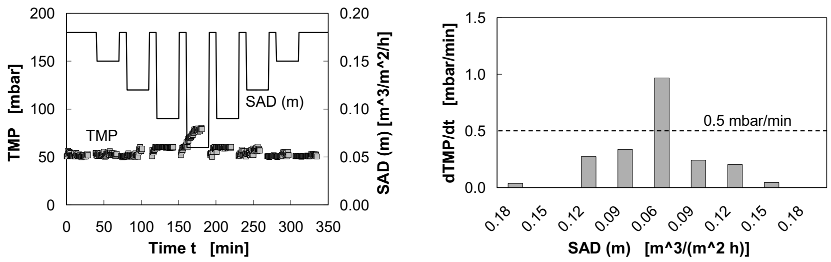

Figure (4.17) Critical aeration rate tests with a single hollow-fibre bundle: TMP and aeration rate evolution (left) and TMP rise for each aeration step (right) ($dV_{air,gross}/dt = 3\ m^3/h$, $v_{CF} = 0.6$ cm/s, $J = 20\ L/(m^2\ h)$, c (SiO_2) = 0.4 vol. %).

In addition to experiments under constant operating conditions, flux-step and aeration-step tests were performed following established methodologies [Le-Clech *et al.*, 2003]. In contrast to the single-fibre studies with continuous aeration, relaxation periods were included for the single bundle tests with intermittent aeration. This slightly modified test protocol suggested by Van der Marel *et al.* [2009] allows estimating the irreversibility of particle deposition. Please refer to Blach [2009] for more details concerning the experimental setup and the test protocols used.

The flux-step method was applied with a step height of 2.5 $L/(m^2\ h)$, a step length of 30 min and a constant net aeration rate $SAD_m = 0.18\ m^3/(m^2\ h)$. The evolutions of setpoint permeate flux and measured TMP and the corresponding fouling rates dTMP/dt for each flux step are presented in **Figure (4.16)**. Firstly, it is observable that the TMP recovers completely during the relaxation period, which suggests that irreversible cake layer formation is negligible. Secondly, the measured TMP values for a silica filtration differ significantly from the pure water filtration values as shown at the bottom of **Figure (4.16)**. This deviation is more pronounced as the solids concentration increases. The latter observation proves that the measurements are restricted to the weak form of critical flux, i.e. adsorption is taking place even for a low-flux operation [Bacchin *et al.*, 2006]. The arbitrary fouling rate threshold for the critical flux determination was defined as 1.5 mbar/min as a compromise for all test runs, see also Le-Clech *et al.* [2003].

The critical aeration rate was estimated with step heights of 0.03 or 0.06 $Nm^3/(m^2\ h)$, a step length of 30 min and a constant permeate flux $J = 20\ L/(m^2\ h)$. The evolutions of TMP and specific aeration demand of the membrane unit (SAD_m) are presented along with the fouling rates for each aeration step in **Figure (4.17)**. It is worth mentioning that the SAD_m is later on also referred to as (net) aeration rate. A continuous increase in fouling rate was detected as the aeration rate decreases, with a more significant enhancement at lower aeration rates. The arbitrary fouling rate threshold for the critical aeration rate determination was defined as 0.5 mbar/min as a compromise for all test runs. No evidence for irreversible phenomena is observable when comparing the ascending and descending stages of the aeration-step test. Therefore, the aeration-step method was restricted to the ascending stage for all subsequent studies.

(4.4) Methodology for process visualisation

The performance of a microfiltration of silica suspensions in different modes of operation was investigated according to the test protocols summarised in the previous section. All these investigations on a meso- or macro-scale provide integral filtration parameters such as the fouling rate or the critical flux only. The methodologies for process visualisation as presented below provide more detailed insights into the filtration process. This allows observing local phenomena such as permeate flow and cake growth on a micro-scale and fibre motion on a meso-scale.

(4.4.1) Nuclear magnetic resonance (NMR) imaging

NMR imaging allows monitoring the composition of a sample by measuring the distribution of mobile protons in any slice of the specimen [Chen *et al.*, 2004b]. For this purpose, the entire shell of the NMR test rig is exposed to a static magnetic field, so that the protons (i.e. the ^{1}H hydrogen nuclei) align with the field. Afterwards, a radio frequency pulse is applied, which creates an oscillating magnetic field from the proton magnetisation perpendicular to the main field. The protons reach an excited state when absorbing energy from the oscillating field. A signal is detected by the receiver coil when the protons return from excitation back to equilibrium. This signal is a function of the individual relaxation properties of the components of the specimen and is transformed to images weighted by the longitudinal (T_1) or transverse relaxation time (T_2).

NMR imaging as a tool for a non-invasive visualisation of micro-scale phenomena was applied using the setup described in section (4.3.1). In the following paragraphs, details concerning (i) the NMR device, (ii) the velocity-encoding pulse sequence, (iii) the cake-visualisation pulse sequence and (iv) the data processing for permeate flow and (iv) cake formation visualisation are introduced. Parts of the NMR methodology presented below and the results presented in section (5.1) were recently published [Buetehorn *et al.*, 2011]. The visualisation of the microfiltration process as a major outcome of these studies is the focus of the report at hand. A more detailed description of the NMR background can be found elsewhere [Utiu, 2011]. Therefore, the following sections are restricted to a brief introduction to NMR imaging in general and to the pulse sequences used in particular.

NMR device

All NMR measurements were performed on a Bruker DSX 200 spectrometer with a field strength of 4.7 T. The spectrometer has a vertical bore of 89 mm in diameter and is equipped with an (x,y,z)-imaging system with a maximum gradient strength of about 1 T/m. For excitation and signal detection, a 20 mm standard birdcage coil was used and operated at a ^1H resonance frequency of 200.047 MHz. The measurements were performed at room temperature (T = 20 °C) and were sub-divided into two categories, (i) dynamic imaging of permeate flow in the membrane lumen and (ii) static imaging of cake layer formation on the membrane surface, see sections below.

Velocity-encoding pulse sequence

It is known that the convective or diffusive displacements of nuclear spins in the presence of a magnetic field gradient alter the phase or amplitude of the NMR signal. This interrelationship can be combined with conventional NMR imaging (NMRI) to obtain velocity images [Callaghan, 1991]. Different flow imaging methods were suggested by a number of research groups [Caprihan and Fukushima, 1990; Callaghan, 1991; Pope and Yao, 1993] and can be classified as follows [Pope and Yao, 1993].

- Inflow/outflow methods make use of the fact that the signal intensity changes if a spin moves into or out of a selected measurement slice.
- Time of flight (TOF) methods can monitor different velocity components based on a frequency-encoding technique.
- Phase-encoding methods as applied in this study make use of phase shifts induced by the motion of spins to measure flow velocities directly.

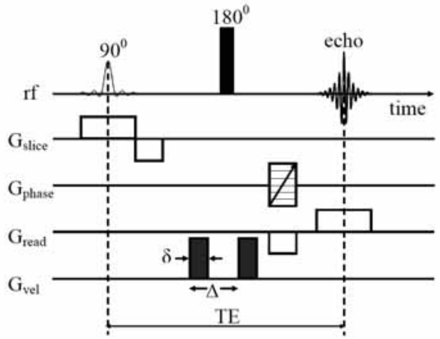

Figure (4.18) Schematic representation of the pulse sequence used for permeate-flow visualisation.

Both the image and the velocity information from an NMR measurement rely on the same principle of spatially-dependent magnetic fields provided by pulsed field gradients (PFGs). In order to obtain a spin density profile such as the image or the velocity information, the space of the measurement volume has to be encoded. For this purpose, a magnetic field with a constant gradient $\vec{G}$ is superposed to the static magnetic field of induction $\vec{B}_0 = (B_x, B_y, B_z)$, which can be expressed as

$$\vec{G} = \left(\frac{\partial B_z}{\partial x}, \frac{\partial B_z}{\partial y}, \frac{\partial B_z}{\partial z} \right) = (G_x, G_y, G_z). \tag{4.3}$$

The velocity-encoding pulse sequence consists of a slice-selective 90° radio frequency (RF) pulse in combination with a 180° refocusing pulse as shown in the first line of **Figure (4.18)**. G_{slice}, G_{phase} and G_{read} are the slice-selective, phase-encoding and frequency-encoding gradients. The echo represents the signal received from the slice of interest in the specimen. In general, the velocity phase-encoding sequence uses a pair of gradient pulses (G_{vel}) of opposite sign but identical area (bipolar gradient pair with pulse duration δ and time separation Δ) to encode velocity information in the phase shift of the signal. The velocity-encoding gradients are applied along the axis of the hollow-fibre membrane and are of the same sign, since a phase inversion is caused in-between the two gradient pulses by a 180° RF pulse.

The magnetic moments or "spins" of the proton exposed to the gradient $\vec{G}$ precess at the Larmor frequency ω associated with the local magnetic field $\vec{B}_0$ at the position $\vec{r}$,

$$\omega(\vec{r}) = \gamma \left(\left| \vec{B}_0 \right| + \vec{G} \cdot \vec{r} \right). \tag{4.4}$$

In a stationary fluid, the nuclear spins accumulate a positive phase shift during the first part and an equal negative phase shift during the second part of a bipolar velocity-encoding gradient. The stationary spins experience a net phase shift of zero. When the fluid flows, spins moving through the specimen are at different locations when applying the bipolar gradients. Therefore, the spins precess at different frequencies and accumulate a non-zero net phase shift. For this reason, the phase shift of the spins corresponds to a time integral of the frequency of precession,

$$\phi(t) = \gamma \int_t \vec{G}(t) \cdot \vec{r} \, dt. \tag{4.5}$$

The position $\vec{r}$ of the moving spins and the gradient $\vec{G}$ are functions of time, whereas the gyromagnetic ratio γ is constant. Using a Taylor series expansion of $\vec{r}$ with respect to time, equation (4.5) leads to

$$\phi(t)=\gamma\int_t \vec{G}(t)\cdot\left[\vec{r}_0+\left(\frac{d\vec{r}}{dt}\right)_{t=0} t+\frac{1}{2}\left(\frac{d^2\vec{r}}{dt^2}\right)_{t=0} t^2+\ldots+\frac{1}{n!}\left(\frac{d^n\vec{r}}{dt^n}\right)_{t=0} t^n\right]dt. \tag{4.6}$$

Neglecting the second term and all higher-order terms, equation (4.6) simplifies to

$$\phi(t)=\gamma\,\vec{r}_0\cdot\int_t \vec{G}(t)\,dt+\gamma\,\vec{v}_0\cdot\int_t \vec{G}(t)\,t\,dt=\gamma\left(\vec{r}_0\cdot\vec{m}_0+\vec{v}_0\cdot\vec{m}_1\right), \tag{4.7}$$

with $\vec{m}_0$ and $\vec{m}_1$ as the zeroth and first order moments of the gradient modulation function and $\vec{v}_0=\left(\frac{d\vec{r}}{dt}\right)_{t=0}$ as the velocity perpendicular to the measurement slice. Therefore, the signal contains two phase modulations, one from position-encoding ($\vec{m}_0$) and another from velocity-encoding ($\vec{m}_1$). In order to separate the velocity information from the spatial information, two pulsed gradient spin echo (PGSE) measurements with different velocity gradient strengths are required. This means that a series of two data sets is measured and separately Fourier-transformed. Subsequently, the phase shift in each pixel is calculated by subtracting the first data set from the second in order to extract the spatial information. This provides a phase shift map which is directly related to the flow velocity perpendicular to the measurement slice. In the resulting velocity images, the intensities correspond to the velocity values of each pixel as an average over the data acquisition time. Further details concerning the NMR settings for permeate-flow visualisation are given in **Table (4.1)** and by Utiu [2011].

Cake-visualisation pulse sequence

In **Figure (4.19)**, the gradient echo sequence for cake-growth visualisation is illustrated. The top line shows the RF pulse sent into the sample and the corresponding echo signal. The other three lines show the slice-selection (slice), the phase-encoding (phase) and the frequency-encoding (read) gradients. The slice-selection gradient was applied in order to select an imaging slice perpendicular to the vertical fibre. The frequency-encoding gradient is applied first in one direction (negative polarity) in order to dephase transverse magnetisation, and second in the opposite direction (positive polarity) to rephrase transverse magnetisation. The maximum signal echo forms when the area under the positive part of the frequency-encoding gradient equals the area under the negative part that precedes the echo. Data acquisition is conducted in the presence of the positive G_{read} gradient. The spatial information of the specimen can be reconstructed by Fourier transformation of the recorded signal.

For the observation of cake layer formation, conventional T_1-weighted NMR images were taken with a standard gradient echo sequence using a short repetition time. This is done to partially saturate the signal from spins with a long longitudinal relaxation time T_1. These spins correspond to relatively low concentrations of colloidal silica, i.e. to the bulk phase signal. Gradient echo imaging was introduced by Frahm and Haase [Matthaei *et al.*, 1985; Frahm *et al.*, 1986a+b; Haase *et al.*, 1986a+b] as a method to speed-up data acquisition. The corresponding pulse sequence is simpler than a spin echo sequence and can be performed more rapidly. This allows a variety of tasks including real-time magnetic resonance imaging (MRI), flow imaging [Frahm *et al.*, 1986a; Haase et al., 1986b] and 3D or volume imaging [Frahm *et al.*, 1986b]. In contrast to a spin echo sequence, no 180° pulse is used for refocusing. The spins are realigned by reversing the direction of their precession rather than changing their phase. Another significant difference to a spin echo sequence is the flip angle of the RF excitation pulse, which can be varied in addition to the repetition time (TR) and the echo time (TE). The flip angle is usually equal or close to 90° for a spin echo sequence, but commonly varies over a range of about 10 to 80° for gradient echo sequences. A larger flip angle provides more pronounced T_1 weights of the image and improves the image contrast.

NMR settings	Velocity pulse sequence	Cake growth pulse sequence
Sequence type	3D phase-encoding	3D gradient echo
Data acquisition time [mm:ss]	Low resolution: 2 x 02:15; high-resolution: 2 x 17:19	03:25
Repetition time (TR) [ms]	1000	100
Echo time (TE) [ms]	7	3
Flip angle [°]	---	45
Number of images averaged [-]	4	8
Field of view (FOV) [mm x mm x mm]	11 x 11 x 2	9 x 9 x 2
Matrix size before zero-filling [pix x pix x pix]	Low-resolution: 32 x 32 x 1; high-resolution: 128 x 128 x 1	256 x 256 x 1
Matrix size after zero-filling [pix x pix x pix]	Low-resolution: 64 x 64 x 1; high-resolution: 256 x 256 x 1	512 x 512 x 1
Spatial resolution before zero-filling (radial) [µm]	Low-resolution: 343.8; high-resolution: 85.9	35.2
Spatial resolution after zero-filling (radial) [µm]	Low-resolution: 171.9; high-resolution: 43	17.6

Table (4.1) NMR settings for permeate-flow and cake-growth visualisation.

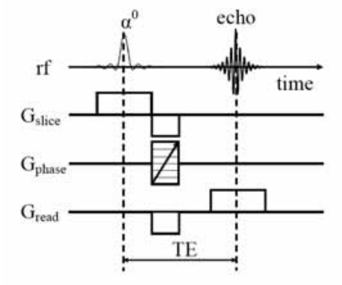

Figure (4.19) Schematic representation of the pulse sequence used for cake-growth visualisation.

In this study, the cake formation was captured simultaneously in three adjacent slices with a thickness of 2 mm each. The centre-lines of the first, second and third slices are located at distances of 5, 10 and 15 mm from the glue connection, thus corresponding to an inter-slice distance of 3 mm. Further details concerning the NMR settings for cake-growth visualisation are given in **Table (4.1)** and by Utiu [2011].

Data processing for permeate flow visualisation

The raw velocity data were zero-filled from 32 x 32 x 1 to 64 x 64 x 1 pixels in a field of view (FOV) of 11 mm x 11 mm x 2 mm. This increased the nominal spatial resolution in radial direction from 343.8 to 171.9 µm. A subsequent Fourier transformation leads to velocity images taken during pure water filtration under steady-state conditions. Each of the images shown in **Figure (4.20)** represents a slice at a certain distance y from the point of permeate extraction. The velocity data characterises the flow averaged over a data acquisition time of 04:30 mm:ss. The bulk-phase flow in vertical (i.e. axial) direction is almost zero due to the lack of bubble- or pump-induced flow in the feed channel. The permeate flow in the pore structure of the membrane is mainly radial (i.e. horizontal), thus leading to relatively small axial velocity components. In addition, the NMR signal of permeating free water protons is saturated by the presence of the membrane material. The observation of the permeate flow in the membrane lumen is of interest, since it allows an estimation of permeate flux distribution along the membrane as discussed in section (5.1.1). All velocity measurements were restricted to a steady-state pure water filtration without particles, so that single NMR measurements at different vertical positions y were sufficient to fully capture permeation conditions along the membrane.

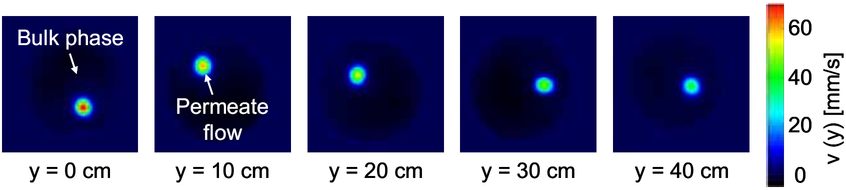

Figure (4.20) Axial permeate velocity distribution in a single hollow-fibre ($J = 30$ L/(m^2 h), c ($CuSO_4$) = 1 g/L).

In addition to the above-mentioned standard settings of the velocity-encoding pulse sequence, a small number of more accurate velocity measurements was performed. For these high-resolution studies, an image matrix of 128 x 128 x 1 pixels was zero-filled to 256 x 256 x 1 pixels for a field of view (FOV) of 11 mm x 11 mm x 2 mm. This corresponds to a nominal spatial resolution in radial direction of 85.9 or 43.0 µm, respectively. The aim of this additional test series was to examine the accuracy of the previous velocity measurements. These settings significantly increased the duration of an NMR measurement to 34:38 mm:ss. Therefore, the latter pulse sequence is not applicable for monitoring transient flow patterns such as alterations in permeate flux distribution caused by cake layer formation.

In **Figure (4.21)**, high- and low-resolution images and the corresponding velocity profiles are compared. The high-resolution measurement provides a better approximation of the laminar velocity profile, indicated by 40 instead of 10 adjacent pixels in the membrane lumen. Therefore, reducing the spatial resolution leads to averaging over wide velocity ranges, which causes a decrease in the maximum value of measured velocities. Moreover, a sharp decline in axial velocity was observed for the high-resolution images, as compared to a rather smooth decline for the lower resolution. Therefore, the hydraulic diameter of the membrane was estimated from the high-resolution images for $J = 10$, 20 and 30 L/(m^2 h) at $y = 0$ cm as the width of the 3D permeate velocity profile.

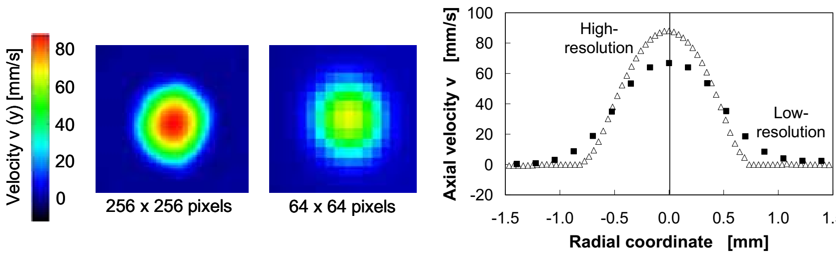

Figure (4.21) Velocity images (left) and axial permeate velocity profiles (right) for high- and low-resolution measurements ($J = 30$ L/(m^2 h), $y = 0$ cm, c ($CuSO_4$) = 1 g/L).

This characteristic internal diameter was found to be 1.7 mm with a relative standard deviation of 1.5 % and is later-on referred to as the **characteristic internal diameter of the hollow-fibre** $d_{i,HF}$. It is worth mentioning that this characteristic diameter is larger than the internal diameter of the support tissue of about 1.2 mm as claimed by the membrane manufacturer. This discrepancy is due to a penetration of the axial permeate flow into the porous structure of the support tissue.

To validate the measured permeate velocity distribution along the fibre, the inflowing and outflowing streams are balanced over a volume element A_m dy according to

$$\dot{V}_y = \dot{V}_{y+dy} + J_{avg}\, A_m = \dot{V}_{y+dy} + J_{avg}\, d_{o,HF}\, \pi\, dy\,. \tag{4.8}$$

In equation (4.8), $\dot{V}_y$ corresponds to the outflowing lumen-side stream (flow in negative y-direction), $\dot{V}_{y+dy}$ to the inflowing lumen-side stream and $J_{avg}\, A_m$ to the permeating stream. The permeating stream is expressed as the product of permeate flux J_{avg} and membrane area A_m, with the outer diameter of the hollow-fibre $d_{o,HF}$ and the infinitesimal distance dy. Using the continuity equation, the lumen-side streams can be described as

$$\dot{V}_y = \overline{v}_y\, A_i = \overline{v}_y\, d_{i,HF}^2\, \frac{\pi}{4} \tag{4.9}$$

and

$$\dot{V}_{y+dy} = \overline{v}_{y+dy}\, d_{i,HF}^2\, \frac{\pi}{4}, \tag{4.10}$$

with the cross-sectional area of the lumen A_i, the average velocity $\overline{v}$ at the vertical position y and y+dy and the internal diameter of the hollow-fibre $d_{i,HF}$. The average velocity is zero at $y = L$ and equals the product of average permeate flux and the ratio of lateral to cross-sectional area of the membrane at the position y = 0 cm. Hence, the boundary conditions used to solve this differential equation are

$$\overline{v}(y = L) = 0 \tag{4.11}$$

and

$$\overline{v}(y = 0) = J_{avg}\, \frac{A_m}{A_i} = J_{avg}\, \frac{d_{o,HF}\, \pi\, L}{d_{i,HF}^2\, \frac{\pi}{4}}\,. \tag{4.12}$$

Equations (4.8) to (4.12) lead to a **distribution of axial permeate velocity** along the membrane of

$$\bar{v}(y) = 4\, J_{avg}\, \frac{d_{o,HF}}{d_{i,HF}^2} (L - y), \tag{4.13}$$

for which the lumen-side pressure loss was neglected. In addition to this simplified approach, efforts have been made to take the lumen-side pressure loss into account [Volmering, 2007]. However, the velocity measurements will be combined with cake formation studies during a later stage of investigations. This requires a proper estimation of transient pressure loss variations and detailed knowledge about the heterogeneity of cake growth. Therefore, the lumen-side pressure loss was neglected and equation (4.13) was used in anticipation of upcoming studies. The overall objective is a simple validation of the NMR methodology under well-defined conditions, which is expected to be challenging for highly transient flow patterns.

The velocity data can be further processed by estimating the average flow velocity from the measured maximum velocity v_{max} and assuming laminar conditions and parabolic velocity profiles [Pangrle *et al.*, 1992; Laukemper-Ostendorf *et al.*, 1998; Hardy *et al.*, 2002],

$$\bar{v}(y) = \frac{1}{2}\, v_{max}(y). \tag{4.14}$$

Subsequently, the **local cumulative permeate flux**

$$J_{cum}(y) = \bar{v}(y) \frac{A_i}{A_m(y)} = \bar{v}(y) \frac{d_{i,HF}^2 \frac{\pi}{4}}{d_{o,HF}\, \pi\, (L - y)} \tag{4.15}$$

is calculated as the product of average velocity and cross-sectional area of the membrane lumen

$$A_i = d_{i,HF}^2 \frac{\pi}{4} \tag{4.16}$$

divided by the lateral area of the hollow-fibre from the very end ($y = L$) to the position y,

$$A_m(y) = d_{o,HF}\, \pi\, (L - y). \tag{4.17}$$

According to equation (4.15), the local cumulative permeate flux equals zero for $y = L$ and equals the average (i.e. setpoint) permeate flux for $y = 0$ cm.

Data processing for cake formation visualisation

The raw cake formation data were zero-filled from 256 x 256 x 1 to 512 x 512 x 1 pixels in a field of view (FOV) of 9 mm x 9 mm x 2 mm. This corresponds to an increase in nominal spatial resolution in radial direction from 35.2 to 17.6 µm. The images shown in **Figure (4.22)** correspond to an instantaneous cake morphology averaged over a data acquisition time of 03:25 mm:ss. Every single NMR measurement was initiated with a dead time of 7 s and ended with a delay of 10 s before the next measurement started.

In **Figure (4.22)**, the bulk phase is characterised by a medium silica concentration and medium signal intensity (grey appearance). The highest silica concentration is occurring in the cake layer, which leads to higher signal intensities and appears as a bright annulus of increasing thickness with time (white). The signal of the water flow in the membrane pore structure is saturated by the presence of the membrane material shown as a black annulus underneath the cake layer. The permeate flow in the membrane lumen shows the highest signal intensity, which is an image artefact due to the large number of protons entering the measurement volume during data acquisition (bright white spot). However, this spot appears to be smaller and in some cases non-circular as the cake layer forms, which is caused by degassing products extracted by the permeate flow.

In **Figure (4.23)**, the longitudinal and transverse relaxation rates $1/T_1$ and $1/T_2$ are plotted versus the silica concentration. The results indicate that an increase in solids concentration causes the relaxation rates to increase linearly, thus leading to an increase in signal intensity for a given measurement period. Silica does not contribute to the proton ^1H NMR signal. Therefore, deviations in relaxation times of free water protons and water protons bound to particles are responsible for the image contrast [Horsfield *et al.*, 1989; Wandelt *et al.*, 1993; Airey *et al.*, 1998]. The cake formation images presented in **Figure (4.22)** correspond to the proton density weighted with the longitudinal relaxation rate $1/T_1$, for which the coefficient of determination for a linear trend line was higher than for $1/T_2$.

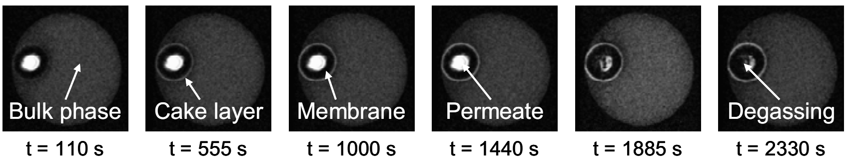

Figure (4.22) Evolution of cake layer formation on the membrane surface ($J = 20$ L/(m^2 h), c (SiO_2) = 0.4 vol. %, y = 0 cm).

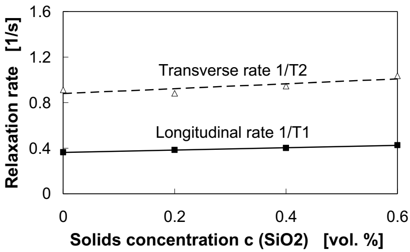

Figure (4.23) Longitudinal and transverse relaxation rates as a function of silica concentration.

The data were further processed using the image processing toolbox in MATLAB®. The routine is based on a conversion of the greyscale images to black-and-white images. Subsequently, the centre of the membrane was identified in each image and the signals from both bulk phase and membrane lumen were masked out. This procedure allows a simple estimation of the number of pixels in the cake layer by calculating the sum of all matrix entries. All white pixels (matrix entry "1") are part of the cake layer, whereas all black pixels (matrix entry "0") are part of the bulk phase, the membrane material or the membrane lumen.

The cross-sectional area of the cake can be calculated as

$$A_{cake}(y) = N_{pix}(y)\, a_{pix}^2 , \tag{4.18}$$

leading to an **average cake layer thickness** at the vertical position y of

$$\delta(y) = \frac{A_{cake}(y)}{d_{o,HF}\ \pi} = \frac{N_{pix}(y)\, a_{pix}^2}{d_{o,HF}\ \pi} , \tag{4.19}$$

with the number of pixels in the cake layer N_{pix}, the pixel size a_{pix} and the outer diameter of the hollow-fibre $d_{o,HF}$. For the derivation of equation (4.19), it was assumed that

$$\delta(y) << d_{o,HF} , \tag{4.20}$$

which is valid for all experimental conditions investigated.

Generally, the second of the three measured slices (i.e. the one in the middle) was chosen for the above data processing. However, it was found that the cake-to-bulk contrast differs significantly among the three slices. Hence, one of the two other slices was chosen in case of a weak image quality in the second slice, leading to positioning inaccuracies of 5 mm. Please refer to Prado [2010] for more details concerning the data processing of cake formation images.

(4.4.2) **Direct observation (DO) of fibre movement**

Wicaksana *et al.* [2006] established a methodology for a direct observation (DO) of bubble-induced fibre movement. They have found that the amplitude and frequency of fibre motion are in good agreement with filtration parameters such as fouling rate dTMP/dt and critical flux J_{crit}, see also section (3.3.2). As a follow-up of these earlier studies, the experimental setup and the test protocols were adapted to fibres fixed at the lower end only. Moreover, the methodology was extended to an observation of fibre motion taking fibre-fibre interactions into account. The internals of the feed tank and the exact position of four different fields of view captured by the video camera are shown in **Figure (4.24)**. A slightly modified design of the fibre support frame was used for membranes of 0.75 instead of 0.9 m in length and is presented on the right-hand side of **Figure (4.24)**. More details concerning the entire test rig can be found in section (4.3.4).

A porous aeration device is located underneath the fibre potting. All fibres of the bundle are filtrating during the observation of fibre motion, so that both lumen and pore structure are filled with water. Since the model suspension containing silica has a milky appearance, pure water without silica particles was filtrated to improve the image contrast. Thereby, the shear thinning characteristics of the suspension are not taken into account for the DO studies. The support frame holds the fibres loosely in position and subdivides the membrane into four parts, see centre of **Figure (4.24)**. The centre line of the first part is located at $y_1 = 0.12$ m, of the second part at $y_2 = 0.4$ m, of the third part at $y_3 = 0.68$ m and of the fourth part at $y_4 = 0.87$ m. These y-coordinates correspond to the centre lines of the fields of view (FOV) captured by the direct observation technique in different vertical positions. A background grid with a mesh size of 1 cm x 1 cm was attached to the outer wall of the tank for a calibration of spatial resolution. In case of bundles with more than one fibre, all but one fibre were marked with waterproof black ink to distinguish the fibre of interest from the others. A conventional video camera (SONY, DCR-TRV50E) with a time resolution of 25 frames/s and an image matrix of 320 x 240 or 720 x 576 pixels was used to record fibre motion under intensive light exposure.

The subsequent analysis was based on a digital frame-by-frame image processing. The images recorded by the camera were extracted from the film sequence using the software DVDVideoSoft® and imported into MATLAB®. All images were converted to black-and-white format to allow for a proper image contrast. The first step of the routine calibrates the spatial resolution based on the background grid of defined mesh size. The second step determines the fibre position in the horizontal centre line of every single image. A comprehensive sensitivity analysis was performed on the modified setup shown on the right-hand side of **Figure (4.24)** (fibre length = 0.75 m), whereof the results can be found elsewhere [Winterscheid, 2009; Wang, 2010].

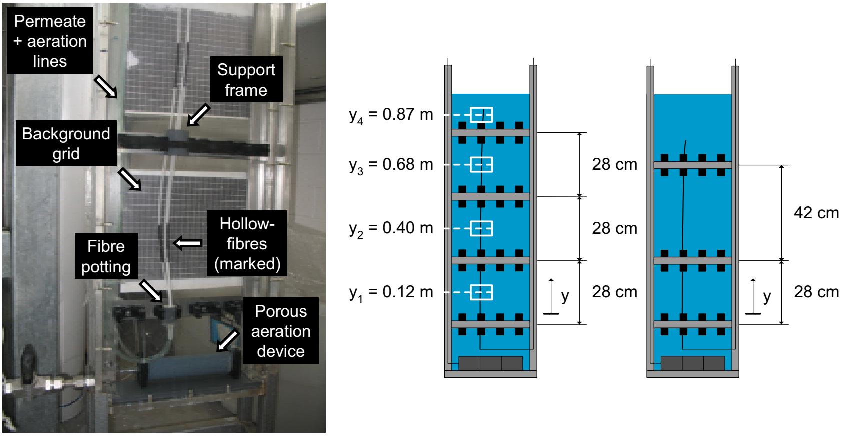

Figure (4.24) Fibre movement test rig: Internals in the feed tank (left), positioning of the field of view (centre) and modified design of the support frame (right) for the direct observation of fibre movement.

This analysis has shown that the velocity of fibre movement is insensitive to the duration of the video sequence as shown in **Figure (4.25)**, but increases as the number of images extracted per unit time increases. The latter trend is due to the fact that also rapid fibre displacements are taken into account at higher frame frequencies. The results are indicating that the increase in fibre velocity levels off in the range of higher time resolutions. Therefore, the highest frame frequency possible and a sequence duration of 5 min were chosen for all fibre motion studies presented below. All upcoming fibre movement results are based on membranes of 0.9 m in length and the standard fibre support frame shown in the centre of **Figure (4.24)**.

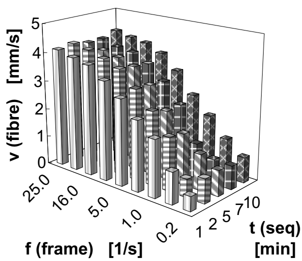

Figure (4.25) Sensitivity analysis for tracking fibre movement: Average fibre velocity as a function of frame frequency and sequence duration (y = 0.47 cm).

The most important outcome of the image processing routine is the evolution of fibre position shown at the top-left of **Figure (4.26)**. It was found that the main fibre movement pattern is sinusoidal, which is superposed by statistic fluctuations of smaller amplitude and frequency. For the first position next to the fibre potting, the overall intensity of fibre motion is relatively low compared to all others. The fibre movement at positions 2 and 3 is much more intensive, expressed by larger amplitudes, higher frequencies and more significant statistic fluctuations compared to the first position. Fibre motion at the uppermost position appears to be less regular, with large variations in amplitude and peaks occurring in a statistic manner. For a further quantification of results, this rather complex evolution of fibre position was subdivided into a number of fibre movement periods. Each period is characterised by three direction changes, i.e. one at the beginning, one at the end and a third one in-between as known from cosine functions. For each period, an average fibre amplitude

$$\mathrm{FA} = \frac{1}{2}\left(\mathrm{FA}_1 + \mathrm{FA}_2\right), \tag{4.21}$$

an average fibre frequency

$$f_{\mathrm{fibre}} = \frac{1}{T_{\mathrm{fibre}}} \tag{4.22}$$

and an **average fibre velocity**

$$v_{\mathrm{fibre}} = 2\,\mathrm{FA}\,f_{\mathrm{fibre}} \tag{4.23}$$

were estimated, see bottom of **Figure (4.26)**. In equations (4.21) to (4.23), FA_1 and FA_2 correspond to the amplitudes and T_{fibre} to the periodic time of fibre motion. This procedure leads to probability density functions (PDFs) like the one of average fibre velocity shown at the top-right of **Figure (4.26)**. The PDFs are relatively wide and consist of several peaks. Nevertheless, the curves are shifted to smaller or larger fibre velocities depending on the vertical position as mentioned above. In order to gain quantitative measures of fibre motion, the values of fibre amplitude, frequency and velocity were averaged over all periods of the corresponding film sequence.

The standard deviations for the determination of amplitude, frequency and velocity of fibre motion are presented in **Figure (4.27)** by error bars. Large deviations relative to the average values occurred for both fibre amplitude and frequency, whereas less fluctuations were observed for the estimation of average fibre velocity. Moreover, the postulation of a more intensive fibre movement in the upper part is represented best by the velocity estimation, with only one exception at the highest position investigated. Therefore, all following studies focussing on the impact of aeration rate and packing density on the intensity of fibre movement will be discussed based on the average fibre velocity.

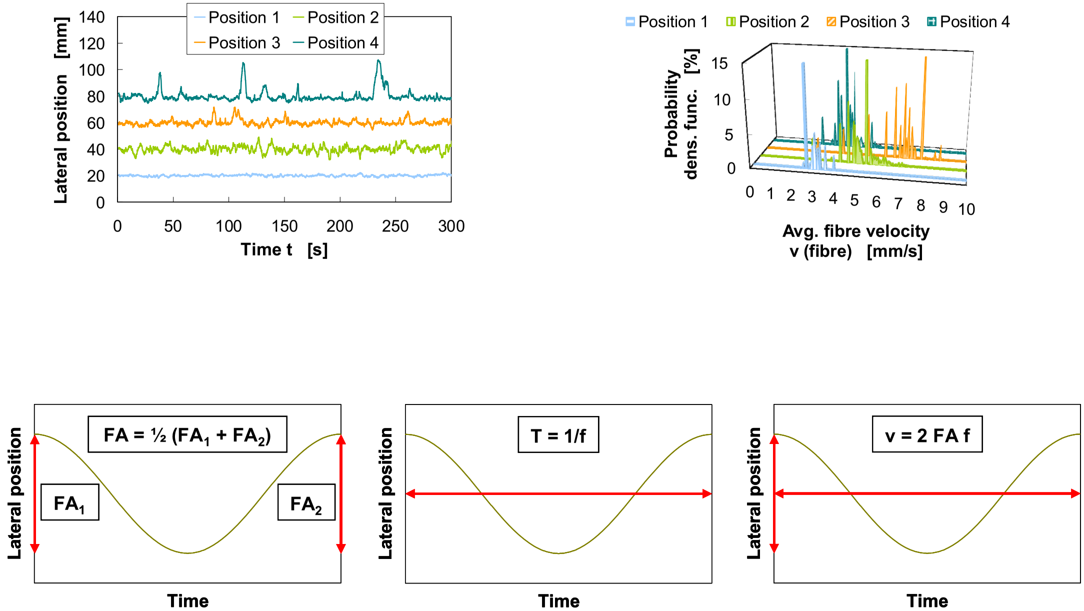

Figure (4.26) Fibre movement observation: Evolution of fibre position (top-left), probability density function of average fibre velocity (top-right) and methodology for determining the amplitude, frequency and velocity of fibre motion (bottom) ($dV_{air}/dt = 6$ L/min, $N_{HF} = 1$).

In addition, the average fibre motion parameters were standardised with the corresponding distance of the centre line of the field of view from the fibre potting, see right-hand side of **Figure (4.27)**. This simple standardisation has no benefit concerning fluctuations in fibre movement intensity. However, these standardised parameters consistently suggest a decrease in fibre movement intensity per unit length as the distance from the fibre potting increases. In other words, the intensity of fibre motion relative to the corresponding fibre length is highest in the lower part of the membrane. The ratio of average fibre velocity $v_{fibre,i}$ and vertical position along the membrane y_i can be interpreted as the average **angular fibre velocity**

$$\omega_{fibre,i} = \frac{v_{fibre,i}}{y_i} . \qquad (4.24)$$

For this reason, deviations in angular fibre velocity indicate the non-uniform character of fibre displacement with $\omega_{fibre,i} \neq \text{const}$ for $i = 1, 2, 3, 4$.

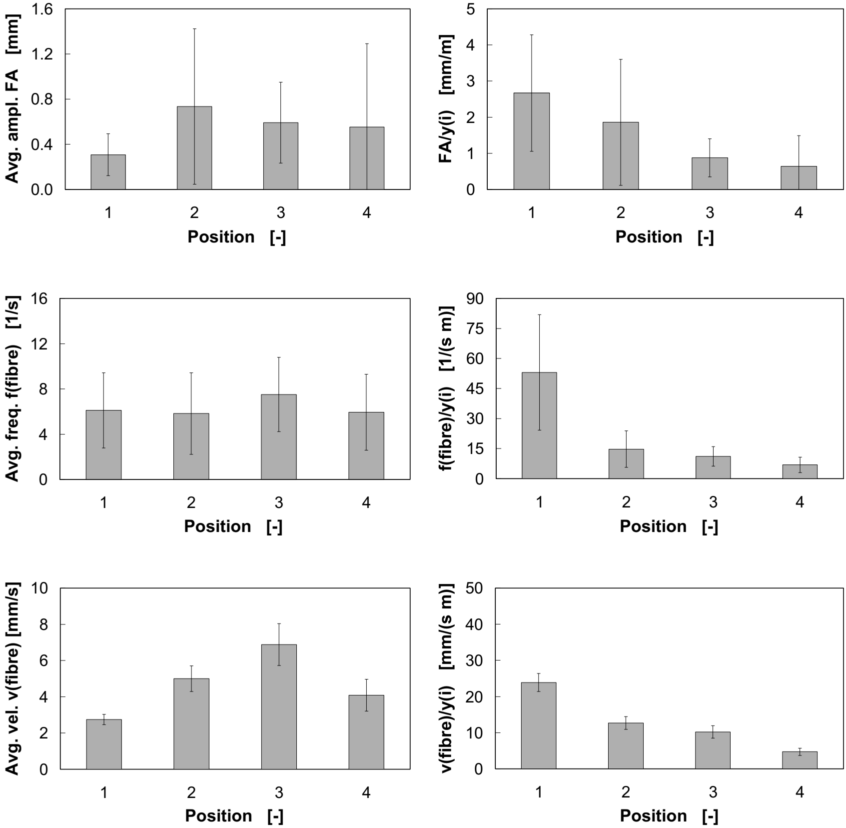

Figure (4.27) Fibre movement observation: Fibre amplitude (top), fibre frequency (centre) and fibre velocity (bottom) for different vertical positions – average value (left) and average value divided by the distance from the fibre potting (right) (dV_{air}/dt = 6 L/min, N_{HF} = 1).

(4.5) CFD modelling approach

Two different computational fluid dynamics (CFD) models were established to evaluate the impact of module design features and operating parameters on hydrodynamic conditions in PURON® hollow-fibre bundles. It is known that these hydraulics are significantly affecting the overall filtration performance [Cui *et al.*, 2003]. Therefore, the CFD outcomes are expected to be helpful to reduce aeration requirements and operational expenses for the coarse bubble aeration of the membrane unit.

(4.5.1) **CFD modelling of turbulent multi-phase flows**

Phenomena such as mass, momentum and energy transport are accurately described by a set of coupled partial differential equations. An analytical solution of these equations provides detailed insights into the spatial and time distribution of parameters like pressure, velocity, turbulence, wall shear and phase distribution. However, flow patterns relevant in chemical engineering are too complex for solving the governing equations analytically in almost all cases. Therefore, the differential equations are approximated by algebraic equations which are solved numerically. For this purpose, a computational grid is created, which serves as a spatial discretisation of the computational domain. A time discretisation is defined by the definition of an appropriate time step for the transient simulation. A variation of process parameters can be implemented by adjusting boundary conditions or fluid properties. Moreover, a suitable definition of available or user-defined models is essential to reduce the unavoidable numerical error as far as possible. In addition to accuracy demands of the desired outcomes, constraints concerning the available computer capacity and the affordable simulation time are limiting criteria. Grid refinement studies and a comparison to reliable experimental investigations are commonly used for model calibration or validation. Please refer to Ferziger and Perić [2002] for more details on computational methods for fluid dynamics.

A proper choice of **multi-phase models** in commercial CFD software packages such as FLUENT® is important. Two different groups of models were established, (i) the Euler-Lagrange approach and (ii) the Euler-Euler approach. Euler-Lagrange multi-phase models treat the fluid phase as a continuum while tracking every single particle, drop or bubble and are applicable to low volume fractions of the dispersed phase only. Euler-Euler multi-phase models treat all phases as interpenetrating continua, with volume fractions which sum to 1 in each cell. The latter group of models is further subdivided as follows [ANSYS, 2009].

- The most complex Euler-Euler multi-phase model is the so-called Eulerian model. This model solves a set of momentum and continuity equations for each phase, whereas all phases share one common pressure field. Significant limitations of this approach are constraints in computer capacity and lack of convergence for highly complex flow patterns. Nevertheless, the Eulerian model is known as a powerful tool for tracking the dispersed phase [Kang *et al.*, 2008]. The model is applicable to dispersed particles smaller than the grid size by predefining a uniform particle size [Ndinisa *et al.*, 2005+2006].

- The mixture model is based on the solution of a single mixture momentum equation for all phases, which significantly reduces computational efforts compared to the Eulerian model. This approach takes into account slip velocities of the dispersed and the continuous phase relative to the mixture.

- The volume of fluid (VOF) model [Hirt and Nichols, 1981] is a surface tracking technique applied to immiscible fluids with particles larger than the grid size [Ndinisa *et al.*, 2005]. A single set of momentum equations is solved for the continuous phase of a two-phase flow. The corresponding solution for the dispersed phase follows directly from the closure condition of volume fraction for incompressible flows [Ferziger and Perić, 2002]. All variables and properties of the fluid are calculated as cell-averages weighted by the corresponding volume fractions. The interpenetration of phases is restricted to the boundary surface, which is typically 1 or 2 grid elements thick. Slip velocities are not taken into account in the VOF model.

A number of **turbulence models** presented in literature have proven to be sufficient for a wide variety of flow patterns in industrial applications. Nevertheless, a direct simulation of turbulence is deemed to be unattainable for practical engineering purposes. Therefore, turbulence models available in FLUENT® are either based on Reynolds-averaged Navier-Stokes (RANS) equations or are restricted to large eddy simulations (LES). For the LES approach, the Navier-Stokes equations are filtered, thus allowing to compute larger eddies while modelling the smaller ones. RANS turbulence models require additional equations to model the so-called Reynolds stresses. Selected turbulence models based on the RANS equations are introduced below, for which the turbulent viscosity is assumed to be an isotropic scalar [ANSYS, 2009].

- The standard k-ε turbulence model is based on the solution of two additional equations, one for the turbulence kinetic energy k and another for its dissipation rate ε. This semi-empirical model is valid for fully-turbulent flows only.

- The renormalisation group (RNG) k-ε turbulence model [Yakhot and Orszag, 1986] improves the accuracy for rapidly strained and swirling flows and flows with high streamline curvature [Lei *et al.*, 2008]. Moreover, the model accounts for effects occurring at low Re numbers. Hence, the RNG k-ε model can be applied over a wider range of operating parameters compared to the standard k-ε model.

- The standard k-ω turbulence model is an empirical model with additional equations for k and its specific dissipation rate ω, which can be interpreted as the ratio of ε and k. Similar to the RNG k-ε model, the k-ω model accounts for low-Re effects.

- The shear-stress transport (SST) k-ω model [Menter, 1994] is a combination of the standard k-ω model in the boundary layer and the standard k-ε model in the bulk flow by incorporating the transport of turbulent shear stress. The SST k-ω model can be applied over a wider range of operating parameters compared to the standard k-ω model, including the flow around curved bodies and flows with separating boundary layers [Dasilva *et al.*, 2004].

An overview of CFD models used in previous numerical studies in MBR research is presented in **Table (3.2)** in section (3.4). Own numerical simulations were conducted using the VOF multi-phase model and the RNG k-ε or SST k-ω turbulence models. The RNG k-ε model was applied for all 3D simulations of both single- and multi-phase flows parallel to the fibres. The SST k-ω turbulence model was deemed to be more appropriate for a 2D simulation of a single-phase flow perpendicular to the hollow-fibres. More details concerning the CFD settings can be found in the sections below, see also [Rahmat, 2009; Breisig, 2010; Tollkötter, 2010].

(4.5.2) X-ray computer tomography (CT) scans

X-ray computer tomography (CT) is a non-invasive measurement technique which requires a distinct difference in electron density between components to be distinguished [Chen *et al.*, 2004a]. CT scanners consist of an X-ray source combined with a detector located at the opposite side of the specimen. Starting from integral values of X-ray attenuation along the path length through the sample from many directions, local values in a measurement plane are mathematically reconstructed. This provides detailed insights into the local composition of the sample. Please refer to Hounsfield [1973] for the fundamentals on CT imaging. A three-dimensional map of the specimen can be created by connecting the 2D cross-sections via image processing. Such kind of 3D model was previously implemented into a CFD simulation to describe the geometry of a structured packing [Buetehorn, 2005; Mahr and Mewes, 2007+2008]. This approach will be adapted to study the single- and multi-phase flow through submerged hollow-fibre bundles as introduced below.

A single hollow-fibre bundle was scanned on-air with an acceleration voltage of 250 kV. Thereby, the effect of buoyancy on the fibre arrangement as occurring in the presence of water or activated sludge is neglected in order to improve the image contrast. A square field of view of 150 mm x 150 mm was reconstructed from an image matrix with 1024 x 1024 pixels using the convolution backprojection method. This corresponds to a spatial resolution of 146.5 µm in radial direction. The distance between two measurement planes was set to 5 mm with a slice thickness of 1 mm. The acquisition time per scan was approximately 30 to 35 s, so that the measurements were restricted to not-moving fibres.

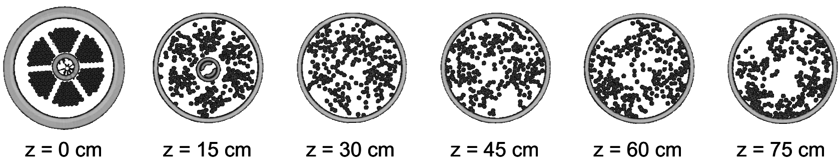

Figure (4.28) CT scans in different vertical positions z: Map of the instantaneous distribution of not-moving fibres in a single hollow-fibre bundle.

With the above-mentioned settings, a virgin PURON® hollow-fibre bundle of 0.85 m in length was scanned to map the instantaneous displacement of not moving fibres. During the measurement, the bundle was hanging upside-down in a tube with an internal diameter of 0.084 m. The loose ends of the fibres were fixed to avoid excessive fibre movement while the sample was rotating during the scan. The CT measurements (Bio-Imaging Research (BIR)) were conducted at the Institute for Multiphase Processes at the Leibniz University of Hannover, Germany, whereof selected results are presented in **Figure (4.28)**.

Each image shows the instantaneous arrangement of not-moving fibres at a certain vertical position z relative to the potting (z = 0 cm). It was observed that the fibres arrange regularly in the lower part of the module, so that segments of high fibre concentration and flow channels without fibres are formed. Moreover, the internal design of the gas sparging device and the housing are represented properly, see also **Figure (4.4)**. It is worth mentioning that the same housing serves as a shell for the single bundle test rig introduced in section (4.3.5). The fibre arrangement becomes less regular as the vertical distance increases due to a weaker impact of fibre potting. The statistic character of fibre arrangement causes the flow field and the gas-liquid phase distribution to be non-uniform. This heterogeneity is intended to be studied using two complementary CFD modelling approaches, which are presented in the sections below.

(4.5.3) Accurate representation of fibres

The first CFD approach aims at representing every single fibre of the bundle accurately, which significantly increases the complexity of the geometry to be implemented. For this purpose, all 150 CT cross-sections were arranged on top of each other and were subsequently connected by using the software VOLUME GRAPHICS STUDIO MAX®. This provides a 3D computer-aided design (CAD) file in stereolithography (STL) format, which is shown as a screenshot in the centre of **Figure (4.29)** (single cross-sections are no longer visible). The STL format approximates the hollow-fibre bundle as triangulated surfaces and leads to non-smooth structures, which affect the generation of a computational mesh significantly. These constraints were met by a number of simplifications as attempts to lower the computational complexity of the simulation, which are summarised below.

- Only the lower 30 cm of the entire 75 cm scan were implemented in order to reduce the size of the computational domain. Furthermore, this simplification restricts the simulation to the part of the bundle where the intensity of fibre motion is assumed to be less pronounced, see left-hand side of **Figure (4.29)**. The latter assumption was qualitatively validated by direct observation of fibre movement in different heights as presented in section (5.2.3).

- Grid refinement by creating prism-type sub-layers where large velocity gradients are expected was unfeasible. Moreover, a simple mesh refinement by decreasing the cell size was limited by the available computer capacity for mesh creation. Initial results of a single-phase simulation are presented on the right-hand side of **Figure (4.29)**, but were found to be mesh-dependent. This makes a further simplification of the entire geometry model necessary.

- The simplified geometry is based on the import of the first CT cross-section only, which is subsequently extruded to a length of 30 cm. All fibres were redrawn with an ideal circular cross-sectional shape and are straight, so that the flow-channels are observable throughout the entire bundle. The length of the gas sparger was restricted to 17.9 cm. The velocity contour shown at the top-right of **Figure (4.30)** suggests that a symmetrical flow field exists. Therefore, only one half of the bundle was implemented into the simulation. In addition to the 3D parallel flow, a 2D simulation of perpendicular flow through the simplified geometry model was established and is presented at the bottom of **Figure (4.30)**. For the parallel flow case, a reduction in the number of tetrahedral elements by 75 % was leading to an increase in total pressure loss of 1.3 %. A reduction in the number of prism elements of 40 % for the perpendicular flow was followed by an increase in total pressure loss of 17 %.

The CFD results using the simplified approach were sufficiently independent of the computational grid for a qualitative comparison of results, whereas the wall shear stress cannot be predicted with this mesh. Therefore, all following investigations based on the accurate representation of fibres are restricted to an estimation of overall single-phase pressure loss correlations as a calibration for the second CFD model. The inlet velocity of water was set in the range of typical liquid velocities in submerged MBRs. Please refer to **Table (4.2)** for the most relevant settings of both parallel and perpendicular flow simulations or to Rahmat [2009] for more details on the first geometry modelling approach.

CFD MODEL 1	Parallel flow	Perpendicular flow
Software	ANSYS CFX 11.0	ANSYS CFX 11.0
Domain	3D, axis-symmetric, H = 30 cm + 5 cm inlet channel	2D, axis-symmetric
Mesh	Tetrahedral (1,607,580 cells)	Prism (36,512 cells)
Inlet	Parabolic velocity profile	Inlet velocity
Outlet	Opening, atmospheric pressure	Opening, atmospheric pressure
Inlet channel wall	Slip wall, smooth	---
Wall	No slip, smooth wall	Free slip
Multi-phase model	None, single-phase flow of water	None, single-phase flow of water
Turbulence model	RNG k-ε model	SST k-ω model
Solver	Step 1: Transient (First order backward Euler) + Upwind	Step 1: Steady-state + Upwind
	Step 2: Steady-state + High resolution	Step 2: Steady-state + High resolution

Table (4.2) Accurate fibre representation: CFD parameters for parallel and perpendicular flow conditions.

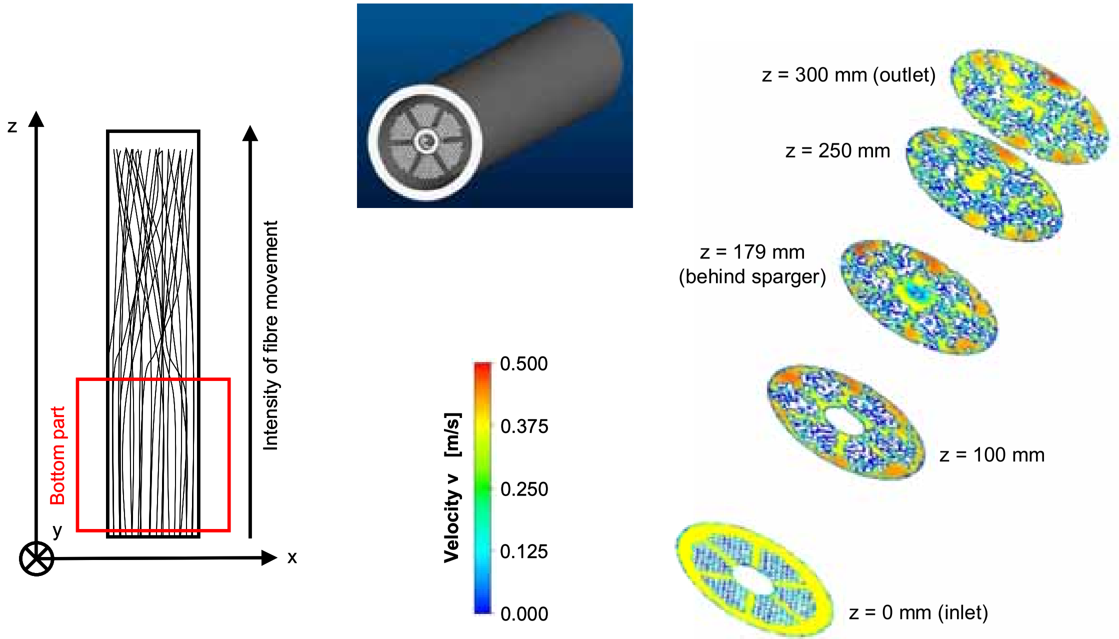

Figure (4.29) Accurate fibre representation: Schematic of the hollow-fibre bundle (left), 3D representation of the bundle in STL format (centre) and single-phase velocity contours in different heights (right) (L = 300 mm, $v_{avg, inlet}$ = 0.3 m/s).

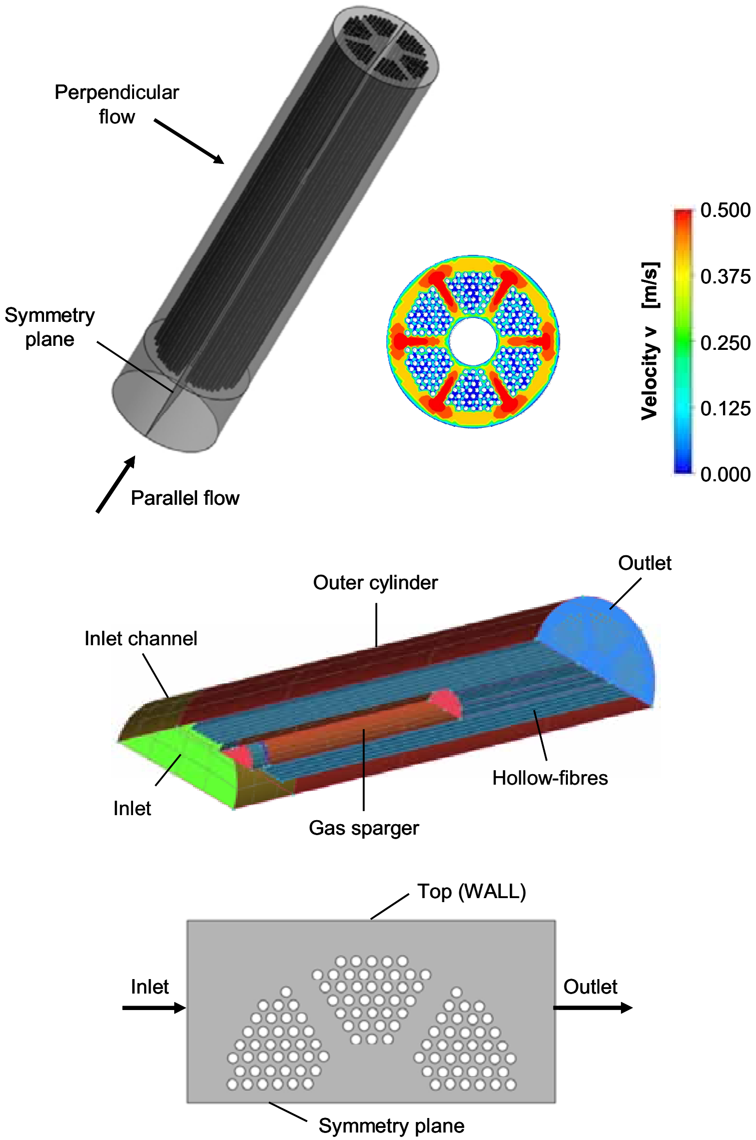

Figure (4.30) Accurate fibre representation: Simplified geometry model and single-phase velocity contour (top) as well as schematics of the computational domain for parallel (centre) and perpendicular flow conditions (bottom) ($z = 150$ mm, $L = 300$ mm, $v_{avg,\ inlet} = 0.3$ m/s).

(4.5.4) Porous medium approach

Mesh-independent results were found to be difficult to achieve for an accurate representation of fibres as discussed in the previous section. Therefore, the second CFD approach is based on defining a heterogeneous porous medium. This porous medium mirrors the impact of fibre arrangement in an abstract manner as schematically shown in **Figure (4.31)**, making mesh creation and refinement easier. More precisely, this approach is based on calculating a set of matrices describing the flow resistance exposed to the bubble-entrained upward and radial flow. The **porosity matrix** $\varphi = f(x, y, z)$ is a function of all three spatial coordinates. In addition, **friction factor matrices** $\xi = (\xi_x, \xi_y, \xi_z) = f(\varphi, Re)$ as a function of porosity and Re number are to be implemented to calibrate the heterogeneous porous medium. Similar to the first modelling approach, the CT scans in different vertical positions z are used. However, instead of directly connecting the CT scans, a further image processing in MATLAB® was performed to determine the distribution of local porosity.

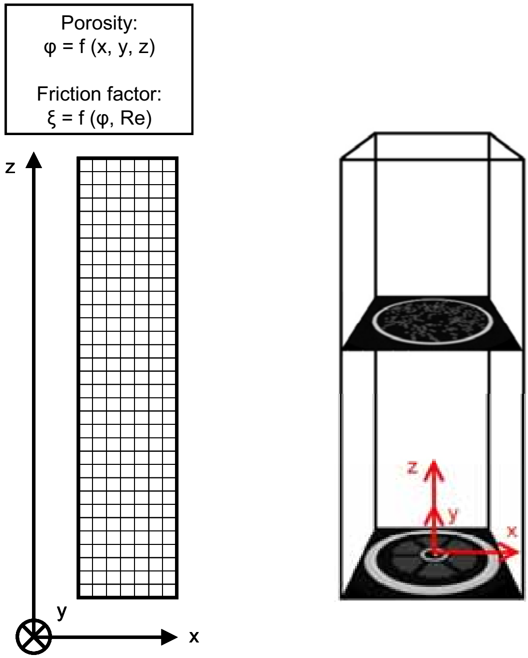

Figure (4.31) Porous medium approach: Schematic of the hollow-fibre bundle (left) and the arrangement of CT images for defining porosity and friction factor values (right).

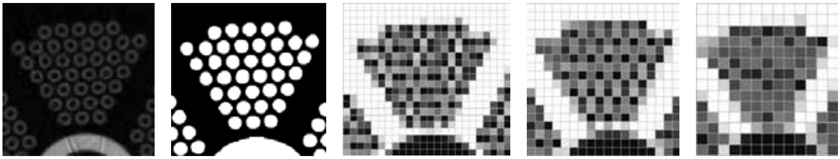

Figure (4.32) Porous medium approach: Detail of a CT scan showing a single hollow-fibre segment (1), segment after image processing (2) and segment after compression of porosity data for three different grid sizes, (3) to (5).

In **Figure (4.32)**, one fibre segment of the first CT cross-section at z = 0 cm is highlighted, which is separated by flow channels on all sides. These grey-scale images (1) were converted to black-and-white images (2). A matrix entry of "1" (white) corresponds to solid material and an entry of "0" (black) to an empty volume element. In a number of image processing steps [Gerhards, 2010], the CT cross-sections were cut and centred and the gas sparger as well as the membrane lumens were represented as no-flow regions. Subsequently, a rectangular grid was applied to calculate local porosity values averaged over one grid element. This leads to a reduction of matrix entries to be imported into the simulation. White-coloured pixels correspond to an empty volume element (porosity = 1) and black-coloured pixels to no-flow areas (porosity = 0) in the final porosity images. All grey pixels with porosity values between 0 and 1 are only partly occupied by the bundle, so that fluid flow is allowed to a certain extend.

Results of data compression for a grid size of 1.3, 1.6 and 2.2 mm/pixel are shown in **Figure (4.32)**, (3) to (5). When comparing the three different spatial resolutions, it is obvious that averaging over less matrix entries preserves more details of the original scan. A compression with lower spatial resolution suffers from a significant loss of information such as the presence of flow channels. Nevertheless, data compression is essential to reduce the complexity of the simulation and ensures a proper convergence. Therefore, a spatial resolution of 1.6 mm/pixel (4) was chosen as a trade-off between a detailed and an easy-to-compute CFD model. This resolution allows representing the flow channels in-between two fibre segments with 3 to 4 adjacent pixels.

As a next step, friction factor correlations need to be defined. These correlations can be derived from CFD simulations with an accurate representation of fibres or from pressure loss measurements. Both strategies are presented in the sections below.

(4.5.5) Pressure loss correlation

Pressure loss correlations are frequently used in plant design and construction for dimensioning purposes or an estimation of energy consumption. In the framework of this study, these correlations are used to calibrate the heterogeneous porous medium approach. This is done by linking the Re number of the bubble-entrained liquid flow through the bundle to the friction factor ξ, which depends on the local porosity φ. Pressure loss correlations of the form $\xi = f(\varphi, Re)$ for both parallel and perpendicular flow conditions were then imported into the CFD code.

A membrane bundle consists of numerous cylindrical tubes (i.e. hollow-fibres) arranged irregularly along the height. Therefore, attempts were made to model the pressure loss by taking into account similarities to parallel or perpendicular external flows through tube banks [VDI, 1997; Wang *et al.*, 2010]. However, tube banks are characterised by an equidistant and regular arrangement of pipes, whereas hollow-fibres arrange randomly and form flow channels. This flow channelling is known from packed beds, for which numerous Ergun-type pressure loss correlations were established. One Ergun-type correlation is the **Forchheimer equation** (adapted from [Dullien, 1979])

$$\xi_{Forch} = \frac{2\, D_{Forch}\, d_{h,bundle}^2\, \varphi_{bundle}}{Re_{bundle}} + C_{Forch}\, d_{h,bundle}\, \varphi_{bundle}^2 = \frac{D_1}{Re_{bundle}} + C_2\,. \tag{4.25}$$

The Forchheimer equation is the standard pressure loss correlation in the CFD software FLUENT® and was thus favoured over tube bank correlations [Rahmat, 2009].

The hydraulic diameter of the bundle is defined as

$$d_{h,bundle} = \frac{\left(d_{i,tube}^2 - N_{HF}\, d_{o,HF}^2\right)}{d_{i,tube} + N_{HF}\, d_{o,HF}}, \tag{4.26}$$

the porosity of the bundle as

$$\varphi_{bundle} = \frac{\left(d_{i,tube}^2 - N_{HF}\, d_{o,HF}^2\right)}{d_{i,tube}^2}, \tag{4.27}$$

the **Re number** of an external single-phase water flow through the bundle as

$$Re_{bundle} = \frac{\left(\frac{\bar{v}_{inlet}}{\varphi_{bundle}}\right) d_{h,bundle}\, \rho_{H_2O}}{\eta_{H_2O}}, \tag{4.28}$$

the **friction factor** as

$$\xi_{Forch} = \frac{\Delta p_{tot}}{\frac{1}{2}\rho_{H_2O}\left(\frac{\bar{v}_{inlet}}{\varphi_{bundle}}\right)^2} \frac{d_{h,bundle}}{L} \tag{4.29}$$

and the length-specific pressure loss as (adapted from [Dullien, 1979])

$$\frac{\Delta p_{tot}}{L} = D_{Forch}\, \eta_{H_2O}\, \bar{v}_{inlet} + C_{Forch}\, \frac{1}{2}\rho_{H_2O}\, \bar{v}_{inlet}^2 \,. \tag{4.30}$$

In equations (4.25) to (4.30), D_{Forch} and C_{Forch} correspond to the Forchheimer pressure loss coefficients,

$$D_1 = 2\, D_{Forch}\, d_{h,bundle}^2\, \varphi_{bundle} \tag{4.31}$$

and

$$C_2 = C_{Forch}\, d_{h,bundle}\, \varphi_{bundle}^2 \tag{4.32}$$

to dimensionless constants, $d_{i,tube}$ to the internal diameter of the housing, N_{HF} to the number of fibres per bundle, $d_{o,HF}$ to the outer diameter of the fibre, $\bar{v}_{inlet}$ to the superficial inlet velocity as well as ρ_{H2O} and η_{H2O} to the density and dynamic viscosity of water. It is worth mentioning that all definitions and characteristic dimensions were adjusted to a single-phase flow of pure water through a PURON® hollow-fibre bundle as a case study. In the following sections, a parameter fitting of the Forchheimer coefficients is presented based on CFD simulations and corresponding validation experiments.

Numerical estimation of pressure loss

The simplified CFD model with an accurate representation of fibres (see section (4.5.3)) was applied to a single-phase flow of pure water with different setpoint inlet velocities. A parabolic velocity profile and a superficial inlet velocity between 0.01 and 1 m/s were defined for the parallel flow case. These are typical values of liquid velocity in submerged MBRs. For the perpendicular flow, a superficial inlet velocity in the range of 0.01 to 10 m/s was set. The simulated pressure drop values were transferred to friction factors and plotted as a function of Re number as shown in **Figure (4.33)**. The least square method was applied to fit the data points by adapting the parameters D_1 and C_2 of the Forchheimer equation.

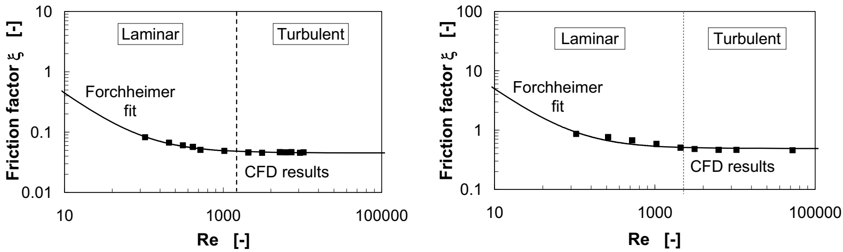

Figure (4.33) CFD model calibration: Numerical estimation of the friction factor as a function of Re number for a single-phase parallel (left) or perpendicular flow (right).

For both parallel and perpendicular flow patterns, a laminar or transitional region and a turbulent region were observed. The friction factor decreases in the laminar region and is constant in the turbulent region as Re increases. A critical Re number was approximated between 1000 and 2000 for the parallel flow and between 2000 and 3000 for the perpendicular flow. The parameter fitting leads to the pressure loss correlation

$$\xi_{Forch} = \frac{4}{Re_{bundle}} + 0.05 \tag{4.33}$$

for the parallel flow and

$$\xi_{Forch} = \frac{44.87}{Re_{bundle}} + 0.49 \tag{4.34}$$

for the perpendicular flow.

The pressure loss estimated by the CFD simulation is equal to the total pressure loss, which is attributed to both friction in the bundle and friction at the surrounding wall. Since wall friction was not taken into account for the perpendicular flow simulation, the corresponding Forchheimer coefficients

$$D_{Forch} = \frac{D_1}{2\, d^2_{h,bundle}\, \varphi_{bundle}} = \frac{44.87}{2\, d^2_{h,bundle}\, \varphi_{bundle}} \tag{4.35}$$

and

$$C_{Forch} = \frac{C_2}{d_{h,bundle}\, \varphi^2_{bundle}} = \frac{0.49}{d_{h,bundle}\, \varphi^2_{bundle}} \tag{4.36}$$

can be directly calculated. For the parallel flow simulation, wall friction was taken into account to allow for a better comparability to pressure loss measurements conducted for model validation. For this reason, the pressure loss caused by friction at the surrounding walls of the computational domain

$$\frac{\Delta p_{wall}}{L} = \frac{\Delta p_{tot}\left(\varphi_{bundle} = 1, d_{h,bundle} = d_{i,tube}\right)}{L} = \frac{D_1\, \bar{v}_{inlet}\, \eta_{H_2O}}{2\, d_{i,tube}^2} + \frac{C_2\, \bar{v}_{inlet}^2\, \rho_{H_2O}}{2\, d_{i,tube}} \tag{4.37}$$

is subtracted from the total pressure loss

$$\frac{\Delta p_{tot}}{L} = \frac{\Delta p_{wall}}{L} + \frac{\Delta p_{bundle}}{L} \tag{4.38}$$

as the direct CFD outcome. This leads to the contribution of the hollow-fibre bundle to the total pressure loss

$$\frac{\Delta p_{bundle}}{L} = \frac{D_1\left(1 - \frac{d_{h,bundle}^2\, \varphi_{bundle}}{d_{i,tube}^2}\right)}{2\, d_{h,bundle}^2\, \varphi_{bundle}}\, \bar{v}_{inlet}\, \eta_{H_2O} + \frac{C_2\left(1 - \frac{d_{h,bundle}\, \varphi_{bundle}^2}{d_{i,tube}}\right)}{d_{h,bundle}\, \varphi_{bundle}^2}\, \frac{1}{2}\, \bar{v}_{inlet}^2\, \rho_{H_2O}, \tag{4.39}$$

with

$$D_{Forch} = \frac{D_1\left(1 - \frac{d_{h,bundle}^2\, \varphi_{bundle}}{d_{i,tube}^2}\right)}{2\, d_{h,bundle}^2\, \varphi_{bundle}} = \frac{4\left(1 - \frac{d_{h,bundle}^2\, \varphi_{bundle}}{d_{i,tube}^2}\right)}{2\, d_{h,bundle}^2\, \varphi_{bundle}} \tag{4.40}$$

and

$$C_{Forch} = \frac{C_2\left(1 - \frac{d_{h,bundle}\, \varphi_{bundle}^2}{d_{i,tube}}\right)}{d_{h,bundle}\, \varphi_{bundle}^2} = \frac{0.05\left(1 - \frac{d_{h,bundle}\, \varphi_{bundle}^2}{d_{i,tube}}\right)}{d_{h,bundle}\, \varphi_{bundle}^2} \tag{4.41}$$

as the Forchheimer coefficients for the parallel flow case. The fitted parameters of the Forchheimer model for parallel and perpendicular flow conditions are summarised in equations (4.35) and (4.36) as well as (4.40) and (4.41). These parameters are representing both laminar and turbulent flow regimes. While the viscous term containing D_{Forch} is dominating in the laminar region, it approaches zero for higher Re numbers. Therefore, the friction factor is insensitive to Re variations in the turbulent region [VDI, 1997]. The numerically derived pressure loss correlation for the parallel flow was validated experimentally. A validation of the numerical pressure loss correlation for perpendicular flow conditions is still to be done.

Experimental validation and implementation of pressure loss correlations

The pressure loss in a hollow-fibre bundle was measured for different parallel feed flow conditions using a simple U-tube manometer (REISS D116/8). For this purpose, the single bundle test rig introduced in section (4.3.5) was equipped with the pressure loss test cell shown in **Figure (4.34)**.

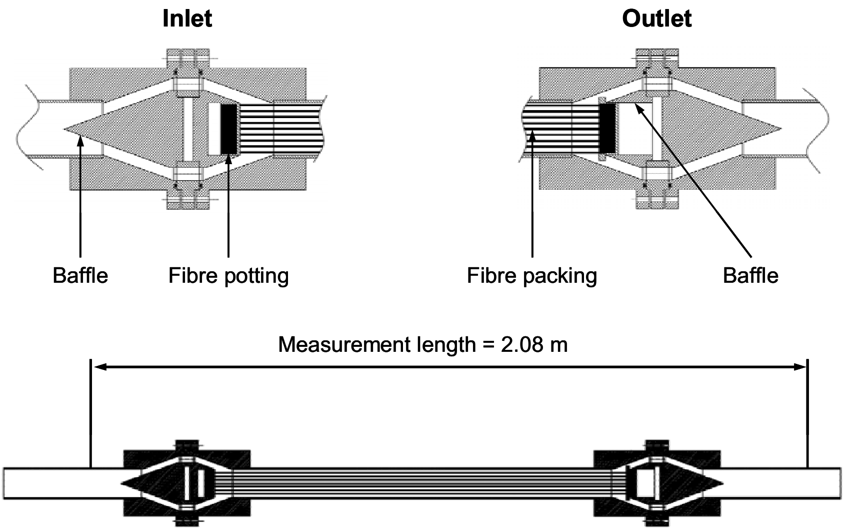

Figure (4.34) Technical drawings of the pressure loss test cell: Detailed view of the inlet (top-left) and outlet design (top-right) and overview of the entire test cell (bottom).

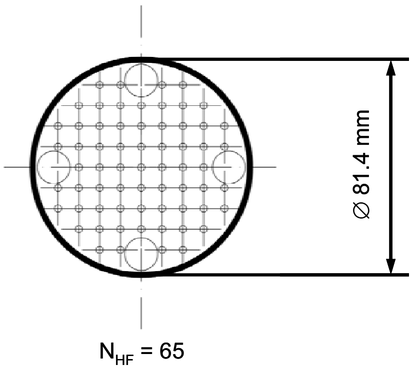

Figure (4.35) Pressure loss test cell: Technical drawing of a fibre plate for a packing containing 65 not-moving hollow-fibres.

The construction of the test cell allows measuring the pressure difference between the inlet and the outlet over a flow path length of 2.08 m with an accuracy of ± 0.1 mbar. During the experiment, pure water is pumped through the cell with the desired feed flow rate in the range of 940 up to 4880 L/h (GEORG FISCHER SK20). These flow rates correspond to superficial inlet velocities ranging from 0.05 to 0.24 m/s. The test cell was operated in horizontal position and was equipped with a packing of 65 not-moving hollow-fibres as illustrated in **Figure (4.35)**.

The device shown above allows a defined positioning of 65 hollow-fibres fixed at both ends. The fibres were evenly distributed over the cross-section. Intensive fibre motion was inhibited by slightly stretching the fibres. Efforts to account for shear thinning characteristics of the model fluid by adding xathan gum were of little benefit. This is presumably due to the fact that the estimation of the apparent viscosity is rather arbitrary for non-Newtonian fluids and may cause misleading conclusions. The impact of permeate extraction on the shell-side flow field is assumed to be negligible as previously stated by Wang *et al.* [1994] and Ndinisa *et al.* [2005]. Please refer to Lattermann [2009] and Stodollick [2010] for more details concerning the experimental procedure.

In **Figure (4.36)**, the measured specific pressure loss and the corresponding friction factor are plotted as a function of superficial inlet velocity or Re number. Each experiment was temperature-corrected according to equations (3.5) and (3.6) and repeated several times. The pressure loss without fibres was measured for all setpoint feed flow rates as a reference and was subtracted from the pressure loss in the bundle. This procedure allows estimating the pressure loss due to friction in the bundle only, whereas friction at the tube wall is not taken into account. In addition to the experimental data points, also the Forchheimer least square fit based on the CFD results is shown on the right-hand side of **Figure (4.36)**.

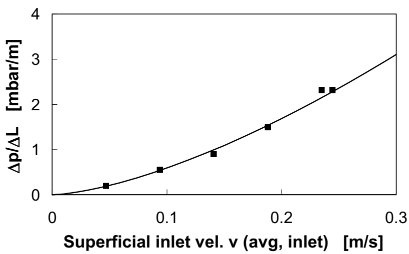

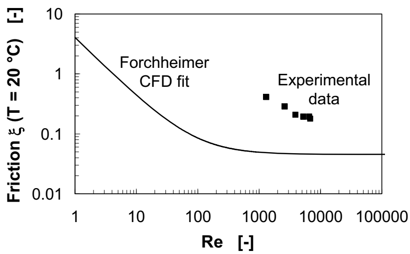

Figure (4.36) Experimental calibration of the CFD model: Length-specific pressure loss as a function of superficial inlet velocity (left) and friction factor as a function of Re number in comparison to the Forchheimer correlation (right).

The potential trend line shown on the left-hand side of **Figure (4.36)** indicates that the length-specific pressure loss in the bundle is a function of the superficial inlet velocity to the power of 1.5. A laminar flow is characterised by the domination of the viscous term with a velocity exponent of 1 according to equation (4.30). The inertia term with an exponent of 2 dominates for turbulent flows [VDI, 1997]. Therefore, the flow through the hollow-fibre bundle is in transition from laminar to turbulent conditions. It is expected that the packing density significantly affects the overall pressure drop. However, the manufacturing of bundles of higher packing density was found to be non-straightforward and is intended to be further optimised for future studies.

Plotting the friction factor as a function of Re number for the experimental results shows that all measured data points are above $Re_{crit,CFD} = 1000$. However, the experimental results suggest a transition from laminar to turbulent conditions for $Re > Re_{crit,exp} = 4000$. The Forchheimer equation based on the CFD results underestimates the measured pressure losses by up to one order of magnitude. The computational grid used for the parallel flow CFD studies is of a simple tetrahedral type. As previously mentioned in section (4.5.3), efforts to create hybrid meshes with prism-type sub-layers in close proximity to the membranes were not successful. Therefore, the above discrepancies may be attributable to a non-realistic representation of velocity gradients in boundary layers. The resulting underestimation of pressure loss and friction factor leads to an underestimation of flow channelling by the CFD model. For this reason, the formation of bypass jets is expected to be even more pronounced under real conditions.

No experimental validation of pressure loss correlations for the perpendicular flow case is available at this stage of investigations. Therefore, the numerically derived pressure loss correlations were implemented as a calibration for the heterogeneous porous medium approach. This was deemed to be sufficient for a qualitative comparison of single- and multi-phase flow patterns, whereas a comprehensive quantification is inappropriate due to large deviations compared to validation experiments.

The Forchheimer coefficients given in equations (4.35) and (4.36) respectively (4.40) and (4.41) were imported into the CFD code FLUENT®. It was found that user-defined profiles are advantageous compared to user-defined functions (UDFs) in this case [Breisig, 2010]. For this purpose, six matrices were created, i.e. one matrix for the viscous and another for the inertia term for each spatial direction x, y and z. The coordinates x and y correspond to the perpendicular flow, whereas the z direction describes the parallel flow (see coordinate system in **Figure (4.31)**). Since pressure loss correlations for the air flow are not available at this stage, the gas friction factors were assumed to be equal to the water friction factors multiplied by the ratio of gas to liquid viscosity. With this approach, the compressibility of the gas phase and additional friction terms originating from two-phase interactions [Cui *et al.*, 2003] were neglected. The porosity matrix as an outcome of the CT image processing in MATLAB®

forms the last of altogether seven matrices to be implemented with 633,750 entries each. Please refer to Breisig [2010] for more details.

(4.5.6) CFD parameters for the heterogeneous porous medium approach

Initial CFD simulations based on the heterogeneous porous medium approach were conducted following the methodology presented in the previous sections. The computational domain consists of the porous medium of 75 cm, an inlet channel of 5 cm (single-phase flow) or 60 cm (two-phase flow) and an outlet channel of 5 cm in length. During the first step of the multi-phase simulation, a Taylor bubble with an initial length of 14 cm rises along the inlet channel to allow for a proper adjustment of bubble shape. It is worth mentioning that friction at the inner wall of the tubular housing was not taken into account, since such kind of housing does not exist in real submerged membrane modules. However, it is known that external slug flow conditions are occurring in relatively confined submerged membrane units as well [Cui *et al.*, 2003]. Therefore, a defined slug flow prior to penetrating into the porous medium was favoured over a computationally demanding simulation of air injection.

The two-phase simulation was initialised with the results of a converged single-phase simulation of pure water flowing through the same geometry. The two-phase flow was assumed to be incompressible and was described by the VOF multi-phase and the RNG k-ε turbulence model. A background water flow in the range of typical circulation velocities in full-scale MBR units was taken into account [Drews *et al.*, 2008; Prieske *et al.*, 2008]. The setpoint outlet pressure corresponds to a submergence depth of 45 cm (single-phase flow) or 40 cm (multi-phase flow). The liquid was assumed to be Newtonian, with a shear-independent dynamic viscosity as a function of MLSS concentration according to [Busch *et al.*, 2007]

$$\eta = 1.05\,\eta_{H_2O}\,\exp(0.08\,\mathrm{MLSS}) \tag{4.42}$$

for MLSS < 9.122 g/L and to

$$\eta = \eta_{H_2O}\,\left(0.0254\,\mathrm{MLSS}^2 - 0.1674\,\mathrm{MLSS} + 1.5918\right) \tag{4.43}$$

for MLSS > 9.122 g/L. The computational grid consists of 1,506,200 (single-phase flow) or 2,480,800 (two-phase flow) unstructured quadrangular volume elements with a common cell height of 1 mm. A preliminary mesh independence study for a single-phase flow indicated a proper spatial discretisation [Breisig, 2010], although a more comprehensive study under multi-phase flow conditions is still to be done. However, the grid was deemed to be sufficient for a semi-quantitative comparison of single- and multi-phase flow patterns as presented in section (5.4). The time discretisation was defined by a time step of 0.1 ms for the transient two-phase simulation. This corresponds to a Courant number at the inlet of [Ferziger and Perić, 2002]

$$Co = \frac{\overline{v}_{inlet}\,\Delta t}{\Delta z} = 0.01 \ldots 0.05\,, \tag{4.44}$$

with the superficial inlet velocity $\overline{v}_{inlet}$, the time step Δt and the spatial dicretisation in the main flow direction Δz. However, Co changes significantly throughout the domain depending on the local flow velocity, with values around $Co = 40$ for a multi-phase flow through the porous medium. Please refer to **Table (4.3)** or to Tollkötter [2010] for more details concerning the CFD settings of the heterogeneous porous medium approach.

(4.5.7) Concluding remarks on the CFD methodology

A CFD approach based on CT scans and pressure loss correlations for model calibration was established to investigate the multi-phase flow through submerged hollow-fibre bundles. Similar CFD models published in literature are restricted to a porous medium described by a homogeneous porosity and a single set of friction factors in x, y and z direction [Kang *et al.*, 2008; Saalbach und Hunze, 2008; Brannock *et al.*, 2009+2010a+b]. Thereby, the impact of irregular fibre arrangement, gas spargers and flow channels on the hydrodynamic conditions are not taken into account. These parameters are represented properly by the methodology developed in this study. Therefore, the heterogeneous porous medium approach is superior for module design optimisation purposes compared to other CFD models. Nevertheless, an interaction of fibres with the flow pattern was not yet implemented into the simulation. This interaction is expected to influence the formation and durability of bypass streams in regions of lower fibre concentration.

CFD MODEL 2	Single-phase flow	Multi-phase flow
Software	ANSYS FLUENT 12.0	ANSYS FLUENT 12.0
Domain	3D, asymmetric, H = 75 cm + 5 cm inlet + 5 cm outlet	3D, asymmetric, H = 75 cm + 60 cm inlet + 5 cm outlet
Mesh	Unstructured quadrangular, quad pave, 1,506,200 cells (height = 1 mm)	Unstructured quadrangular, quad pave, 2,480,800 cells (height = 1 mm)
Inlet	0.1 to 0.5 m/s superficial liquid velocity (plug flow)	Patched Taylor bubble, 0.1 to 0.5 m/s superficial liquid velocity (plug flow)
Outlet	Opening, pressure head (i.e. submergence depth) of 45 cm	Opening, pressure head (i.e. submergence depth) of 40 cm
Wall	No shear, smooth wall, roughness = 0.0	No shear, smooth wall, roughness = 0.0
Multi-phase model	Single-phase flow of water with raised viscosity	Step 1: Single-phase flow of water with raised viscosity
		Step 2: VOF (water with raised viscosity + air)
Turbulence model	RNG k-ε model	RNG k-ε model
Solver	General: PISO (iterative, segregated), Δt = 0.01 s	General: PISO (iterative, segregated)
	Transient (2nd order Upwind)	Step 1: Transient (1st order Upwind), Δt = 1 ms
		Step 2: Transient (2nd order), geo-reconstruct (interphase calculation), Δt = 0.1 ms

Table (4.3) CFD parameters for the heterogeneous porous medium approach.

(5) Results

This chapter gives an overview of the impact of hydrodynamic conditions on the microfiltration performance on different scales. On a micro-scale, local phenomena such as permeate flow and cake growth were visualised with NMR imaging (section (5.1)). These localised measurements are supplemented with a number of integral measurements of permeability decline while filtrating with a single hollow-fibre (meso-scale, section (5.2)) or a single hollow-fibre bundle (macro-scale, section (5.3)). In addition, a direct observation of fibre movement allowed estimating the intensity of fibre motion and fibre-fibre interactions (meso-scale, section (5.2.3)). Complementary CFD simulations (macro-scale, section (5.4)) were conducted using the same geometry as for the single bundle tests.

(5.1) Micro-scale NMR imaging

The flow velocity in the lumen of a single hollow-fibre and the cake growth on the membrane surface were investigated by NMR imaging. The velocity measurements allow estimating the distribution of local cumulative permeate flux along the fibre. Cake growth and removal were measured for different vertical positions, permeate fluxes, solids concentrations and aeration conditions. Parts of these NMR results were recently published [Buetehorn *et al.*, 2011].

(5.1.1) Determination of permeate flux distribution

NMR velocity imaging was applied to visualise the steady-state permeate flow in the lumen of a single hollow-fibre. For these tests, pure water was filtrated in submerged outside-in mode at constant permeate flux. The average (i.e. setpoint) permeate flux was measured at y = 0 cm. The distribution of local permeate flux along the membrane can be estimated by changing the vertical position of the entire test rig relative to the stationary NMR device. The overall objective of the velocity measurements is to validate this methodology under well-defined conditions. In future studies, the methodology will be extended to highly transient filtration processes. A description of the experimental setup, the test protocol, the NMR settings and the subsequent data processing is given in sections (4.3.1) and (4.4.1).

Velocity profile along the membrane

In **Figure (5.1)**, the measured maximum permeate velocity is plotted as a function of vertical position and average permeate flux for all parameter combinations investigated. It was found that an increase in average permeate flux causes the maximum velocity to increase linearly. An increase in distance from the point of permeate extraction leads to a linear decrease in maximum permeate velocity. The latter trend is caused by an acceleration of lumen-side permeate flow due to an accumulation of permeate collected from the fibre end (y = L) towards to the point of permeate extraction (y = 0 cm).

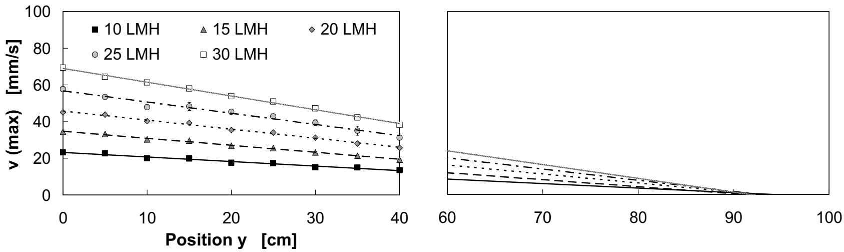

Figure (5.1) Maximum permeate velocity as a function of vertical position and average permeate flux with linear trend lines (c ($CuSO_4$) = 1 g/L).

This observation is in agreement with previous findings reported by Pangrle *et al.* [1992]. Moreover, the linear velocity profile indicates that the lumen-side pressure loss is lower than the pressure loss experienced by the liquid permeating through the pore structure. Each experiment was repeated three times, indicating a measurement error of 1.5 % on average and 7.1 % maximum. It is known that the permeate velocity drops to zero at the very end of the fibre (i.e. at y = L = 1 m). This is predicted by all trend lines shown in **Figure (5.1)** with an average deviation of 7.6 % and a maximum deviation of 9.0 %. These discrepancies are presumably due to slight variations in effective membrane lengths and an insufficient positioning of the experimental setup for measurements at $y \neq 0$ cm.

The directly measured maximum velocities were compared to velocity values averaged over all pixels in the membrane lumen. For this purpose, the pixel with the maximum velocity value in each image was assumed to be located exactly in the centre of an ideal circular lumen with $d_{i,HF}$ = 1.7 mm. The maximum and average velocities for the low-resolution measurements are presented in **Figure (5.2)**.

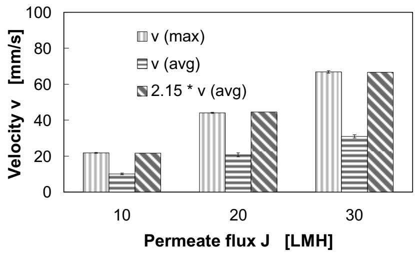

Figure (5.2) Comparison of maximum and average permeate velocities measured with the lower spatial resolution as a function of setpoint permeate flux ($d_{i,HF}$ = 1.7 mm, y = 0 cm, c ($CuSO_4$) = 1 g/L).

It was found that the ratio of maximum velocity v_{max} and average velocity $\overline{v}$ for the low-resolution images,

$$\left.\frac{v_{max}}{\overline{v}}\right|_{low-resolution} = 2.15\,, \tag{5.1}$$

corresponds to a factor of 2.15. A factor of 2 characterises a laminar flow through circular tubes, see equation (4.14). This slight deviation from the parabolic velocity profile is presumably due to a flow channel partially blocked by the porous support tissue. Nevertheless, Re numbers of less than 55 clearly indicate a laminar permeate flow. It is worth mentioning that the ratio according to equation (5.1) equals 2.79 for the high-resolution measurements, which indicates a loss of information when analysing low-resolution instead of high-resolution images.

The predicted maximum velocity profiles along the fibre according to equation (4.13) are compared to the measured maximum velocity data points in **Figure (5.3)**. It was found that the model slightly underestimates the measured velocities. This discrepancy may be due to the fact that the lumen-side pressure loss was neglected for the derivation of the simplified model. This pressure loss leads to a decrease in permeate pressure from the fibre end towards the point of permeate extraction, which causes an increase in local TMP. For this reason, higher driving forces close to the point of permeate extraction are occurring, which are not represented by the simplified model. Nevertheless, relative deviations of 4.4 % on average and a maximum deviation of 9.8 % indicate an acceptable agreement with experimental data. Please note that all following velocity data processing is restricted to the quicker data acquisition at lower spatial resolution in combination with equation (5.1).

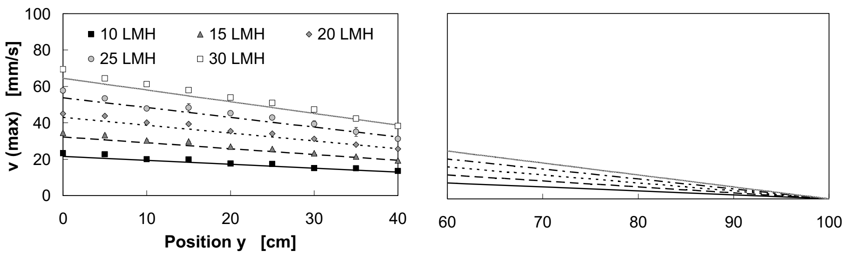

Figure (5.3) Comparison of experimental results to the simplified model: Permeate velocity as a function of vertical position and average permeate flux ($d_{i,HF}$ = 1.7 mm, v_{max} = 2.15 v_{avg}, c ($CuSO_4$) = 1 g/L).

Estimation of local cumulative permeate flux

The local cumulative permeate flux J_{cum} as described in section (4.4.1) can be estimated from the distribution of average permeate velocity along the membrane. This parameter equals the average (i.e. setpoint) permeate flux J_{avg} at the position y = 0 cm,

$$J_{cum}(y=0) = J_{avg} \neq f(y), \tag{5.2}$$

and was calculated according to equation (4.15). J_{cum} is plotted as a function of vertical position and average permeate flux in **Figure (5.4)**. It is shown that an increase in average permeate flux or a decrease in distance from the point of permeate extraction is followed by an increase in J_{cum}.

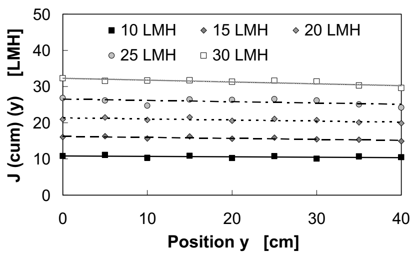

Figure (5.4) Local cumulative permeate flux as a function of vertical position and average permeate flux with linear trend lines (c ($CuSO_4$) = 1 g/L).

The negative slope of the curves increases as the average permeate flux increases, with the steepest slope of -0.05 L/(m^2 h cm) occurring for J_{avg} = 30 L/(m^2 h). These trends indicate that lumen-side pressure losses affect the permeate flux distribution for a steady-state filtration of pure water, with a maximum flux decline of 2 L/(m^2 h) for a membrane length of 40 cm. This flux decline is relatively low compared to previous studies of Chang and Fane [2001], whereas similar trends were observed by Hardy *et al.* [2002]. In addition, the local cumulative permeate flux estimated for the position y = 0 cm is on average 6.9 % higher than the pump-controlled permeate flux. This may be due to a smaller effective membrane area and slightly higher actual flux values.

(5.1.2) Cake growth determination

Particle deposition during a microfiltration of silica suspensions was investigated by NMR imaging using the same experimental setup as for the velocity measurements presented above. Parameters such as vertical position along the fibre, permeate flux, silica concentration, air pressure and duration of aeration were investigated. For this purpose, a series of NMR images was taken by consecutive NMR measurements, allowing a step-wise observation of transient cake growth at a certain vertical position. A description of the experimental setup, the test protocol, the NMR settings and the subsequent data processing is presented in sections (4.3.1) and (4.4.1).

Reproducibility of cake formation

Before evaluating the impact of operating parameters on the microfiltration performance, the reproducibility of TMP and cake height evolution was investigated. Therefore, an experiment was repeated three times under reference conditions. The corresponding TMP rise is plotted for all three test runs in **Figure (5.5)**. The filtration performance is characterised by an increase in TMP rise during the first part of the experiment, whereas the TMP slope levels off during a second filtration stage. This decrease in fouling rate dTMP/dt is presumably attributed to gravity and back-diffusion, which counteract drag forces caused by the permeating liquid. For a filtration with hollow-fibre membranes at imposed permeate flux, the feed flow passes through concentric lateral areas. These areas are getting smaller as the flow approaches the membrane, so that the curvature of the fibres results in an acceleration of feed flow. Gravitational forces and/or diffusion gain more relevance as the cake layer thickness increases and drag forces weaken due to a decline in radial flow velocity. This reduction in deposition-enhancing forces is followed by a more pronounced particle removal. Therefore, the inflexion point of the function TMP = f (t) indicates if particle deposition dominates (first filtration stage) or if the removal of particles or particle aggregates from the cake layer is governing (second filtration stage). In addition, a constant particle deposition on curved surfaces is characterised by a decreasing cake growth rate with time. This is due to a smaller cake growth increment for a continuously increasing effective membrane area (membrane + growing deposition layer) and is therefore an effect complementary to the enhanced particle back-transport for thicker cakes. The TMP evolutions for the three test runs show average fouling rates between 0.34 and 0.41 mbar/s during the experiment.

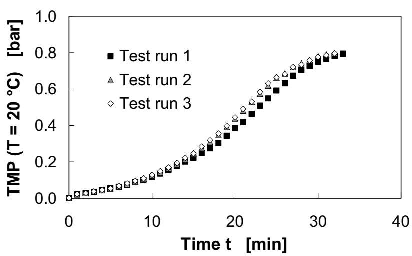

Figure (5.5) Reproducibility of results: Evolution of TMP for three different test runs ($J = 20$ L/(m^2 h), c (SiO_2) = 0.4 vol. %, y = 0 cm).

NMR cake formation images were processed following the strategy described in the materials and methods section. The cake thickness versus time is plotted in **Figure (5.6)** for the three different test runs and is measurable after about 5.5 min of filtration. This delay may be due to both limitations in spatial resolution and/or a transition from concentration polarisation (not detectable) to particle deposition (detectable) at a critical concentration in the boundary layer, see section (3.2.3). The cake thickness continuously increases and the cake growth rate decreases during the experiment, which is in good agreement with the TMP evolutions. A logarithmic trend line fits the measured cake height evolutions best. Larger fluctuations in cake layer thickness were observed for TMP > 600 mbar, which may be due to thicker cakes and less pronounced drag forces at the end of the experiment.

The interrelationship between TMP (integral measurement) and cake layer thickness (local measurement at position y) is shown in **Figure (5.7)**. The TMP increases exponentially for all three test runs as the cake thickness increases. In addition to classical cake formation caused by particle deposition only, also cake compaction may occur. The latter effect would explain the increase in slope with increasing cake thickness. Alternatively, an initial cake build-up close to the point of permeate extraction and a delayed cake build-up closer to the fibre end and/or a continuously reducing growth rate of cakes forming on curved surfaces may cause the exponential rise.

In **Figure (5.8)**, the ratio of TMP (integral measurement) divided by the corresponding cake thickness (local measurement at position y) is plotted versus time for the three different test runs. This ratio is later on referred to as TMP-cake height ratio and describes the TMP required to overcome 1 µm of cake thickness at the vertical position y. Hence, the evolution of this ratio characterises the dynamics of cake formation. The trend line shows a linear increase in TMP-cake height ratio with time. This indicates that the cake was either compacted, was predominantly formed in other parts of the membrane at the end of the experiment or that the cake growth rate was reduced as the deposition layer continuously grows on the curved membrane surface. However, an isolation of these three phenomena is unfeasible since changes in local cake porosity or local permeate flux are not detectable with the current NMR approach.

These very first experiments have shown an acceptable reproducibility of results for both TMP rise and cake layer formation. The cake growth was represented best by (i) a logarithmic trend line for the evolution of cake thickness, (ii) an exponential trend line for the TMP as a function of cake thickness and (iii) a linear trend line for the evolution of the TMP-cake height ratio. Therefore, the same regression lines will be applied for all subsequent data processing for a better comparability of results.

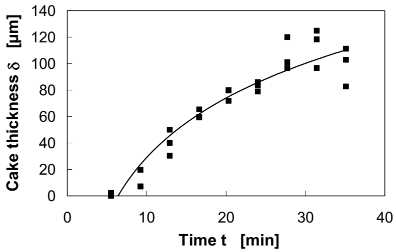

Figure (5.6) Reproducibility of results: Evolution of cake layer thickness with a logarithmic trend line (data points of three different test runs, J = 20 L/(m^2 h), c (SiO_2) = 0.4 vol. %, y = 0 cm).

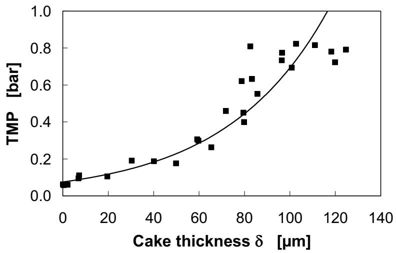

Figure (5.7) Reproducibility of results: TMP as a function of cake layer thickness with an exponential trend line (data points of three different test runs, J = 20 L/(m^2 h), c (SiO_2) = 0.4 vol. %, y = 0 cm).

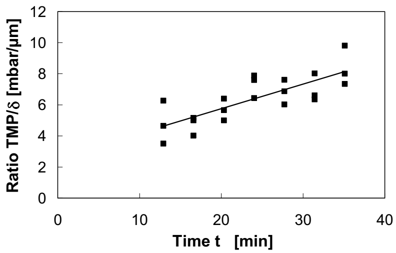

Figure (5.8) Reproducibility of results: Evolution of TMP-cake height ratio with a linear trend line (data points of three different test runs, J = 20 L/(m^2 h), c (SiO_2) = 0.4 vol. %, y = 0 cm).

Distribution of cake properties along the membrane

A number of researchers have found that cake layer formation in microfiltration processes occurs non-uniformly along the membrane [Gourgues *et al.*, 1992; Wakeman, 1994; Song, 1998; Bacchin *et al.*, 2002]. This leads to alterations in the local particle deposition rate due to higher filtration resistances where the local cake layer is thicker. Hence, the design of the NMR setup allows measuring at different vertical positions to investigate heterogeneous cake growth patterns. Deviations in TMP evolution for different vertical positions were found to be in the range of the measurement inaccuracy. The evolution of cake thickness, the TMP as a function of cake thickness and the evolution of TMP-cake height ratio are presented in **Figure (5.9)** for three different vertical positions. It is observed that the data points scatter more for positions $y \neq 0$ cm. One explanation could be the fact that the membrane orientation in the test cell is not straight, i.e. the membrane touches the inner wall in an uncontrolled manner. This membrane-wall contact is inhibited at y = 0 cm, where the membrane is fixed with glue. This glue connection serves as a spacer and leads to a better reproducibility of results compared to all other vertical positions.

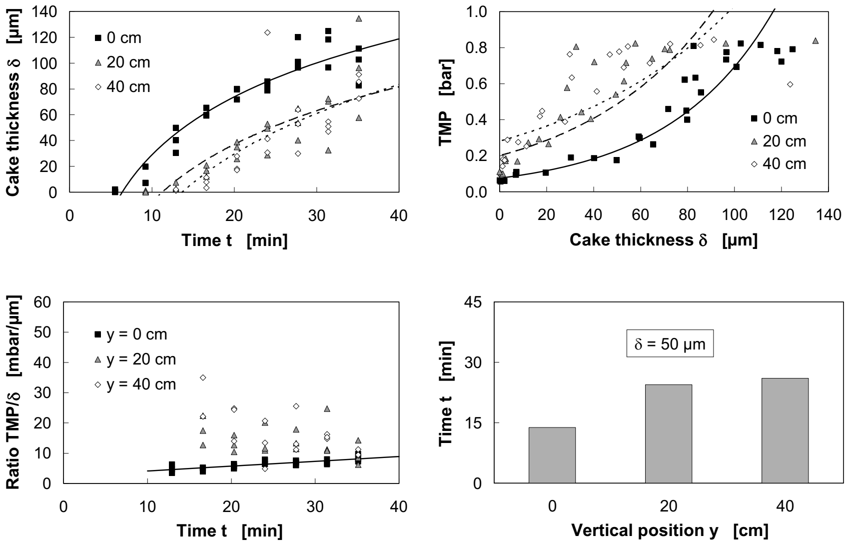

Figure (5.9) Impact of vertical position: Evolution of cake layer thickness (top-left), TMP versus cake layer thickness (top-right), evolution of TMP-cake height ratio (bottom-left) and time to reach 50 µm cake thickness (bottom-right) for the vertical positions y = 0, 20 and 40 cm (J = 20 L/(m^2 h), c (SiO_2) = 0.4 vol. %).

In future studies, the experimental setup will be further improved to allow for a precise positioning of the fibre in the test cell and an automatic positioning of the test rig relative to the measurement slice. Nevertheless, qualitative conclusions can be drawn despite this scatter of data points for $y \neq 0$ cm. The cake layer at $y = 0$ cm appears to be thicker than at the other positions during the entire experiment and for the whole range of TMP. However, only marginal differences in cake growth were found when comparing the vertical positions $y = 20$ and 40 cm. This can be observed by estimating the time required to reach 50 µm cake layer thickness, as illustrated at the bottom-right of **Figure (5.9)**. This characteristic time span suggests that the cake is formed next to the point of permeate extraction first, with a delayed cake growth towards the end of the fibre. Moreover, the function $TMP = f(\delta)$ and the evolution of TMP-cake height ratio show qualitatively similar trends and do not provide additional information for $y \neq 0$ cm compared to the evolution of cake thickness.

These very first investigations conducted at different vertical positions y have shown that a heterogeneous cake layer is formed on the membrane surface. However, detailed knowledge about local cake porosity changes and transients in local permeate flux are still lacking. For this reason, efforts will be made to improve the NMR approach for future studies. At this stage, all further data processing is restricted to the evolution of cake thickness at $y = 0$ cm.

Impact of average permeate flux

Similar to the studies conducted at different vertical positions y, the TMP as a function of the volume of deposited particles indicates that two filtration stages are observable, see **Figure (5.10)** as compared to **Figure (8.2)** in Annexe (8.2). The first stage is characterised by an increase of the slope $dTMP/dV(SiO_2)$, whereas the slope levels off during the second stage of filtration. A decrease in average permeate flux leads to a significant reduction of $dTMP/dV(SiO_2)$. This trend is due to an increased particle transport to the membrane by an increase in permeate flux, which leads to a rapidly growing cake layer. Moreover, this increase in driving force causes a higher solid compressive pressure in the cake, which enhances the affinity to cake compaction. This affinity can be estimated by enhancement factors as introduced in section (8.1). At first, this characteristic parameter increases with increasing average permeate flux and slightly drops in higher permeate flux ranges. This observation may be attributed to a less pronounced cake compaction in the range of higher permeate fluxes.

The impact of average permeate flux on the cake layer thickness was investigated at $y = 0$ cm, see **Figure (5.11)** and **Figure (8.2)** in Annexe (8.2). An increase in setpoint permeate flux was consistently followed by a more rapidly growing cake layer. The time span to reach an arbitrary threshold of 50 µm cake thickness was decreasing with an increase in permeate flux. This may be due to an enhanced particle transport to the membrane, enhanced drag forces and/or cake compaction as the permeate flux increases.

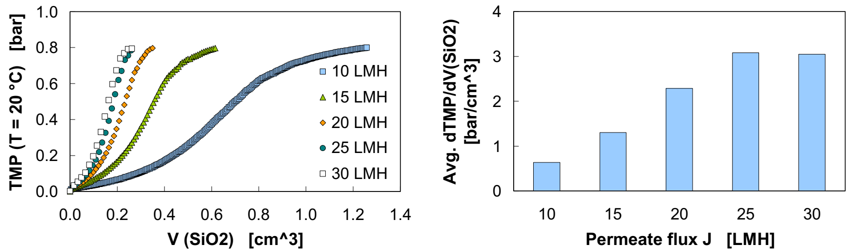

Figure (5.10) Impact of average permeate flux: TMP as a function of the volume of deposited particles (left) and the slope of the curves versus the average permeate flux (right) (c (SiO_2) = 0.4 vol. %, y = 0 cm).

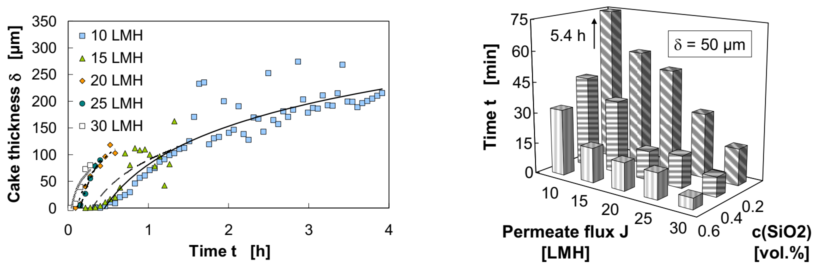

Figure (5.11) Impact of average permeate flux on the evolution of cake layer thickness (c (SiO_2) = 0.4 vol. %) (left) and time to reach 50 µm cake thickness for three different solids concentrations (right) (y = 0 cm).

The logarithmic trend lines show relatively weak correlations due to a severe scattering of data points at the end of the experiment. This scattering is more pronounced for low permeate fluxes and slowly growing cake layers. It is worth mentioning that these fluctuations are also affected by unavoidable variations in cake-to-bulk contrast, which are likely occurring during longer NMR experiments.

Impact of solids concentration

The concentration of silica particles in the model suspension affects the particle transport to the membrane. The TMP as a function of the volume of deposited particles resulting from filtration experiments with different solids concentration are presented in **Figure (5.12)**. Despite significantly different fouling rates dTMP/dt (see **Figure (8.3)** in Annexe (8.2)), the curves TMP = f (V (SiO_2)) almost overlap for solids concentrations of 0.2 to 0.6 vol. % (see **Figure (5.12)**).

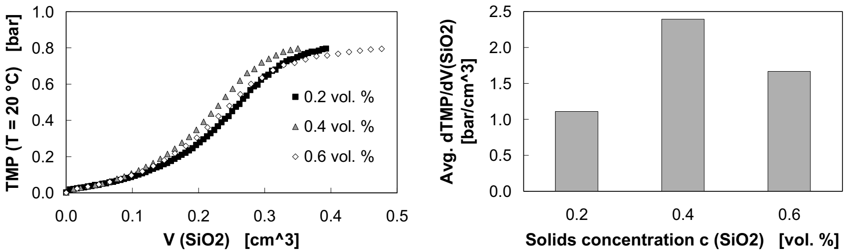

Figure (5.12) Impact of solids concentration: TMP as a function of the volume of deposited particles (left) and the slope of the curves versus the solids concentration (right) (J = 20 L/(m^2 h), y = 0 cm).

Although the particle deposition rate is higher and the cake grows faster, this suggests that an increase in solids concentration does not affect the affinity to cake compaction in the range of solids concentration investigated. However, the enhancement factors scatter and do not provide clear evidence for the significance of cake compaction as a function of solids concentration.

The impact of solids concentration on the evolution of cake thickness at y = 0 cm is presented in **Figure (5.13)** and **Figure (8.3)** in Annexe (8.2). In agreement with the TMP evolutions, an increase in solids content and particle deposition rate causes an increase in cake layer thickness and a decrease in time to reach 50 µm cake thickness. The data points scatter more severely in case of slowly growing cake layers, i.e. for low solids concentrations.

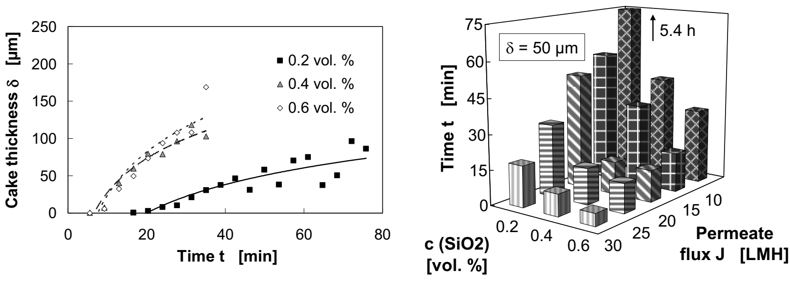

Figure (5.13) Impact of solids concentration on the cake layer thickness versus time (J = 20 L/(m^2 h)) (left) and time to reach 50 µm cake thickness (right) for five different permeate fluxes (y = 0 cm).

Efficiency of air bubbling

In submerged microfiltration processes, flow is induced by injecting bubbles to generate shear at the membrane surface and partly remove the cake layer. In **Figure (5.14)**, the efficiency of cake layer removal is expressed as the cake thickness divided by its initial thickness after 35 min of filtration. The removal efficiency after 1, 2 and 3 consecutive aeration cycles with continuous filtration is presented on the left-hand side, see section (4.3.1) for more details concerning the aeration sequence. In general, it was found that cake removal is enhanced as the aeration pressure or the duration of aeration increases, see below for more details.

- Aerating for 30 s at 0.3 bar relative air pressure causes a gradual decrease in cake thickness after 1, 2 or 3 consecutive aeration cycles. While the cake thickness observed after the first cycle does not provide evidence for cake layer removal, the second and third cycle cause a significant decrease in cake height.

- Increasing the duration of aeration from 30 to 60 s causes a rapid decrease in cake thickness after the first cycle, whereas less benefit is due to the subsequent aeration steps.

- Increasing the aeration pressure from 0.3 to 0.5 bar with a cycle duration of 30 s indicates a more efficient cake removal due to the first aeration cycle, as compared to no removal for the lower aeration pressure. Once more, the second and third aeration steps did not contribute significantly to any further cake removal.

- Regarding the first aeration cycle, longer aeration periods of 60 s with an air pressure of 0.5 bar did not lead to any significant difference in cake removal compared to shorter aeration cycles of 30 s. Nevertheless, a slight gradual decline in cake thickness was due to cycles 2 and 3 for the longer aeration period at 0.5 bar.

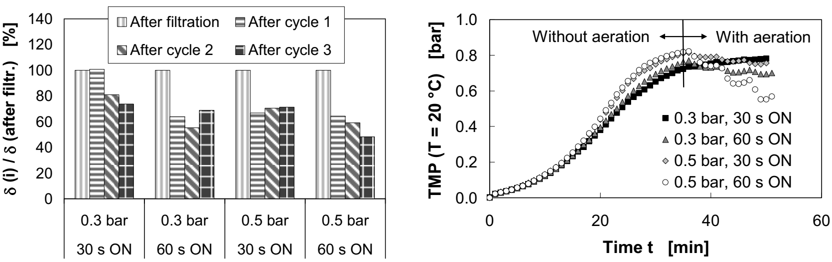

Figure (5.14) Cake thickness after each aeration cycle relative to the initial thickness after 35 min of filtration (left) and the corresponding TMP evolutions (right) as a function of aeration pressure and duration of aeration (J = 20 L/(m^2 h), c (SiO_2) = 0.4 vol. %, y = 0 cm).

These outcomes suggest that a critical aeration pressure may exist, above which a single and relatively short aeration cycle leads to a removal of more than 30 % of the initial cake layer thickness. Aeration pressures below this value require more than just one aeration cycle to achieve similar removal efficiencies. Moreover, as long as the aeration pressure is above this critical value, the filtration performance is less sensitive to variations in duration of aeration. These observations are in good agreement with previous findings that a critical aeration rate for enhancing the filtration performance exists [Ueda *et al.*, 1997].

The TMP evolutions corresponding to the four different aeration strategies are presented on the right-hand side of **Figure (5.14)**. The first part of the curves is equivalent to the two-stage cake formation introduced in the previous sections. The second part is characterised by fluctuations in TMP in response to surface shear due to air bubbling. The amplitude of these fluctuations becomes larger as the aeration pressure or the duration of aeration increases. This observation is consistent with the above cake removal determination. Interestingly, the gradual decrease in cake thickness observed for an aeration with 0.3 bar for 30 s is less pronounced in the integral TMP evolution. Furthermore, a pronounced gradual TMP recovery for an aeration with 0.3 bar for 60 s or with 0.5 bar for 30 s was measured, which was in both cases not accompanied with a corresponding gradual cake removal at y = 0 cm. The most significant gradual decrease in TMP was observed for an aeration with 0.5 bar for 60 s, for which a significant removal due to the first aeration cycle and only a slight gradual removal due to aeration cycles 2 and 3 was measured. These discrepancies further demonstrate limitations in evaluating cake growth and removal without knowledge about the distribution of these properties along the membrane.

It is expected that the efficiency of cake layer removal is higher if the filtration is interrupted during aeration, i.e. in the absence of drag forces holding the cake layer in position. However, this so-called relaxation strategy was not applicable to the NMR studies presented above since all NMR parameters were adjusted to permeation conditions. No-permeation conditions without filtration led to a worse cake-to-bulk contrast, which makes a quantitative determination of cake removal using the filtration pulse sequence impossible.

Concluding remarks

The applied NMR methodology provides insights into the microfiltration process which are not accessible with conventional monitoring techniques. Therefore, the outcomes presented in this section will help to further optimise the microfiltration process. Nevertheless, it is essential to note that these measurements are restricted to thin slices at a certain vertical position only. On the other hand, knowledge of the distribution of filtration properties over the entire membrane length is required to describe the self-accelerating fouling for a filtration at constant permeate flux. Hence, an integral monitoring of the filtration performance was conducted in a number of single fibre and single bundle filtration tests to close the gap between localised NMR results and the operation of pilot-scale MBRs.

(5.2) Meso-scale single fibre filtration tests

Microfiltration of suspensions has been extensively investigated during the past decades. In most of the previous studies, single membranes were applied for a filtration at constant TMP while monitoring the permeate flux decline. Numerous approaches were introduced to predict the time to reach steady-state conditions, the steady-state permeate flux or the distribution of cake properties along the membrane. Therefore, single fibre cross-flow filtration tests at constant TMP were conducted in the framework of this study for comparison with results published in literature. These efforts form the first part of a series of meso-scale filtration experiments using the same hollow-fibres and model suspensions presented above. In contrast to the NMR studies, only an integral monitoring of the filtration performance was performed. All subsequent filtration experiments are taking into account additional effects such as bubble-induced tangential flow, fibre movement and fibre-fibre interactions. Thereby, the complexity of the system is increased step-wise.

(5.2.1) Cross-flow filtration tests

The cross-flow test rig introduced in section (4.3.2) was operated at constant TMP while monitoring the permeate flux decline due to cake layer formation. The resulting total filtration resistance as a function of cumulative permeate mass is presented in **Figure (5.15)** for different setpoint TMPs. The transient filtration stage is characterised by an increase in filtration resistance as the permeate mass increases, whereas rather constant filtration resistances were observed under steady-state conditions. A comparison of these results to well-known blocking filtration laws as summarised by Hermia [1982] did not provide evidence for the existence of a single pore blocking mechanism, see section (3.2.3). More complex flux decline patterns were observed instead, which may be attributable to a successive or simultaneous coexistence of more than one type of pore blocking mechanism as previously stated by Wessling [2001].

Longer transient filtration stages are desirable, since the time-averaged permeate flux is higher. The time to reach steady-state varies between 3.5 and 22 min for all parameter combinations investigated as shown in **Figure (8.4)** in Annexe (8.2). However, the cumulative permeate mass collected during the transient filtration stage is favourable as an indicator of the filtration performance at TMP = const, see section (2.2.1). Higher values of cumulative permeate mass indicate that the cake layer grows slower, is thinner or more porous. An isolation of these phenomena is unfeasible with an integral monitoring of the filtration performance.

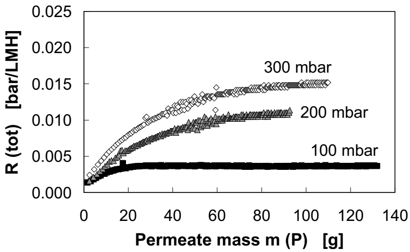

Figure (5.15) Impact of setpoint TMP on the total filtration resistance as a function of cumulative permeate mass for a single fibre cross-flow filtration (v_{CF} = 0.08 m/s, c (SiO_2) = 0.4 vol. %).

The impact of operating parameters and suspension properties on this characteristic permeate mass is presented in **Figure (5.16)**, while the observed trends are summarised below.

- It was found that the characteristic permeate mass increases as the TMP increases. Significantly lower deviations in the range of higher TMPs indicate that the benefit of a higher driving force (i.e. more permeate collected during the transient filtration stage) levels off. This suggests a limiting TMP of 200 mbar as the threshold for an improved transient filtration stage.

- Other researchers have found that variations in cross-flow velocity do not affect the transient filtration performance [Davis, 1992; Belfort *et al.*, 1994]. However, contradictory trends were observed in this study as shown at the top-right of **Figure (5.16)**. An increase in cross-flow velocity was followed by an increase in collected permeate mass. The enhancement factors (see section (8.1)) were consistently decreasing, thus indicating a less pronounced impact in the range of higher cross-flow velocities.

- A higher concentration of silica particles is causing an increase in particle deposition rate without affecting the driving force of the process. Therefore, the cake layer grows faster for a given TMP, which leads to a decrease in cumulative permeate mass and thicker cakes. This expectation is confirmed by the results presented at the bottom of **Figure (5.16)**, showing a decrease in permeate mass with an increase in solids concentration. The corresponding enhancement factors are decreasing and are indicating a highly non-proportional interrelationship between these two parameters.

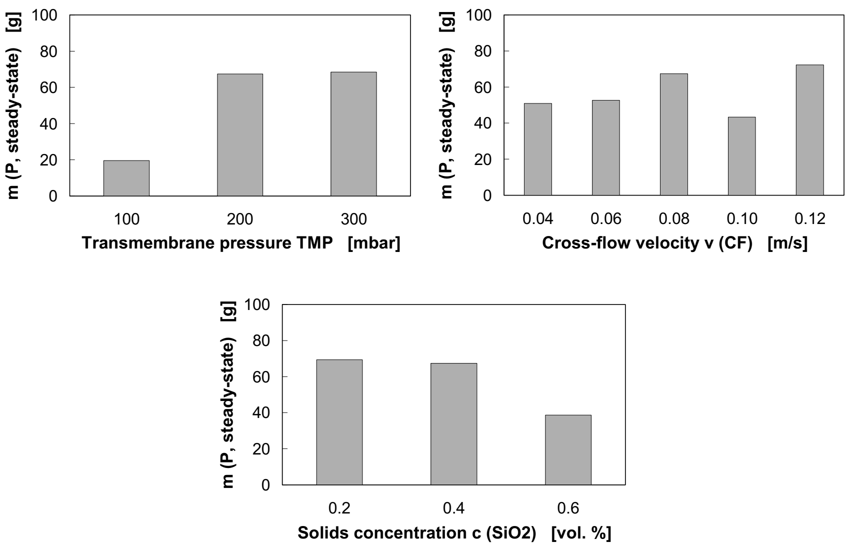

Figure (5.16) Impact of setpoint TMP (v_{CF} = 0.08 m/s, c (SiO_2) = 0.4 vol. %) (top-left), cross-flow velocity (TMP = 200 mbar, c (SiO_2) = 0.4 vol. %) (top-right) and solids concentration (TMP = 200 mbar, v_{CF} = 0.08 m/s) (bottom) on the cumulative permeate mass collected during the transient filtration stage for a single fibre cross-flow filtration.

In addition to this characteristic permeate mass, also the final total filtration resistance under steady-state conditions was estimated and is presented in **Figure (5.17)** and discussed below.

- It was observed that the steady-state resistance increases as the setpoint TMP increases. The results indicate a less pronounced impact of TMP variations on the final total filtration resistance in the range of higher driving forces. These observations are qualitatively consistent with the limiting flux theory as introduced in section (3.2.3). However, this upper limit for a steady-state filtration was not reached under the filtration conditions investigated.

- An increase in cross-flow velocity led to an increase in final resistance with decreasing enhancement factor as presented at the top-right of **Figure (5.17)**. This unexpected trend is presumably due to a selective particle deposition since larger particles are more likely entrained than smaller ones (see section (3.2.3)). In this case, cakes of high specific flow resistance are formed, which may be further compacted by infiltration of fine particles into the existing cake structure. Moreover, high cross-flow velocities may lead to an almost complete removal of the first layer of deposited particles, so that the affinity to pore blocking would be enhanced. The less significant impact of an increase in cross-flow velocity in the range of higher velocities confirms this theory. Nevertheless, it is important to note that the impact of variations in cross-flow velocity on the final total filtration resistance is in the range of the measurement inaccuracy.

- An increase in silica content leads to an increase in final filtration resistance with decreasing enhancement factor, see bottom of **Figure (5.17)**. This observation suggests that higher solids concentrations are leading to rapidly growing and thick cake layers, thus causing an increase in solid compressive pressure in the cake. However, this impact levels off in the range of higher solids concentrations.

In conclusion, the cumulative permeate mass collected during the transient filtration stage was increasing as the TMP increases, the cross-flow velocity increases or the solids concentration decreases. The final total filtration resistance was decreasing with decreasing TMP, decreasing cross-flow velocity or decreasing solids concentration.

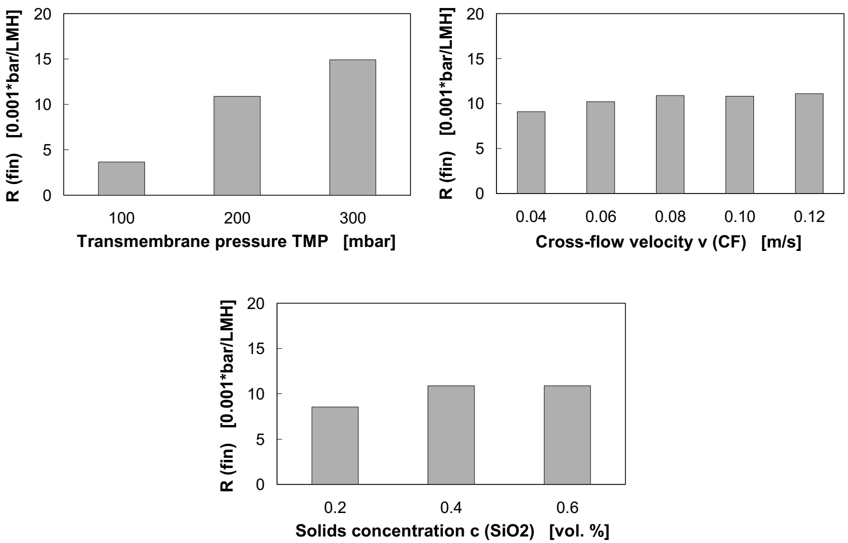

Figure (5.17) Impact of setpoint TMP (v_{CF} = 0.08 m/s, c (SiO_2) = 0.4 vol. %) (top-left), cross-flow velocity (TMP = 200 mbar, c (SiO_2) = 0.4 vol. %) (top-right) and solids concentration (TMP = 200 mbar, v_{CF} = 0.08 m/s) (bottom) on the final total filtration resistance for a single fibre cross-flow filtration.

When comparing enhancement factors relative to reference conditions, it was found that all interrelationships listed above are non-proportional. However, modelling the transient or steady-state filtration performance for an operation at TMP = const is beyond the scope of this study. For this reason, the following general conclusions were drawn for a better interpretation of filtration studies at imposed permeate flux.

- A comparison with established blocking filtration laws suggests that a successive or simultaneous coexistence of mechanisms rather than a single pore blocking mechanism is governing the filtration performance.

- The limiting flux was not reached under the filtration conditions investigated. A less significant impact of TMP variations on the transient and steady-state filtration performance for higher TMP values was found. These observations are consistent with the reversible cake layer formation theory.

- A higher cross-flow velocity enhances the removal of larger particles from the cake, leading to a selective particle deposition, an extended pore blocking stage and/or an infiltration of smaller particles, so that the specific filtration resistance increases. However, this marginal impact was in the range of the overall measurement inaccuracy and was neglected for all upcoming studies.

- The extent of irreversible phenomena such as pore blocking or the formation of cakes non-removable by the cross-flow was not detectable with this approach. Nevertheless, the porosity of the cake structure seems to be influenced by the solid compressive pressure. Therefore, cake compaction due to a continuous TMP rise is likely occurring under constant permeate flux conditions as well.

- The cumulative permeate mass was found to be a good measure for the transient filtration stage. However, no benefit of the total resistance plotted versus the permeate mass are expected for a filtration at constant permeate flux. Therefore, all subsequent data processing will be based on either TMP evolutions or fouling rates expressed as dTMP/dt plotted versus the corresponding process parameter.

(5.2.2) Submerged filtration tests

The meso-scale filtration performance in submerged mode was investigated by using both the single fibre and the fibre movement test rig as described in sections (4.3.3) and (4.3.4). While the investigations on the first setup are focussing on operating parameters and feed characteristics, the impact of bubble-induced fibre motion on the overall filtration performance was investigated with the second test rig.

Impact of operating parameters and feed characteristics

The single fibre test rig introduced in section (4.3.3) consists of a tubular shell with an internal diameter of 26.7 mm. Since the membrane is located in close proximity to the wall of the test cell, intensive fibre motion is inhibited due to an unavoidable membrane-wall contact. Nevertheless, a slight movement of the quasi-tight fibre was observable, but is deemed to be negligible compared to the fibre movement studies.

The fouling rate dTMP/dt averaged over all filtration cycles of the test run is plotted as a function of permeate flux and solids concentration in **Figure (8.5)** in Annexe (8.2). The average fouling rate increases with increasing setpoint permeate flux or increasing solids concentration. Once more, these trends are attributed to an enhanced transport of particles towards the membrane and rapidly growing cake layers. These observations are qualitatively consistent with the above NMR studies without aeration and are thus not further discussed.

The aeration of the membrane unit is known as an efficient, but costly method to control cake layer formation in submerged membrane processes. Therefore, the main objective of this part of the study is to improve the aeration sequence in order to reduce aeration requirements. For this purpose, the impact of variations in net aeration rate, gross aeration rate and aeration frequency on the fouling rate were investigated and are presented in **Figure (5.18)**. Please refer to **Table (5.1)** or to section (3.2.2) for more details on the aeration parameters.

The net aeration rate equals the average amount of air injected into the suspension per unit time throughout the entire filtration experiment. The fouling rate and the enhancement factor introduced in section (8.1) decrease significantly as the net aeration rate increases, before the fouling rate reaches a plateau. This plateau value characterises critical aeration conditions [Ueda *et al.*, 1997] and is due to a complete removal of the cake layer even for intermediate aeration rates. However, such kind of plateau was not observable in the range of higher aeration frequencies.

The gross aeration rate corresponds to the average amount of air injected into the suspension per unit time throughout a single aeration cycle. An increase in gross aeration rate leads to a reduction in fouling rate first, before the fouling rate starts rising again. This unexpected trend was consistently found for two different aeration sequences and suggests that an optimum gross aeration rate exists. Below this threshold, a clear benefit of higher superficial gas velocities was observable. Above this value, counteracting phenomena such as alterations in the multi-phase flow pattern like variations in bubble coalescence, gas slug length and gas hold-up may cause detrimental effects. It is important to note that these phenomena are significantly affected by the tube diameter, gas sparger design and submergence depth. Therefore, a direct transfer of findings to large-scale membrane units with significantly different design features is difficult. Nevertheless, it is known that external slug flow conditions are also occurring in relatively unconfined membrane units [Cui *et al.*, 2003], so that an optimum gross aeration rate may be observable in large-scale microfiltration processes as well.

The aeration frequency corresponds to the number of aeration cycles (i.e. shear periods) per unit time. An increase in aeration frequency for a net aeration rate of 0.55 L/min was followed by a significant decrease in fouling rate. This observation indicates potentials to further optimise the efficiency of air bubbling and to reduce operational expenses for air sparging simultaneously.

In conclusion, the submerged filtration tests using quasi-tight single fibres have shown that the impact of permeate flux and solids concentration on the overall filtration performance is in good agreement with both cross-flow and submerged filtration tests without air bubbling. A critical net aeration rate, an optimum gross aeration rate and a significant impact of aeration frequency on the fouling rate were observed. While investigations on the additional impact of bubble-induced fibre movement are presented below, the above aeration parameters were further investigated on a macro-scale as discussed in section (5.3).

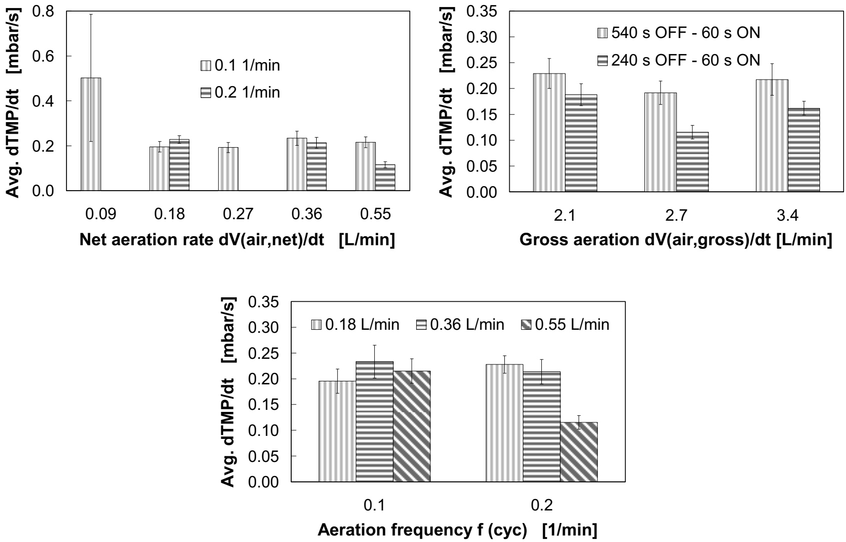

Figure (5.18) Impact of net aeration rate (p_{air} = 0.3 bar) (top-left), gross aeration rate (top-right) and aeration frequency (p_{air} = 0.3 bar) (bottom) on the average fouling rate for a submerged, quasi-tight single fibre (error bars according to equations (4.1) and (4.2), $J = 20\ L/(m^2\ h)$, c (SiO_2) = 0.4 vol. %).

Aeration sequence [s OFF - s ON]	**Air pressure p_{air}** [bar]	**Gross aeration rate $dV_{air,gross}/dt$** [L/min]	**Net aeration rate $dV_{air,net}/dt$** [L/min]	**Aeration frequency f_{cyc}** [1/min]
540-60	0.25	2.06	0.21	0.1
240-60		2.14	0.43	0.2
580-20	0.30	2.58	0.09	0.1
560-40		2.67	0.18	0.1
540-60		2.73	0.27	0.1
520-80		2.66	0.36	0.1
480-20		2.71	0.55	0.1
280-20		2.59	0.17	0.2
260-40		2.74	0.37	0.2
240-60		2.72	0.55	0.2
540-60	0.35	3.37	0.34	0.1
240-60		3.27	0.66	0.2

Table (5.1) Aeration parameters for the single fibre filtration tests.

Impact of fibre movement

In submerged filtration processes, air bubbling is applied to generate shear at the membrane surface. For hollow-fibre membrane configurations, the interaction of this multi-phase flow pattern with the membrane unit causes a statistic fibre movement. This fibre motion is known to contribute to the removal of the cake layer for loose hollow-fibres potted at both ends [Wicaksana *et al.*, 2006]. The investigations presented in this section are a follow-up of this earlier study and are dealing with fibres fixed at the bottom end only and fibre bundles of different packing density.

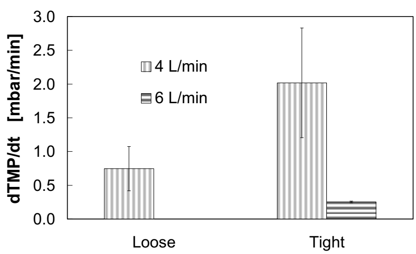

Figure (5.19) Average TMP rise for loose and tight fibres as a function of aeration rate (adapted from Buetehorn *et al.* [2009]).

The average fouling rate is plotted as a function of net aeration rate in **Figure (5.19)** for experiments with continuous aeration using a single hollow-fibre and the modified setup shown on the right-hand side of **Figure (4.24)**. A comparison of filtration tests with fibres fixed at one end (referred to as loose fibres) or both ends (referred to as tight fibres) is illustrated. The error bars are indicating that the TMP rise is not sufficiently reproducible. This weak reproducibility may be due to the transient character of the multi-phase flow pattern and/or the statistic bubble-induced fibre movement.

Despite these severe fouling rate fluctuations under the same operating conditions, an enhanced removal of deposited matter and lower fouling rates were observed with an increase in aeration rate for a tight fibre. Furthermore, a very low standard deviation in average fouling rate for an aeration rate of 6 L/min suggests a complete removal of the cake layer. The latter observation is indicating that a critical aeration rate in the range of 6 L/min exists, above which nearly no cake layer is formed on the membrane surface. In addition, a significant decrease in average TMP was determined when comparing filtration tests with tight and loose fibres. This trend is presumably due to the impact of (i) additional shear forces originating from the lateral fibre movement and (ii) collisions of the moving fibres and the support frame [Buetehorn *et al.*, 2009].

Critical aeration rate tests were conducted subsequent to the trials with constant operating conditions. In contrast to a filtration with constant aeration, a step-wise decrease in aeration rate allows (i) operating without any cake formation during the earlier stages of filtration and (ii) determining the aeration step in which particle deposition is initiated. Therefore, a better reproducibility of determining the critical aeration rate compared to the filtration tests with constant aeration was observed, see **Figure (4.13)**. For the critical aeration tests, the non-modified setup shown in the centre of **Figure (4.24)** was equipped with fibre bundles of up to 4 membranes and was operated according to the aeration-step method. Using this test rig instead of the modified setup shown on the right-hand side of **Figure (4.24)** was affecting the reproducibility of fouling rates, for which significant fluctuations were observed. Hence, the following discussion of results is solely based on the critical aeration rates $dV_{air, crit}/dt$ rather than the actual fouling rates dTMP/dt.

The TMP slopes for different permeate flow rates, loose versus tight fibres and different packing densities are presented in **Figure (5.20)**. An increase in permeate flow rate from 2 to 3 mL/min leads to an increase in critical aeration rate from 2 to 8 L/min. This is due to the formation of stable deposition layers also for higher aeration rates if the permeate flow rate increases. However, the critical aeration rate was found to be insensitive to variations in fibre tightness. Moreover, no clearly defined impact of packing density on the critical aeration rate was observable.

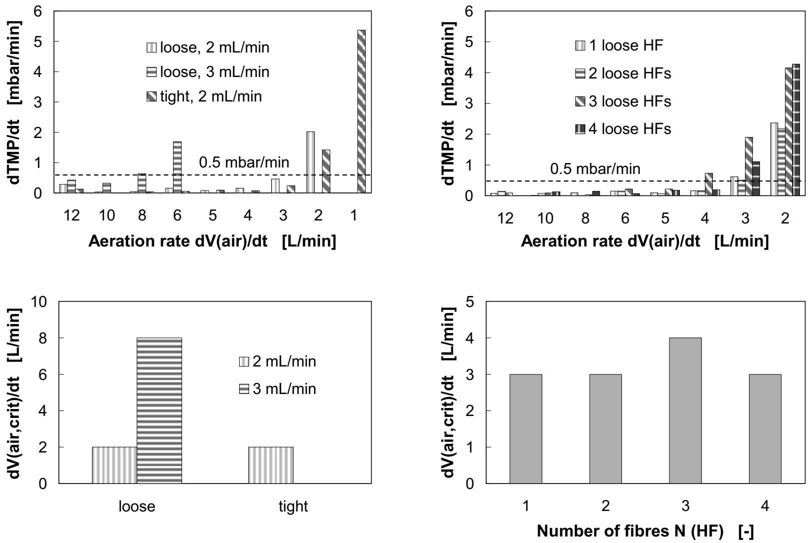

Figure (5.20) Impact of fibre looseness and permeate flow rate (c (SiO_2) = 0.4 vol. %) (left) or packing density (dV(P)/dt = 2 mL/min, c (SiO_2) = 0.4 vol. %) (right) on the critical aeration rate.

In summary, the investigations presented in this section have shown that bubble-induced fibre movement enhances the filtration performance. This benefit was qualitatively observable as a decrease in average fouling rate, whereas a further parameter variation was hindered by a weak reproducibility of results. Critical aeration rate experiments show a better reproducibility, but the expected trends were not detectable with the aeration-step protocol used. Nevertheless, critical flux and critical aeration rate studies were continued in macro-scale single bundle filtration tests as presented in section (5.3).

(5.2.3) Direct observation of fibre movement

The investigations presented in the previous section have shown that operating parameters such as the aeration rate are influencing the filtration performance. Moreover, it was found that bubble-induced fibre motion contributes to the removal of the cake layer. Therefore, the fibre movement setup as presented in section (4.3.4) was used for a filtration of pure water to track fibre motion in different vertical positions with continuous aeration and various packing densities. This methodology was adapted from Wicaksana *et al.* [2006] and is introduced in section (4.4.2).

The impact of aeration rate on the intensity of fibre movement is presented in **Figure (5.21)**. It was found that an increase in air flow rate is consistently followed by an increase in average fibre velocity for all fibre positions investigated. Moreover, it was observed that the average velocity increases towards the upper end of the fibre and decreases at the fibre top (position 4). This finding justifies the assumption made in section (4.5.3) that the intensity of fibre movement in the lower part of the hollow-fibre bundle is less pronounced than in greater distance from the fibre potting. The ratio of average fibre velocity and distance from the fibre potting corresponds to the angular fibre velocity. This parameter is plotted at the top-right of **Figure (5.21)** and increases with increasing aeration rate and decreasing distance from the fibre potting. Thus, the highest angular fibre velocity is occurring at the bottom part of the fibre. Interestingly, the impact of vertical position on the (angular) fibre velocity is relatively insensitive to the actual aeration rate. Hence, it is assumed that an increase in fibre movement intensity occurs to the same extent over the entire length of the fibre as the aeration rate increases. This postulation allows averaging the time-averaged values also over the length of the membrane.

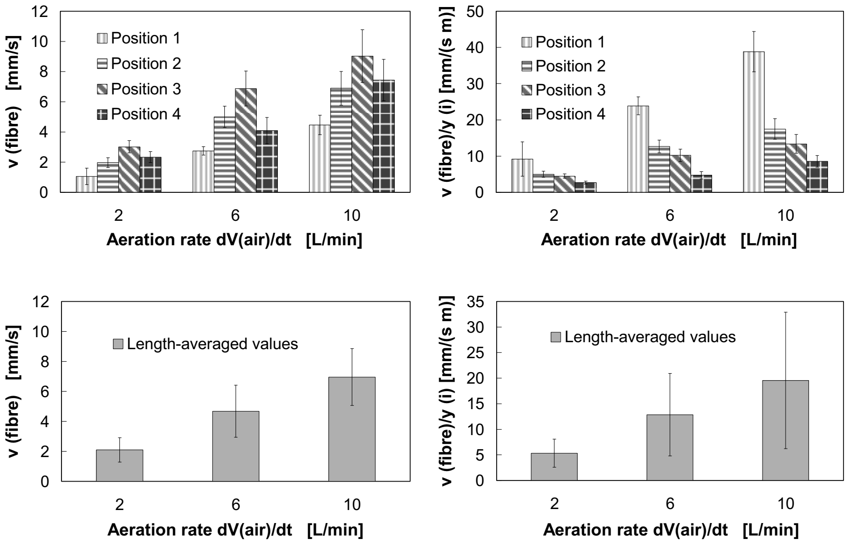

Figure (5.21) Time- (top) respectively time- and length-averaged (bottom) fibre velocity (left) and ratio of fibre velocity and distance from the fibre potting (right) as a function of aeration rate ($N_{HF} = 1$).

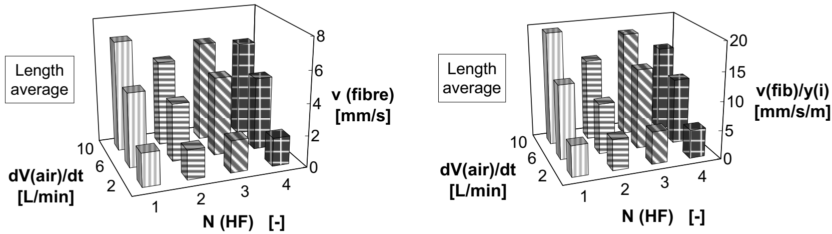

Figure (5.22) Time- and length-averaged fibre velocity (left) and ratio of fibre velocity and distance from the fibre potting (right) as a function of aeration rate and packing density.

The time- and length-averaged fibre velocities are plotted as a function of aeration rate at the bottom-left of **Figure (5.21)**. The error bars are characterising the non-uniformity of fibre motion along the membrane. An increase in fibre velocity with increasing aeration rate and decreasing enhancement factor (see section (8.1)) is observable, with less benefit for an increase above 6 L/min. The time- and length-averaged angular fibre velocity as shown at the bottom-right of **Figure (5.21)** confirms a levelling off in fibre motion enhancement as the aeration rate increases. This observation is consistent with previous findings indicating that a critical aeration rate for the fibre movement intensity exists [Wicaksana *et al.*, 2006].

The impact of packing density on the time-averaged fibre velocity and angular fibre velocity does not show any clearly-defined trend for the vertical positions and aerations rates investigated, see **Figure (8.6)** in Annexe (8.2). This unexpected observation is presumably due to the highly statistic character of fibre motion, which is affected by a number of unavoidable experimental errors such as slight differences in fibre orientation, curvature or stickiness. The latter effect may be further enhanced by adhering fibres due to permeate suction. Therefore, length-averaged values of both time-averaged fibre velocities and angular fibre velocities were calculated and are presented in **Figure (5.22)**. Also in this case, no clearly-defined impact of packing density on the time- and length-averaged fibre velocity and angular fibre velocity were found. This indicates that both the local and the length-averaged intensity of fibre motion are insensitive to packing density variations. In other words, more pronounced fibre-fibre interactions for denser bundles are not significantly affecting the motion of the fibre in the range of packing density investigated (bundles of 1 to 4 hollow-fibres).

In conclusion, a direct observation of fibre movement has been conducted based on a frame-by-frame image processing. A probability density function was derived from the evolution of fibre position. The time-averaged fibre velocity was confirming assumptions made for the CFD approach. The angular fibre velocity averaged over time and the length of the membrane consistently increases with an increase in aeration rate, but was insensitive to packing density variations. These findings will be compared with parameters describing the performance of submerged microfiltration processes in future studies. This could be achieved by correlating the fouling rate, the critical flux or the critical aeration rate with the time- and length-averaged angular fibre velocity.

(5.3) Macro-scale single bundle filtration tests

In the previous sections, a number of single fibre and small fibre bundle studies provided insights into the filtration performance on different scales. These experiments have shown that the fibre motion is significantly affecting the overall filtration performance. Therefore, macro-scale filtration tests with bundle configurations consisting of 228 fibres form the last experimental part of this study. The overall objective was to close the gap between lab-scale experiments and piloting tests as frequently performed in industrial process design. These investigations were conducted with the single bundle test rig introduced in section (4.3.5), which is operated at constant permeate flux in quasi-submerged mode, in submerged mode with a superposed cross-flow or in cross-flow mode.

All upcoming results are expressed as fouling rates dTMP/dt for estimating the critical flux or the critical aeration rate as indicators of the overall filtration performance, see section (3.2.3). Filtration experiments with constant operating conditions are in good agreement with the flux- or aeration-step tests summarised below and can be found elsewhere [Blach, 2009]. Fouling rate thresholds were defined as suggested by Le-Clech *et al*. [2003]. It is worth mentioning that the definition of these thresholds significantly affects the outcomes of data processing. Therefore, the weak form of critical conditions is commonly regarded as a qualitative measure for comparative studies only. For the following discussion of results, fouling rate thresholds of 1.5 mbar/min for the critical flux determination and of 0.5 mbar/min for the critical aeration rate determination were defined as a compromise for all test runs.

(5.3.1) Quasi-submerged filtration

The single-bundle test rig was operated in quasi-submerged mode at constant permeate flux first. This means that a minimum cross-flow velocity of 0.6 cm/s was set to refill the amount of permeate extracted from the feed channel. It was found that an increase in permeate flux or a decrease in specific aeration demand of the membrane unit (also referred to as SAD_m or (net) aeration rate) leads to an increase in fouling rate as presented at the top of **Figure (5.23)**. Large variations in enhancement factor (see section (8.1)) characterise the strongly non-proportional impact of both permeate flux and aeration rate variations on the microfiltration performance. Higher permeate flux values are linked to an enhanced particle transport and at the same time higher drag forces perpendicular to the membrane. The counteracting surface shear is more pronounced with increasing aeration rate. An increase in solids concentration leads to an increase in fouling rate with an increase in enhancement factor. This trend is due to a higher gross particle deposition rate at higher solids concentrations.

Plotting the fouling rate versus the corresponding setpoint permeate flux or aeration rate allows estimating critical filtration parameters. An increase in silica content is followed by a continuous decrease in critical flux or increase in critical aeration rate as presented at the bottom of **Figure (5.23)**. Critical flux values of 22.5 up to 32.5 L/(m^2 h) are in the same range compared to previous pilot-scale activated sludge filtration tests using the same module configuration [Buetehorn *et al.*, 2007a+b; Schulz, 2007]. This qualitative agreement justifies drawing general conclusions which are transferable to real MBR processes.

Table (5.2) provides an overview of aeration parameters for the single bundle filtration tests. The resulting critical flux and critical aeration rate values are plotted for two different gross aeration rates in **Figure (5.24)**. The gross aeration rate is equal to the average amount of air injected into the suspension per unit time throughout a single aeration cycle. Therefore, an increase in gross aeration rate by a factor of 2 for the same specific aeration demand SAD_m corresponds to a decrease in aeration frequency by a factor of 0.5.

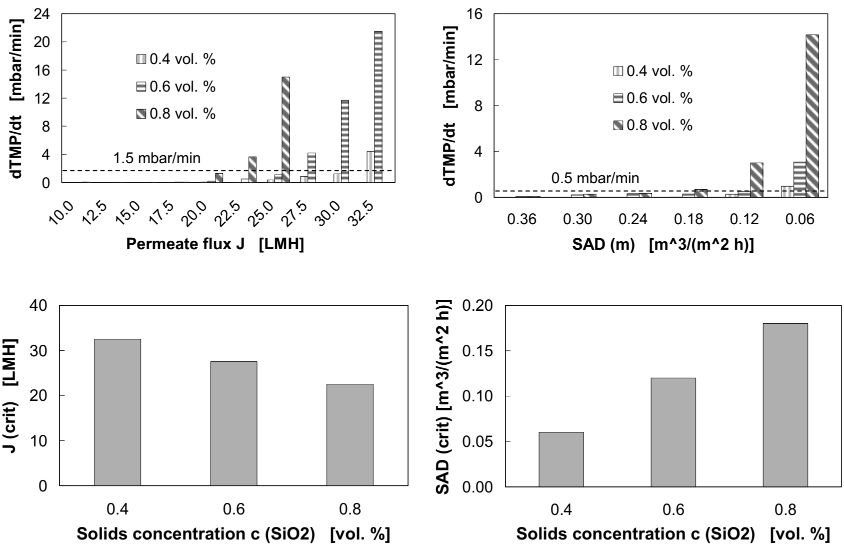

Figure (5.23) Single bundle filtration tests in quasi-submerged mode: Impact of solids concentration on the critical flux (SADm = 0.18 m^3/(m^2 h)) (left) and the critical aeration rate (J = 20 L/(m^2 h)) (right) ($dV_{air,gross}/dt$ = 3 m^3/h, v_{CF} = 0.6 cm/s).

The investigations have shown that variations in aeration frequency for SAD_m = const significantly affect the filtration performance. The fouling rate and the critical aeration rate were found to decrease as the aeration frequency increases, whereas the critical flux remained the same. This observation confirms the outcome of the submerged single fibre filtration tests, indicating the benefit of higher aeration frequencies at the same net aeration rate. These findings are relevant for reducing operating expenses of real MBR processes, which are mainly caused by the coarse bubble aeration of the membrane unit as discussed in section (1).

It is worth mentioning that the critical flux plateau shown in **Figure (5.24)** characterises filtration conditions, for which the occurrence of a fouling rate beyond the threshold is insensitive to a further increase in gross aeration rate. This means that a more pronounced surface shear does not affect the filtration performance. Therefore, phenomena non-removable by surface shear like adsorption of matter, particles too small for a hydraulic back-transport and/or an internal pore blocking are governing the filtration process.

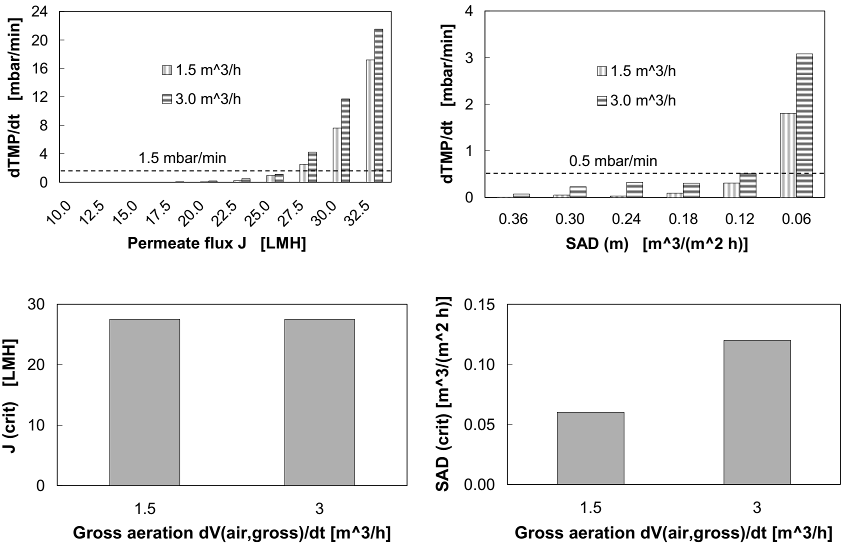

Figure (5.24) Single bundle filtration tests in quasi-submerged mode: Impact of gross aeration rate on the critical flux (SADm = 0.18 $m^3/(m^2\ h)$) (left) and the critical aeration demand (J = 20 $L/(m^2\ h)$) (right) (v_{CF} = 0.6 cm/s, c (SiO_2) = 0.6 vol. %).

Aeration sequence [s OFF - s ON]	Gross aeration rate $dV_{air,gross}/dt$ [m^3/h]	Net aeration rate $dV_{air,net}/dt$ [$L/(m^2\ min)$]	Specific aeration demand SAD_m [$m^3/(m^2\ h)$]	Aeration frequency f_{cyc} [1/min]
28-2	1.5	1	0.06	2
13-2		2	0.12	4
8-2		3	0.18	6
5.5-2		4	0.24	8
4-2		5	0.3	10
3-2		6	0.36	12
58-2	3	1	0.06	1
28-2		2	0.12	2
18-2		3	0.18	3
13-2		4	0.24	4
10-2		5	0.3	5
8-2		6	0.36	6

Table (5.2) Aeration parameters for the single bundle filtration tests.

(5.3.2) Operation with a superposed cross-flow

The circulation velocity in submerged membrane bioreactor configurations is in the range of 0.1 to 0.3 m/s [Drews *et al.*, 2008; Prieske *et al.*, 2008]. This liquid circulation is a consequence of the buoyancy-driven rise of air bubbles and causes the formation of riser and downcomer regions in the membrane compartment. Therefore, the liquid flow in the riser due to gas sparging is superposed by a liquid circulation flow. This circulation flow was taken into account in the experiments by a superposed feed flow rate above the minimum value required for the quasi-submerged filtration.

The impact of a superposed cross-flow velocity on the fouling rate is presented for three different aeration conditions on the left-hand side of **Figure (5.25)**. As expected, an increase in aeration rate is followed by a significant decrease in fouling rate. In addition, an increase in superposed cross-flow velocity leads to a decrease in fouling rate with decreasing enhancement factors. Even for relatively low specific aeration demands, an operation with the lowest feed flow rate investigated caused an almost complete removal of the cake layer.

On the right-hand side of **Figure (5.25)**, fouling rates for a cross-flow filtration without aeration are shown for three different permeate flux values. This mode of operation is characterised by a significant impact of cross-flow velocity on the fouling rate, with decreasing enhancement factors as the cross-flow velocity increases.

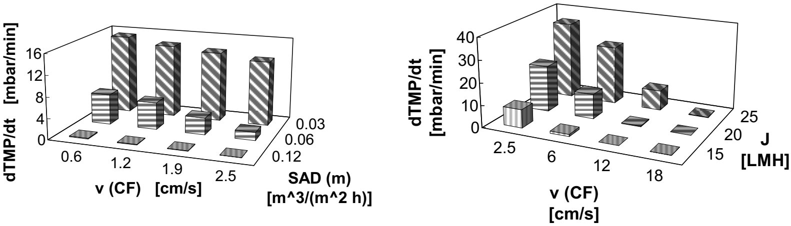

Figure (5.25) Single bundle filtration tests: Fouling rate as a function of specific aeration demand and superposed cross-flow velocity ($dV_{air,gross}/dt = 3\ m^3/h$, $J = 20\ L/(m^2\ h)$) (left) and as a function of cross-flow velocity and permeate flux ($SAD_m = 0$) (right) (c (SiO2) = 0.6 vol. %).

When comparing fouling rates observed for pump-induced cross-flow velocities with and without aeration, a clear benefit of air bubbling in addition to the circulating flow becomes evident. These results are indicating that both the circulation flow and air bubbling contribute to the removal of the cake layer. Therefore, also the design of the downcomer should be taken into account when optimising submerged microfiltration processes.

(5.3.3) Concluding remarks

The macro-scale single bundle filtration tests are indicating that the fouling rate is reduced as the permeate flux decreases, the solids concentration decreases, the aeration rate increases, the aeration frequency increases, the superposed cross-flow increases or the setpoint cross-flow velocity increases. These observations are qualitatively in agreement with previous findings of single fibre filtration tests in submerged mode. However, a selective particle deposition, an extended pore blocking stage and/or and infiltration of smaller particles as observed for a single fibre filtration at constant TMP were not found for the single bundle filtration tests at constant permeate flux. A more detailed comparison of results gained at different scales is presented in section (6.2) based on enhancement factors.

(5.4) Macro-scale CFD simulations

The CT scans have shown that fibres in PURON® bundles arrange irregularly, which exposes an anisotropic resistance to both single- and multi-phase flows. This resistance was implemented into a CFD simulation by porosity and friction factor matrices for both laminar and turbulent flow conditions in all three spatial directions. The simulation results based on an accurate representation of fibres are presented along with an overall description of the approach in section (4.5). Simulation results based on the porous medium approach for (i) a single-phase flow of water with raised viscosity and (ii) a two-phase flow of water with raised viscosity and air are discussed in the following sections. Please refer to Tollkötter [2010] for more details on the CFD settings and a more comprehensive overview of the outcomes.

(5.4.1) Impact of superficial inlet velocity on the single-phase flow pattern

It is known that a background circulation flow is occurring in large-scale membrane units operated in submerged mode [Drews *et al.*, 2008; Prieske *et al.*, 2008]. The filtration tests using a single hollow-fibre bundle as presented in section (5.3.3) have shown that this background flow significantly contributes to the enhancement in filtration performance. Therefore, a single-phase flow of water with raised viscosity was studied prior to the addition of the gas phase.

In **Figure (5.26)**, velocity contours in the heterogeneous porous medium for three different superficial inlet velocities $v_{inlet} = \overline{v}_{inlet}$ and MLSS = 10 g/L are compared. Firstly, it is evident that design features of the hollow-fibre bundle such as the gas sparger and higher fibre concentrations are represented properly by the porous medium. These no-flow areas are observable as stagnant liquid.

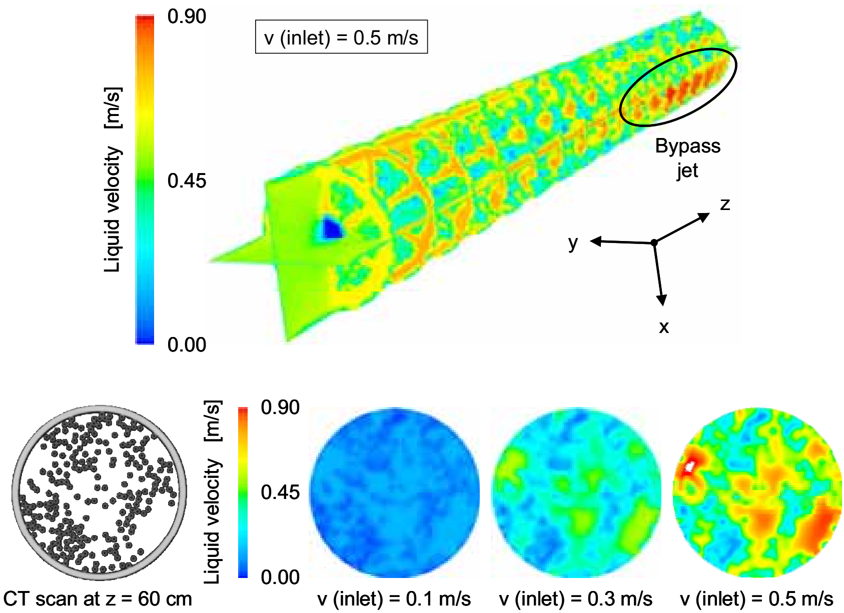

Figure (5.26) Single-phase CFD results: Velocity contours in the heterogeneous porous medium for a superficial inlet velocity of 0.5 m/s (top) and in a cross-section at z = 60 cm for three different superficial inlet velocities (bottom) with MLSS = 10 g/L.

Secondly, the velocity distribution in the bottom part of the bundle is rather uniform as compared to the upper part. This is due to the fact that the bottom part of the bundle is characterised by a regular fibre arrangement because of the formation of fibre segments and flow channels, whereas the upper part shows a less regular fibre arrangement. In the upper part, dead zones with relatively low flow velocities occur in regions where more fibres are present and bypass jets of high velocity are found where fibres are absent. This is observable at the bottom of **Figure (5.26)** when comparing the CT cross-section with the corresponding velocity contours in the porous medium.

An increase in local fibre concentration enhances macroscopic effects such as dewatering and inhibits an efficient hydrodynamic removal of deposited matter. Hence, these regions show a higher affinity to module blocking compared to areas of lower fibre concentration. In other words, the benefit of a high local velocity where fibres are absent remains unused. From this point of view, a major objective in membrane module development is not only to provide a maximum of surface shear, but also to distribute the shear evenly over the entire cross-section. The results have shown that flow channelling appears to be insensitive to variations in superficial inlet velocity, as expressed by similar standard deviations in liquid velocity averaged over all cross-sections shown in **Figure (5.26)**.

The porous medium approach does not allow estimating wall shear stresses acting on the surface of the membranes to evaluate the efficiency of cake layer removal. This is due to the fact that the membrane surface is not visible as such and is solely represented by an increase in local friction factor. Therefore, the turbulent viscosity

$$\eta_{turb} = \rho\, C_{\mu}\, \frac{k^2}{\varepsilon}, \tag{5.3}$$

which is commonly used to represent turbulence effects in the RANS equations [Ferziger and Perić, 2002], was chosen as an indirect measure of deviations in surface shear. In equation (5.3), ρ corresponds to the fluid density, C_{μ} to a parameter of the RNG k-ε turbulence model, k to the turbulence kinetic energy and ε to the dissipation rate of k. It is worth mentioning that an accurate prediction of turbulence properties by applying models based on the RANS equations is unfeasible. Therefore, all following turbulent viscosities are used for a qualitative comparison only.

At the top of **Figure (5.27)**, contours of liquid velocity and turbulent viscosity in a cross-section at z = 60 cm are compared. This comparison suggests that areas of high liquid velocity are corresponding to areas of low turbulent viscosity and vice versa. This interrelationship can be attributed to differences in fibre arrangement. A local accumulation of fibres causes the formation of bypass jets where fibres are absent and the friction factors are lower, thus leading to lower turbulence intensities. In contrast, the remaining liquid flowing through areas of low porosity is exposed to high friction, which causes an increase in turbulent viscosity. It is worth mentioning that a self-destabilisation of flow in regions of higher velocity, which is generally observable in high Re number regions, is deemed to be less relevant in the range of operating parameters investigated (Re ≤ 2247).

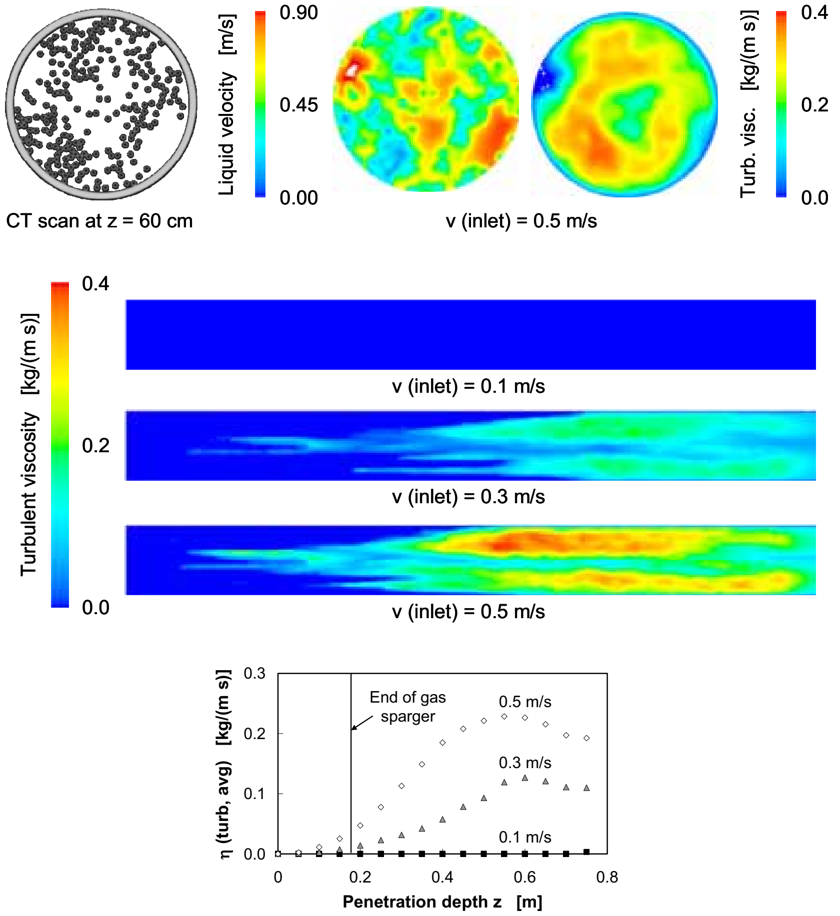

Figure (5.27) Single-phase CFD results: Contours of liquid velocity and turbulent viscosity at z = 60 cm (top), contours of turbulent viscosity in z-direction (centre) and area-weighted average of turbulent viscosity as a function of penetration depth z (bottom) for three different superficial inlet velocities and MLSS = 10 g/L.

In the centre of **Figure (5.27)**, contours of turbulent viscosity in the main direction of flow are presented for three different inlet velocities. It was found that an increase in superficial inlet velocity leads to a more pronounced turbulence, with a lower turbulence intensity in the bottom part of the bundle where the fibres arrange regularly. The numerical studies presented in section (4.5.5) were indicating that a critical Re number of 1000 exists. Using equation (4.28), the above inlet velocities can be transferred to Re numbers of 423, 1270 and 2117 for MLSS = 10 g/L. This suggests that a transition from laminar to turbulent flow conditions occurs between 0.1 and 0.3 m/s inlet velocity. This estimation is in good agreement with the above deviations in turbulent viscosity, i.e. the turbulent viscosity equals zero for $v_{inlet} = 0.1$ m/s and increases as v_{inlet} increases. However, an experimentally derived critical Re number of 4000 does not support this theory, see section (4.5.5).

The area-weighted average of turbulent viscosity in a number of cross-sections of the hollow-fibre bundle is plotted versus the penetration depth z at the bottom of **Figure (5.27)**. For an inlet velocity of 0.1 m/s, the flow pattern appears to be laminar with turbulent viscosities equal to zero throughout the entire bundle. An increase in inlet velocity to 0.3 m/s was followed by non-zero turbulent viscosities at the inlet, which increase with penetration depth until approaching $z = 0.6$ m. For $z > 0.6$ m, the turbulent viscosity drops due to the formation of a pronounced bypass jet as observable at the top of **Figure (5.26)**. A further increase in superficial inlet velocity from 0.3 to 0.5 m/s leads to an increase in turbulent viscosity with an increase in enhancement factor (see section (8.1)). Although the slope of turbulent viscosity as a function of penetration depth is much steeper in the first part of the bundle, the overall shape of the curve is not affected by an increase in superficial inlet velocity above 0.3 m/s.

Figure (8.7) in Annexe (8.2) illustrates numerically and experimentally derived pressure loss correlations of the form $\xi = f(\mathrm{Re})$. The deviation of experimental data points from the Forchheimer fit and the results of the first CFD model (CFD accurate) were previously discussed in **Figure (4.36)** in section (4.5.5). It was stated that this model underestimates the experimentally observed friction factor by up to one order of magnitude due to an insufficient discretisation of velocity gradients in boundary layers. According to **Figure (8.7)**, the CFD results based on the heterogeneous porous medium approach (model 2) slightly overestimate the experimental results. The latter deviation is presumably due to a forced penetration of flow through the cross-section partially blocked by the hollow-fibre bundle (model 2), as compared to a pattern solely flowing through channels without fibres (model 1 + experiments). Therefore, this discrepancy is an intrinsic weakness of the second CFD model, which leads to an overestimation of total pressure loss. The total pressure loss was found to increase as the inlet velocity increases (results not shown).

(5.4.2) Impact of MLSS concentration on the single-phase flow pattern

The mixed liquor suspended solids (MLSS) concentration is the dominating parameter affecting the rheological properties of activated sludge [Rosenberger, 2003]. In addition, shear-thinning characteristics and in some cases a limiting shear stress were observed by numerous researchers, see section (3.1) for more details. However, these non-Newtonian characteristics are neglected for these very first CFD studies to reduce the complexity of the simulation. The impact of differences in MLSS content on the dynamic viscosity of a Newtonian model fluid was taken into account using equations (4.42) and (4.43). Three different dynamic viscosities were implemented into the CFD simulation. These dynamic viscosities are corresponding to MLSS concentrations of 10 and 15 g/L as observed in MBR sludge [Pinnekamp and Friedrich, 2003] and of 3.5 g/L to represent the properties of the silica suspension, see section (4.2).

In **Figure (5.28)**, contours of liquid velocity in a cross-section at z = 60 cm (top) and of turbulent viscosity in the main direction of flow (centre) are shown for the three different MLSS concentrations for v_{inlet} = 0.3 m/s. The impact of MLSS on the cross-sectional velocity distribution appears to be less significant, with a more evenly distributed liquid velocity as the MLSS increases. This trend is observable by bypass jets of lower velocity for higher dynamic viscosities, but the same average velocity over the cross-section for all MLSS values. Nevertheless, similar standard deviations in liquid velocity averaged over all cross-sections shown in **Figure (5.26)** suggest that the impact of MLSS on flow channelling is only marginal. In contrast, the impact of MLSS on the turbulent viscosity in the main direction of flow was more significant. It was found that the turbulence intensity (see **Figure (5.28)**) and the total pressure loss (results not shown) decrease as the MLSS increases. This observation is attributed to a suppression of the onset of turbulence at higher dynamic viscosities and more pronounced internal friction. The above MLSS concentrations are corresponding to Re numbers of 2247, 1270 and 651 for v_{inlet} = 0.3 m/s with $Re_{crit,CFD}$ = 1000. In agreement with this, also the turbulent viscosity contours based on the heterogeneous porous medium approach suggest a transition from turbulent to laminar flow conditions between 10 and 15 g/L MLSS.

The area-weighted average of turbulent viscosity in the corresponding cross-section is plotted as a function of penetration depth at the bottom of **Figure (5.28)** for the three different MLSS concentrations. An increase in MLSS concentration leads to a decrease in turbulent viscosity with a decrease in enhancement factor. For the highest MLSS concentration, the turbulent viscosity equals almost zero throughout the entire computational domain. At lower MLSS concentrations, non-zero turbulent viscosities were observed right from the inlet of the porous medium. As mentioned before, the turbulent viscosity increases with penetration depth z until a pronounced bypass jet occurs for z > 0.6 m, which causes a decrease in turbulent viscosity.

The shape of the turbulent viscosity plotted as a function of penetration depth is similar for the two lower solids concentrations.

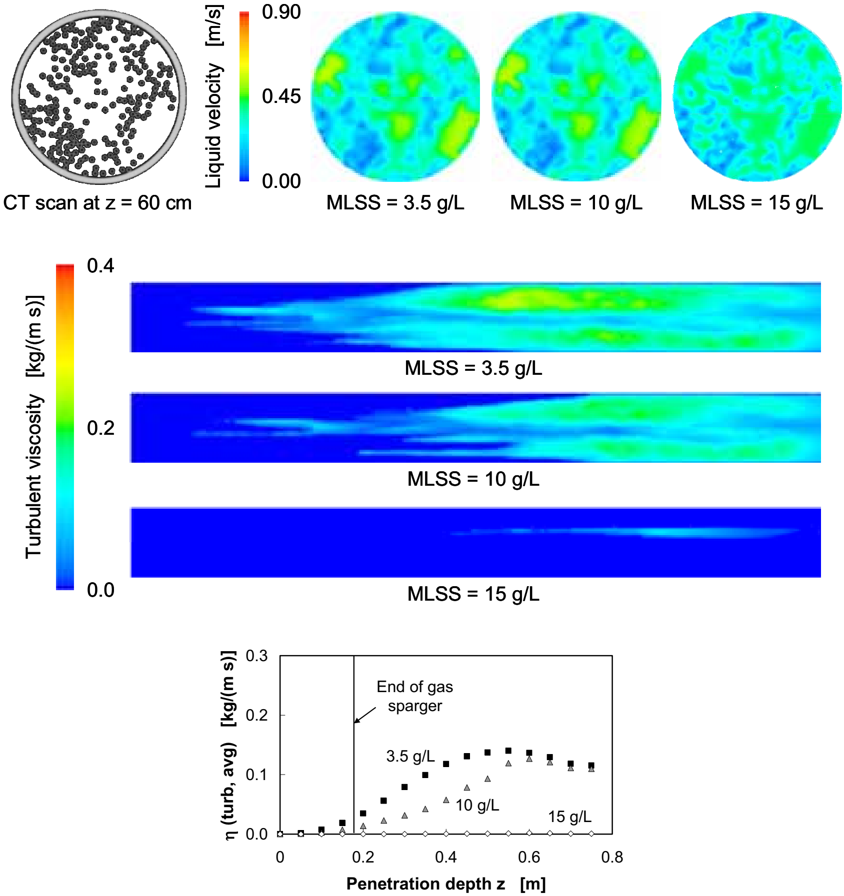

Figure (5.28) Single-phase CFD results: Contours of liquid velocity at z = 60 cm (top), contours of turbulent viscosity in z-direction (centre) and area-weighted average of turbulent viscosity as a function of penetration depth z (bottom) for three different MLSS concentrations and v_{inlet} = 0.3 m/s.

(5.4.3) Initial results of multi-phase simulations

The addition of a gas phase to a liquid flow without affecting the average liquid velocity increases the shear stress at the membrane surface [Ducom *et al.*, 2002; Drews *et al.*, 2008]. Therefore, gas-liquid flows are commonly applied in MBR processes to enhance the filtration performance [Cui *et al.*, 2003]. For the multi-phase CFD simulations, a Taylor bubble flow was created in the inlet channel to allow for a realistic shape and rise velocity of the bubble prior to its penetration into the porous medium. In **Figure (5.29)**, the resulting phase distribution and velocity vectors of the mixture are shown for $v_{inlet} = 0.3$ m/s and MLSS = 10 g/L. A typical Taylor bubble with a round nose and a flat tail was formed [Taha and Cui, 2002]. Velocity vectors in different heights of the bubble are indicating that the transition from upward to downward flow and the acceleration of the falling liquid film towards the bubble tail are represented properly in the simulation. This is observable by a more pronounced downward flow in the outermost part of the cross-sectional vector field with a greater distance from the bubble nose. Please note that the friction at the inner wall of the tubular housing was neglected to allow for a better approximation of the full-scale module, which leads to non-zero velocities at the tube wall.

More detailed insights into the two-phase flow pattern such as velocity vectors and a turbulent viscosity contour in the main direction of flow are presented in **Figure (5.30)**. The velocity in the bubble is higher than in the surrounding liquid, which is due to significant differences in dynamic viscosities of the two phases. The liquid film is falling with a velocity in the range of 0.2 to 0.55 m/s depending on the vertical position relative to the bubble, which is consistent with previous studies [Clarke and Issa, 1997; Nogueira *et al.*, 2006]. The bubble rises with a velocity of approximately 0.5 to 0.55 m/s, as compared to a model estimation of about 1 m/s [Ratkovich *et al.*, 2009]. This deviation may be due to significant differences in dynamic viscosity of the continuous phase, which affects the bubble rise velocity [Drews *et al.*, 2008]. The wake region behind the bubble is observable in the turbulent viscosity contour. Its length equals the tube diameter multiplied by a factor of 1.3, as compared to a factor of 2 as reported by Hout *et al.* [2002]. The wake region originates from the circular wall jet penetrating into the liquid behind the bubble [Nakoryacov *et al.*, 1989; Taha and Cui, 2002] and causes the formation of vortices, which are visible in the vector field. A second region of higher turbulence was occurring close to the bubble nose where the liquid film is formed. This turbulence is presumably a consequence of the transition from upward to downward flow.

It is important to note that the quality of the mesh is not sufficiently high to allow for a proper resolution of velocity gradients in the liquid film. However, a grid refinement to account for steep gradients in the boundary layer was deemed to be inappropriate, since bubble deformation in the fibre bundle rather than the initial Taylor bubble flow are the focus of this study. Nevertheless, the slug flow pattern is in acceptable agreement with previous findings, so that a well-defined Taylor bubble flow approaches the porous medium.

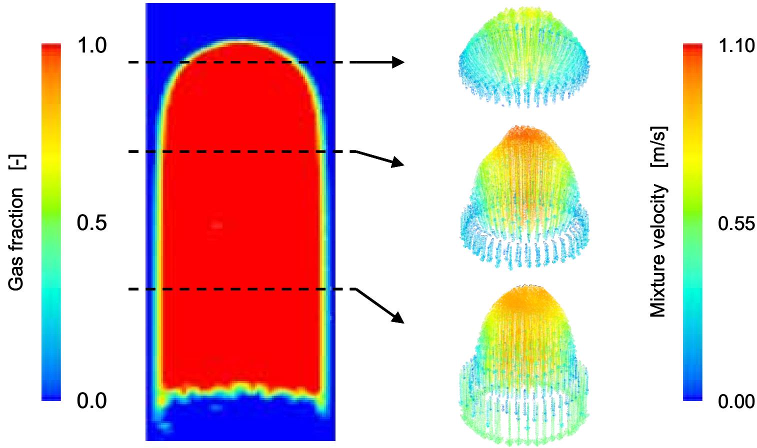

Figure (5.29) Multi-phase CFD results: Contour of the gas fraction (left) and velocity vectors (right) in the inlet channel for v_{inlet} = 0.3 m/s and MLSS = 10 g/L.

The penetration of a bubble into the heterogeneous porous medium is shown as the phase distribution and the corresponding mixture velocity in **Figure (5.31)**. The deformation of the bubble is significantly affected by module design features such as the air sparger and the local fibre arrangement. This means that the flow avoids areas of higher friction by the formation of bypass jets where the resistance is lower. For this reason, higher gas fractions and mixture velocities are expected in flow channels without fibres as compared to the fibre segments.

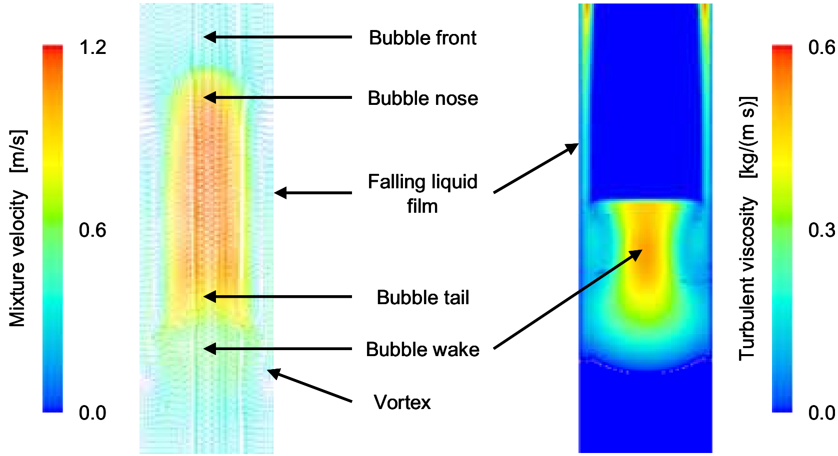

Figure (5.30) Multi-phase CFD results: Velocity vectors (left) and contour of the turbulent viscosity (right) in the inlet channel for v_{inlet} = 0.3 m/s and MLSS = 10 g/L.

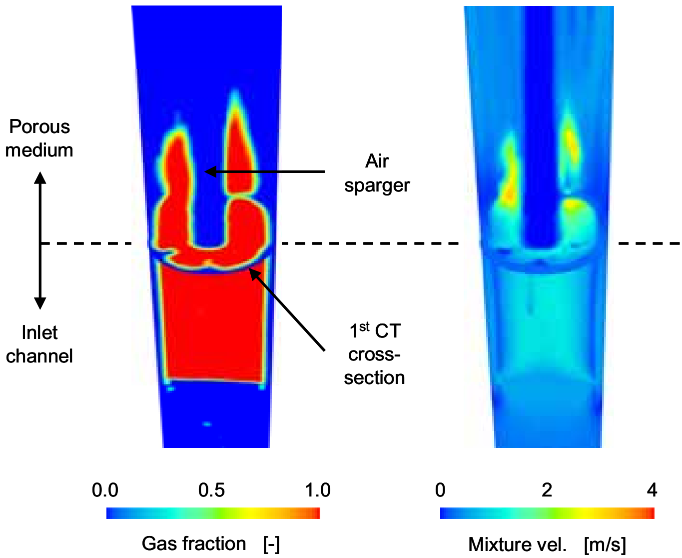

Figure (5.31) Multi-phase CFD results: Contour of the gas fraction (left) and mixture velocity contour (right) for a bubble penetrating into the porous medium for v_{inlet} = 0.3 m/s and MLSS = 10 g/L.

The passage of the bubble through the first CT cross-section at z = 0 cm is illustrated in **Figure (5.32)** as the phase distribution and the mixture velocity for different points in time. The results are indicating that the flow preferentially bypasses fibre segments. Star-shaped areas of higher mixture velocity according to the flow channel locations are observable when the bubble nose touches the porous medium (t*). This flow channelling is less pronounced as the penetration depth of the bubble increases, so that high mixture velocities are observable in parts of the fibre segments as well. The phase distribution contours in this cross-section do not provide evidence for a bubble breakup. Nevertheless, a complex non-circular bubble shape due to the flow channel confinement was predicted by the simulation.

Additional results of multi-phase CFD simulations using the heterogeneous porous medium approach are published elsewhere [Tollkötter, 2010]. These studies are focussing on the rise of the bubble through the porous medium and the impact of non-regular fibre arrangement on the multi-phase flow pattern. However, proper pressure loss correlations for the gas phase flow and for multi-phase flows of different gas fraction as well as a more comprehensive validation of these numerical correlations are still lacking. Extremely long simulation times make a mesh refinement study for multi-phase simulations and a comparison of different module configurations rather difficult. Therefore, a further optimisation of the overall CFD approach is desirable before drawing general conclusions. The discussion of initial CFD results is thus restricted to a proof of principle in the thesis at hand.

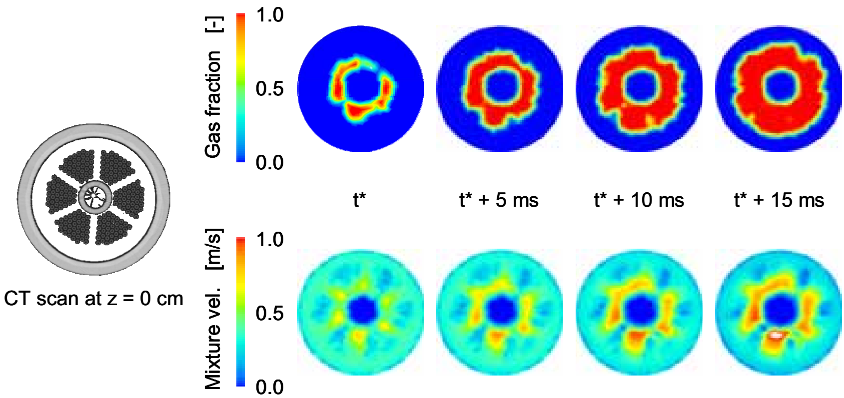

Figure (5.32) Multi-phase CFD results: Contours of the gas fraction (top) and velocity (bottom) in a cross-section at z = 0 cm as a function of time for v_{inlet} = 0.3 m/s and MLSS = 10 g/L.

(5.4.4) Concluding remarks

Single-phase CFD simulations of water with raised viscosity have shown that the design features of the hollow-fibre bundle are represented properly by the heterogeneous porous medium. Bypass jets and low-flow areas were identified and successfully correlated to deviations in turbulence properties of the flow pattern. An increase in superficial inlet velocity or a decrease in MLSS concentration causes an increase in turbulent viscosity. A critical Re number of 1000 as observed by the first CFD model was confirmed by the second CFD approach by the onset of turbulence for higher Re numbers.

Initial multi-phase CFD simulations have been conducted as a proof of principle. These studies have shown that well-defined slug flow conditions are occurring during the first simulation step. The bubble shape, the velocity of the falling film and the length of the bubble wake were found to be in acceptable agreement with previous findings. The penetration of the bubble into the porous medium causes the formation of bypass jets, with higher mixture velocities where fibres are absent. However, time constraints and limitations in available computer capacity make a further simplification of the multi-phase simulation appropriate. Potentials for a further optimisation are (i) a more comprehensive validation of pressure loss correlations for model calibration, (ii) the choice of numerical models which are computationally less demanding and (iii) a coarser spatial discretisation as far as possible.

(6) **Discussion**

Phenomena governing the microfiltration performance were investigated by applying the methodology introduced in section (4). The corresponding outcomes are presented in detail in section (5). This chapter aims at (i) summarising the most relevant findings, (ii) drawing general conclusions by directly comparing results gained at different scales and (iii) outlining potentials and limitations for future studies.

(6.1) **Summary**

Table (6.1) gives an overview of the impact of operating conditions and feed characteristics on various process parameters with reference to previous studies. On a **micro-scale**, it was found that the distribution of local cumulative permeate flux varies as a function of setpoint permeate flux and vertical position y. This was observed for a filtration of pure water without particles and indicates the significance of lumen-side pressure loss on the filtration performance. For a submerged filtration of model suspensions containing colloidal silica, the formation of heterogeneous cakes of greater thickness close to the permeate extraction were observed. The cake growth rate was found to increase as the permeate flux or the solids concentration increases. The cake removal efficiency due to air bubbling was enhanced with an increase in aeration pressure or duration of aeration. The micro-scale visualisation of the filtration process was in good agreement with an integral monitoring of TMP evolution. These results are indicating that a gravity-driven and/or diffusive back-transport of deposited particles (see also Sethi and Wiesner [1997]) gains more relevance as the cake thickness increases. Cake compaction may occur as the cake layer grows, leading to an increase in solid compressive pressure [Lu and Hwang, 1995; Hwang and Liu, 2002] and in some cases cake collapse [Tarabara *et al.*, 2004]. However, distinguishing between cake compaction effects, a delayed cake growth in some parts of the membrane and a reduced growth rate for cakes forming on curved surfaces was unfeasible with the current NMR approach. Previous NMR studies conducted by Airey *et al.* [1998] were focussing on the determination of maximum cake thickness for an inside-out filtration of colloidal silica in cross-flow mode at constant TMP. The NMR investigations presented in the thesis at hand are a follow-up of these earlier studies. They are the first attempt to quantitatively measure transient and heterogeneous cake growth patterns in submerged mode as a function of setpoint permeate flux, solids concentration and aeration conditions.

An integral monitoring of the filtration performance on a **meso-scale** was conducted in both cross-flow (TMP = const) and submerged mode (J = const). For a filtration at constant TMP, the time to reach steady-state conditions was represented by the permeate mass collected during the transient filtration stage. This characteristic mass was found to increase as the TMP increases, the cross-flow velocity increases or the solids concentration decreases. Moreover, the steady-state filtration resistance was increasing with increasing TMP, increasing cross-flow velocity or increasing solids concentration. The TMP-dependence of the steady-state filtration resistance suggests that the limiting flux [Song, 1998] was not reached under the experimental conditions investigated. A selective particle deposition [Fischer and Raasch, 1984], an extended pore blocking stage [Song, 1998] and/or an infiltration of small particles [Melin and Rautenbach, 2007] may occur, since an increase in cross-flow velocity was followed by a rise in filtration resistance. This unexpected observation is consistent with previous findings [Lu and Hwang, 1995; Hwang and Liu, 2002; Drews *et al.*, 2010], but was in the range of the measurement inaccuracy. A comparison with well-known blocking filtration laws [Hermia, 1982] indicates a successive or simultaneous coexistence of phenomena rather than the existence of a single pore blocking mechanism [Wessling, 2001].

Single fibre filtration tests at constant permeate flux have shown that the fouling rate dTMP/dt increases as the setpoint permeate flux increases and the solids concentration increases. A decrease in fouling rate was observable for higher net aeration rates and a more pronounced fibre movement. The critical aeration rate appeared to be independent of variations in fibre movement or packing density. Interestingly, a benefit of increasing the aeration frequency for the same net aeration rate and an optimum gross aeration rate were observed. The latter trends indicate potentials for further process optimisation, see section (6.2). The bubble-induced fibre movement was tracked following the methodology introduced by Wicaksana *et al.* [2006]. The intensity of fibre motion was expressed as a time- and length-averaged angular fibre velocity and was found to increase with increasing aeration rate. This may lead to more pronounced lateral surface shear and a more efficient cake removal. Furthermore, the fibre movement intensity was insensitive to packing density variations. This finding suggests that more pronounced fibre-fibre interactions at higher packing densities do not affect the movement of the fibre in the range of packing density investigated (bundles consisting of 1 to 4 hollow-fibres). However, Bérubé and co-workers attributed the enhancement in filtration performance to fibre collisions rather than an increase in surface shear [Bérubé and Lei, 2006; Bérubé *et al.*, 2006; Chan *et al.*, 2007]. According to the latter results, cake removal is expected to be enhanced by more pronounced physical fibre-fibre contacts at higher packing densities, which is complementary to the effect of lateral surface shear. In conclusion, the interrelationship between fibre movement or fibre-fibre interactions and the overall filtration performance is not fully understood at this stage.

Single bundle filtration tests on a **macro-scale** were conducted in both quasi-submerged (J = const) and cross-flow mode (J = const). These investigations have consistently shown that an increase in permeate flux, an increase in solids concentration and a decrease in aeration rate are followed by an increase in fouling rate dTMP/dt. The critical flux according to its weak form [Le-Clech *et al.*, 2003] increases with a decrease in solids concentration or an increase in aeration rate. Moreover, the critical aeration rate was increasing at higher solids concentrations. Similar to the submerged single fibre filtration, an increase in aeration frequency at constant net aeration rate causes the fouling rate or the critical aeration rate to decrease. The critical flux was not affected by variations in aeration frequency. This allows postulating that a reduction of net aeration rate does not negatively affect the filtration performance if the aeration frequency is adjusted accordingly. In addition, a circulating background flow as observed in full-scale membrane units [Drews *et al.*, 2008; Prieske *et al.*, 2008] was found to reduce the TMP rise and to improve the overall filtration performance.

Complementary CFD simulations were performed to qualitatively evaluate the impact of operating parameters on the flow through single hollow-fibre bundles. The CFD model is based on a heterogeneous porous medium approach. The properties of the porous medium were calibrated by own CT scans and pressure loss correlations. This methodology allows evaluating the impact of irregular fibre arrangement on the multi-phase flow pattern, which was not investigated in previous CFD studies in the field of MBRs, see section (3.4). Single-phase simulations have shown that the distribution of cross-flow velocity and turbulent viscosity highly depend on the local fibre arrangement, the superficial inlet velocity and the MLSS concentration. In regions of higher local porosity, the local velocity is higher and the turbulent viscosity lower. An increase in superficial inlet velocity or a decrease in MLSS concentration causes an increase in turbulent viscosity. Interestingly, bypass streams were found to reduce the average turbulent viscosity in the corresponding cross-section of the hollow-fibre bundle. Initial multi-phase simulations have shown that a proper Taylor bubble flow is developed before the bubble enters the porous medium. Higher mixture velocities were observed in flow channels compared to fibre segments when the bubble penetrates into the porous medium. These very first multi-phase simulations serve as a proof of principle. A comparison of bundles of different size, packing density or fibre arrangement is envisaged for future studies.

Scale of investigations	**Parameter**	**Trend**	**Mode of operation**	**Previous studies**
Micro-scale	Maximum permeate velocity	$v_{max}\uparrow$ with $J\uparrow$ and $y\downarrow$	Submerged, J = const, single fibre	[Pangrle *et al.* , 1992]
	Local cumulative permeate flux	$J_{cum}\uparrow$ with $J_{avg}\uparrow$ and $y\downarrow$	Submerged, J = const, single fibre	[Hardy *et al.* , 2002]
	Local cake thickness	Thicker cakes at y = 0 cm	Submerged, J = const, single fibre	No previous NMR results for submerged microfiltration.
	Cake growth rate	Growth rate $\uparrow$ with $J\uparrow$ and $c_{SiO2}\uparrow$	Submerged, J = const, single fibre	No previous NMR results for submerged microfiltration.
	Cake removal efficiency	Efficiency $\uparrow$ with $dV_{air,gross}/dt\uparrow$	Submerged, J = const, single fibre	No previous NMR results for submerged microfiltration.
Meso-scale	Time to reach steady-state	$m_{P,ss}\uparrow$ with $TMP\uparrow$, $v_{CF}\uparrow$ and $c_{SiO2}\downarrow$	Cross-flow, TMP = const, single fibre	[Belfort *et al.* , 1994; Hong *et al.* , 1997; Wang and Song, 1999; Zhang and Song, 2000]
	Final filtration resistance	$R_{tot,fin}\uparrow$ with $TMP\uparrow$, $v_{CF}\uparrow$ and $c_{SiO2}\uparrow$	Cross-flow, TMP = const, single fibre	[Belfort *et al.* , 1994; Wang and Song, 1999; Zhang and Song, 2000]
	Fouling rate	$dTMP/dt\uparrow$ with $J\uparrow$, $c_{SiO2}\uparrow$, $dV_{air,net}/dt\downarrow$, $f_{cyc}\downarrow$ and fibre motion$\downarrow$	Submerged, J = const, single fibre	[Cui *et al.* , 2003; Le-Clech *et al.* , 2006; Wicaksana *et al.* , 2006; Drews, 2010]

Meso-scale	Critical aeration rate	$(dV_{air,net}/dt)_{crit} \neq f$ (fibre motion, N_{HF})	Submerged, J = const, single fibre	[Ueda *et al.*, 1997; Cui *et al.*, 2003]
	Fibre movement	Fibre motion $\uparrow$ with $dV_{air,net}/dt \uparrow$	Submerged, J = const, single fibre	[Wicaksana *et al.*, 2006]
Macro-scale	Fouling rate	$dTMP/dt \uparrow$ with $J \uparrow$, $c_{SiO2} \uparrow$, $SAD_m \downarrow$ and $f_{cyc} \downarrow$	Submerged, J = const, single bundle	[Cui *et al.*, 2003; Le-Clech *et al.*, 2006; Drews, 2010]
	Critical flux	$J_{crit} \uparrow$ with $c_{SiO2} \downarrow$ and $SAD_m \uparrow$ [Blach, 2009] $J_{crit} \neq f(f_{cyc})$	Submerged, J = const, single bundle	[Bacchin *et al.*, 2006; Le-Clech *et al.*, 2006; Drews, 2010]
	Critical aeration rate	$SAD_{m,crit} \uparrow$ with $c_{SiO2} \uparrow$ and $f_{cyc} \downarrow$	Submerged, J = const, single bundle	[Ueda *et al.*, 1997; Cui *et al.*, 2003]
	(Superposed) Cross-flow	$dTMP/dt \uparrow$ with $v_{CF} \downarrow$	(Superposed) Cross-flow, J = const, single bundle	[Drews *et al.*, 2008; Prieske *et al.*, 2008]
	Local cross-flow velocity	$v_{CF} \uparrow$ with $N_{HF} \downarrow$, $v_{inlet} \uparrow$ and MLSS $\downarrow$	Single-phase CFD simulation, single bundle	No previous CFD studies based on statistic fibre arrangement.
	Turbulent viscosity	$\eta_{turb,local} \uparrow$ with $N_{HF} \uparrow$, $v_{inlet} \uparrow$ and MLSS $\downarrow$ Bypass jet $\Rightarrow \eta_{turb,avg} \downarrow$	Single-phase CFD simulation, single bundle	No previous CFD studies based on statistic fibre arrangement.
	Mixture velocity	$v_{mix} \uparrow$ with $N_{HF} \downarrow$	Multi-phase CFD simulation, single bundle	No previous CFD studies based on statistic fibre arrangement.

Table (6.1) Overview of the most relevant outcomes.

(6.2) General conclusions and recommendations

The impact of setpoint permeate flux, solids concentration, cross-flow velocity and net aeration rate on the fouling rate was discussed in section (5) based on enhancement factors. These enhancement factors are plotted as a function of the above-mentioned process parameters in **Figure (6.1)** to allow for a direct comparison of trends observed at different scales. As claimed in section (8.1), an estimation of enhancement factors aims at characterising the (non-)proportionality of the interrelationship between two different parameters if only few data points are available.

It is obvious that none of the relationships presented in **Figure (6.1)** shows a plateau with enhancement factors of one. This indicates the non-proportional character of the functions

$$\frac{dTMP}{dt} = f(J), \tag{6.1}$$

$$\frac{dTMP}{dt} = f\left(c_{SiO_2}\right), \tag{6.2}$$

$$\frac{dR_{tot}}{dm_P} = f\left(v_{CF}\right) \quad \text{and} \tag{6.3}$$

$$\frac{dTMP}{dt} = f\left(\dot{V}_{air,net}\right). \tag{6.4}$$

In general, an increase in permeate flux or solids concentration is followed by increasing slopes of the functions (6.1) to (6.4) and an increase in enhancement factor. The single fibre NMR studies without aeration have shown that this impact is less pronounced in the range of higher permeate fluxes and higher solids concentrations. In contrast, disproportionate relationships were observed for both single fibre and single bundle filtration tests with aeration. An increase in cross-flow velocity or net aeration rate leads to decreasing slopes of the corresponding fouling rate curves for both single fibre and single bundle filtration tests.

In addition, larger deviations from proportionality are occurring for the single bundle compared to the single fibre filtration tests. This is characterised by standard deviations of all enhancement factors for the single bundle tests which are up to 3.5 times larger than those for the single fibre tests. Moreover, more pronounced deviations from proportionality were observed for a single fibre filtration with intermittent aeration compared to an operation without aeration, with ratios of standard deviations of up to 1.9. These trends suggest that the functions (6.1) to (6.4) show a less pronounced proportionality for larger membrane units and complex multi-phase flows compared to a single fibre cross-flow filtration.

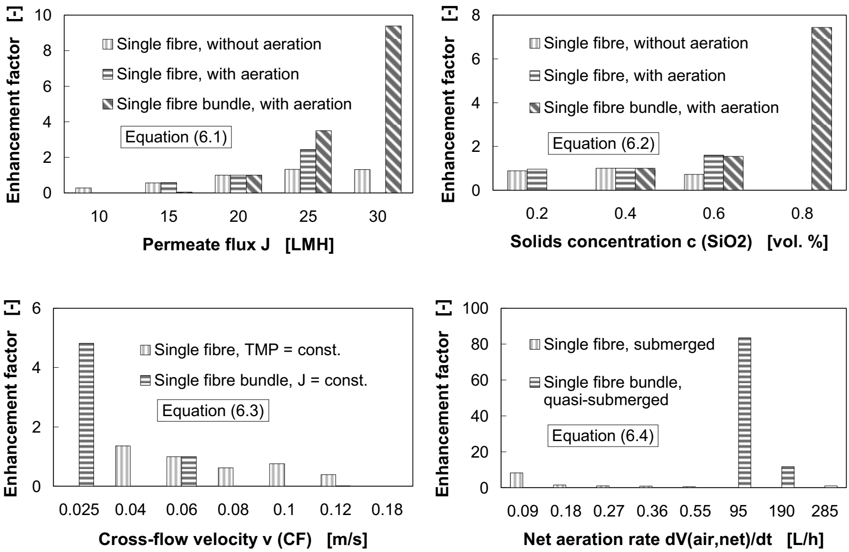

Figure (6.1) Comparison of scales: Impact of permeate flux (top-left), solids concentration (top-right), cross-flow velocity (bottom-left) and net aeration rate (bottom-right) on the enhancement in filtration performance according to equations (6.1) to (6.4) for both single fibre and single fibre bundle filtration tests.

When comparing standard deviations of enhancement factors, the impact of permeate flux appears to be more significant than that of the solids concentration. This is presumably due to higher driving forces and a higher affinity to cake compaction for an operation at imposed flux. The current results do not provide evidence whether cake layer removal due to aeration is more effective than a pump-induced cross-flow, since the total liquid velocity in axial direction was not the same for both modes of operation.

From these findings, the following general conclusions can be drawn.

- The transferability of outcomes gained in lab-scale filtration experiments to industrial-scale processes is limited since the governing phenomena are significantly different. Therefore, conducting a limited number of pilot-scale experiments to complement lab-scale studies is essential for an optimisation of industrial membrane processes.

- The packing density affects the overall process performance in different ways. In general, an increase in packing density is followed by a constriction of the feed channel. This leads to a higher risk of module blocking and higher pressure losses [Melin and Rautenbach, 2007], but also to an acceleration of flow and increased shear forces [Ueda *et al.*, 1997]. Furthermore, a higher packing density causes more pronounced deviations in bulk concentration (dewatering effect). Complex phenomena such as permeate competition of individual fibres [Yeo *et al.*, 2006] and fibre-fibre interactions [Bérubé *et al.*, 2006] gain more relevance. Therefore, membrane module development can be regarded as a trade-off between an economic module design (high packing densities, low foot prints) and a module design closer to lab-scale conditions (fibre in a bundle behaves like single fibre). The optimal packing density is the highest density for which the filtration performance is not governed by module blocking, pressure losses, dewatering effects and an inhibited fibre motion.

- The particle deposition rate is affected by the setpoint permeate flux and the solids concentration. The impact of variations in permeate flux appears to be more significant than the impact of variations in solids concentration. Hence, a low-flux operation at higher solids concentration is advantageous compared to a high-flux operation at lower solids concentration. Even for similar particle deposition rates under both operating conditions, the affinity to cake compaction is expected to be lower if the permeate flux is sufficiently low.

(6.3) Potentials and limitations for future studies

Moving forward, hydrodynamics of microfiltration processes will be further investigated according to this experimental and numerical multi-scale approach. For this purpose, the following potentials and limitations were identified.

- **NMR imaging** will be applied to pursue the non-invasive visualisation of the microfiltration process. In general, the NMR results presented in the thesis at hand are consistent with an integral monitoring of the filtration performance or simple modelling approaches and are thus interpreted as a proof of principle. For future studies, a novel pulse sequence will be used to capture permeation and cake formation simultaneously with sufficient time and spatial resolution. Moreover, processing variations in NMR signal intensity may allow determining variations in particle concentration in the cake layer. This would provide an appropriate measure for cake compaction phenomena. The overall objective of upcoming research activities will be a fundamental understanding of the self-accelerating character of a submerged microfiltration at imposed flux [Zhang *et al.*, 2006]. Major drawbacks for these studies may be unavoidable fluctuations in the NMR signal intensity, which make an automated image processing more difficult.

- All upcoming **integral filtration experiments** using single fibres or single bundles will focus on evaluating potentials for optimising the aeration sequence. A higher aeration frequency, an optimal gross aeration rate and an appropriate fibre movement were found to be the most promising strategies to meet this challenge. Efforts will be made to further improve the methodology for estimating the intensity of bubble-induced fibre movement, which will be subsequently correlated with the overall filtration performance. In addition to the direct observation technique introduced above, Yeo *et al.* [2007] have proven that particle image velocimetry (PIV) is a powerful tool to monitor the flow field in the vicinity of a single moving fibre. However, an observation of fibre-fibre interactions using PIV remains challenging.

- Membrane fouling due to the adsorption of matter was observed as a creeping increase in TMP for a filtration under subcritical conditions. Phenomena such as pore blocking, selective particle deposition or cake compaction were likely occurring, but were not directly detectable with the applied techniques. Interestingly, these results are contradictory to characterisation experiments, indicating that repulsive rather than attractive particle-particle and particle-membrane interactions are expected. The investigations suggest that deposition-enhancing forces weaken as the cake thickness increases. This was leading to an enhanced removal of deposited particles by gravity and/or diffusion, which was recently evaluated in collaboration with the University of Twente (Enschede, The Netherlands) [Çulfaz *et al.*, 2010]. The cake formation was heterogeneous and was influenced by the permeate flux, the solids concentration, the cross-flow velocity and aeration conditions. Therefore, the **silica suspensions** used have shown similar filtration properties compared to activated sludge as reported in literature [Le-Clech *et al.*, 2006; Drews, 2010]. Nevertheless, the silica particles are relatively small and rigid, so that the cake properties significantly differ from deposited biomass in MBR processes. Moreover, typical foulants such as extracellular polymeric substances (EPS) are not represented by the model substance. Using a biological model suspension to account for the above drawbacks would make the transferability of outcomes to full-scale MBR processes easier, but may lead to a worse reproducibility of results. In addition, the need for a high cake-to-bulk image contrast for the NMR measurements further limits the range of applicable model suspensions. However, integral filtration experiments using activated sludge or supernatant (i.e. sludge clarified by sedimentation [Judd, 2006]) will be conducted in future studies to evaluate the transferability to pilot-scale MBR units.

- The **CFD approach** will be further optimised to compare prototype hollow-fibre bundles of different size, packing density and fibre arrangement. This optimisation may include (i) a better approximation of pressure loss correlations for model calibration and (ii) efforts to reduce computational demands of the simulation. An improved model calibration will be based on pressure loss correlations taking the gas fraction of the multi-phase flow into account. For this purpose, a number of additional pressure loss simulations and measurements for both single- and multi-phase flows will be performed. A validation of potential CFD outcomes such as the gas-liquid phase distribution and the bubble-induced turbulence is still lacking. Thus, the upcoming studies will be restricted to a qualitative comparison of bundle configurations. Furthermore, attempts will be made to account for permeate extraction or dewatering effects. Bubble-induced fibre motion could be implemented by empirical models based on the direct observation of fibre movement or by coupling fluid flow and transient fibre displacement. Nevertheless, it is important to note that these model extensions will further increase computational demands and make the overall CFD approach less attractive.

(7) References

[1] Agranovski I.E., Braddock R.D., Crozier S., Whittaker A., Minty S., Myojo T. (2003). Study of Wet Porous Filtration. In: *Separation and Purification Technology*, 30 (2003) 129-137.

[2] Aimar P., Meireles M., Sanchez V. (1990). A Contribution to the Translation of Rejection Curves into Pore Size Distributions for Sieving Membranes. In: *Journal of Membrane Science*, 54(3) (1990) 321-338.

[3] Airey D., Yao S., Wu J., Chen V., Fane A.G., Pope J.M. (1998). An Investigation of Concentration Polarization Phenomena in Membrane Filtration of Colloidal Silica Suspensions by NMR Micro-Imaging. In: *Journal of Membrane Science*, 145 (1998) 145-158.

[4] Altena F.W., Belfort G. (1984). Lateral Migration of Spherical Particles in Porous Flow Channels: Application to Membrane Filtration. In: *Chemical Engineering Science*, 39 (1984) 343-355.

[5] ANSYS (2009). *ANSYS FLUENT 12.0 – Theory Guide*. ANSYS Inc., April 2009.

[6] Bacchin P., Aimar P., Sanchez V. (1995). Model for Colloidal Fouling of Membranes. In: *AIChE Journal*, 41(2) (1995) 368-376.

[7] Bacchin P., Si-Hassen D., Starov V., Clifton M.J., Aimar P. (2002). A Unifying Model for Concentration Polarization, Gel-Layer Formation and Particle Deposition in Cross-Flow Membrane Filtration of Colloidal Suspensions. In: *Chemical Engineering Science*, 57 (2002) 77-91.

[8] Bacchin P. (2004). A Possible Link Between Critical and Limiting Flux for Colloidal Systems: Consideration of Critical Deposit Formation Along a Membrane. In: *Journal of Membrane Science*, 228 (2004) 237-241.

[9] Bacchin P., Aimar P., Field R.W. (2006). Critical and Sustainable Fluxes: Theory, Experiments and Applications. In: *Journal of Membrane Science*, 281 (2006) 42-69.

[10] Battistoni P. (1997). Pre-Treatment, Measurement Execution Procedure and Waste Characteristics in the Rheology of Sewage Sludges and the Digested Organic Fraction of Municipal Solid Wastes. In: *Water Science and Technology*, 36(11) (1997) 33-41.

[11] Belfort G., Davis R.H., Zydney A.L. (1994). The Behaviour of Suspensions and Macromolecular Solutions in Crossflow Microfiltration. In: *Journal of Membrane Science*, 96(1-2) (1994) 1-58.

[12] Bérubé P.R., Lei E. (2006). The Effect of Hydrodynamic Conditions and System Configurations on the Permeate Flux in a Submerged Hollow Fiber Membrane System. In: *Journal of Membrane Science*, 271 (2006) 29-37.

[13] Bérubé P.R., Afonso G., Taghipour F., Chan C.C.V. (2006). Quantifying the Shear at the Surface of Submerged Hollow Fiber Membranes. In: *Journal of Membrane Science*, 279 (2006) 495-505.

[14] Blach T. (2009). *Untersuchung des Filtrationsverhaltens eines getauchten Hohlfasermembranmoduls zur Abtrennung von Feststoffen aus wässrigen Suspensionen*. Diploma Thesis, Chemical Process Engineering (AVT.CVT), RWTH Aachen University, Germany, December 2009.

[15] Blatt W.F., Dravid A., Michaels A.S., Nelsen L. (1970). Solute Polarization and Cake Formation in Membrane Ultrafiltration: Causes, Consequences, and Control Techniques. In: Flinn J.E. (Ed.), *Membrane Science and Technology*, Plenum Press, New York, 1970.

[16] Blümich, B. (2000). NMR Imaging of Materials. In: *Monographs on the Physics and Chemistry of Materials*, 57, Clarendon Press, Oxford, 2000.

[17] Braeken L., Bettens B., Boussu K., Van der Meeren P., Cocquyt J., Vermant J., Van der Bruggen B. (2006). Transport Mechanisms of Dissolved Organic Compounds in Aqueous Solution during Nanofiltration. In: *Journal of Membrane Science*, 279 (2006) 311-319.

[18] Brannock M.W.D., De Wever H., Wang Y., Leslie G. (2009). Computational Fluid Dynamics Simulations of MBRs: Inside Submerged versus Outside Submerged Membranes. In: *Desalination*, 236 (2009) 244-251.

[19] Brannock M., Leslie G., Wang Y., Buetehorn S. (2010a). Optimising Mixing and Nutrient Removal in Membrane Bioreactors: CFD Modelling and Experimental Validation. In: *Desalination*, 250 (2010) 815-818.

[20] Brannock M., Wang Y., Leslie G. (2010b). Mixing Characterisation of Full-Scale Membrane Bioreactors: CFD Modelling with Experimental Validation. In: *Water Research*, 44 (2010) 3181-3191.

[21] Breisig H.F. (2010). *Modeling the Geometry of a Submerged Hollow-Fiber Membrane Module in FLUENT®*. Mini Thesis, Chemical Process Engineering (AVT.CVT), RWTH Aachen University, Germany, February 2010.

[22] Brian P.L.T. (1965). Concentration Polarization in Reverse Osmosis Desalination with Variable Flux and Incomplete Salt Rejection. In: *Industrial and Engineering Chemistry Fundamentals*, 4 (1965) 439-445.

[23] Buetehorn S. (2005). *Modellieren des anisotropen Druckverlustes in strukturierten Packungen*. Diploma Thesis, Institute for Multiphase Processes (IMP), Leibniz University of Hannover (LUH), Germany, September 2009.

[24] Buetehorn S., Koh C.N., Wintgens T., Melin T., Volmering D., Vossenkaul K. (2007a). Investigating the Impact of Membrane Pore Size Distribution on the Performance in Activated Sludge Filtration and the Susceptibility to Fouling. In: *Proceedings of the 11th Aachener Membran Kolloqium (AMK)*, Aachen, Germany, March 28-29, 2007.

[25] Buetehorn S., Schulz W., Lyko S., Wintgens T., Melin T., Volmering D., Voßenkaul K. (2007b). Comparative Long-Term Activated Sludge Filtration in Submerged Mode using Polyether Sulphone (PES) Hollow-Fibre Membranes. In: *Proceedings of the 7th Aachener Tagung Wasser und Membranen (AWM)*, Aachen, Germany, October 30-31, 2007.

[26] Buetehorn S., Koh C.N., Wintgens T., Volmering D., Vossenkaul K., Melin T. (2008). Investigating the Impact of Production Conditions on Membrane Properties for MBR Applications. In: *Desalination*, 231 (2008) 191-199.

[27] Buetehorn S., Brannock M., Le-Clech P., Leslie G., Volmering D., Vossenkaul K., Wintgens T., Melin T. (2009). Observation of Cake Layer Formation and Removal on Microporous Hollow-Fibre Membranes. In: *Desalination and Water Treatment*, 9 (2009) 82-85.

[28] Buetehorn S., Carstensen F., Wintgens T., Melin T., Volmering D., Vossenkaul K. (2010). Permeate Flux Decline in Cross-Flow Microfiltration at Constant Pressure. In: *Desalination*, 250 (2010) 985-990.

[29] Buetehorn S., Utiu L., Küppers M., Blümich B., Wintgens T., Wessling M., Melin T. (2011). NMR Imaging of Local Cumulative Permeate Flux and Local Cake Growth in Submerged Microfiltration Processes. In: *Journal of Membrane Science*, 371 (2011) 52-64.

[30] Busch J., Cruse A., Marquardt W. (2007). Modeling Submerged Hollow-Fiber Membrane Filtration for Wastewater Treatment. In: *Journal of Membrane Science*, 288 (2007) 94-111.

[31] Buwa V.V., Ranade V.V. (2002). Dynamics of Gas-Liquid Flow in a Rectangular Bubble Column: Experiments and Single/Multi-Group CFD Simulations. In: *Chemical Engineering Science*, 57 (2002) 4715-4736.

[32] Cabassud C., Laborie S., Durand-Bourlier L., Lainé J.M. (2001). Air Sparging in Ultrafiltration Hollow Fibers: Relationship between Flux Enhancement, Cake

Characteristics and Hydrodynamic Parameters. In: *Journal of Membrane Science*, 181(1) (2001) 57-69.

[33] Callaghan P.T. (1991). *Principles of Nuclear Magnetic Resonance Microscopy*. Oxford Clarendon Press, Oxford, 1991.

[34] Camacho Ramos M. (2009). *Characterisation of Model Fluids used for Hydrodynamic Investigations in MBRs*. Final report of the MBR-Train Project, MEST-CT-2005-021050, Aachen, Germany, December 2009.

[35] Campos J.B.L.M., Guede de Carvalho J.R.F. (1988). An Experimental Study of the Wake of Gas Slugs Rising in Liquids. In: *Journal of Fluid Mechanics*, 196 (1988) 27-37.

[36] Caprihan A., Fukushima E. (1990). Flow Measurements by NMR. In: *Physics Reports - Review Section of Physics Letters*, 198(4) (1990) 195-235.

[37] Carroll T. (2001). The Effect of Cake and Fibre Properties on Flux Declines in Hollow-Fibre Microfiltration Membranes. In: *Journal of Membrane Science*, 189 (2001) 167-178.

[38] Chan C.C.V., Bérubé P.R., Hall E.R. (2007). Shear Profiles inside Gas Sparged Submerged Hollow Fiber Membrane Modules. In: *Journal of Membrane Science*, 297 (2007) 104-120.

[39] Chang S., Fane A.G. (2000a). Characteristics of Microfiltration of Suspensions with Inter-Fibre Two-Phase Flow. In: *Journal of Chemical Technology and Biotechnology*, 75 (2000) 533-540.

[40] Chang S., Fane A.G. (2000b). Filtration of Biomass with Axial Inter-Fibre Upward Slug-Flow: Performance and Mechanism. In: *Journal of Membrane Science*, 180(1) (2000) 57-68.

[41] Chang S., Fane A.G. (2001). The Effect of Fibre Diameter on Filtration and Flux Distribution – Relevance to Submerged Hollow Fibre Modules. In: *Journal of Membrane Science*, 184(2) (2001) 221-231.

[42] Chang S., Fane A.G. (2002). Filtration of Biomass with Laboratory-Scale Submerged Hollow Fibre Modules – Effect of Operating Conditions and Module Configuration. In: *Journal of Chemical Technology and Biotechnology*, 77 (2002) 1030-1038.

[43] Chang S., Fane A.G., Vigneswaran S. (2002a). Modeling and Optimizing Submerged Hollow Fiber Membrane Modules. In: *AIChE Journal*, 48(10) (2002) 2203-2212.

[44] Chang S., Fane A.G., Vigneswaran S. (2002b). Experimental Assessment of Filtration of Biomass with Transverse and Axial Fibres. In: *Chemical Engineering Journal*, 87 (2002) 121-127.

[45] Chellam S., Wiesner M.R. (1997). Particle Back-Transport and Permeate Flux Behavior in Crossflow Membrane Filters. In: *Environmental Science and Technology*, 31 (1997) 819-824.

[46] Chen V., Li H., Fane A.G. (2004a). Non-Invasive Observation of Synthetic Membrane Processes – A Review of Methods. In: *Journal of Membrane Science*, 241 (2004) 23-44.

[47] Chen J.C., Li Q., Elimelech M. (2004b). In Situ Monitoring Techniques for Concentration Polarization and Fouling Phenomena in Membrane Filtration. In: *Advances in Colloid and Interface Science*, 107 (2004) 83-108.

[48] Chisti M.Y., Halard B., Moo-Young M. (1988). Liquid Circulation in Airlift Reactors. In: *Chemical Engineering Science*, 43(3) (1988) 451-457.

[49] Cho B.D., Fane A.G. (2002). Fouling Transients in Nominally Sub-Critical Flux Operation of a Membrane Bioreactor. In: *Journal of Membrane Science*, 209 (2002) 391-403.

[50] Chung K.Y., Edelstein W.A., Belfort G. (1993). Dean Vortices with Wall Flux in a Curved Channel Membrane System. 6. Two Dimensional Magnetic Resonance Imaging of the Velocity Field in a Curved Impermeable Slit. In: *Journal of Membrane Science*, 81 (1993) 151-162.

[51] Clarke A., Issa R.I. (1997). A Numerical Model of Slug Flow in Vertical Tubes. In: *Computers and Fluids*, 26(4) (1997) 395-415.

[52] Clift R., Grace J.R., Weber M.E. (1978). *Bubbles, Drops and Particles*. Academic Press, New York, 1978.

[53] Creber S.A., Vrouwenvelder J.S., Van Loosdrecht M.C.M., Johns M.L. (2010). Chemical Cleaning of Biofouling in Reverse Osmosis Membranes evaluated using Magnetic Resonance Imaging. In: *Journal of Membrane Science*, 362 (2010) 202-210.

[54] Cui Z.F., Chang S., Fane A.G. (2003). The Use of Gas Bubbling to Enhance Membrane Processes. In: *Journal of Membrane Science*, 221 (2003) 1-35.

[55] Çulfaz P.Z., Buetehorn S., Utiu L., Küppers M., Blümich B., Melin T., Wessling M., Lammertink R.G.H. (2010). Fouling Behavior of Microstructured Hollow Fiber Membranes in Dead-End Filtrations: Critical Flux Determination and NMR Imaging of Particle Deposition. In: *Langmuir*, 27(5) (2011) 1643-1652.

[56] Dasilva A., Heran M., Sintford C., Grasmick A. (2004). Optimization of Flow Shear Stress Through a Network of Capillary Fibers with the Use of CFD. In: *International Journal of Chemical Reactor Engineering*, 2(A23) (2004) 1-11.

[57] Davis R.H., Leighton D.T. (1987). Shear-Induced Transport of a Particle Layer along a Porous Wall. In: *Chemical Engineering Science*, 42(2) (1987) 275-281.

[58] Davis R.H., Birdsell S.A. (1987). Hydrodynamic Model and Experiments for Cross-Flow Microfiltration. In: *Chemical Engineering Communications*, 49 (1987) 217-234.

[59] Davis R.H. (1992). Modeling of Fouling of Crossflow Microfiltration Membranes. In: *Separation and Purification Methods*, 21(2) (1992) 75-126.

[60] Delnoij E., Kuipers J.A.M., Swaaij W.P.M. (1997). Computational Fluid Dynamics applied to Gas-Liquid Contactors. In: *Chemical Engineering Science*, 52 (1997) 3623-3631.

[61] Dentel S. (1997). Evaluation and Role of Rheological Properties in Sludge Management. In: *Water Science and Technology*, 36(11) (1997) 1-8.

[62] Dirckx C.J., Clark S.A., Hall L.D., Antalek B., Tooma J., Hewitt J.M., Kawaoka K. (2000). Magnetic Resonance Imaging of the Filtration Process. In: *AIChE Journal*, 46 (2000) 6-14.

[63] Donoghue C., Brideau M., Newcomer P., Pangrle B., DiBiasio D., Walsh E., Moore S. (1992). Use of Magnetic Resonance Imaging to Analyze the Performance of Hollow-Fiber Bioreactors. In: *Annals of the New York Academy of Sciences*, 665 (1992) 285-300.

[64] Drew D.A., Schonberg J.A., Belfort G. (1991). Lateral Inertial Migration of a Small Sphere in Fast Laminar Flow Through a Membrane Duct. In: *Chemical Engineering Science*, 46 (1991) 3219-3224.

[65] Drews A., Prieske H., Kraume M. (2008). Optimierung der Blasen- und Zirkulationsströmung in Membranbelebungsreaktoren. In: *Chemie Ingenieur Technik*, 12 (2008) 1795-1801.

[66] Drews A., Prieske H., Meyer E.L., Senger G., Kraume M. (2010). Advantageous and Detrimental Effects of Air Sparging in Membrane Filtration: Bubble Movement, Exerted Shear and Particle Classification. In: *Desalination*, 250 (2010) 1083-1086.

[67] Drews A. (2010). Membrane Fouling in Membrane Bioreactors – Characterisation, Contradictions, Cause and Cures. In: *Journal of Membrane Science*, 363 (2010) 1-28.

[68] Ducom G., Puech F.P., Cabassud C. (2002). Air Sparging with Flat Sheet Nanofiltration: A Link between Wall Shear Stresses and Flux Enhancement. In: *Desalination*, 145 (2002) 97-102.

[69] Dufresne R., Lebrun R.E., Lavallee H.C. (1997). Comparative Study on Fluxes and Performances during Papermill Wastewater Treatment with Membrane Bioreactor. In: *Canadian Journal of Chemical Engineering*, 75 (1997) 95-103.

[70] Dullien F.A.L. (1979). *Porous Media, Fluid Transport and Pore Structure*. Academic Press, UK, 1979.

[71] Eka Akzo Nobel (2005). *BINDZIL® 9950 Colloidal Silica*. Product data sheet, Bohus, Sweden, 2005.

[72] Fane A.G., Yeo A., Law A., Parameshwaran K., Wicaksana F., Chen V. (2005). Low Pressure Membrane Processes ~ Doing More with less Energy. In: *Desalination*, 185 (2005) 159-165.

[73] Ferziger J.H., Perić M. (2002). *Computational Methods for Fluid Dynamics*. Springer-Verlag, Berlin-Heidelberg/New York, 2002.

[74] Field R.W., Wu D., Howell J.A., Gupta B.B. (1995). Critical Flux Concept for Microfiltration Fouling. In: *Journal of Membrane Science*, 100 (1995) 259-272.

[75] Fimbres-Weihs G.A., Wiley D.E. (2007). Numerical Study of Mass Transfer in Three-Dimensional Spacer-Filled Narrow Channels with Steady Flow. In: *Journal of Membrane Science*, 306 (2007) 228-243.

[76] Fischer E., Raasch J. (1984). Querstromfiltration. In: *Chemie Ingenieur Technik*, 56(8) (1984) 573-578.

[77] Frahm J., Haase A., Matthaei D. (1986a). Rapid NMR Imaging of Dynamic Processes using the FLASH Technique. In: *Magnetic Resonance Medicine*, 3(2) (1986) 321-327.

[78] Frahm J., Haase A., Matthaei D. (1986b). Rapid 3-Dimensional MR Imaging using the FLASH Technique. In: *Journal of Computer Assisted Tomography*, 10(2) (1986) 363-368.

[79] Fujita K., Takizawa S. (1994). Study on Hydraulics of Backwashing and Air-Scrubbing in Hollow Fiber Filtration. In: *Journal of Japan Water Works Association*, 63(3) (1994) 94-101.

[80] Futselaar H., Zoontjes R.J.C., Reith T., Rácz I.G. (1993). Economics Comparison of Transverse and Longitudinal Flow Hollow Fibre Membrane Modules for Reverse Osmosis and Ultrafiltration. In: *Desalination*, 90 (1993) 345-361.

[81] Gerhards G. (2010). *Bearbeitung von Röntgentomographieaufnahmen in MATLAB® als Grundlage für Computational Fluid Dynamics (CFD)-Simulationen*. Mini Thesis, Chemical Process Engineering (AVT.CVT), RWTH Aachen University, Germany, February 2010.

[82] Ghidossi R., Daurelle J.V., Veyret D., Moulin P. (2006a). Simplified CFD Approach of a Hollow Fiber Ultrafiltration System. In: *Chemical Engineering Journal*, 123 (2006) 117-125.

[83] Ghidossi R., Veyret D., Moulin P. (2006b). Computational Fluid Dynamics applied to Membranes: State of the Art and Opportunities. In: *Chemical Engineering and Processing*, 45(6) (2006) 437-454.

[84] Ghosh R., Cui Z.F. (1999). Mass Transfer in Gas-Sparged Ultrafilration: Upward Slug Flow in Tubular Membranes. In: *Journal of Membrane Science*, 162 (1999) 91-103.

[85] Gourgues C., Aimar P., Sanchez V. (1992). Ultrafilration of Bentonite Suspensions with Hollow Fiber Membranes. In: *Journal of Membrane Science*, 74 (1992) 51-69.

[86] Granath K.A., Kvist B.E. (1967). Molecular Weight Distribution Analysis by Gel Chromatography on Sephadex. In: *Journal of Chromatography*, 28 (1967) 69-81.

[87] Green G., Belfort G. (1980). Fouling of Ultrafiltration Membranes: Lateral Migration and the Particle Trajectory Model. In: *Desalination*, 35 (1980) 129-147.

[88] Günder B. (1999). *Das Membranbelebungsverfahren in der kommunalen Abwasserreinigung*. Kommissionsverlag R. Oldenbourg, München, 1999.

[89] Guibert D., Ben Aim R., Rabie H., Cote P. (2002). Aeration Performance of Immersed Hollow-Fiber Membranes in a Bentonite Suspension. In: *Desalination*, 148 (2002) 395-400.

[90] Haase A., Frahm J., Matthaei D., Hanicke W., Merboldt K.D. (1986a). FLASH Imaging – Rapid NMR Imaging using Low Flip-Angle Pulses. In: *Journal of Magnetic Resonance*, 67(2) (1986) 258-266.

[91] Haase A., Matthaei D., Hanicke W., Frahm J. (1986b). Dynamic Digital Subtraction Imaging using Fast Low-Angle Shot MR Movie Sequence. In: *Radiology*, 160 (1986) 537-541.

[92] Hammer B.E., Heath C.A., Mirer S.D., Belfort G. (1990). Quantitative Flow Measurements in Bioreactors by Nuclear Magnetic Resonance Imaging. In: *Biotechnology*, 8 (1990) 327-330.

[93] Han X. (2010). *Bewertung unterschiedlicher Belüftungsstrategien zur Deckschichtkontrolle in getauchten Membranbioreaktorprozessen*. Mini Thesis,

Chemical Process Engineering (AVT.CVT), RWTH Aachen University, Germany, in preparation.

[94] Hardy P.A., Poh C.K., Liao Z., Clark W.R., Gao D. (2002). The Use of Magnetic Resonance Imaging and to Measure the Local Ultrafiltration Rate in Hemodialyzers. In: *Journal of Membrane Science*, 204 (2002) 195-205.

[95] Hartmant P., Aimar P. (1996). Coagulation of Colloids Retained by Porous Wall. In: *AIChE Journal*, 42(12) (1996) 3523-3532.

[96] Heath C.A., Belfort G., Hammer B.E., Mirer S.D., Pimbley J.M. (1990). Magnetic Resonance Imaging and Modelling of Flow in Hollow-Fiber Bioreactors. In: *AIChE Journal*, 36(4) (1990) 547-558.

[97] Henze M., Grady Jr. C., Gujer W., Marias T., Matsuo T. (1987). *Activated Sludge Model No. 1*. Arrowsmith Ltd., Bristol, 1987.

[98] Hermia J. (1982). Constant Pressure Blocking Filtration Laws – Application to Power-Law Non-Newtonian Fluids. In: *Transactions of the Institution of Chemical Engineers*, 60 (1982) 183-187.

[99] Hirt C.W., Nichols B.D. (1981). Volume of Fluid (VOF) Method for the Dynamics of Free Boundaries. In: *Journal of Computational Physics*, 39(1) (1981) 201- 225.

[100] Hlavacek M., Bouchet F. (1993). Constant Flowrate Blocking Laws and an Example of their Application to Dead-End Microfiltration of Protein Solutions. In: *Journal of Membrane Science*, 82 (1993) 285-295.

[101] Hlavacek M., Remy J.F. (1995). Simple Relationships among Zeta-Potential, Particle Size Distribution, and Cake Specific Resistance for Colloid Suspensions Coagulated with Ferric Chloride. In: *Separation Science and Technology*, 30(4) (1995) 549-563.

[102] Hong S., Faibish R.S., Elimelech M. (1997). Kinetics of Permeate Flux Decline in Crossflow Membrane Filtration of Colloidal Suspensions. In: *Journal of Colloidal and Interface Science*, 196 (1997) 267-277.

[103] Hounsfield G.N. (1973). Computerized transverse axial scanning (tomography): Part I. Description of system. In: *British Journal of Radiology*, 46 (1973) 1016-1022.

[104] Horsfield M.A., Fordham E.J., Hall C., Hall L.D. (1989). ^{1}H NMR Imaging Studies of Filtration in Colloidal Suspensions. In: *Journal of Magnetic Resonance*, 81 (1989) 593-596.

[105] Hout R.V., Gulitsaki A., Barnea D., Shemer L. (2002). Experimental Investigation of the Velocity Field induced by a Taylor Bubble rising in a Stagnant Water. In: *International Journal of Multiphase Flow*, 28 (2002) 579-596.

[106] Hwang K., Liu H., Lu W. (1998). Local Properties of Cake in Cross-Flow Microfiltration of Submicron Particles. In: *Journal of Membrane Science*, 138 (1998) 181-192.

[107] Hwang K.J., Yu Y.H., Lu W.M. (2001) Cross-Flow Microfiltration of Submicron Microbial Suspension. In: *Journal of Membrane Science*, 194 (2001) 229-243.

[108] Hwang K.J., Liu H.C. (2002). Cross-Flow Microfiltration of Aggregated Submicron Particles. In: *Journal of Membrane Science*, 201 (2002) 137-148.

[109] Jajuee B., Margaritis A., Karamanev D., Bergougnou M.A. (2006). Measurements and CFD Simulations of Gas Holdup and Liquid Velocity in Novel Airlift Membrane Contactor. In: *AIChE Journal*, 52(12) (2006) 4079-4089.

[110] Jönsson A.S., Jönsson B. (1996). Ultrafiltration of Colloidal Dispersions – A Theoretical Model of the Concentration Polarization Phenomena. In: *Journal of Colloid and Interface Science*, 180 (1996) 504-518.

[111] Joshi J.B. (2001). Computational Flow Modelling and Design of Bubble Column Reactors. In: *Chemical Engineering Science*, 56 (2001) 5893-5933.

[112] Judd S. (2006). *The MBR-Book – Principles and Applications of Membrane Bioreactors in Water and Wastewater Treatment*. Elsevier, Amsterdam, 2006.

[113] Kang. C.W., Hua J., Lou J., Liu W., Jordan E. (2008). Bridging the Gap between Membrane Bioreactor (MBR) Pilot and Plant Studies. In: *Journal of Membrane Science*, 325 (2008) 861-871.

[114] Kilian H. (2009). *Experimentelle Untersuchung des Filtrationsverhaltens von Mikrofiltrations-Hohlfasermembranen für unterschiedliche Betriebsweisen unter Verwendung einer SiO_2-Modelldispersion*. Diploma Thesis, Chemical Process Engineering (AVT.CVT), RWTH Aachen University, Germany, ´December 2009.

[115] Koch Membrane Systems GmbH (2008). *PURON® Hollow Fiber Module – Hollow Fiber Submerged Membrane Module for MBR Applications*. Product data sheet, Aachen, Germany, 2008.

[116] Kwon D.Y., Vigneswaran S., Fane A.G., Ben Aim R. (2000). Experimental Determination of Critical Flux in Cross-Flow Microfiltration. In: *Separation and Purification Technology*, 19 (2000) 169-181.

[117] Laborie S., Cabassud C., Durand-Bourlier L., Lainé J.M. (1997). Flux Enhancement by a Continuous Tangential Gas Flow in Ultrafiltration Hollow Fibres for Drinking Water Production: Effects of Slug-Flow on Cake Structure. In: *Filtration and Separation*, 34(8) (1997) 887-891.

[118] Lattermann C. (2009). *Konstruktion einer Testzelle zur Druckverkustmessung in Hohlfasermembranmodulen unterschiedlicher Packungsdichte*. Mini Thesis, Chemical Process Engineering (AVT.CVT), RWTH Aachen University, Germany, March 2009.

[119] Laukemper-Ostendorf S., Lemke H.D., Blümler P., Blümich B. (1998). NMR Imaging of Flow in Hollow Fiber Hemodialyzers. In: *Journal of Membrane Science*, 138 (1998) 287-295.

[120] Le-Clech P., Jefferson B., Chang I.S., Judd S.J. (2003). Critical Flux Determination by the Flux-Step Method in a Submerged Membrane Bioreactor. In: *Journal of Membrane Science*, 227 (2003) 81-93.

[121] Le-Clech P., Chen V., Fane A.G. (2006). Fouling in Membrane Bioreactors used in Wastewater Treatment. In: *Journal of Membrane Science*, 284 (2006) 17-53.

[122] Lei Y.G., He Y.L., Chu P., Li R. (2008). Design and Optimization of Heat Exchangers with Helical Baffles. In: *Chemical Engineering Science*, 63 (2008) 4386-4395.

[123] Leighton D., Acrivos A. (1987a). Measurement of Shear-Induced Self-Diffusion in Concentrated Suspensions of Spheres. In: *Journal of Fluid Mechanics*, 177 (1987) 109-131.

[124] Leighton D., Acrivos A. (1987b). The Shear-Induced Migration of Particles in Concentrated Suspensions In: *Journal of Fluid Mechanics*, 181 (1987) 415-439.

[125] Leonard E.F., Vassilieff C.S. (1984). The Deposition of Rejected Matter in Membrane Separation Processes. In: *Chemical Engineering Communications*, 30 (1984) 209-217.

[126] Li H., Fane A.G., Coster H.G.L., Vigneswaran S. (1998). Direct Observation of Particle Deposition on the Membrane Surface During Crossflow Microfiltration. In: *Journal of Membrane Science*, 149 (1998) 83-97.

[127] Li H., Fane A.G., Coster H.G.L., Vigneswaran S. (2000). An Assessment of Depolarisation Models of Crossflow Microfiltration by Direct Observation Through the Membrane. In: *Journal of Membrane Science*, 172 (2000) 135-147.

[128] Liu R., Huang X., Sun Y.F., Qian Y. (2003). Hydrodynamic Effect on Sludge Accumulation over Membrane Surfaces in a Submerged Membrane Bioreactor. In: *Process Biochemistry*, 39 (2003) 157-163.

[129] Lotito V., Spinosa L., Mininni G., Antonacci R. (1997). The Rheology of Sewage Sludge at Different Steps of Treatment. In: *Water Science and Technology*, 36(11) (1997) 79-85.

[130] Lu W.M., Ju S.C. (1989). Selective Particle Deposition in Crossflow Filtration. In: *Separation Science and Technology*, 24(7+8) (1989) 517-540.

[131] Lu W.M., Hwang K.J. (1993). Mechanism of Cake Formation in Constant Pressure Filtrations. In: *Separations Technology*, 3(3) (1993) 122-32.

[132] Lu W.M., Hwang K.J. (1995). Cake Formation in 2-D Cross-Flow Filtration. In: *AIChE Journal*, 41(6) (1995) 1443-1455.

[133] Lyko S., Al-Halbouni D., Wintgens T., Janot A., Hollender J., Dott W., Melin T. (2007). Polymeric Compounds in Activated Sludge Supernatant – Characterisation and Retention Mechanisms at a Full-Scale Municipal Membrane Biorecator. In: *Water Research*, 41 (2007) 3894-3902.

[134] Lyko S., Wintgens T., Al-Halbouni D., Baumgarten S., Tacke D., Drensla K., Janot A., Dott W., Pinnekamp J., Melin T. (2008). Long-Term Monitoring of a Full-Scale Membrane Biorecator – Characterisation of Foulants and Operational Performance. In: *Journal of Membrane Science*, 317 (2008) 78-87.

[135] Mahr B., Mewes D. (2007). CFD Modelling and Calculation of Dynamic Two-Phase Flow in Columns Equipped with Structured Packing. In: *IChemE*, 85(A8) (2007) 1112-1122.

[136] Mahr B., Mewes D. (2008). Two-Phase Flow in Structured Packings: Modeling and Calculation on a Macroscopic Scale. In: *AIChE Journal*, 54(3) (2008) 614-626.

[137] Marselina Y., Lifia, Le-Clech P., Stuetz R.M., Chen V. (2009). Characterisation of Membrane Fouling Deposition and Removal by Direct Observation Technique. In: *Journal of Membrane Science*, 341 (2009) 163-171.

[138] Martinelli L., Guigui C., Line A. (2010). Characterisation of Hydrodynamics induced by Air Injection related to Membrane Fouling Behaviour. In: *Desalination*, 250 (2010) 587-591.

[139] Matthaei D., Frahm J., Haase A., Hanicke W. (1985). Regional Physiological Functions Depicted by Sequences of Rapid Magnetic Resonance Images. In: *LANCET*, 2(8460) (1985) 893-893.

[140] Meier J.G. (2008). *Auswirkungen von Pulveraktivkohle auf die Nanofiltration von Kläranlagenablauf*. Ph.D. Thesis, Chemical Process Engineering (AVT.CVT), RWTH Aachen University, Germany, URN: urn:nbn:de:hbz:82-opus-25562, June 2009.

[141] Melin T., Rautenbach R. (2007). *Membranverfahren – Grundlagen der Modul- und Anlagenauslegung*. Springer-Verlag, Berlin/Heidelberg, 2007.

[142] Menter F.R. (1994). Two-Equation Eddy-Viscosity Turbulence Models for Engineering Applications. In: *AIAA Journal*, 32(8) (1994) 1598-1605.

[143] Metzger U., Le-Clech P., Stuetz R.M., Frimmel F.H., Chen V. (2007). Characterisation of Polymeric Fouling in Membrane Bioreactors and the Effect of Different Filtration Modes. In: *Journal of Membrane Science*, 301 (2007) 180-189.

[144] Michaels A.S. (1968). New Separation Technique for the CPI. In: *Chemical Engineering Progress*, 64(12) (1968) 31-43.

[145] Mikkelsen L. (2001). The Shear Sensitivity of Activated Sludge – Relations to Filterability, Rheology and Surface Chemistry. In: *Colloids and Surfaces*, 182 (2001) 1-14.

[146] Moeller G., Torres L.G. (1997). Rheological Characterization of Primary and Secondary Sludges treated by both Aerobic and Anaerobic Digestion. In: *Bioresource Technology*, 61 (1997) 207-211.

[147] Moshage U. (2004). *Rheologie kommunaler Klärschlämme – Methoden und Praxisrelevanz*. Ph.D. Thesis, Gesellschaft zur Förderung des Institutes für Siedlungswasserwirtschaft an der Technischen Universität Braunschweig, ISSN: 0934-9731, Braunschweig, 2004.

[148] Mulder M. (1996). *Basic Principles of Membrane Technology*. Kluwer Academic Publishers, Dordrecht, 1996.

[149] Mulherkar P., Van Reis R. (2004). Flex Test: A Fluorescent Dextran Test for UF Membrane Characterization. In: *Journal of Membrane Science*, 236 (2004) 171-182.

[150] Nagaoka H., Ueda S., Miya A. (1996). Influence of Bacterial Extracellular Polymers on the Membrane Separation Activated Sludge Process. In: *Water Science and Technology*, 34(9) (1996) 165-172.

[151] Nakanishi K., Tadokoro T., Matsuno R. (1987). On the Specific Resistance of Microorganisms. In: *Chemical Engineering Communications*, 62 (1987) 187-201.

[152] Nakoryacov V.E., Kashinsky O.N., Petukhov A.V., Gorelik R.S. (1989). Study of Local Hydrodynamic Characteristics of Upward Slug-Flow. In: *Experiments in Fluids*, 7 (1989) 560-566.

[153] Ndinisa N.V., Wiley D.E., Fletcher D.F. (2005). Computational Fluid Dynamics Simulations of Taylor Bubbles in Tubular Membranes – Model Validation and Application to Laminar Flow Systems. In: *Chemical Engineering Research and Design*, 83(A1) (2005) 40-49.

[154] Ndinisa N.V., Fane A.G., Wiley D.E., Fletcher D.F. (2006). Fouling Control in a Submerged Flat Sheet Membrane System: Part II – Two-Phase Flow Characterization and CFD Simulations. In: *Separation Science and Technology*, 41 (2006) 1411-1445.

[155] Nogueira S., Riethmuler M.L., Campos J.B.L.M., Pinto A.M.F.R. (2006). Flow in the nose Region and Annular Film Around a Taylor Bubble Rising Through Vertical Columns of Stagnant and Flowing Newtonian Liquids. In: *Chemical Engineering Science*, 61 (2006) 845-857.

[156] Pangrle B.J., Walsh E.G., Moore S.C., DiBiasio D. (1989). Investigation of Fluid Flow Patterns in a Hollow Fibre Module using Magnetic Resonance Velocity Imaging. In: *Biotechnology Techniques*, 3 (1989) 67-72.

[157] Pangrle B.J., Walsh E.G., Moore S.C., DiBiasio D. (1992). Magnetic Resonance Imaging of Laminar Flow in Porous Tube and Shell Systems. In: *Chemical Engineering Science*, 47 (1992) 517-526.

[158] Petsev D.N., Starov V.M., Ivanov I.B. (1993). Concentrated Dispersions of Charged Colloidal Particles: Sedimentation, Ultrafiltration and Diffusion. In: *Colloids and Surfaces A*, 81 (1993) 65-81.

[159] Pignon F., Magnin A., Piau J.M., Cabane B., Aimer P., Meireles M., Lindner P. (2000). Structural Characterisation of Deposits Formed during Frontal Filtration. In: *Journal of Membrane Science,* 174 (2000) 189-204.

[160] Pinnekamp J., Friedrich H. (2003). *Membrane Technology for Waste Water Treatment*. FiW, Aachen, 2006.

[161] Pöyry GKW GmbH (2009). *Ermittlung energetischer Beurteilungskriterien für Membrankläranlagen mit Hohlfasermodulen und deren Verifizierung am Beispiel einer Großanlage*. Final report of the research project, Essen, Germany, February 2009.

[162] Poh C.K., Hardy P.A., Liao Z.J., Huang Z., Clark W.R., Gao D.Y. (2003a). Effect of Spacer Yarns on the Dialysate Flow Distribution of Hemodialyzers: A Magnetic Resonance Imaging Study. In: *ASAIO Journal*, 49 (2003) 440-448.

[163] Poh C.K., Hardy P.A., Liao Z.J., Huang Z., Clark W.R., Gao D. (2003b). Effect of Flow Baffles on the Dialysate Flow Distribution of Hollow-Fiber Hemodialyzers: A Nonintrusive Experimental Study using MRI. In: *Journal of Biomechanical Engineering*, 125 (2003) 481-489.

[164] Pope J.M., Yao S. (1993). Quantitative NMR Imaging of Flow. In: *Concepts in Magnetic Resonance Part A*, 5(4) (1993) 281-302.

[165] Pope J.M., Yao S., Fane A.G. (1996). Quantitative Measurements of the Concentration Polarisation Layer Thickness in Membrane Filtration of Oil-Water Emulsions using NMR Micro-Imaging. In: *Journal of Membrane Science*, 118 (1996) 247-257.

[166] Porter M.C. (1972). Concentration Polarization with Membrane Ultrafiltration. In: *Industrial and Engineering Chemistry, Product Research and Development*, 11 (1972) 234-248.

[167] Prado C. (2010). *Bildauswertung in MATLAB zur Untersuchung der Deckschichtbildung in getauchten Mikrofiltrationsprozessen.* Mini Thesis, Chemical Process Engineering (AVT.CVT), RWTH Aachen University, Germany, in preparation.

[168] Proff E., Lohmann J. (1997). Rheologische Charakterisierung flüssiger Klärschlämme. In: *Korrespondenz Abwasser*, 44(9) (1997) 1615-16-21.

[169] Prieske H., Drews A., Kraume M. (2008). Prediction of the Circulation Velocity in a Membrane Bioreactor. In: *Desalination*, 231 (2008) 219-226.

[170] Rahmat K.A. (2009). *Modelling the Pressure Drop of a Single Phase Flow Through Hollow-Fibre Bundles of Different Packing Density*. Diploma Thesis, Chemical Process Engineering (AVT.CVT), RWTH Aachen University, Germany, May 2009.

[171] Ratkovich N., Chan C.C.V., Berube P.R., Nopens I. (2009). Experimental Study and CFD Modelling of a Two-Phase Slug Flow for an Airlift Tubular Membrane. In: *Chemical Engineering Science*, 64 (2009) 3576-3584.

[172] Rautenbach R., Schock G. (1988). Ultrafiltration of Macromolecular Solutions and Cross-Flow Microfiltration of Colloidal Suspensions. A Contribution to Permeate Flux Calculations. In: *Journal of Membrane Science*, 36 (1988) 231-242.

[173] Reid R.C., Prausnitz J.M., Poling B.E. (1987). *The Properties of Gases and Liquids*. McGraw-Hill, New York, 1987.

[174] Romero C.A., Davis R.H. (1988). Global Model of Cross-Flow Microfiltration Based on Hydrodynamic Particle Diffusion. In: *Journal of Membrane Science*, 39 (1988) 157-185.

[175] Romero C.A., Davis R.H. (1990). Transient Model of Cross-Flow Microfiltration. In: *Chemical Engineering Science*, 45 (1990) 13-25.

[176] Rosenberger S., Kubin K., Kraume M. (2002). Rheology of Activated Sludge in Membrane Bioreactors. In: *Engineering in Life Sciences*, 2(9) (2002) 269-275.

[177] Rosenberger S. (2003). *Charakterisierung von belebtem Schlamm in Membranbelebungsreaktoren zur Abwasserreinigung*. Ph.D. Thesis, VDI-Verlag, Düsseldorf, 2003.

[178] Saalbach J., Hunze M. (2008). Flow Structures in MBR-Tanks. In: *Water Science and Technology*, 57(5) (2008) 699-705.

[179] Schmitz P., Wandelt B., Houi D., Hildenbrand M. (1993). Particle Aggregation at the Membrane Surface in Crossflow Microfilration. In: *Journal of Membrane Science*, 84 (1993) 171-183.

[180] Schulz W. (2007). *Untersuchung der Foulingeigenschaften von Hohlfasermembranen in getauchten Systemen in der kommunalen Abwasserbehandlung*. Diploma Thesis, Chemical Process Engineering (AVT.CVT), RWTH Aachen University, Germany, June 2007.

[181] Sethi S., Wiesner M.R. (1997). Modeling of Transient Permeate Flux in Cross-Flow Membrane Filtration Incorporating Multiple Particle Transport Mechanisms. In: *Journal of Membrane Science*, 136 (1997) 191-205.

[182] Sigloch H. (1991). *Technische Fluidmechanik*. VDI-Verlag, Düsseldorf, 1991.

[183] Slatter P. (1997). The Rheological Characterisation of Sludges. In: *Water Science and Technology*, 36(11) (1997) 9-18.

[184] Sofia A., Ng W.J., Ong S.L. (2004). Engineering Design Approaches for Minimum Fouling in Submerged MBR. In: *Desalination*, 160 (2004) 67-74.

[185] Somoza Parada I. (2010). *Untersuchung der Deckschichtbildung und der permeatseitigen Geschwindigkeitsverteilung eines Mikrofiltrationsprozesses mittels Nuclear Magnetic Resonance (NMR) Imaging*. Mini Thesis, Chemical Process Engineering (AVT.CVT), RWTH Aachen University, Germany, February 2010.

[186] Song L. (1998). Flux Decline in Crossflow Microfiltration and Ultrafiltration: Mechanisms and Modeling of Membrane Fouling. In: *Journal of Membrane Science*, 139 (1998) 183-200.

[187] Song L., Elimelech M. (1995). Theory of Concentration Polarization in Cross-Flow Filtration. In: *Journal of the Chemical Society, Faraday Transactions*, 91 (1995) 3389-3398.

[188] Ståhlberg F., Nordell B., Ericsson A., Greitz T., Perrson B., Sperber G. (1986). Quantitative Study of Flow Dependence in NMR Images at low Flow Velocities. In: *Journal of Computer Assisted Tomography*, 10(6) (1986) 1006-1015.

[189] Stamatakis K., Tien C. (1993). A Simple Model of Cross-Flow Filtration Based on Particle Adhesion. In: *AIChE Journal*, 39(8) (1993) 1292-1302.

[190] Stodollick J. (2010). *Messen des Druckverlustes während der Durchströmung von Hohlfasermembranmodulen unterschiedlicher Packungsdichte*. Mini Thesis, Chemical Process Engineering (AVT.CVT), RWTH Aachen University, Germany, February 2010.

[191] Sulaiman M.Z., Sulaiman N.M., Abdellah B. (2001). Prediction of Dynamic Permeate Flux During Cross-Flow Ultrafiltration of Polyethylene Glycol Using Concentration Polarization-Gel Layer Model. In: *Journal of Membrane Science*, 189 (2001) 151-165.

[192] Sur H.W., Cui Z.F. (2001). Experimental Study on the Enhancement of Yeast Microfiltration with Gas Sparging. In: *Journal of Chemical Technology and Biotechnology*, 76 (2001) 477-484.

[193] Taha T., Cui Z.F. (2002). CFD Modelling of Gas Sparged Ultrafiltration in Tubular Membranes. In: *Journal of Membrane Science*, 210 (2002) 13-27.

[194] Taha T., Cheong W.L., Field R.W., Cui Z.F. (2006a). Gas-Sparged Ultrafiltration ising Horizontal and Inclined Tubular Membranes – A CFD Study. In: *Journal of Membrane Science*, 279 (2006) 487-494.

[195] Taha T., Cui Z.F. (2006b). CFD Modelling of Slug Flow Inside Square Capillaries. In: *Chemical Engineering Science*, 61 (2006) 665-675.

[196] Tarabara V.V., Koyuncu I., Wiesner M.R. (2004). Effect of Hydrodynamics and Solution Ionic Strength on Permeate Flux in Cross-Flow Filtration: Direct Experimental Observation of Filter Cake Cross-Sections. In: *Journal of Membrane Science*, 241 (2004) 65-78.

[197] Tollkoetter A. (2010). *Numerische Simulation einer mehrphasigen Strömung durch ein Hohlfasermembranmodul*. Mini Thesis, Chemical Process Engineering (AVT.CVT), RWTH Aachen University, Germany, August 2010.

[198] Truckenbrodt E. (1988). *Lehrbuch der angewandten Fluidmechanik*. Springer-Verlag, Berlin/Heidelberg, 1988.

[199] Ueda T., Hata K., Kikuoka Y., Seino O. (1997). Effects of Aeration on Suction Pressure in a Submerged Membrane Bioreactor. In: *Water Research*, 31(3) (1997) 489-494.

[200] Utiu L. (2011). *Functional NMR and MRI for Analysis of Materials.* Ph.D. Thesis, Macromolecular Chemistry (ITMC), RWTH Aachen University, Germany, in preparation.

[201] Van der Marel P., Zwijnenburg A., Kemperman A., Wessling M., Temmink H., Van der Meer W. (2009). An Improved Flux-Step Method to Determine the Critical Flux and the Critical Flux for Irreversibility in a Membrane Bioreactor. In: *Journal of Membrane Science*, 332 (2009) 24-29.

[202] VDI-Gesellschaft Verfahrenstechnik und Chemieingenieurwesen (1997). *VDI-Wärmeatlas – Berechnungsblätter für den Wärmeübergang*. Springer-Verlag, Berlin/Heidelberg, 1997.

[203] Volmering D. (2007). *Analyse der chemischen Reinigung des Puron-Modulsystems*. Mini Thesis, Chemical Process Engineering (AVT.CVT), RWTH Aachen University, Germany, February 2007.

[204] Waite T.D., Schafer A.I., Fane A.G., Heuer A. (1999). Colloidal Fouling of Ultrafiltration Membranes: Impact of Aggregate Structure and Size. In: *Journal of Colloid and Interface Science*, 212 (1999) 264-274.

[205] Wakeman R.J. (1994). Visualisation of Cake Formation in Crossflow Microfiltration. In: *Trans IChemE*, 72(A) (1994) 530-540.

[206] Wandelt B., Schmitz P., Houi D. (1993). Investigations of Transient Phenomena in Crossflow Microfiltration of Colloidal Suspensions using NMR Micro-Imaging. In: *Proceedings of the 6th World Filtration Congress*, Nagoya, Japan, May 18-21, 1993.

[207] Wang Y., Howell J.A., Field R.W., Wu D. (1994). Simulation of Crossflow Filtration for Baffled Tubular Channels and Pulsatile Flow. In: *Journal of Membrane Science*, 95 (1994) 243-258.

[208] Wang L., Song L. (1999). Flux Decline in Crossflow Microfiltration and Ultrafiltration: Experimental Verification of Fouling Dynamics. In: *Journal of Membrane Science*, 160 (1999) 41-50.

[209] Wang Y., Brannock M., Cox S., Leslie G. (2010). CFD Simulations of Membrane Filtration Zone in a Submerged Hollow Fibre Membrane Bioreactor using a Porous Media Approach. In: *Journal of Membrane Science*, 363 (2010) 57-66.

[210] Wang X. (2010). *Bildauswertung in MATLAB zur Untersuchung der blaseninduzierten Faserbewegung in getauchten Hohlfasermembranmodulen*. Diploma Thesis, Chemical Process Engineering (AVT.CVT), RWTH Aachen University, Germany, September 2010.

[211] Weigand R.J., Altena F.W., Belfort G. (1985). Lateral Migration of Spherical Particles in Laminar Porous Tube Flows: Application to Membrane Filtration. In: *Physicochemical Hydrodynamics*, 6 (1985) 393-413.

[212] Wessling M. (2001). Two-Dimensional Stochastic Modelling of Membrane Fouling. In: *Separation and Purification Technology*, 24 (2001) 375-387.

[213] Wicaksana F., Fane A.G., Chen V. (2005). The Relationship between Critical Flux and Fibre Movement Induced by Bubbling in a Submerged Hollow Fibre System. In: *Water Science and Technology*, 51(6-7) (2005) 115-122.

[214] Wicaksana F., Fane A.G., Chen V. (2006). Fibre Movement induced by Bubbling using Submerged Hollow Fibre Membranes. In: *Journal of Membrane Science*, 271 (2006) 186-195.

[215] Wiesner M.R., Clark M.M., Mallevialle J. (1989). Membrane Filtration of Coagulated Suspensions. In: *Journal of Environmental Engineering*, 115(1) (1989) 20-40.

[216] Winterscheid C. (2009). *Untersuchung der blaseninduzierten Faserbewegung in getauchten Hohlfasermembranmodulen*. Mini Thesis, Chemical Process Engineering (AVT.CVT), RWTH Aachen University, Germany, August 2009.

[217] Yakhot V., Orszag S. (1986). Renormalization Group Analysis of Turbulence. I. Basic Theory. In: *Journal of Scientific Computing*, 1(1) (1986) 3-51.

[218] Yao S., Costello M., Fane A.G., Pope J.M. (1995a). Non-Invasive Observation of Flow Profiles and Polarisation Layers in Hollow Fibre Membrane Filtration Modules using NMR Micro-Imaging. In: *Journal of Membrane Science*, 99 (1995) 207-216.

[219] Yao S., Pope J.M., Fane A.G. (1995b). Chemical Shift Selective Flow Imaging: Applications in Membrane Filtration of Oil-Water Emulsions. In: *Bulletin of Magnetic Resonance*, 17 (1995) 220-221.

[220] Yao S., Fane A.G., Pope J.M. (1997). An Investigation of the Fluidity of Concentration Polarisation Layers in Crossflow Membrane Filtration of an Oil-Water Emulsion using Chemical Shift Selective Flow Imaging. In: *Journal of Magnetic Resonance Imaging*, 15 (1997) 235-242.

[221] Yeo A.P.S., Law A.W.K., Fane A.G. (2006). Factors Affecting the Performance of a Submerged Hollow Fiber Bundle. In: *Journal of Membrane Science*, 280 (2006) 969-982.

[222] Yeo A.P.S., Law A.W.K., Fane A.G. (2007). The Relationship between Performance of Submerged Hollow Fibers and Bubble-Induced Phenomena Examined by Particle Image Velocimetry. In: *Journal of Membrane Science*, 304 (2007) 125-137.

[223] Zhang J., Parker D.L., Leypoldt J.K. (1995). Flow Distributions in Hollow Fiber Hemodialyzers using Magnetic Resonance Fourier Velocity Imaging. In: *ASAIO Journal*, 41(3) (1995) M678-M682.

[224] Zhang M., Song L. (2000). Mechanisms and Parameters Affecting Flux Decline in Cross-Flow Microfiltration and Ultrafiltration of Colloids. In: *Environmental Science and Technology*, 34 (2000) 3767-3773.

[225] Zhang J., Chua H.C., Zhou J., Fane A.G. (2006). Factors Affecting the Membrane Performance in Submerged Membrane Bioreactors. In: *Journal of Membrane Science*, 284 (2006) 54-66.

[226] Zsigmondy R., Bachmann W. (1922). Filter and Method of Producing Same. *US Patent 1,421,341*, July 22, 1922.

(8) Annexe

(8.1) Estimation of relative deviations and enhancement factors

A sensitivity analysis to evaluate the impact of process parameters on the filtration performance can be found in sections (5) and (6). This comparison is based on determining relative deviations and the corresponding enhancement factors, which were estimated as follows.

The sixth data point of an exemplary data set shown in **Table (8.1)** and plotted in **Figure (8.1)** was chosen as a reference. This means that all deviations and enhancement factors are calculated relative to these reference operating conditions. Relative deviations of the function $y = f(x)$ are calculated as

$$\text{Relative deviation}\,[\%] = 100\,\frac{(y_{ref} - y_i)}{y_{ref}} \tag{8.1}$$

and the corresponding enhancement factors as

$$\text{Enhancement factor}\,[-] = \frac{\dfrac{y_i}{y_{ref}}}{\dfrac{x_i}{x_{ref}}}. \tag{8.2}$$

The relative deviation is a frequently-used measure for quantifying the impact of parameter variations on the filtration performance. The estimation of enhancement factors for different data points allows evaluating the (non-)proportionality of the function $y = f(x)$. More precisely, a proportional relationship between x and y as shown in **Figure (8.1)** is characterised by an enhancement factor of 1.0 for $i = 1, 2, \ldots, 10$. In contrast, an increase in enhancement factor with an increase in parameter x corresponds to a disproportionate impact on the process performance y ($dy/dx \uparrow$ with $x \uparrow$). Consistently, a decrease in enhancement factor indicates that the impact is levelling off in the range of higher x values ($dy/dx \downarrow$ with $x \uparrow$). This methodology is useful for evaluating data sets with only few measurement points, whereas simply fitting the measured data points is more appropriate for more comprehensive data sets.

x	x_1	x_2	x_3	x_4	x_5	$x_6 = x_{ref}$	x_7	x_8	x_9	x_{10}
y = f (x)	y_1	y_2	y_3	y_4	y_5	$y_6 = y_{ref}$	y_7	y_8	y_9	y_{10}

Table (8.1) Exemplary data set.

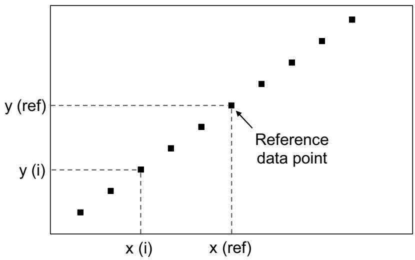

Figure (8.1) Estimation of relative deviations and enhancement factors.

(8.2) Additional figures

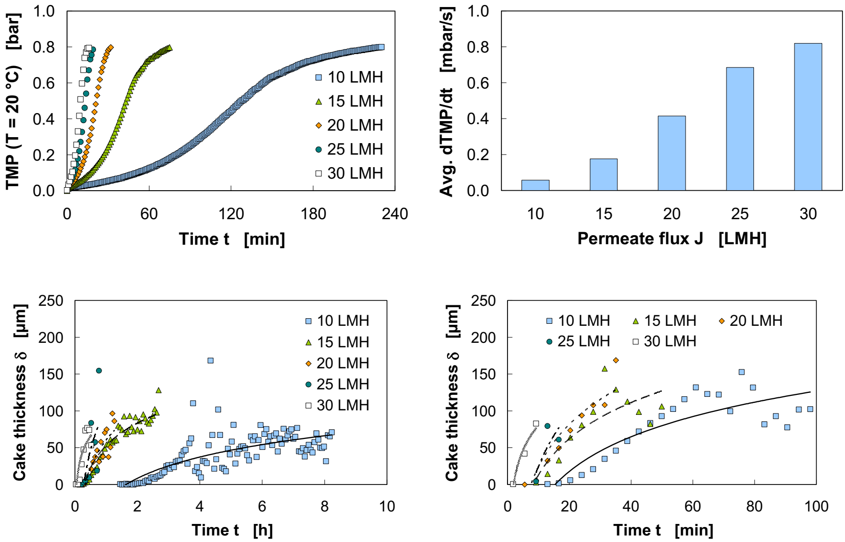

Figure (8.2) Impact of average permeate flux on the TMP evolution (top-left) and the fouling rate (top-right). Impact of average permeate flux on the evolution of cake layer thickness for c (SiO_2) = 0.2 vol. % (bottom-left) and c (SiO_2) = 0.6 vol. % (bottom-right) (y = 0 cm), see also **Figure (5.10)** and **Figure (5.11)**.

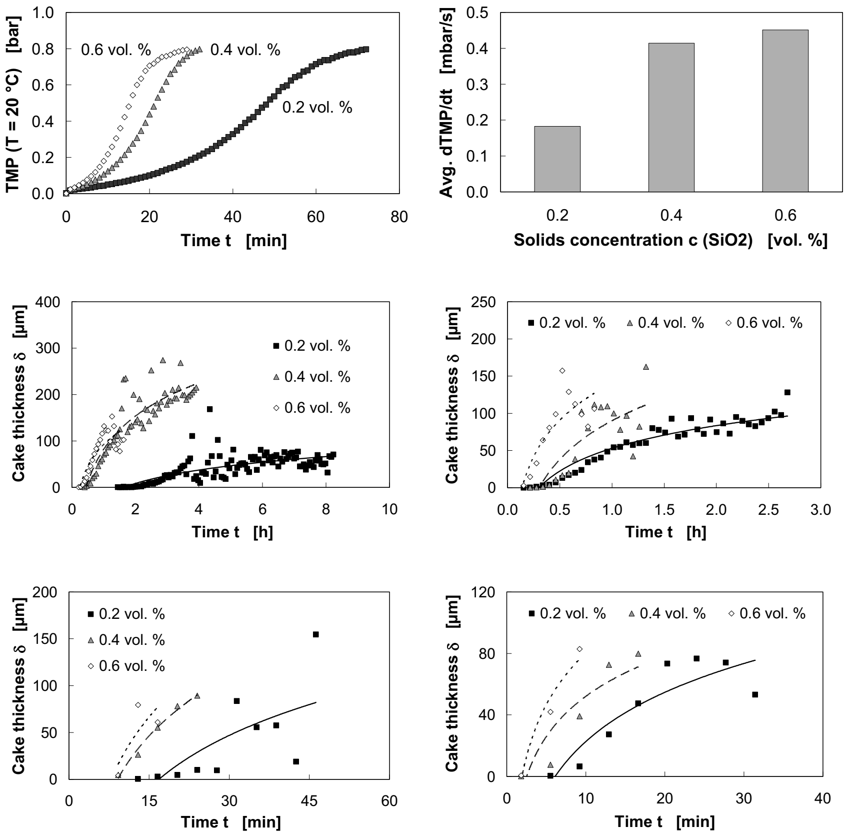

Figure (8.3) Impact of solids concentration on the TMP evolution (top-left) and the fouling rate (top-right). Impact of solids concentration on the evolution of cake layer thickness for J = 10 LMH (centre-left), J = 15 LMH (centre-right), J = 25 LMH (bottom-left) and J = 30 LMH (bottom-right) (y = 0 cm), see also **Figure (5.12)** and **Figure (5.13)**.

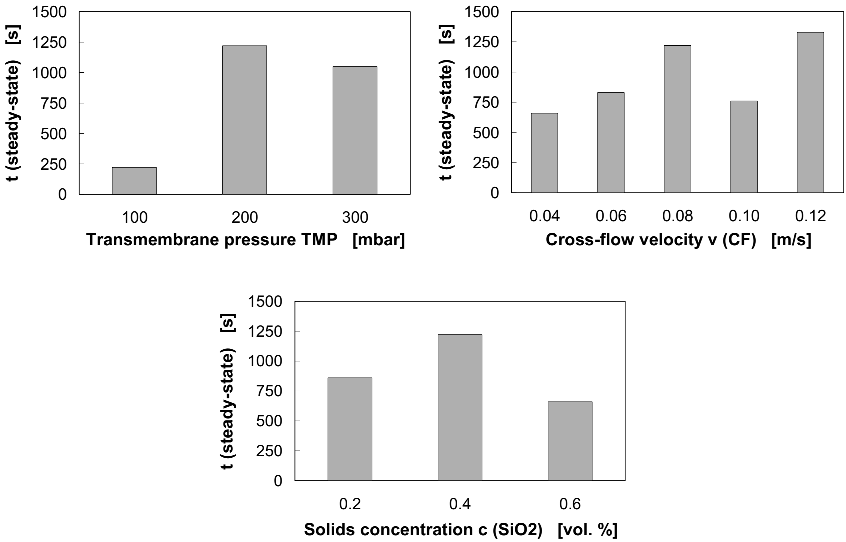

Figure (8.4) Impact of setpoint TMP (v_{CF} = 0.08 m/s, c (SiO_2) = 0.4 vol. %) (top-left), cross-flow velocity (TMP = 200 mbar, c (SiO_2) = 0.4 vol. %) (top-right) and solids concentration (TMP = 200 mbar, v_{CF} = 0.08 m/s (bottom) on the time to reach steady-state conditions for a single fibre cross-flow filtration.

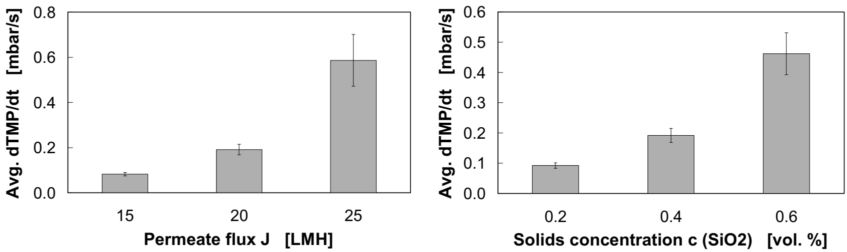

Figure (8.5) Impact of setpoint permeate flux (c (SiO_2) = 0.4 vol. %) (left) and solids concentration (J = 20 L/(m^2 h)) (right) on the average fouling rate for a submerged, quasi-tight single fibre (error bars according to equations (4.1) and (4.2), 540 s OFF – 60 s ON, p_{air} = 0.3 bar).

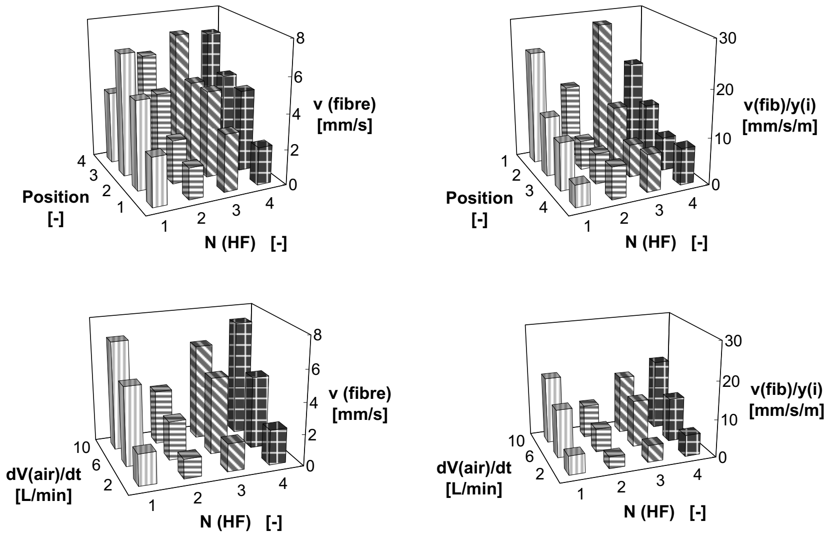

Figure (8.6) Time-averaged fibre velocity (left) and ratio of averaged fibre velocity and distance from the fibre potting (right) for different vertical positions ($dV_{air}/dt = 6$ L/min) (top) and aeration rates (position 2) (bottom) as a function of packing density.

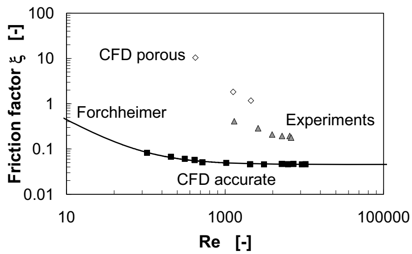

Figure (8.7) Friction factor as a function of Re number: Comparison of numerical results according to model 1 (CFD accurate + Forchheimer fit) and model 2 (CFD porous) with experimental results, see also **Figure (4.36)**.

(9) Curriculum vitae

Name:	Steffen Bütehorn
Date of birth:	August 15, 1979
Place of birth:	Großburgwedel, Germany

School & Military service

1992-1999	Gymnasium Mellendorf, Wedemark, Germany (Degree: Abitur)
1999-2000	Stabs- und Fernmeldebataillon 1, Rotenburg-Wümme, Germany

Academic education

2000-2002	Intermediate Diploma in Mechanical Engineering, Leibniz University of Hannover (LUH), Germany
2004	Student Research Project, Institute for Multiphase Processes (LUH): "*Measurement of Concentration Fields in Stirred Vessels using Laser Induced Fluorescence (LIF)*"
2004	Scholarship of the Dr.-Jürgen-Ulderup-Stiftung
2004	Student Research Project, Department of Chemical Engineering, University College London (UCL), UK: "*Catalytic Degradation of Polyethylene (PE) to Chemicals and Fuel over Zeolite-Based Catalysts as a Tertiary Polymer Recycling Process*"
2005	Diploma Thesis, Institute for Multiphase Processes (LUH): "*Modelling Anisotropic Pressure Drop in Structured Packings*"
2005	Diploma in Mechanical Engineering, Specialisation Energy Technology and Chemical Engineering (Degree: Dipl.-Ing.)
2005-2010	Ph.D. Student in Chemical Process Engineering (AVT.CVT), RWTH Aachen University, Germany
2008	Scholarship of the German Academic Exchange Service (DAAD)
2008	Professional Practicum Student, UNESCO Centre for Membrane Science and Technology, University of New South Wales (UNSW), Sydney, Australia
2010	Ph.D. in Mechanical Engineering, Specialisation Chemical Engineering